Static GTAW: experimental and numerical investigations and heat flux parameter estimation

Sreedhar Unnikrishnakurup

Collège Doctoral du Languedoc-Roussillon

THÈSE

Pour obtenir le grade de

Docteur

Délivré par l'**UNIVERSITÉ DE MONTPELLIER II**

Préparée au sein de l'école doctorale **I2S**
Et de l'unité de recherche **LMGC-UMR 5508**

Spécialité: **Mécanique et Génie Civil**

Présentée par **Sreedhar UNNIKRISHNAKURUP**

Etude expérimentale et numérique d'un essai de soudage TIG statique et estimation des paramètres du flux de chaleur

Soutenue le 29 janvier 2014 devant le jury composé de

L. Autrique	Professeur	Université Angers	Rapporteur
P. LE Masson	Professeur	Université de Bretagne Sud	Rapporteur
P. Paillard	Professeur	Université de Nantes	Président
S. Rouquette	MCF	Université Montpellier II	Co-encadrant
F. Soulié	MCF	Université Montpellier II	Co-encadrant
G. Fras	Professeur	Université Montpellier II	Directeur

UNIVERSITÉ MONTPELLIER 2
SCIENCES ET TECHNIQUES

I dedicate this thesis to

my parents

my wife

and

all my teachers

Contents

Abstract

Gas Tungsten Arc Welding (GTAW) process is generally used for assemblies that require high quality weld joint. The microstructure and the weld joint rely mainly on the thermal cycle due to the welding operation, the chemical composition of the metallic material and the complex flow of molten metal in the weld pool. Moreover the fluid flow in the weld pool play a major role in the temperature distribution and the final weld pool shape. Better understanding of the physical phenomena involved in the welding operation, more exactly in the weld pool, are the fundamental step for improving the GTAW operation, for example to increase the productivity and to avoid defects. In the present research work, a two dimensional axi-symmetric multiphysics model was established in order to predict the weld pool shape evolution in the frame of a static Gas Tungsten Arc Welding using a finite element numerical approach. The weld pool model included various driving forces such as self-induced electromagnetic (Lorentz force), surface tension (Marangoni force), buoyancy and the arc plasma drag force. The stated GTAW model is used for predicting the velocity and temperature distribution in the fusion zone and the final weld pool shape. In order to validate the GTAW model, an experimental set up was defined for synchronizing the acquisition of time dependent data such as temperature, weld pool radius and welding process parameters (current and voltage). Image processing algorithms were developed for the time dependent weld pool size identification from the high speed camera images. Comparison between experimental and calculated data exhibited quite good agreement but some discrepancies are still exist on the temperature field and weld pool radius. These discrepancies can be caused by the incoming heat flux from the arc plasma into the work piece. The heat flux was modeled with a Gaussian function itself described with few parameters;two of these required to be estimated: GTAW efficiency and Gaussian distribution. An inverse approach is used for estimating these parameters from the available experimental data: temperature, weld pool radius and macrographs. The Levenberg-Marquardt method is used to solve the inverse heat transfer problem coupled to an iterative process regularization. Afterward the inverse heat transfer problem was investigated through few numerical cases in order to verify its robustness to three sorts of error in the input data (measurement noise, sensor location error and inaccuracies associated with the thermophysical properties). The inverse approach was robust to errors introduced on measurement data. However, errors on the position of sensors or on the knowledge of material thermo-physical properties are problematic on the GTAW efficiency estimation. Finally the inverse problem was solved with experimental measurement. The estimated parameters are in good agreement with the literature. The evaluated error on the estimated parameters is less than 10%.

Resumé

Identification de la zone de fusion de soudure est important dans la recherche contemporaine pour optimiser procédé de soudage et achive soudures structurellement saines et relible. Il est bien connu dans la littérature que la taille et la forme de la zone de fusion finale est très dépendante sur le transfert de chaleur et l'écoulement du fluide dans la région de la piscine de soudure. Dans le présent travail de recherche, un modèle multiphysique 2D-axisymétrique a été créé dans le but de prédire l'évolution piscine en forme de soudure dans le cadre d'un soudage á l'arc de gaz de tungstène statique en utilisant une approche numérique par éléments finis. Le modèle de piscine soudure a été développé en tenant compte des différentes forces motrices dans la piscine convection de soudure comme électromagnétique auto-induite (force de Lorentz), la tension de surface (Marangoni vigueur), la flottabilité et la force de traînée de plasma d'arc. On constate que le modèle peut être efficacement utilisé pour la prédiction de la forme du bain de fusion, de la vitesse et de la distribution de la température dans la zone de fusion. Les résultats des simulations montrent la dépendance des principales forces motrices du développement de la piscine géométrie de la soudure et une comparaison raisonnable avec les données expérimentales pour l'acier inoxydable 304. Un dispositif expérimental fiable est utilisé pour l'acquisition et la synchronisation des différentes données expérimentales. algorithmes de traitement d'image ont été développés pour le temps de soudage piscine identification dépend de la taille des images de la caméra á haute vitesse. Comparaison entre les données expérimentales et calculées exposé des divergences importantes sur le champ de température. Ces écarts sont supposés être dû au flux de chaleur entrant dans le plasma d'arc dans la pièce de travail. Le flux de chaleur a été modélisé avec une fonction de Gauss lui-même décrit avec quelques paramètres, parmi ceux-ci deux ont été identifiés comme mal connu : l'efficacité TIG et de la distribution gaussienne. Une approche inverse est utilisée pour estimer ces paramètres á partir des données expérimentales disponibles : la température, le rayon de la piscine soudure et macrographies. La méthode de Levenberg-Marquardt est utilisé pour résoudre le problème de transfert de chaleur inverse couplée á un processus itératif d'estimation des paramètres comme le problème direct est tout á fait non linéaire. Une analyse approfondie de sensibilité a été réalisée afin de trouver la meilleure position pour les capteurs thermiques en tenant compte des conditions expérimentales sévères. Ensuite, le problème de transfert de chaleur inverse a été étudiée á travers quelques cas numériques afin de vérifier la robustesse de trois sortes d'erreurs dans les données d'entrée. La démarche inverse est robuste aux erreurs introduites sur les données de mesure. Toutefois, des erreurs sur la position de capteurs ou sur la connaissance des propriétés du matériau thermo-physiques sont problématiques sur l'efficacité de TIG d'estimation. Ces deux sortes d'erreurs peuvent être abordés á travers un pré rigoureux et une méthodologie expérimentale poste.

Acknowledgements

This thesis dissertation is a part of the three years of research work that has been carried out at the Welding research group (AS) of Mechanical and Civil Engineering Laboratory of University of Montpellier 2. During my stay at UM2, I have been supported by a great number of kind people who contributed to the present work. With immense pleasure I take this opportunity to convey my gratitude to all of them in my humble acknowledgement.

First of all I would like to thank my thesis supervisors, Dr. Sebastien Rouquette and Dr. Fabien Soulie for their initiation and supervision of this study and for their continuous support and engagement in the research work. I am grateful to the vibrant efforts and skilful leadership of both of them in this dissertation attaining its present form. Without those I would never have made it this far. Their guidance of the research effort, professional expertise, demand for excellence and encouragement brought the best from all involved. I gratefully acknowledge Pr. Gilles Fras for his advice and supervision. Thank you very much for the trust and confidence that you showed in me.

I would like to acknowledge University of Montpelier 2 and French National centre for scientific research (CNRS) for providing the financial support during my PhD studies.

I am also thankful to the previous and present members of the welding research team. Special mention must be made of Dr. Cyril Bordreuil for his helpful discussions and provoking comments which have been both inspirational and enjoyable. Many thanks to him for the help he provided during the data analysis of the high speed camera results. Other members include Reine Bonnet-Causse, Dr. Frederic Deschaux-Beaume and Denis Cervellin who provided their expertise and friendship. I would also like to acknowledge Aurelie Niel, Julien Chapuis, Vincent Villaret, Remi Lazarewicz, Alexis Chiocca, Bachir Mezrag and Romain Monier. My sincere thanks also go to the faculty members of GMP department of IUT Nimes.

I would like to acknowledge my thesis committee members Pr. Laurent Autrique, Pr. Philippe Le Masson and Pr. Pascal Paillard for their valuable advice and suggestions on my work. I am very appreciative to them for giving their time to review and comment on this thesis.

A special thanks to Wei Zhang, Abderrazak Traidia, Tuck Chow Choo and Zaki Saptari Saldi for their outstanding contributions in the welding research. Their thesis manuscripts gave me clear ideas when needed. Sincere thanks to all of you.

Moving towards more personal acknowledgements, I would like to execute a big of aggregated thanks towards all my family and friends[1]. I am proud of the warm friendships from my colleagues Sarah Amouri, Cecile Batier, Patrick Mutabaruka, Emna, Lhassan Amarsid, Kejtan Wojtacki, Paul Shumacker, Mahmoud, Adil Benaarbia, Benjamin and

[1] You know who you are.

Tariq Madani. The warm friendship from Indian friends at Montpellier throughout this period has been invaluable. I express my sincere gratitude to Bejoy, Nadendla Eswar, Kannan, Mathew Francis, Nicky Mathew, Bhoopathi, Manoj, Madhura Joshi and Anu Asokan. It is a pleasure to thank Christopher, Karine and Marianne for their friendship.

I am, of course, particularly indebted to my parents and my brother for their monumental, unwavering support and encouragement on all fronts. Particularly my mother, thank you for your continuous prayers. They have truly always been there for me, and without them none of this would have been even remotely possible. Thanks to my brother and his family who always help me whenever I need. I am also grateful to my parents-in-law for their love and support. Finally I would like to express my sincere gratitude to my wife Gayathri Manju for her patience, understanding and encouragement during the preparation of this thesis research. The past 18 months have been long adventurous accompanied with many wonderful and happy moments as well as some difficult and unpleasant times. Thank you for your love, sacrifices and strength.

Montpellier *Sreedhar UNNIKRISHNAKURUP*
February 2014

Introduction

Welding operation consists in a local melting of two metallic parts in order to assembly it. The required energy for melting the metallic material can be electric, chemical, laser beam etc. In Gas Tungsten Arc Welding (GTAW), the energy is provided by an electrical arc generated between a tungsten electrode and the metallic slabs to weld. A gaseous shielding with an inert gas (Argon or Helium) is used in order to prevent any oxidation of the molten metal as well as of the tungsten electrode. Furthermore, this inert gaseous shielding facilitates the initiation and stabilizes the electrical arc. GTAW is a joining process widely used in industries such as nuclear power, aeronautics, petro-chemical etc. because of the high quality of the obtained joint such as strength, ductility and corrosion resistance. GTAW is used with numerous metallic materials such as all the iron based, nickel-copper alloys, aluminium alloys and titanium alloys. Figure 1 presents some of the common applications of GTAW process in industry. These properties are related to the

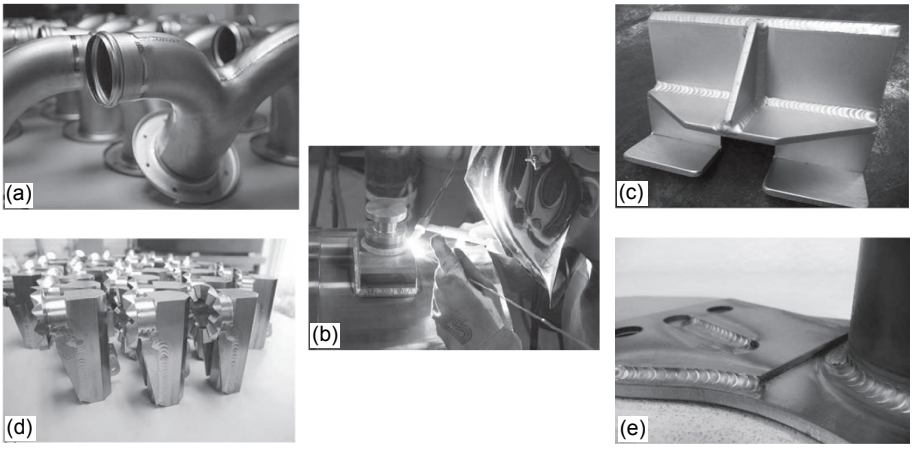

Figure 1: GTAW applications: (a) GTAW application to tubular assemblies (b) GTAW welding (c) Aluminum alloy welds (d) Welded titanium component (e) Chromium-molybdenum steel component [1]

final microstructure of the joint. The final microstructure is the result of thermal cycles caused by the welding operation: the interaction of the heat source (in the arc plasma) and the metallic material. This interaction leads to a fast heating and melting of the metal then formation of the weld pool (molten metal). In the weld pool, the molten metal is subject to complex flows which in turns significantly affect the temperature field, thermal cycle and the weld pool geometry. When the heat source moves away, the weld pool cools and the molten metal solidifies. As the temperature decreases more or less rapidly, various solid-state phase transformations take place resulting in the final microstructure of the joint. The final microstructure relies on several parameters such as the metal chemical composition (alloying elements and presence of impurity etc.), the heat source

generated by the electrical arc (intensity, tension), operating conditions (shielding gas, electrode type, welding speed) or the geometry of the welded slabs (length, thickness etc.). All this parameters have to be controlled in order to avoid any weld defects. For example, inappropriate cooling may results in adverse microstructure or residual stresses and distortions due to the incompatible plastic strain [2]. As well as metallic work-pieces incorrectly prepared or/and cleaned can produce porosity. An incorrect welding speed is quite often the cause of humping defect. Hot cracking is another cause of unwanted defect in GTAW welding [2, 3].

Numerical simulation is a powerful tool for better understanding the phenomena involved in GTAW and especially for the comprehension of the complex flows in the weld pool. The increase of computer's power, in the last two decades, made affordable the simulation of multiphysics problems like welding. Effect of molten metal surface tension, electromagnetism or arc plasma flow on the weld pool formation and growth has been widely investigated. In order to simulate correctly the welding operation of a metallic material, a heat transfer and fluid flow modeling is required. Once the modeling is defined correctly, the simulation of the stated modeling becomes a powerful method for optimizing the welding operation in order to increase the productivity without defects. The set up of such predictive welding model requires experimental validation. Some model's parameters need to be calibrated or estimated from experimental measurements. This stage is compulsory. Nonetheless, experimental observation of welding operation is challenging [4]. Physical measurements of important parameters such as temperature and velocity fields and the thermal gradient in the weld pool are extremely difficult due to the small size of the weld pool, the presence of plasma in the vicinity of weld pool and the rapid changes of temperature in arc spot welds. Nevertheless valuable insight have been gained in the detailed mathematical description of heat and mass transfer in the weld pool.

The main objective of the study is to understand the basic mechanisms that drive the fluid flow and heat transfer in the stationary GTA weld pool. Quantitative values of the weld characteristics are always necessary to optimize the welding process. This investigation will mainly focus on the prediction of thermal cycles and the velocity distribution in 2D-axisymmetric stationary GTAW process with a planar surface (considering the low welding currents use <150 A) and a prescribed heat flux and current density on the surface. The major objectives are stated below:

- Establish a transient numerical model to provide detailed insight about the heat transfer and fluid flow phenomena during stationary GTAW process
- Investigate and identify the major driving forces in the weld pool convection and study the influence on the weld pool development
- Study the effect of welding power, welding duration and surface active elements such as sulfur on the weld pool formation
- Validate the numerical model using the experimental measurements
- Optimize the assumed heat flux parameters using inverse parameter optimization technique

The methodology adopted in this research work connected with the thesis presentation is shown in figure 2. The thesis includes an introduction, four chapters and finally conclusion and perspective. The outline of the thesis chapters are as follows.

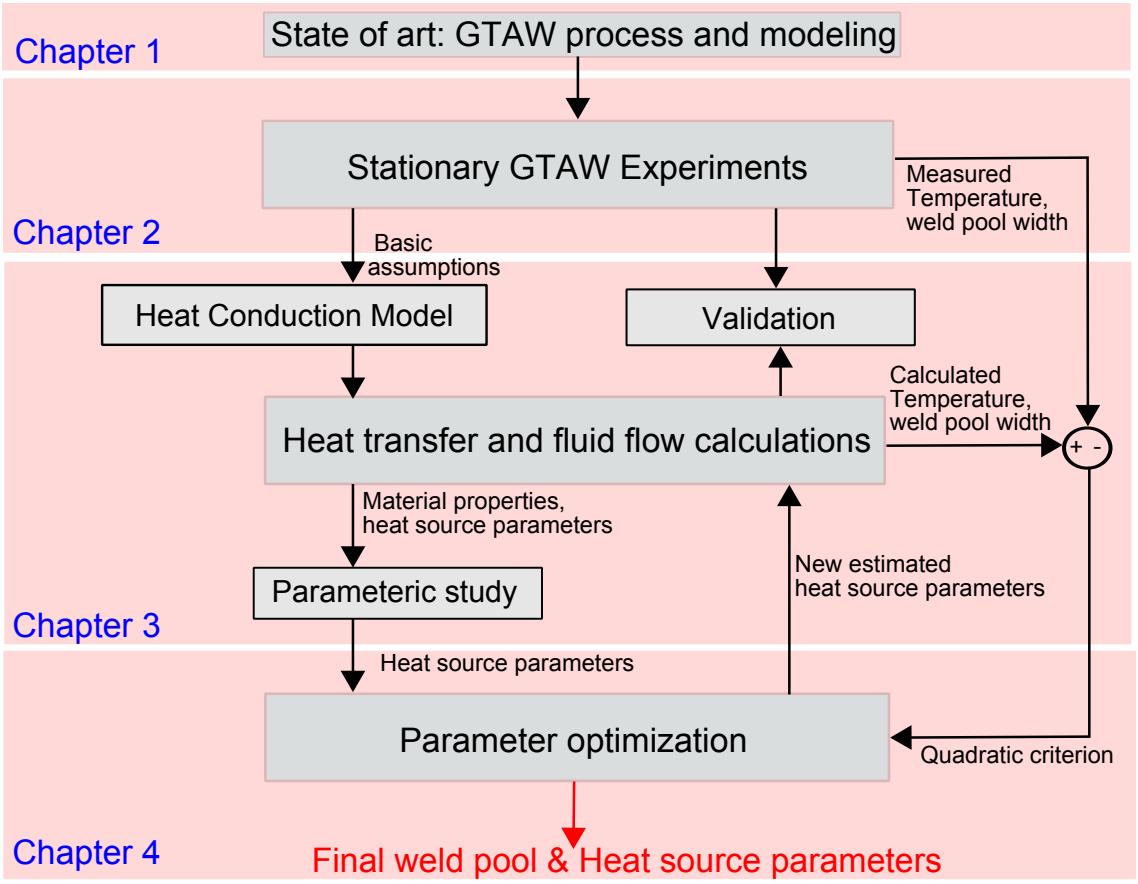

Figure 2: The methodology used in the thesis

Chapter 1 focuses on the state of art of the numerical investigations carried out in the field of GTAW. First section presents a general introduction to the Gas tungsten arc welding process and major parameters used. Later, the basic transport and physical phenomena associated with the weld pool development is presented. A brief effort to cover the historical works related with the mathematical and numerical modeling of heat transfer and fluid flow phenomena in GTAW is presented. Final section gives a general mathematical model for heat transfer and fluid flow phenomena in the weld pool with some major boundary conditions and source terms associated with the numerical model.

Chapter 2 deals with the experimental work on the stationary GTAW process. The major aim targeted by the experimental study is to identify the effect of welding energy, material composition and the welding duration on the major weld characteristics such as temperature evolution, weld pool size and shape. In order to achieve these major objectives, stationary gas tungsten arc welding process with argon shielding is realized on stainless steel 304L disc material. A synchronized data acquisition associated with the multi-physics welding bench is used to analyze the process parameters (such as current and voltage), temperature evolution (using thermocouple) and the time dependent weld

pool formation (using high speed camera). Finally a post weld analysis on the welded samples were carried out to identify the weld pool size and shape (postmortem analysis) and also to verify the composition of minor element present (using EPMA).

Chapter 3 presents the transient heat transfer and fluid flow simulation for the stationary GTAW process. This chapter begins with a simple heat conduction simulation for the temperature prediction and weld pool evolution with discussion on the possibilities and the limitations of using this model. Then introduced the Magneto-thermo-hydrodynamic simulation. The evolution of temperature and velocity fields are studied using the two-dimensional axi-symmetric numerical model developed using COMSOL Multiphysics software. A detailed analysis is carried out by considering different forces in the weld pool such as buoyancy, electromagnetic, surface tension and arc drag force. A study has been carried out on the dependency of temperature coefficient of surface tension and its variation with temperature and the minor alloying elements such as sulfur. A comparison of the developed conduction and convection model is done by comparing the temperature distribution and the weld pool evolution to find out the relative importance of the two heat transfer mechanisms in the weld pool. A dimensionless analysis is also carried out to study the heat transfer mechanism. Verification of the simulation results were performed by comparing the numerical results for thermal cycles, weld pool radius evolution and the final weld pool geometry with the corresponding experimental data. A parametric study has been carried out to identify the most influential model parameters that can considerably disturb the weld pool development.

Chapter 4 deals with the heat source parameter estimation using the inverse thermo-convective problem. The Levenberg-Marquardt method with an iterative regularization technique is used for the resolution of the stated inverse problem. A few numerical cases are carried out in order to validate the identification of the unknown parameters (efficiency and Gaussian radii) with ideal input data and with noised input data. The aim of the noised input data shows how robust is the chosen inverse method and the accuracy of the estimated parameters when the noise measurement is known. Finally the inverse thermo-convective problem is solved with experimental data and the resulting parameters are analyzed according to the different inaccuracies on the experimental measurements.

Chapter 1

Gas Tungsten Arc Welding: Background

Contents

1.1 Introduction

Among various processes for joining metals, “welding” is considered as the one of the oldest methods, in which thermal energy is used to increase metals ability of plastic flow or melting the metal and then diffuse mutually to form the joint. In terms of methods of heating employed, welding process can be classified into several groups. Among these,

gas flame heating is considered as the traditional heat source for welding. After electricity becomes widely available, arc produced by the electric discharge becomes the most commonly used welding heat source. Electric resistance welding also becomes a popular welding heat source, which needed passage of electric current and pressure for the metal contact to form a joint. In 1950's, electron beams were made available as heat source for welding. The very high energy density electron beam welding needs vacuum atmosphere. Later, laser light generated by the laser resonator is also used as heat source. Heating by mechanical friction, ultrasonic vibration and chemical reaction were also used in the past for joining the metal [5, 6].

Gas Tungsten Arc Welding (GTAW) is the most versatile of the arc processes. Welds can be made with or without filler metal, and very thin materials of just a few thousandths of an inch (less than one millimeter) can be welded. GTAW can be used in all welding positions to join just about all weldable ferrous and nonferrous alloys [7].

Some of the major advantages of this method are high quality and the excellent finishing of the weld, low-distortion, free of spatter associated with other methods, possibility of welding in any position, applicable with or without filler wire, precise control of welding heat, excellent control of the weld pool, applicable with a range of power supplies, suitable for almost all metals including dissimilar ones, accessible cost of the equipment and also possibility of welding structures in close contact. The major disadvantages are generation of complex region of stresses and deformations, leading sometimes to undesirable results such as material distortion, residual stresses, generation of fragile micro structures, grain growth, cracks, fissures, and changes in mechanical, physical and chemical properties among others [1].

The main objective of this research work is to understand and quantify the weld pool formation in Gas Tungsten Arc welding based on numerical and experimental approach. A multiphysics numerical simulation model is necessary to accurately predict the fundamental transport phenomena occurring in the weld pool region. In particular, the research work seeks quantitatively predict the liquid convection in the weld pool, temperature distribution in the weldment, thermal cycles and weld bead size and shape. The major topics covered in this review are listed below:

- Gas Tungsten arc welding process: This section reviews the major regions of GTAW process and the process parameters.

- The basic transport phenomena during GTAW, which includes electrical arc phenomena, the deposition and conduction of heat, the liquid convection and various driving forces, governing conservation equation and their numerical solutions, are reviewed.

- The prediction of behavior in a given physical situation consists of the values of the relevant variables governing the process. In case of welding phenomena a complete prediction should give us the values of velocity, pressure and temperature. Prediction of heat transfer and fluid flow process can be obtained by two main methods: Experimental investigation and theoretical calculation. This part also covers the state of art in the numerical simulation of the welding process and analyze different approaches to understand the advantages and drawbacks.

1.2 GTAW fundamentals

1.2.1 GTAW principle

Gas Tungsten Arc Welding (GTAW) is a joining process which uses the heat generated by the electrical arc maintained between the non-consumable tungsten electrode and the work piece as shown in Figure 1.1. This process is also known as tungsten inert gas (TIG) welding. An inert gas shielding is employed to give electric arc stability and also to prevent any atmospheric contamination. For the joints where the filler wire is required, a welding rod is fed into the weld zone and melted with the base metal [8].

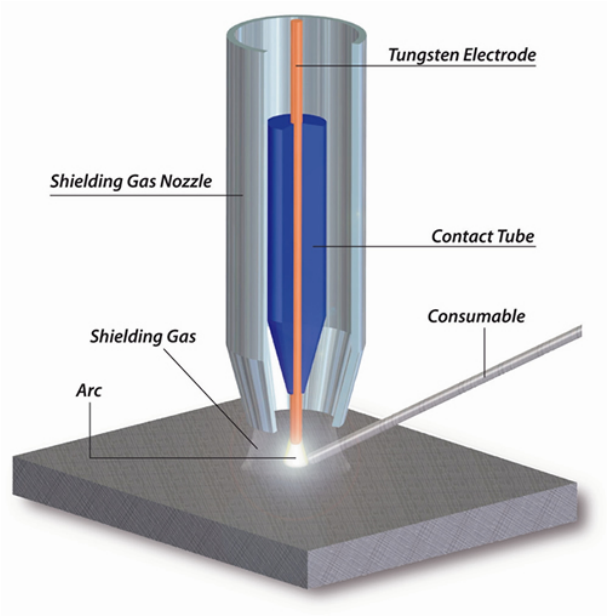

Figure 1.1: GTAW Process [9]

The aim of welding processes is to obtain a weld which has the same chemical, metallurgical and mechanical properties as compared to the base metal itself. So to achieve such conditions, the molten weld pool has to be protected from the atmosphere during the welding operations; otherwise atmospheric oxygen and nitrogen will combine readily with the molten weld metal and result in a weak porous weld. In gas tungsten arc welding the weld zone is shielded from the atmosphere by an inert gas. The commonly used shielding gas for the welding process is Argon or Helium. Argon is generally recommended because of its general suitability for a wide variety of metals, and the considerably lower flow rates required and also it's low cost compared with helium.

GTAW can be used in all welding positions to join just about all weldable ferrous and nonferrous alloys. Autogenous GTA welding (without filler metal) is used in thin square edged sections (2mm), while V and X type edge preparations are needed in thicker sections. In this case, addition of filler metal is necessary. The weld control is excellent in GTAW because the welder can establish a molten pool and then add filler metal as desired. This excellent control yields exceptional fusion and wetting at the beginning of the weld, thus avoid incomplete fusion, which can take place initially when using consumable

electrode processes. This process is extensively used for welding thin components of stainless steel, aluminum, magnesium or titanium alloys as well pieces of carbon and low alloy steels [7, 8].

1.2.2 Features of weld zones

The phenomenon of arc welding is described by the flow of electrons between the anode and the cathode by applying an electromagnetic field. The flow of electrons between cathode and anode ionizes the inert gas which allows the initiation of the electrical arc. The shielding gas plays a key role in ionization and arc stability (If the ionization potential of the inert gas is low, the arc will be easier to strike and stabilize. Fusion welding is a process in which intense heat source is applied to join the components. The materials gets heated up rapidly and form a molten weld pool. When the liquid pool solidifies, the materials get jointed together. The interaction between the base material and the heat source leads to a series of physical and chemical processes, which culminate in the final weld composition, geometry, structure and properties [8, 10–12].

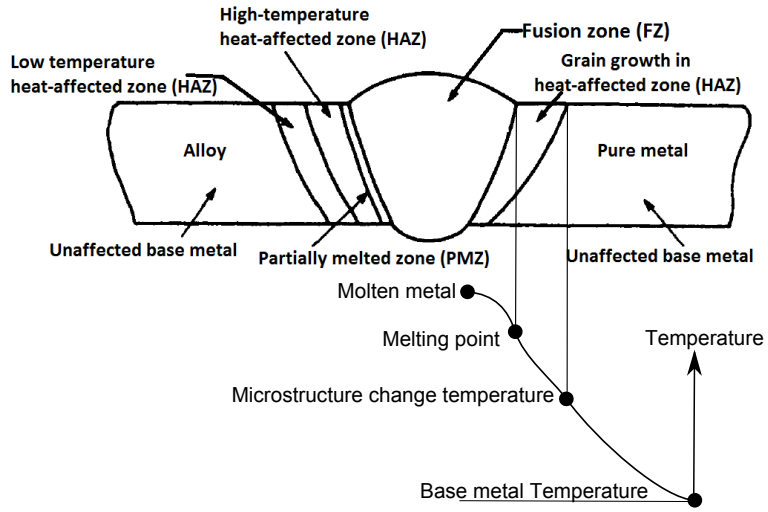

Figure 1.2: The classical zones in a weld [13]. Right half shows the weld regions in pure metal and left half for a alloy

The fusion welds exhibit distinct microstructural regions as a direct result of various effects of the heat. Figure 1.2 shows the schematic of a typical fusion weld in a pure and in an alloyed crystalline metallic material. Due to the heating temperature of the pure material rise above its melting point or the alloy to raise above its liquidus temperature, complete melting or fusion occurred, producing a fusion zone (FZ). Fusion zone is a mixture of filler metal and base metal melted together homogeneously due to convection. Outside this region or zone, where the temperature of the alloy was below the liquidus but above the solidus, a partially-melted zone (PMZ) was produced. Since the pure material melts at one distinct and unique temperature, as opposed to over a range of temperatures, no PMZ is found in pure metals. From the center line of the heat source and the resulting weld, the temperature was lower, but may have been high enough to have caused some observable microstructural changes due to solid-phase transformations. This may occur due to allotropic phase changes, recrystallization and/or grain growth (in

cold-worked material), or aging, over aging, or resolutioning in precipitation-hardanable systems. When such observable microstructural changes occur, the region is referred to as the heat-affected zone (HAZ). Degradation in mechanical properties may occur in this region. In some cases there is a possibility to occur more than one heat-affected zone, if several different processes or reactions can and do occur in the material system at different temperatures. For example a cold-worked alloy that exhibits a phase transformation. In figure 1.2, there is a region in which recrystallization and grain growth occur at a relatively low temperature, and a region of phase change at higher temperature. These different regions are often referred to as high-temperature and low-temperature heat-affected zones. Further away from the weld (heat source) center line, the temperature did not rise high enough to cause any noticeable change in the microstructure. This region is called unaffected base metal zone, which is surrounding the HAZ and likely to be in a state of high residual stress, due to the shrinkage in the fusion zone.[13].

1.2.3 GTAW welding energy and efficiency

GTAW efficiency:

During welding, the workpiece absorbs a part of the total energy supplied by the heat source. This energy is used for the formation of the molten weld pool and diffuses through the weld pool region by conduction and convection to the entire base material to form a transient temperature field. This energy is responsible for the structure and properties of the weld region [14].

For arc welding, the arc efficiency (η), which defines the fraction of the arc energy that is transferred to the workpiece, is given as [14, 15]:

$$\eta = 1 - \frac{q_e + (1-n)q_p + mq_w}{VI} \tag{1.1}$$

where q_e is the rate of the heat transferred to the electrode from the welding arc, q_p is the rate of heat radiated and convected from the arc column, n is the proportion of heat output from the arc column that is transferred into the workpiece, q_w is the rate of heat absorbed by the workpiece, m is the fraction of absorbed energy that is radiated away and lost, and V and I are welding voltage and current, respectively.

When a consumable electrode is used, such as in Gas Metal Arc welding, q_e is also transferred to the workpiece and therefore the arc efficiency is thus given as [14, 15]:

$$\eta = 1 - \frac{(1-n)q_p + mq_w}{VI} \tag{1.2}$$

It should be noted that although Eqs. 1.1 and 1.2 are useful in explaining the manner in which various types of heat loss affect arc efficiency. However, evaluation of the values of q_e, q_p, q_w, n and m from theoretical considerations is very difficult. Therefore a common practice is to experimentally determine the arc efficiency under various welding conditions. In the literature, experimentally measured arc efficiency is available for various arc welding processes including GTAW [14]. Recently, Nils *et. al.* [16] carried out a review of literature that specifies the arc efficiency values for GTAW process. Figure 1.3 shows the published range of arc efficiency values between 1955 and 2011. They showed that the published arc efficiency values lie in a wide range between 0.36 and 0.95 for GTAW DCEN (direct current electrode negative) process.

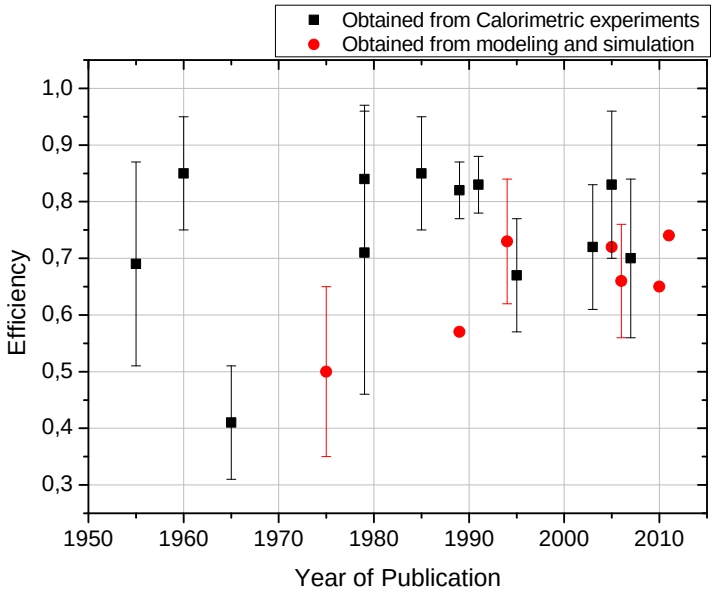

Figure 1.3: Published arc efficiency values for GTAW process [16]

1.2.4 GTAW equipment and welding parameters

The major components of a GTAW equipment are power source (DC or AC/DC), an inert gas cylinder fitted with a gas regulator/flow meter, coolant system, GTAW torch and a remote controlling system as shown in figure 1.4. The torch cable consists of gas

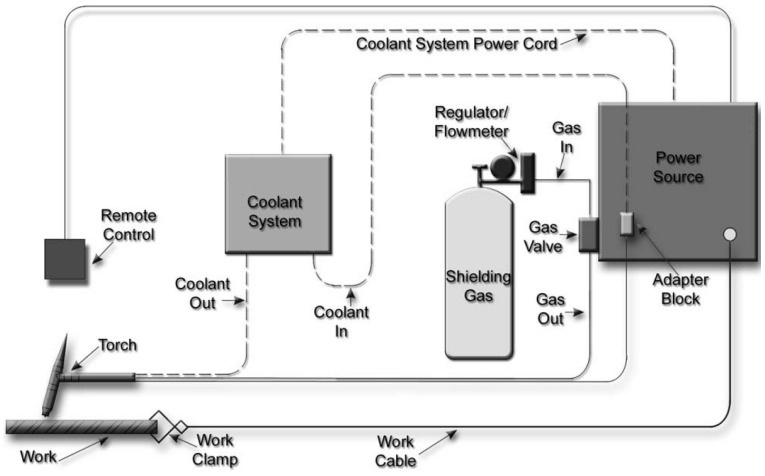

Figure 1.4: Gas Tungsten Arc Welding Equipment [17]

hose from the gas valve, electric cables from the power source and water hose from the coolant system for cooling the torch. The work cable is clamped on the work piece using the work clamp to close the electrical circuit. The electric arc is produced by the passage of current through the conductive ionized shielding gas. The established arc between the tip of the electrode and the work piece produces heat that melts the base metal. After the establishment of the arc and the weld pool, the torch moves along the joint and the arc progressively melts the surface.

The function of the GTAW torches is to hold the tungsten electrode and provide a means of conveying shielding gas to the arc zone as shown in Figure 1.5. Depending on the method of cooling used, different types of welding torches are available such as gas cooled and water cooled torches. The gas cooled torches are limited to a maximum welding current of 200 amperes, where as water cooled torches can typically withstand 300 to 500 amperes. In GTAW process, tungsten alloys are used as electrode. These electrodes are non-consumable because they do not melt and transfer to the weld. The melting point of Tungsten electrode is $3410°C$. The Tungsten electrode serves as one of the electrical terminals of the arc which supplies heat required for welding [17]. According to the chemical composition of the tungsten alloy different types are available in the industry, among them EWTh - Thoriated Tungsten Electrode and EWCe - Ceriated Tungsten Electrode are most popular.

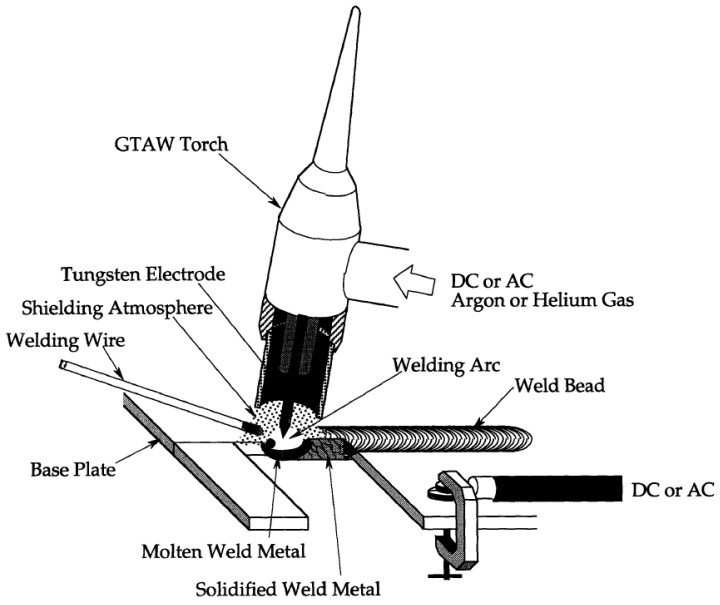

Figure 1.5: Gas Tungsten Arc Welding torch [17]

GTAW process input parameters:

- Current mode: Continuous Direct current (DC) and pulsed DC for all the ferrous, titanium alloys and Nickel alloys, Alternative Current (AC) for light weight metal like aluminum.
- The arc length (workpiece-electrode distance that varies from 1 to 5 mm), or the arc voltage (usually around 10 V to 15 V).
- The GTAW electrode (material, diameter and tip angle) are typically available in diameters from 0.25 to 6 mm and in standard lengths ranging from 75 to 600 mm [1].
- The gas nozzle (internal diameter, material) and the shielding gas composition (argon, helium or mixture of different gases) and the gas flow rate (usually from 5 to 30 L/min).

- The welding speed (from 8 to 10 cm/min).
- In the case of filler metal GTA welding, one must specify the feeding wire material (usually the same as base metal), diameter (between 0.6mm and 5 mm), and feeding speed (usually less than 100 cm/min) [18]

1.2.5 Effect of various input parameters on the GTAW Performance

1.2.5.1 Effect of arc height or arc voltage on the weld pool

The arc length in GTAW is usually from 2 to 5 mm. If the arc length increases, the voltage to maintain the arc stability must increase, but the heat input to work-piece decreases due to radiation losses from the column of the arc. This cause a decrease in the weld penetration and cross section area of the melted material with increasing arc length [13].

1.2.5.2 Effect of welding current and polarity

The welding current has a direct influence on weld bead shape and quality of the weld. The constant current power source for GTAW welding may be either alternating current (AC) or direct current (DC). Alternating current is normally used for welding of aluminum and magnesium. Direct current is usually preferred for the ferrous metals and the other non-ferrous metals. For direct current itself there are different choices, they are: direct current electrode negative(straight polarity, DCEN), and direct current electrode positive (reverse polarity, DCEP). Each of these current types has its applications, and its advantages and disadvantages. The straight polarity (DCEN) is normally used for GTAW welding of practically all metals except aluminum and magnesium. The torch is connected to the negative terminal of the power source and the work lead is connected to the positive terminal. When the arc is established, electron flow is from the negative electrode to the positive work piece as shown in figure 1.6. In a DC arc approximately 70% of the

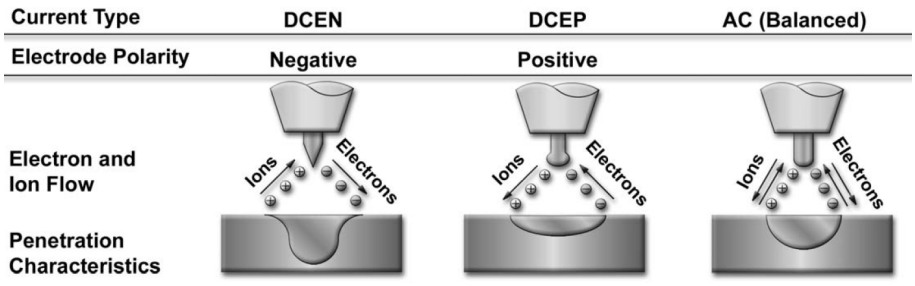

Figure 1.6: Effect of current and polarity on weld bead shape [19]

heat will be concentrated at the positive side of the arc, therefore the greatest amount of heat is distributed into the workpiece and it produces higher weld penetration depth. Figure 1.6 illustrates the different current types used in GTAW process, the electrode polarity, electron and ion flow directions and the penetration characteristics in each case [13]. Square wave AC is nowadays being used instead of normal sine wave because it facilitates the assistance of arc re-strike each half cycle and adjusting of the arc cleaning effect or the penetration depth.

1.2.5.3 Effect of welding speed

For a same amount of energy, the increased welding speed causes a reduction in the heat input. The electromagnetic field and the arc pressure have less influence on the change in welding speed because they are dependent on the current. The increase in the weld speed produces a decrease in the weld cross section area, consequently depth of penetration and weld width also decrease. the D/W ratio has a weak dependence on travel speed [20]. This shows that the travel speed does not influence the mechanisms involved in the weld pool formation, but it has influence on the volume of melted material. The generally used normal welding speeds ranges 100-500 mm/min depending on current, material type and the thickness of the material [21].

1.2.5.4 Effect of shielding gas

Shielding gases are used in GTAW in order to prevent atmospheric contamination and to get better arc stability. The contamination in the weld can produce porosity, weld cracking, scaling and even change in the chemical composition. Gases with low ionization potential facilitate the ignition of the electric arc and those with low thermal conductivity tend to increase the arc stability.

Table 1.1: Gas shielding properties employed in GTAW [8]

Gas	*Chemical symbol*	*Molecular weight (g/mol)*	*Density (g/L)*	*Ionization potential (eV)*
Argon	Ar	39.95	1.784	15.7
Carbon dioxide	CO_2	44.01	1.978	14.4
Helium	He	4.00	0.178	24.5
Hydrogen	H_2	2.016	0.090	13.5
Nitrogen	N_2	28.01	1.25	14.5
Oxygen	O_2	32.00	1.43	13.2

Table 1.1 presents the typical gases used as a protection in GTAW process. The ionization potential for argon and helium are 15.7 and 24.5 eV (electron volts), respectively. Since it is easier to ionize argon than helium, arc initiation is easier and the voltage drop across the arc is lower with argon. Also, since the argon is heavier than helium, it offers more effective shielding than helium. With DCEP or AC, argon also has a greater oxide cleaning action than helium. The lower cost also make argon preferable for GTAW than helium [8].

1.2.5.5 Effect of electrode diameter, preparation and contamination

Tungsten electrode with 2% cerium or thorium have better electron emissivity (ability of electrode tip to emit electrons), current carrying capacity, and resistance to contamination than pure tungsten electrodes. As a result arc starting is easier and the arc is more stable [8]. The size of the electrode to be used is determined by the welding current required.

Table 1.2 presents the recommended current ratings for different diameters of electrodes using argon shielding gas. Larger electrodes permit higher currents to be used. Smaller diameter electrodes may be used for welding thinner materials or while welding out of position.

Table 1.2: Recommended electrode diameters and current range employed with Ar shielding gas [22]

Electrode diameter (mm)	*Current (A)*
1.0	20-50
1.6	50-80
2.4	80-160
3.2	160-225
4.0	225-330
5.0	330-400
6.4	400-550

The tungsten tips are either balled, ground or chemically sharpened during their preparation. The common method used is grinding, which should be performed with the axis of the electrode perpendicular to the axis of the grinding wheel. The electrode vertex angle influences the weld penetration depth and the weld shape. The commonly used electrode angles vary between 30° and 120°. An increased arc pressure and penetration depth can be observed for small angle electrodes with high tip shape deterioration. Electrode angles from 60° to 120° maintain tip shape for longer periods and produce welds with adequate penetration and depth-to-width ratio [21].

The accidental dipping of the electrode tip into the molten weld pool or touching the tungsten with the filler metal are the two main causes of contamination. Also due to improper shielding gas or insufficient gas flow may oxidize the electrode. The contamination may cause the improper arc characteristics and leads to the tungsten inclusion the weld pool [17].

1.3 GTAW : A Multiphysics problem

The present research work deals with the heat transfer and fluid flow modeling for the identification of weld pool dimensions during the static GTAW process. The computational domain of the numerical model is limited to the sample (disc), which means the explicit modeling of the heat source. The four states solid, liquid, gas, and plasma of several material exist simultaneously in a small volume. There exists physical interactions which is associated with electric, magnetic, thermal, chemical, solid and fluid processes. Figure 1.7 shows the fundamental concept of GTAW process, which is materialized by the tight energy balance among the cathode, arc column and weld pool. A remarkable difference in temperature and voltage can be observed at the interface boundary of electrode-arc plasma and plasma-metal surface. Figure 1.9 shows the main typical regions

of interest during GTAW process. Here the whole welding process is generally associated with four different zones such as electrode, arc plasma, weld pool and solid metal. There occur an inter-facial boundary between each of these zones as shown in figure 1.9, such as electrode-arc plasma, plasma-metal surface and liquid-solid.

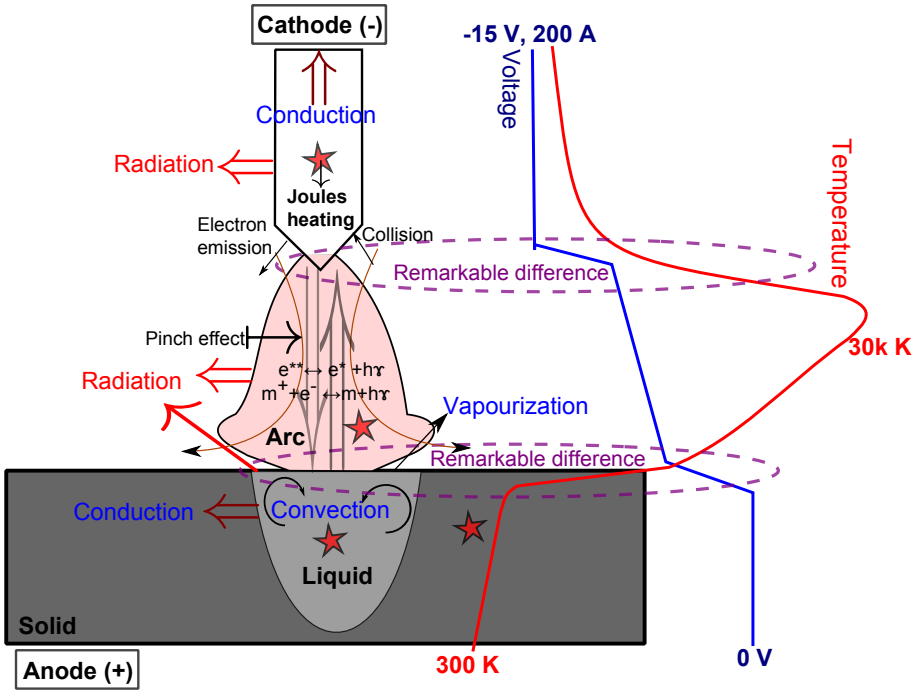

Figure 1.7: Schematic of the transport phenomena occurring during the GTAW process [23]

1.3.1 Over all presentation of the different phenomena involved during GTAW operation

The GTAW process involves different physical phenomena such as plasma domain interaction, heat transfer, fluid flow, electromagnetism, metallurgy, solid mechanics and free surface deformation. All these phenomena are strongly coupled though not equally important or relevant at all for all welding processes. Figure 1.8 methodically shows some of the interactions and coupling effects. Depending on the region of interest and the field parameters need to find out, such as temperature, velocity, microstructure, displacement, strain and stress, different type of numerical approaches are available in literature [18, 24, 25]. If geometrical changes close to the weld are of primary interest, modeling of fluid flow will be essential. Neglecting the physics of weld pool due to its insignificant effect on macroscopic effect of welding, all the bidirectional coupling associated with fluid flow in the weld pool can be ignored. Simulations that concerns with the identification of the evolution of weld pool geometry require the computation of temperature and fluid flow fields. Electromagnetic fields are also considered as important for high welding currents. In view of the objective of the current research study, the major fields considered are thermal, fluid flow and electromagnetism. Some of the couplings were ignored for the simplification of analysis due to their weak nature.

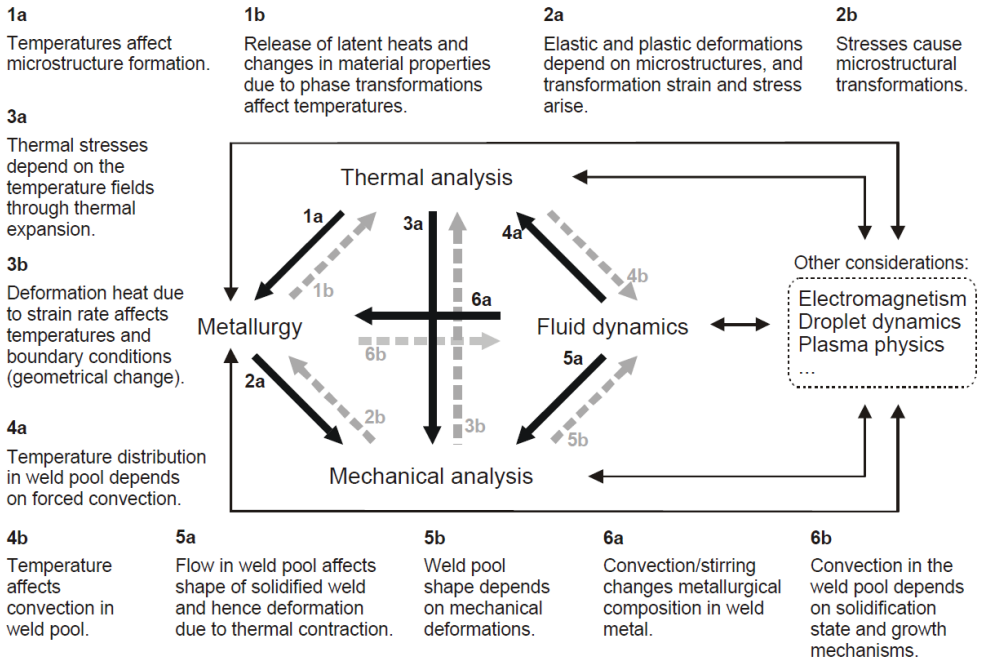

Figure 1.8: Major interactions and coupling effect occurring during welding. Strong and weak dependencies are illustrated with black and grey arrows, respectively [24].

1.3.2 Cathode

The cathode (tungsten electrode- for DC straight polarity) for GTAW process is considered as non-consumable. The passage of current through the electrode heated up the cathode mainly due to Joule heating. The surface heating also takes place due to the collision of atoms and ions from the outer space, and the top area, known as cathode spot, which get cooled by the emission of electrons. Normally a few percentage of thorium oxide is present in tungsten electrode to improve the emission ability. Before the arc process the surface of the electrode will be oxidized. In comparison to pure tungsten, the tungsten oxide is much easier to melt and evaporate. During the arc process the thorium oxide gets evaporate from the cathode. The evaporated tungsten oxide gets dissociate to tungsten and oxygen. The evaporated tungsten atom from the outer space impinges and gets crystallize on the cooler tungsten electrode surface away from the electrode tip. A very complicated chemical and physical reaction occur on the cathode surface [23].

1.3.3 The arc plasma

The welding arc can be considered as an electric conductor that converts electrical energy into heat. The high intensity heat distribution and it can easily control through electrical means made the arc favorable heat source for many welding processes. The welding arc is also a source of radiation, which may help to remove the surface oxides in addition to supplying heat. A welding arc is a particular group of electrical discharges that are formed and sustained by the development of gaseous conduction medium. The current carriers for the gaseous medium are produced by thermal mechanisms due to the high temperature of the arc. Many kinds of welding arcs have been conceived, each with a unique application in the metal joining [26].

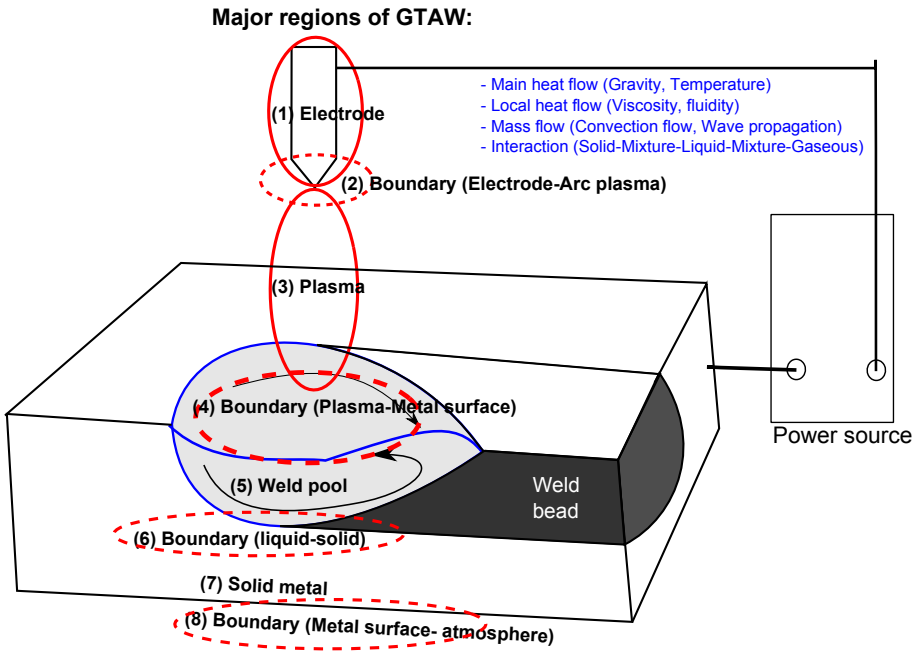

Figure 1.9: Schematic of the different regions in GTAW process [23]

Generally arc is described by an electric field between the positive anode and negative cathode surrounded by an ionization gas. In arc welding, the intense heat needed to melt metal is produced by an electric arc. On the metal there is a thin layer of surface electrons, which are accelerated in the field towards the anode. These electrons collide with the atoms in the gas, causing impact ionization where the atoms are decomposed into electrons and positive ions, which causes further ionization. The current of electrically charged particles in the arc and the temperature are interrelated as high temperatures increase ionization causes the temperature rise due to the released energy [27]. The arc ignition is accomplished by the short circuit current, which occurs as the anode and the cathode are brought into brief contact. The short circuit current shortly increases the temperature and the current and subsequently the arc can be maintained in the electric field existing under normal welding conditions. The arc is surrounded by a magnetic field directing the charged particles towards the center of the arc, causing the arc to localize in spots on the anode and the cathode. When the electrically charged particles impact on the anode and cathode, the anode and the cathode spots are heated to high temperatures of approximately $3000°C$ to $5000°C$ causes the metal to melt [10, 11].

The arc current is carried by plasma, the ionized state of a gas composed of nearly equal numbers of electrons and ions of gas atoms and molecules. The electrons which support most of the current conduction, flow out of a negative terminal (cathode) and move towards a positive terminal (anode) which is schematically represented in figure 1.10. Mixed with the plasma are other states of matter, including molten metals, slags, vapours, neutral and excited gaseous atoms, and molecules. The heated gas of the arc attains a maximum temperature between $5000K$ and $50000K$, depending on the kind of shielding gas and the intensity of current carried by the plasma [26]. By this high energy, the arc can heat up most kinds of metals to their melting point quickly. To maintain the arc steadily and shield it from the atmosphere, various kinds of processes such as shielded

arc welding, plasma arc welding, and submerged arc welding have been developed. These welding processes are widely used in almost all types of manufacturing industries [28].

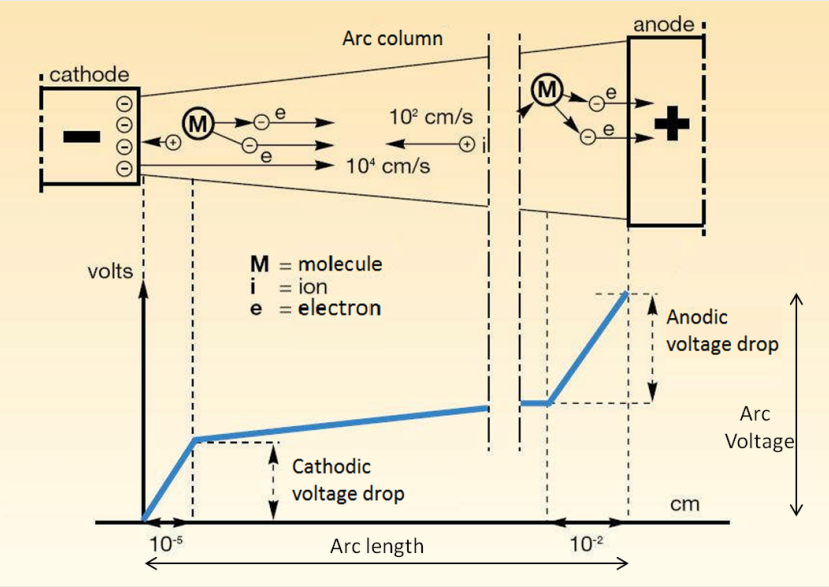

Figure 1.10: Schematic representation of voltage distribution along an arc for GTAW process [29]

The electric arc consist of three regions or spaces: (1) The cathode fall space (2) The arc column fall space and the (3) The anode fall space. These are schematically shown in figure 1.10 as a plot of arc potential between the welding electrode and workpiece. The area over which the currrent actually flows into the arc terminals is called anode and cathode spots.

1.3.4 Anode

As shown in figure 1.9, the anode (work piece- for DC straight polarity) has three different regions. The weld pool(melting zone), mushy zone (boundary liquid solid) and the solid zone (HAZ and the unaffected base metal), each of these regions can be differentiate according to the physical phenomena occurring in it.

1.3.4.1 The weld pool

The weld pool of few millimeters is created in the workpiece material due to the heating from the arc plasma. During welding, the development of the weld pool is determined by the arc-metal interaction, heat flow and fluid flow, the thermophysical properties of the material, and the associated boundary conditions [30]. Figure 1.11 shows the different physical phenomena associated with the liquid weld pool convection. The characteristics of the weld pool such as dimension, shape, microstructure etc. mainly depend on the type and composition of material, the welding energy, the shielding gas used and the electrode geometry.

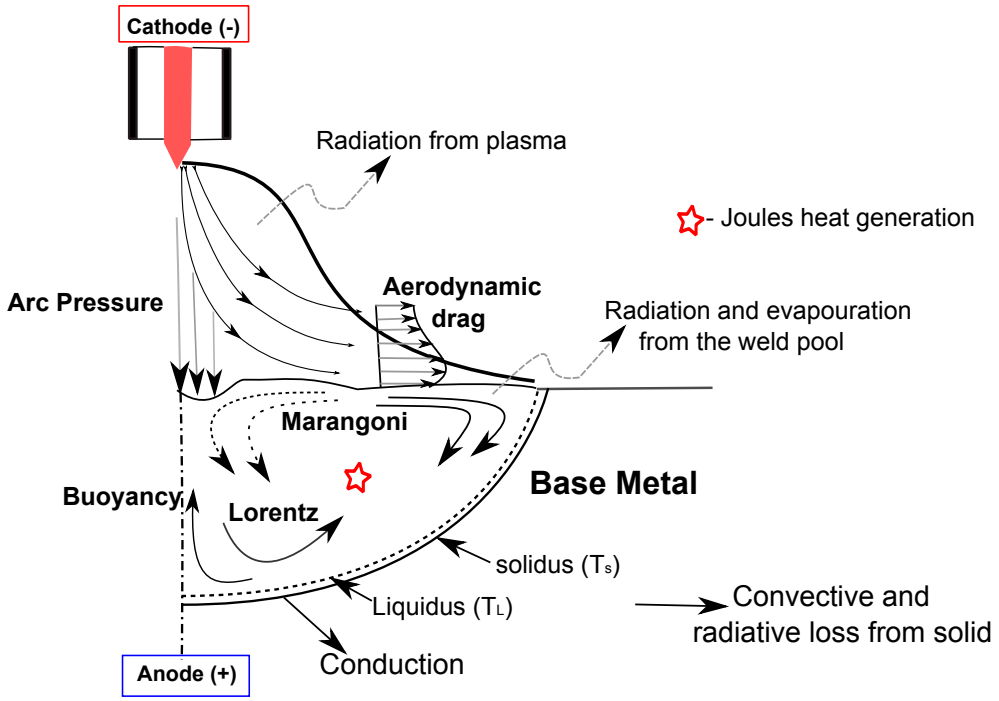

Figure 1.11: Schematic representation of the physical phenomena associated with weld pool convection during GTAW process

The flow inside the weld pool is very important for the weld characteristics, as it modifies the temperature distribution and thermal gradient that will affect the solidification process as well. The flow is very complex and there is no analytical expression to describe this flow. Convective heat transfer is often very important in determining the size and shape of the weld pool, the weld macro and micro structures and the weldability of the material. Convection in the weld pool is driven by the surface tension gradient, buoyancy, arc drag, arc pressure and electromagnetic forces [8, 14, 30–36]. The calculation of convective heat transfer is highly complicated because it involves the solution of the equations of conservation of mass, momentum and energy. Hence numerical simulation is often utilized. In order to predict accurately the convective heat transfer phenomena in the weld pool, the proper incorporation of the effect of various driving forces is necessary.

Figure 1.12 shows the various driving forces that govern the molten metal flow in the weld pool. They can be classified into two categories: the volumetric forces and surface forces. The gravitational force and the electromagnetic force which are acting in the weld pool are considered as volumetric forces. The thermocapillary shear stress, arc pressure and the arc drag force are acting on the boundary of the weld pool and are considered as surface forces.

1.3.4.2 Heat Affected Zone (HAZ)

In the HAZ, material is not melted, but there occur a change in the microstructure and mechanical properties due to the arc heating. The HAZ can be conveniently divided into a number of sub zones where there is a well-defined gradient of microstructure (depending on the material being welded) and this is illustrated for the case of a transformable steel in figure 1.13. Each sub-zone refers to a different type of microstructure and the

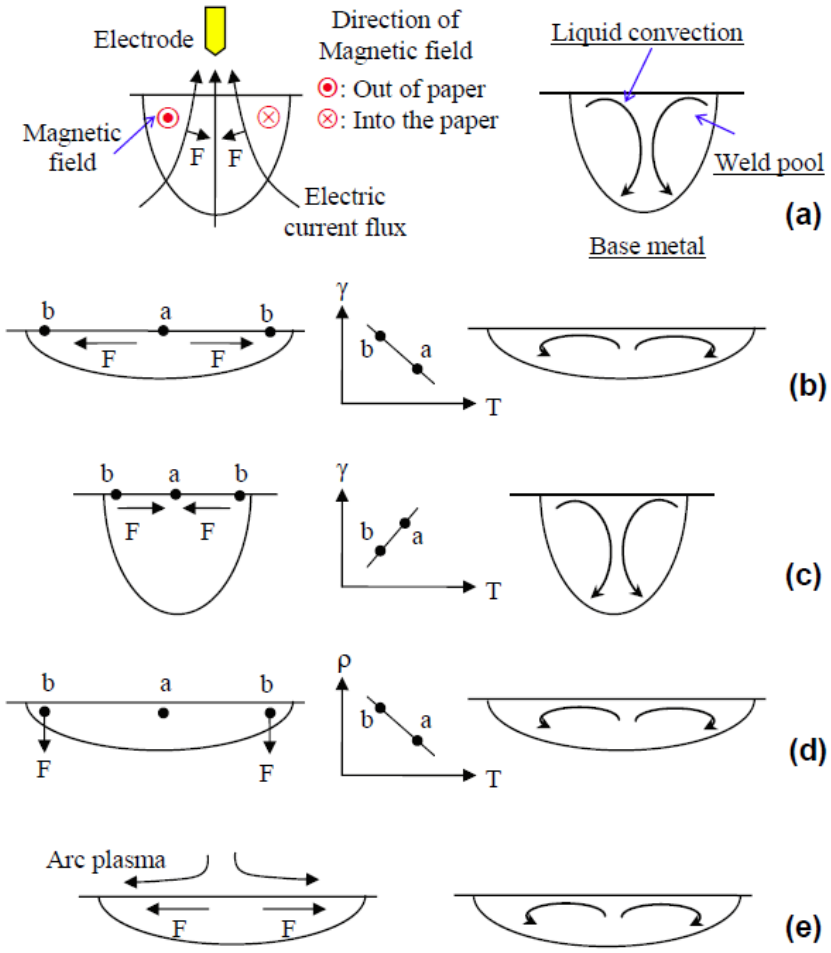

Figure 1.12: Various driving forces and the resulting liquid convection in the gas tungsten arc weld pool- 2D representation (a) Lorentz force: Electric current and magnetic field causes the Lorentz force fluid motion: Liquid metal flows downward along the weld pool axis and rise along the weld pool boundary (b) Marangoni force: Warmer liquid metal having a lower surface tension at point b than point a. Fluid convection: From point of low surface tension a to point at high surface tension b. Surface tension gradient force with negative $\partial\gamma/\partial T$. (c) Surface tension gradient force with positive $\partial\gamma/\partial T$. (d) Buoyancy force: Cooler liquid metal at point b is heavier than point a. weld pool motion due to BF: causing gravity sink along the pool boundary and rise along the pool axis (e) High speed outward movement of plasma arc lead to outward shear stress. Metal flowing from the center to the edge of the pool [37]. Where the symbol γ is the surface tension

amount of change in the microstructure depends on the amount of heat input, peak temperature reached, time at the elevated temperature, and the rate of cooling. Very high peak temperatures (T_p) in the regions immediately adjacent to the fusion line results in coarsening of the austenite (γ) grains, and this in turn increases the hardenability of this region relative to the other subzones. As the peak temperature decreases with distance from the fusion line, the austenite grain size decreases sharply. Regions of the HAZ further away from the fusion line become only partially austenitic during the heating. As a result of the marked change in the microstructure, the mechanical properties also change in HAZ and, usually, this zone remains as the weakest section in the weldment [38, 39].

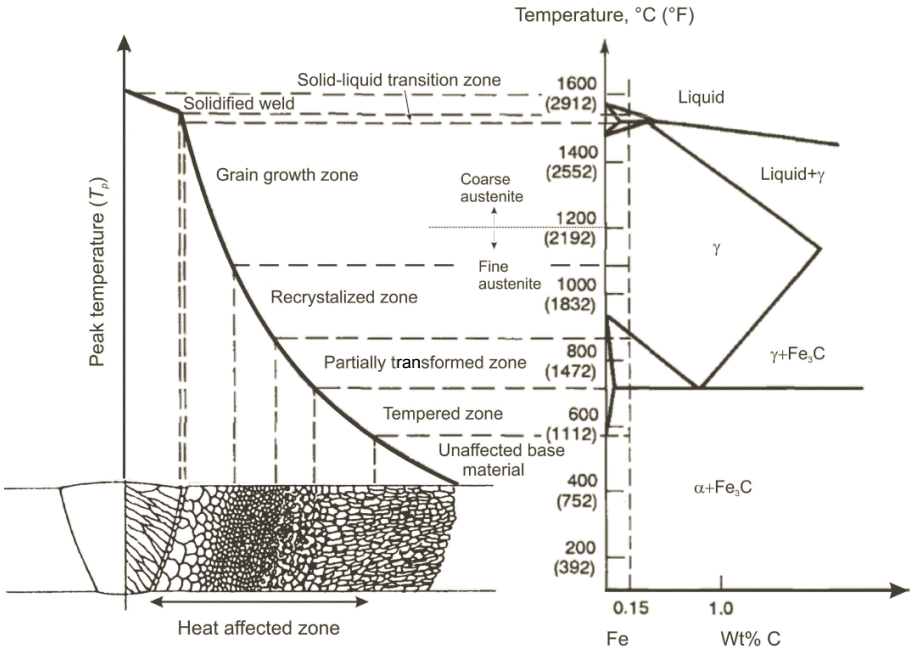

Figure 1.13: Different zones in a steel weld in relation with Iron-Carbon equilibrium diagram [39]

1.4 GTAW Modeling- Historical overview

A brief history and the recent development in the welding simulation is stated in this section.

In order to obtain a broad overview of the factors affecting heat flow in real welding situation, researchers worked with the analytical modeling approach. The analytical theory of heat transfer under conditions applicable to welding was established in the 1930s by Rosenthal [40]. He implemented moving coordinate system to develop solutions for point and line heat sources taking many assumptions to make the problem linear and analytically solvable. He assumed that there is no heat transfer between the plates and surroundings, material properties are treated as constant through out the process and infinite plate dimensions. During the 1940s and 1950s, the theory was extended and refined. Since the pioneering work of Rosenthal, considerable interest in the thermal aspects of welding was expressed by many researchers [41–47].

In lining with the aim of the research thesis, simulation of the vicinity of the fusion zone in transient welding conditions, the recent literature shows a tremendous progress in the understanding of the various phenomena during the process of welding [18, 48–51]. For the past few decades, due to tremendous improvements in the computing capability, lot of research works have been carried out in the transient temperature, velocity and pressure prediction in the weld pool [18, 37, 52–62]. For example, the models of heat and mass transfer have evolved from simple two dimensional steady state models to complex three-dimensional transient models considering the free surface flow under metal droplet impact [18, 63]. Many of the everyday welding situation encountered the transient welding conditions such as weld start and stops, track-welding routines, static spot welds, and solidifying weld craters. The behavior of these kind of process are completely different from their moving weld counterparts. This is mainly because the thermal profile never reach a steady state value. The heating and cooling rates of transient welds are much higher than that of the steady state welding conditions. This can lead to solidification cracking and formation of non equilibrium phases [15, 64]. Traditionally there are three main approaches for solving the governing conservation equations for a heat transfer and fluid flow problem: (1) The finite volume method [32, 65–68], (2) The finite element method (FE) [15, 18, 57, 64, 69], (3) The boundary element method (BE). Each method has found its extensive applications in solving engineering problems.

Oreper *et al.*[32] carried out a study on the velocity and temperature field evolution, solidification rate, and thermal gradient using a two dimensional model and is considered as one of the initial attempts to model the transient welding conditions. A crude grid system was used due to the hardware limitation at that time (1980's). The calculations were provided useful temperature and velocity fields from that study. Oreper and Szekely [31] studied the arc welding of thick metal block by assuming the arc to be static. They assumed a axisymmetric temperature and fluid flow field. They obtained the solutions for those values of heat inputs that render the pool partially penetrated and noted that the location of the phase front is not changed appreciably by the flow of molten metal. For the welding conditions they analyzed, the Lorentz forces dominate buoyancy forces, and they found the thermocapillary forces to have a significant influence on the isotherm. However they admit that their finite difference mesh is not fine enough to resolve the free surface boundary layer. They also used a dimensionless analysis and numerical modeling to understand the role of conduction and convection in the weld pool heat transfer for materials with different thermophysical properties.

Kou and Sun [65] carried out the computer simulation of weld pool fluid flow and its effects on the weld penetration. They computed the steady state two dimensional heat and fluid flow in static arc weld by considering the buoyancy force, electromagnetic force and the thermocapillary force at the weld pool surface. The computer model developed agreed well with the available analytical solution and was consistent with weld convection phenomena experimentally observed by previous investigators. The governing equations were solved using finite difference method. Akira *et al.* [66] conducted numerical analysis of heat and mass transfer in the static TIG arc weld pool by considering electromagnetic, buoyancy, surface tension and aero-dynamic drag forces. They have paid a special attention on the anode size or heat source size under the same heat input. A finite difference method was employed to solve the governing equations. They concluded that the flow speed caused by surface shear stress such as aerodynamic drag force and surface tension

are fastest and almost same magnitude. On the other hand the flow induced by body force like electromagnetic force is secondary, and buoyancy force is the weakest among all for a heat input of $Q = 1570J/s$ and a current of $I = 200A$. The study also involved the effect of the arc length on the aero-dynamic arc drag force.

Mclay and Carey [69] developed a finite element formulation and analysis to study coupled heat transfer and viscous flow in a weld pool. The major important implementation of their study are the surface tension driven flow and the moving phase boundary. The results computed using good grid resolution on a CRAY computer reveal the detailed structure of the flow circulation regions and layers. The results give much more details and provide a more comprehensive treatment than those computed previously using finite difference methods.

DebRoy and his group had carried out a bulk volume of studies in the fluid flow and heat transfer modeling of weld pool [58, 64, 70–72]. Zhang *et al.* [15, 64] studied the evolution of temperature and velocity fields during gas tungsten arc spot welding of AISI 1005 steel using a three dimensional transient numerical model. They obtained a good agreement between calculated geometry of the weld fusion zone and the measured one and also for the weld thermal cycles with the experiment. They used a dimensional analysis to understand the importance of heat transfer by conduction and convection at various stages of the evolution of the weld pool and the role of various driving forces for convection in the weld pool. Roy *et al.* [70] used a three dimensional numerical heat transfer and fluid flow model to study the temperature and velocity fields during welding of 304 stainless steel with a pulsed laser beam. Rai *et al.* [71] used three dimensional numerical model to determine the keyhole shape and size with rigorous fluid flow and heat transfer calculations in the liquid and the two phase solid-liquid regions. They used a vorticity based turbulence model to estimate the values of effective viscosity and effective thermal conductivity of the liquid metal in the weld pool. It is shown that the temperature profile and weld pool shape and size depend strongly on the convective heat transfer for low thermal conductivity alloys like stainless steel. For high thermal conductivity aluminum alloys, on the other hand, convection does not play a significant role in determining the shape and size of the weld pool. Ribic *et al.* [58] studied the heat transfer and fluid flow patterns in GTA/Laser hybrid welding using a three dimensional numerical model and tested by comparing model predictions with experimental data. Mishra *et al.* [72] carried out numerical modeling of heat transfer and fluid flow of gas tungsten arc welding of stainless steel with different sulfur concentrations. The numerical and experimental results indicated that sulfur from both the plates mixed rapidly and there was no significant gradient of sulfur concentration in the weld pool except very close to the edges along the fusion boundary. Although the sulfur concentration of the weld pool affected weld geometry, flattering of the arc towards the low sulfur side was found to be an important factor governing the shifting of the weld pool and the missed weld joint.

A topical review by Tanaka and Lowke [57] gives a review of recent papers which have led to the capability of the prediction of weld depths for gas tungsten arc welding, for any given arc current, electrode shape or separation and welding gas. They considered the electrode, the arc plasma and the weld pool, which constitute the welding process, as a unified system. They presented also a review of methodologies for predicting the properties of the arc and also the profile of the weld pool produced by the arc. Weld profiles were

developed using the conservation equations of fluid dynamics for stainless steel different gas protection. The markedly different weld depths which are obtained are related to basic material functions such as specific heat, electrical and thermal conductivity. From the study they found out the temperature dependance of surface tension coefficient has a marked effect on the weld depth and profiles because it can influence the direction of circulatory flow in the weld pool. In another study Tanaka *et. al.* [48] studied the static tungsten-inert-gas (TIG) welding process treated in a unified numerical model, considering the whole region of TIG arc welding namely, tungsten cathode, arc plasma, work piece and the weld pool, taking into account the close interaction between the arc plasma and weld pool as shown in figure 1.14. The interface between the weld pool and arc plasma is treated as an internal boundary, and special numerical treatments were considered at this interface to model the transfer phenomena between the arc plasma and the anode. Unfortunately, their numerical calculations did not include the temperature gradient of surface tension, instead they used some arbitrary value and computed the weld shapes which dependent on the chosen value.

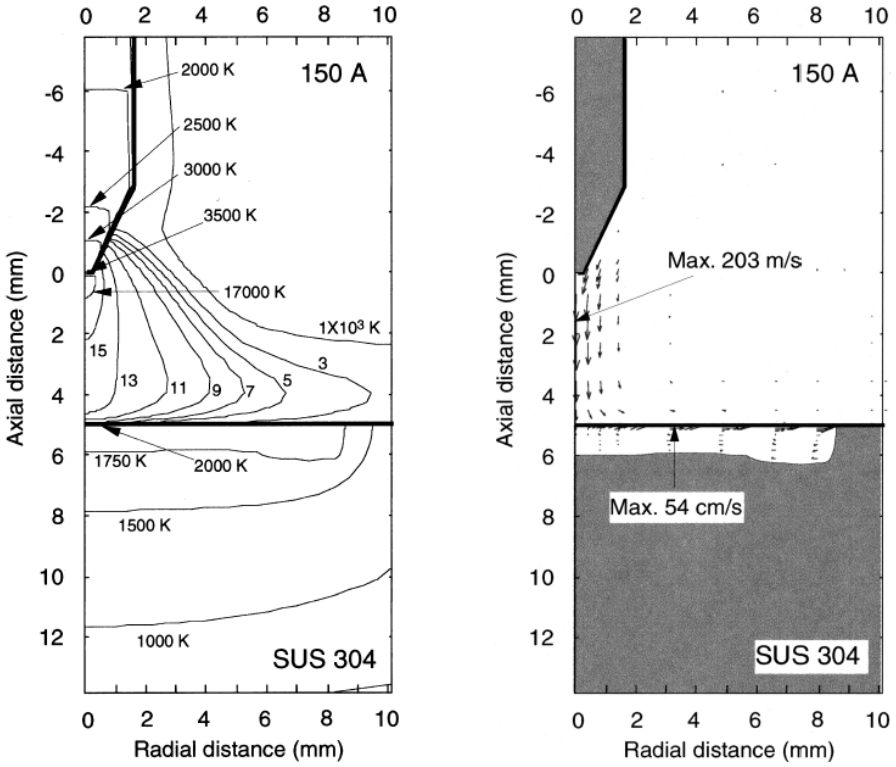

Figure 1.14: 2D calculations of temperature and velocity field for a 150A static argon arc in the welding of a 304 stainless steel sample containing a low concentration of sulfur [48].

Lu *et al.* [73] established a numerical model of the welding arc and weld pool for moving argon shielded gas tungsten arc welding to systematically study the effect of the active element oxygen and the welding parameters on the Marangoni convection and the weld shape.

Recently Traidia *et al.* [18, 34, 60, 61, 74] carried out a lot of work in the development of magneto hydrodynamic models which include the anode, the arc plasma and the cathode

for the prediction of heat transfer and fluid flow both in the arc and the weld pool region. Their unified time dependent model describes the heat transfer, fluid flow and electromagnetic fields in the three regions. One of their study [74] involves the numerical simulations of pulsed TIG welding for both partial and full penetration. Figure 1.15 shows the fully penetrated and partially penetrated weld pool solutions along with arc model for pulsed GTA welding. They used deformable free surface with a temperature dependent surface tension gradient and also considered latent heat of fusion. In another study [60] they used a model which can handle the fully penetrated weld pool case. In another work [61] they proposed a hybrid 2D-3D model for the numerical simulation of gas tungsten arc welding which predict the temperature field as well as shape of the solidified weld joint for different operating parameters. They proposed a novel way to model the effects of the filler metal in GTA welds on both the energy and momentum balances of the weld pool. Some of the important observations from their study are, the weld pool depth is locally decreased in the presence of filler metal, which is due to the energy absorption by the cold feeding wire from the hot molten metal. Their computed results shows the use of negative constant surface tension gradient results in two outward loops in the weld pool, convecting hot fluid elements toward the edges of the weld, whereas the use of temperature dependent surface tension gradient induces four loops in the weld pool corresponding to the regions where this coefficient is either positive or negative.

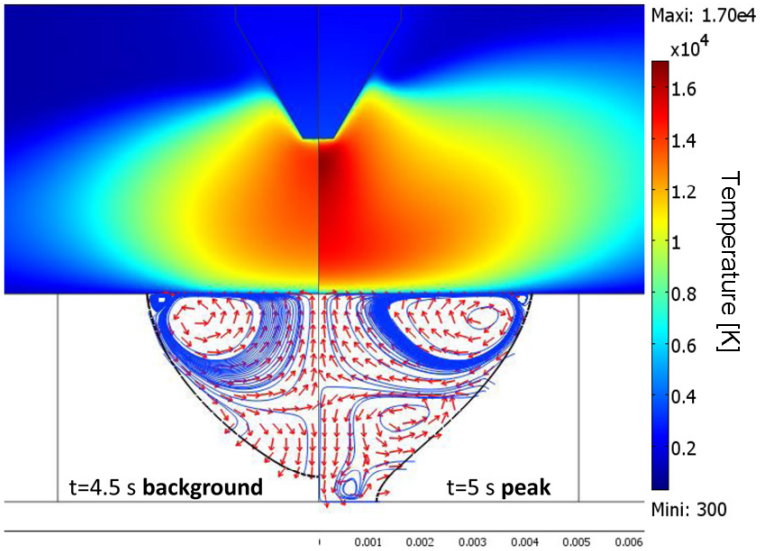

Figure 1.15: Fully and partially penetrated weld pool solutions along with arc model for pulsed GTA welding. Interesting to observe and understand the heat transfer and fluid flow both in the argon arc and weld pool of a AISI 304 stainless steel. [60]

Kong *et al* [62] proposed a three dimensional weld pool model for the moving gas tungsten arc welding process considering free surface and combined the effects of surface tension gradient, buoyancy force, arc pressure and arc drag force. They concluded that the deformation on the weld pool surface and welding speed affect fluid flow and heat flow there by temperature gradients and molten pool dimensions. Dong *et al.* [59] studied the effect of the active element oxygen and welding parameters on the liquid pool convection and the weld shape variations. Their mathematical model include both the welding arc and the weld pool for a moving GTAW of SUS304 stainless steel. They concluded that

the welding parameters change the temperature distribution and current density on the pool surface and as a result a change in the magnitude and direction of the Marangoni convection and the magnitude of the convection induced by the electromagnetic force. Also when the oxygen content is high, the weld shape is narrow and deep because of the inward convection induced by both Marangoni and electromagnetic force for different welding parameters. When the welding speed or electrode gap increases, the temperature gradient of the pool surface is decreased and the inward Marangoni convection is weakened, which make the weld D/W ratio decrease.

Berthier *et al.* [75, 76] developed a two-dimensional axial symmetric model to study the melt pool flow behavior of static TIG and A-TIG welding of stainless steel disc (304L). Their numerical results have shown the effect of an activating flux on the geometry of the weld beads. They also explained the Marangoni effects combined with Lorentz force for both TIG and A-TIG welding. They concluded that the Lorentz force has a significant effect on the weld pool shape in the case of negative surface tension temperature coefficient $\partial\gamma/\partial T$ but have no effect in the positive one.

1.5 GTAW Anode modeling

1.5.1 Mathematical model for heat conduction

A rigorous solution of the complete heat flow equation considering heat transfer by both conduction and convection is complex. As a first step it is often useful to discuss a simplified solution considering only conduction heat flow. This simplification is attractive since analytical solutions can be obtained for the heat conduction equation in many situations, and these solutions can provide interesting insight about the fusion welding process. For example, calculated temperature profiles are useful in determining the weld pool shape and size, cooling rates, the size of the heat affected zone and the resulting weldment structure. The accurate computation of the transient temperature field is the critical first step for the identification of fusion zone boundary and the weld induced imperfections like residual stress, deformations and the weld solidification cracking etc. in arc welding process. This is necessary because the temperature has a first order effect on the microstructure, strain, stress and ultimately on the formation of the defects in welds while they have at most a second order effect on temperature field [77]. In several simple welding systems it is possible to generate fairly reliable results using heat conduction models, which is simpler and computationally inexpensive [78].

The presented mathematical model describes the thermal energy transport for two dimensional solid domain and it includes the following physical processes that govern the weld behavior:

1. 2D heat transfer in the welding sample;
2. transient heat conduction into the workpiece;
3. heat transfer phenomena at the free surface.

The major assumptions used for this simple heat conduction model are as follows:

- Temperature dependent thermophysical properties are considered;

- Gaussian heat distribution is assumed for the welding arc;
- All the exterior boundaries were given convection and radiation boundary condition.

Governing equation and boundary conditions

The distribution of the temperature field induced during the welding can be expressed by the energy balance equation (without heat generation) as follows:

$$\rho C_p(T)\frac{\partial T}{\partial t} = \nabla \cdot (k(T)\nabla T) \tag{1.3}$$

Where ρ = density (kg/m^3)
$k(T)$ = Temperature dependent thermal conductivity (W/mK) is assumed to be isotropic in all directions.

$C_p(T)$ = Temperature dependent Specific heat (J/kgK)

Because of k and c_p are functions of T, Equation 1.3 is non-linear.
Equation 1.3 is subjected to following boundary conditions:

In the region exposed to the environment

$$-k_n\frac{\partial T}{\partial n} = h(T - T_\infty) + \sigma\epsilon(T^4 - T_\infty^4) \tag{1.4}$$

and at the region of heat supply

$$-k_n\frac{\partial T}{\partial n} = q + h(T - T_\infty) + \sigma\epsilon(T^4 - T_\infty^4) \tag{1.5}$$

Where q = The surface heat flux (W/m^2)

k_n = Thermal conductivity normal to surface (W/mK)

$\partial/\partial n$ denotes the differentiation along the outward drawn normal to the boundary surface

h = Convective heat transfer coefficient $(W/m^2K$

σ = Stefan-Boltzmann constant (W/m^2K^4)

ϵ= Emissivity

T_∞ = Temperature at infinity (K)

Due to the inclusion of radiation, this boundary condition is non-linear. In addition, the initial condition must be specified for (x, y, z, t) points in the domain:

$$T(x, y, z, 0) = T_0(x, y, z) \tag{1.6}$$

If the partial differential equation 1.3, boundary condition equations 1.4 or 1.5, and the initial condition equation 1.6 are specified, the problem is well posed and a unique solution exists.

1.5.2 Heat transfer and fluid flow modeling

Generally, in order to describe the heat transfer and fluid flow in the weld pool, the following governing equations, which are presented in the Cartesian-tensor form are needed.

Governing equations

The governing equations that describe the transient development of weld pools due to the coupled conduction and convection heat transfer based on the assumptions are the continuity equation, the momentum equation and the energy equation.

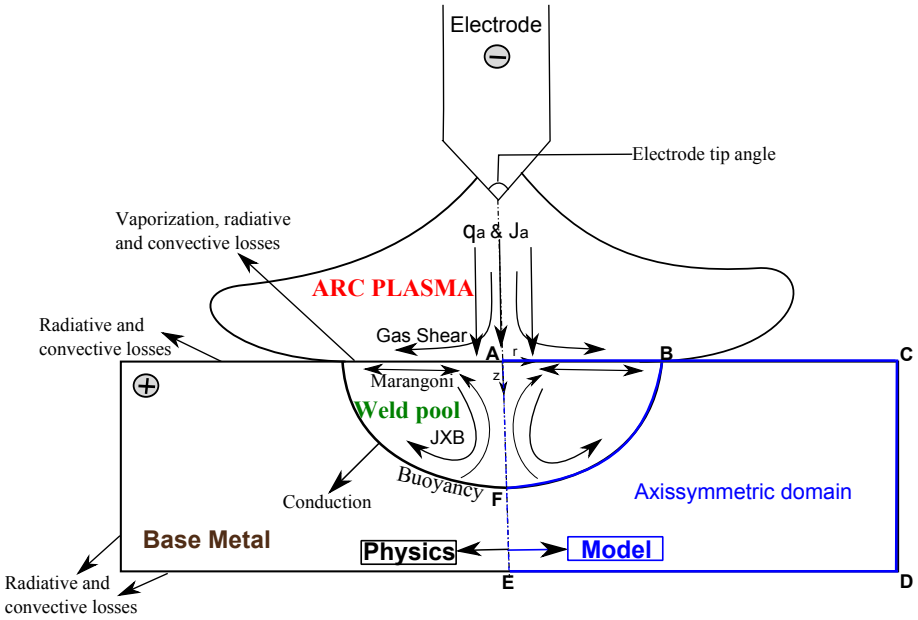

Figure 1.16: Axisymmetrical domain

The classical incompressible Navier-Stokes equations for a Newtonian viscous fluid must be considered to get the velocity, pressure and temperature fields. The classical Navier-Stokes equations which govern the fluid flow in the weld pool can be expressed as follows:

Conservation of mass

$$\nabla \cdot \vec{v} = 0 \tag{1.7}$$

Conservation of momentum

An incompressible, laminar and Newtonian liquid flow is assumed in the weld pool. Thus, the liquid metal circulation in the weld pool can be represented by the following momentum equation:

$$\rho \frac{\partial \vec{v}}{\partial t} + \rho \vec{v} \cdot \nabla \vec{v} = -\nabla \vec{p} + \mu \nabla \cdot \left(\nabla \vec{v} + \nabla^t \vec{v} \right) + \vec{S_u} \tag{1.8}$$

In words:

```
Transient + Convective = pressure gradient + Diffusive + Source
```

The source term for the momentum balance equation is written as $S_u = \boldsymbol{F_v} - Ku$, where $\boldsymbol{F_v}$ is the body force and the second term represents the frictional dissipation of momentum in mushy zone according to Carmann-Kozeny equation for flow through porous media [79] which is detailed in section 1.5.3.3. Body force in the weld pool is the sum of Lorentz force and gravity force. i.e. $\boldsymbol{F}_v = \boldsymbol{F}_L + \boldsymbol{F}_g$. The frictional dissipation term is used to numerically handle the melting and solidification phenomena.

Conservation of Thermal Energy

$$\rho C_p^{eq} \frac{\partial T}{\partial t} + \rho C_p^{eq} \vec{v} \cdot \nabla T = \nabla \cdot (k \nabla T) + Q_v \tag{1.9}$$

In words:

```
Transient + Convective = Diffusive + Source
```

Electromagnetic calculations

The flow of current through the weld pool will give rise to the electromagnetic force. The velocity distribution in the weld pool is affected by these forces. The **Lorentz force** is then given by:

$$F_L = \mathbf{J} \times \mathbf{B} \tag{1.10}$$

Thus, it is important to calculate the current density distribution and magnetic field intensity in the weld pool before calculating the force distribution in the weld pool. The continuity equation for electric charge and current is given by **Gauss law** as

$$\nabla \cdot \mathbf{J} + \frac{\partial \rho_c}{\partial t} = 0 \tag{1.11}$$

Where ρ_c is the charge density. If the electric field is assumed to be quasi-steady state, then the continuity equation becomes:

$$\nabla \cdot \mathbf{J} = 0 \tag{1.12}$$

From **Ohm's law** the equation connecting $\mathbf{J}$ and $\mathbf{B}$ is given by

$$\mathbf{J} = \sigma_e (\mathbf{E} + \mathbf{v} \times \mathbf{B}) \tag{1.13}$$

The term $\mathbf{v} \times \mathbf{B}$ corresponds to the interaction of the velocity field on the magnetic field. This term is very small for a welding process [80]. Assuming the magnetic Reynolds number (ratio of magnetic field induced by convection to the one imposed by the arc) is much less than unity, the current density can be written as:

$$\mathbf{J} = \sigma_e \mathbf{E} \tag{1.14}$$

and since the scalar electric potential, ϕ, is defined as $\mathbf{E} = -\nabla\phi$, Equations 1.12 and 1.14 can be combined to give

$$\nabla^2 \phi = 0 \tag{1.15}$$

assuming that the electrical conductivity is constant for stainless steel. This is the standard Laplace equation for electrical charge continuity. Hence, by solving the above equation for the voltage potential in the entire domain of the work piece, one can obtain the

current and magnetic field distribution.
The current density can be obtained using :

$$\mathbf{J} = -\sigma_e \nabla \phi \tag{1.16}$$

while the magnetic flux density **B** can be derived from **Ampere's law** as

$$\nabla \times \mathbf{B} = \mu_0 \mathbf{J} \tag{1.17}$$

Where σ_e is electrical conductivity, ϕ is the electrical potential, **J** is current density , **B** is the self induced magnetic field intensity and μ_0 the permeability of vacuum. The Lorentz force term accounts for the coupling of hydrodynamics with the electromagnetic field.

1.5.3 Source terms and Auxiliary Phenomenological Equations

1.5.3.1 Heat flux modeling for energy equation

For the GTAW process, the deposition of heat can be characterized as a distributed heat flux on the weldment surface. Many propositions have been found in the literature since Rosenthal's traveling point source model [40, 81] in 1946 to simulate the welding process. Equation 1.18 gives the Rosenthal's analytical solution for temperature for a moving point heat source. This solution gives a good agreement with the experimental results on weld size, but not in the shape of the weld pool. Researchers have found lots of errors in the Rosenthal's analysis in the prediction of temperature near the fusion and HAZ zones. The error mainly occurred due to the infinite temperature heat source assumption and the temperature sensitivity of the material thermal properties [25].

$$T - T_0 = \frac{q}{2\pi kr} exp\left(\frac{-v(r-x)}{2\alpha}\right) \tag{1.18}$$

Pavelic *et al.* [82] introduced the disc model, which is a distributed heat source with Gaussian profile as shown in figure 1.17 to represent a welding arc, in the form:

$$q(x,y) = \frac{f_d U I \eta}{\pi r_H^2} exp\left(-f_d \left[\frac{r}{r_H}\right]^2\right) \tag{1.19}$$

Where U is the welding voltage, I welding current, η the arc efficiency, f_d is the power distribution factor and r_H is the characteristic radial dimensional distribution parameter that defines the region in which 95% of the heat flux is deposited [14]. The efficiency parameter (η) will account for the various heat loss occurring between electrode and the workpiece, which is explained in section 1.2.3. f_d and r_H together define the shape of the Gaussian profile. Higher f_d and smaller r_H indicate a more constrained and intense arc for the same arc efficiency, and vice versa. In literature, two typical values of f_d have been reported: 3 and 0.5. The f_d value of 0.5 was proposed by Tsai et al. [83] based on experimental measurements. On the other hand several weld models [51, 65, 68, 75, 76, 84] used the f_d value of 3. The f_d value of 0.5 is favored for arc welding [37]. The first estimate of weld pool geometry has been provided by Eagar and Tsai [41] based on the distributed traveling heat source on a semi-infinite plate. The assumptions such as the absence of convective and radiative heat losses, constant thermal properties and quasi-steady state semi-infinite medium were similar to Rosenthal model with the only exception of Gaussian

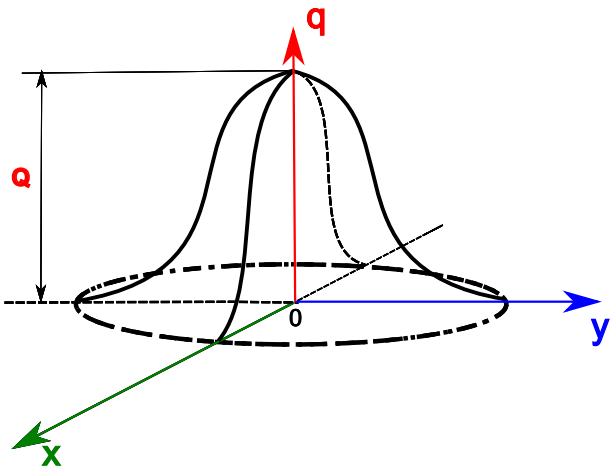

Figure 1.17: Disc model of heat distribution for GTAW used in the present research study

distributed representation of heat source. A lot of researchers validated and verified the usefulness of this model. A detailed survey of various studies can be found in thesis work of Qureshi [25]. This type of thermal energy density distribution is often used as an approximation [83, 85], as illustrated in Fig. 1.19. The dashed line is the Gaussian power distribution.

Goldak et al. [78] come up with a model with double ellipsoidal moving heat source configuration to incorporate this volume heating and the size and shape of the heat source can be easily changed to model both the shallow and deep penetrating welding processes. Figure 1.18 shows Goldak's double ellipsoidal heat source model. The front half of the

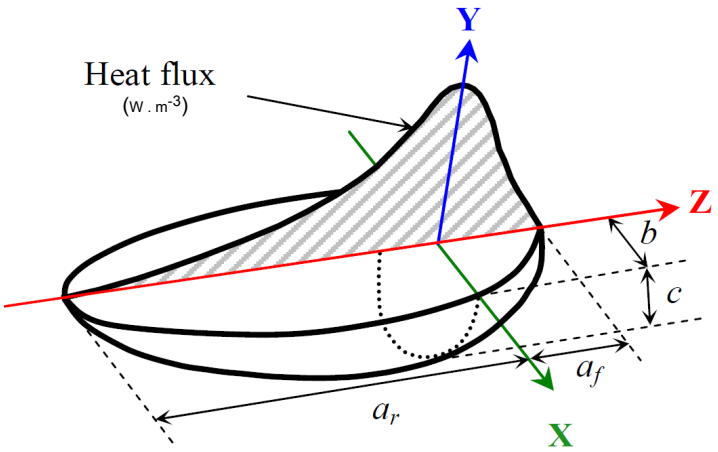

Figure 1.18: Double ellipsoidal heat source model proposed by Goldak [25]

source model is the quadrant of one ellipsoid, and the rear half is the quadrant of another ellipsoid. The power density distribution of the front half is given by equation 1.20 as follows:

$$q(x,y,z) = \frac{6\sqrt{3}\eta Q f_f}{a_f bc\pi\sqrt{\pi}} exp\left(-\frac{3x^2}{b^2} - \frac{3y^2}{c^2} - \frac{3z^2}{a_f^2}\right) \tag{1.20}$$

Similarly, the power density distribution of the rear half is given by equation 1.21 as follows:

$$q(x,y,z) = \frac{6\sqrt{3}\eta Q f_r}{a_r bc\pi\sqrt{\pi}} exp\left(-\frac{3x^2}{b^2} - \frac{3y^2}{c^2} - \frac{3z^2}{a_r^2}\right) \tag{1.21}$$

Where, $Q = VI$ and $f_f + f_r = 2$ Where a_f,a_r,b, c are the shape parameters, q_0 is effective heat input, f_f and f_r are the fractions of heat deposited in the front and rear half, all are heat input parameters. The term $6\sqrt{3}\eta$ is the heat flux distribution parameter and it characterize the concentration level of heat flux distribution, based on the heat flux concentration level or heat flux distribution feature of a welding method to determine its value.

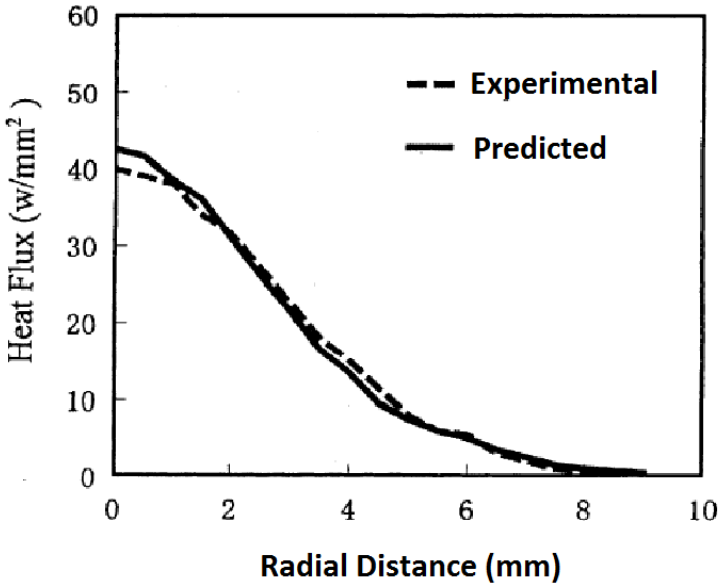

Figure 1.19: Heat flux at the anode (arc current 190A*, arc length* 5.5mm*,* 75 *tip angle argon arc) [85]*

1.5.3.2 Treatment of Latent Heat

To take into account the latent heat of melting, an equivalent heat capacity formulation was used. Enthalpy can be expressed as $H = \int \rho c(T)dT$, the temperature difference of solid phase and liquid phase is ΔT. Therefore the equivalent specific heat is considered as:

$$c_p^{eq} = c_p + \rho \Delta H_f \frac{df_L}{dt} \tag{1.22}$$

Where ΔH_f is latent heat of fusion, f_L is the liquid fraction.

1.5.3.3 Melting and Solidification Modeling

The drag term in momentum equation 1.8 refers to the enthalpy porosity approach to numerically handle the solidification around the melting temperature of the material [79]. Where K is as follows:

$$K = c_1 \frac{(1 - f_L)^2}{f_L^3 + \epsilon} \tag{1.23}$$

and c_1 and ϵ are constants, where the first parameter depends on morphology and size of the dendrites. In the present study the value of c_1 is set to 10^{12}. The latter is intended to avoid division by zero and is equal to 10^{-3}. Therefore, an artificial range for melting and solidification called mushy zone is introduced, where f_L is the liquid fraction, assumed to vary linearly with the temperature in the mushy zone and expressed as follows:

$$f_L = \begin{cases} 1 & T > T_L \\ \frac{T-T_S}{T_L-T_S} & T_S \geq T \geq T_L \\ 0 & T < T_S \end{cases} \tag{1.24}$$

To include the effect of phase change on convection, the phase solid is modeled as an extremely viscous liquid ($\mu_{sol} = 10^5 Kg.m^{-1}.s^{-1}$). An apparent viscosity is then defined with a smoothed switch function that emulates the step of viscosity at the melting temperature. The COMSOL's built in smoothed Heaviside function is also used to smooth out the discontinuity of the other material properties due to the phase-change.

1.5.3.4 Treatment of interface between solid and liquid phase

A fixed grid numerical method is used in the model to track the liquid/solid interface. In this method, the computational mesh is generated only once, and the liquid/solid interface is located using the liquid fraction $f_L(T)$. In this method the governing equation is computed in the whole domain (domain 2). In order to use different physical properties for the different state, we can use the liquid fraction as follows:

$$\alpha = \alpha_L f_L + \alpha_s(1 - f_L) \tag{1.25}$$

Where α is considered physical property and α_L and α_S are respectively the physical properties of liquid and solid phases.
The momentum equation 1.8 is computed in the whole domain 2. The Karman-Kozeny approximation which can be derived from Darcy law, has been widely used in most fixed grid weld pool models.

1.5.3.5 Buoyancy force

The gravity force in the weld pool is the combination of classical inertia force $\vec{F_i} = \rho_0 \vec{g}$ and the buoyancy force $\vec{F_b}$. The high thermal gradients that take place in the weld pool induce a natural convection flow (buoyancy effect) due to the dependence of molten metal density on temperature. The Boussinesq approximation was used in the calculation of buoyancy force driven flow [86]. In other words, the variation of density of the liquid metal is ignored. Figure 1.12(a) and (b) shows the buoyancy force direction and buoyancy driven convection respectively. As shown in figure, the liquid metal rises along the pool center with a low magnitude and fall along the pool boundary due to the local variation of density. This buoyancy force tends to create outward flow which increases the weld pool width. The buoyancy effect can be modeled using the Boussinesq approximation as follows [86]:

$$\vec{F_b} = \rho_0(1 - \beta(T - T_{ref}))\vec{g} \tag{1.26}$$

Where ρ_0, β and T_{ref} are respectively reference density, thermal expansion and a reference temperature of the molten pool. Even though, the gravity force is approximately 10 times larger than the buoyancy force, it does not contribute to the creation of flows, since contrary to buoyancy force, it is constant and does not present any spatial gradient in

the weld pool. But it has significant impact on the free surface shape [18]. Tanaka et al.[57] reported that the velocity field induced by only the buoyancy effect is 10 times lower than that induced by surface forces (Combination of Marangoni shear stress and arc drag force). If buoyancy force is the only driving force for the liquid convection, an order of magnitude of the maximum velocity under buoyancy driven flow is given by [15]:

$$u_{grv} = \sqrt{g\beta\Delta T D} \tag{1.27}$$

Where D is the pool depth. Traidia [18] studied the effect of buoyancy force on the weld shape for horizontal, vertical or overhead welding positions. Figure 1.20 shows the computed steady state weld pools in the vertical case where only buoyancy force is governing the fluid flow in the weld pool.

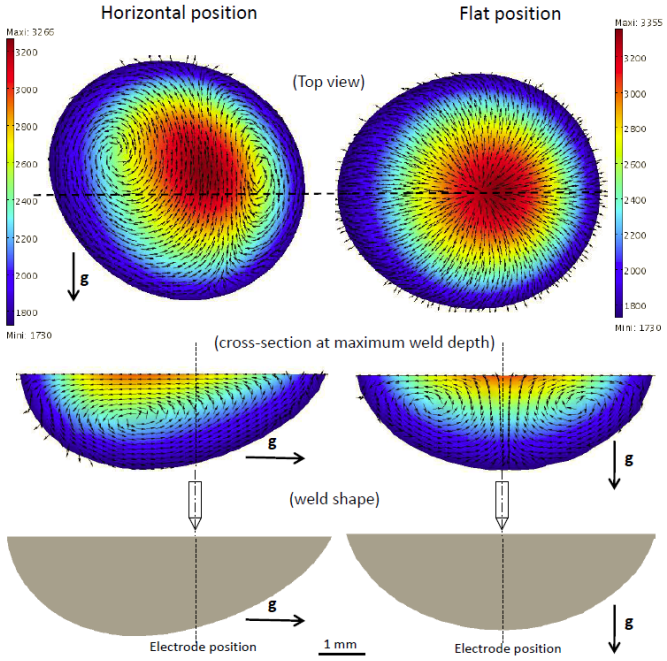

Figure 1.20: Influence of the welding position on the buoyancy induced flow for $I = 150A$ Temperatures are given in K [18].

1.5.3.6 Electromagnetic Force

The electromagnetic force, also called Lorentz force, is caused by the interaction of electric current field and induced magnetic field in the metal work piece. Figure 1.12(c) and (d) shows the direction of the Lorentz force with a direct current electrode negative and the corresponding liquid metal convection respectively. The downward and inward directed electromagnetic force create a flow downwards in the center of the weld pool from the periphery. The electromagnetic force can be expressed as:

$$\vec{F}_{emf} = \vec{J} \times \vec{B} \tag{1.28}$$

Where $\vec{J}$ is the current density vector and $\vec{B}$ is the magnetic flux vector in the weld pool. Tanaka et al.[87] reported that for pure argon shielding gas, the fluid velocities induced by only the Lorentz forces are 4 times lower than that induced by surface forces. Traidia

[18] made a study on the impact of chemical composition of the shielding gas on the magnitude of Lorentz forces. Figure 1.21 shows the dependence of the shielding gas in the Lorentz force distribution. The maximum value of radial electromagnetic component is 14 times more important for a pure helium arc than for a pure argon arc, while the axial component is much more important (54 times).

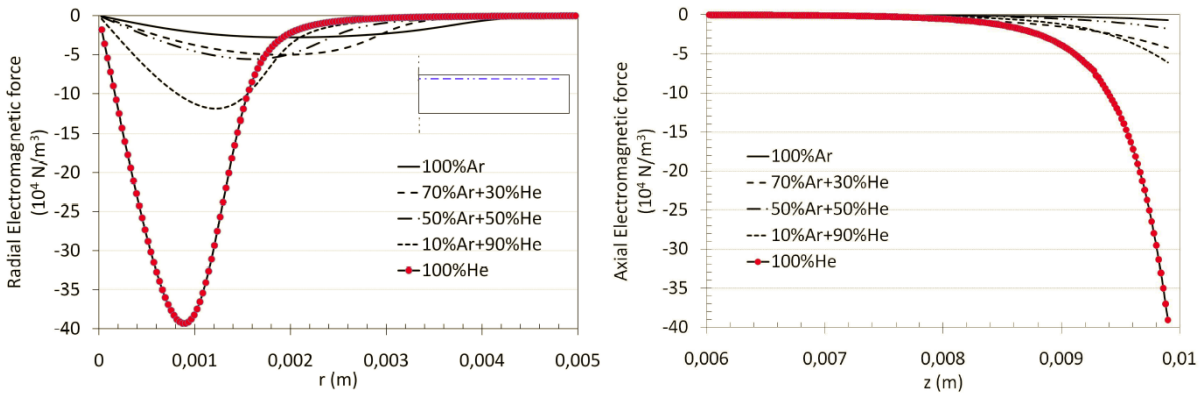

Figure 1.21: Variation of radial and axial component of electromagnetic forces for different shielding gases [18]

1.5.3.7 Surface tension modeling as a function of temperature and sulfur content

Surface tension (γ) is a thermophysical property of the liquid metal, which may generate a shear stress at the liquid/gas interface. The spatial gradient of surface tension is a stress, which is known as the Marangoni stress. This stress arises due to the spatial variation of temperature and composition, which can be expressed as [15]:

$$\tau = \frac{\partial \gamma}{\partial T}\frac{\partial T}{\partial r} + \frac{\partial \gamma}{\partial C}\frac{\partial C}{\partial r} \tag{1.29}$$

Where τ is the shear stress due to surface tension, T is the temperature, r is the distance along the surface from the heat source, and C is the concentration of surface active element. In most cases, the difference in surface tension is due to the spatial temperature variation. In other words the $\partial\gamma/\partial C$ term in equation 1.28 is zero, and shear stress depends only on $\partial\gamma/\partial T$ and the spatial temperature gradient $\partial T/\partial r$ at the weld pool surface. $\partial\gamma/\partial T$ is commonly known as 'surface tension gradient' or 'the thermal gradient of surface tension'. It has been identified that this coefficient has a great influence on the flow directions in the weld pool [18, 35, 53, 88].

In the absence of a surface active element, the temperature coefficient of surface tension ($\partial\gamma/\partial T$) is less than zero for many materials. As shown in figure 1.22, when this coefficient is negative, the surface tension is highest at the edges of the weld pool, and the thermocapillary flow is outward from low to high surface tension region, figure 1.22 (a), which results in a wide and shallow weld. For a positive surface tension gradient, surface flow is inward and heat is swept to the bottom of the weld pool and produces a narrow and deep weld figure 1.22 (b). The change in $\partial\gamma/\partial T$ from a positive value at

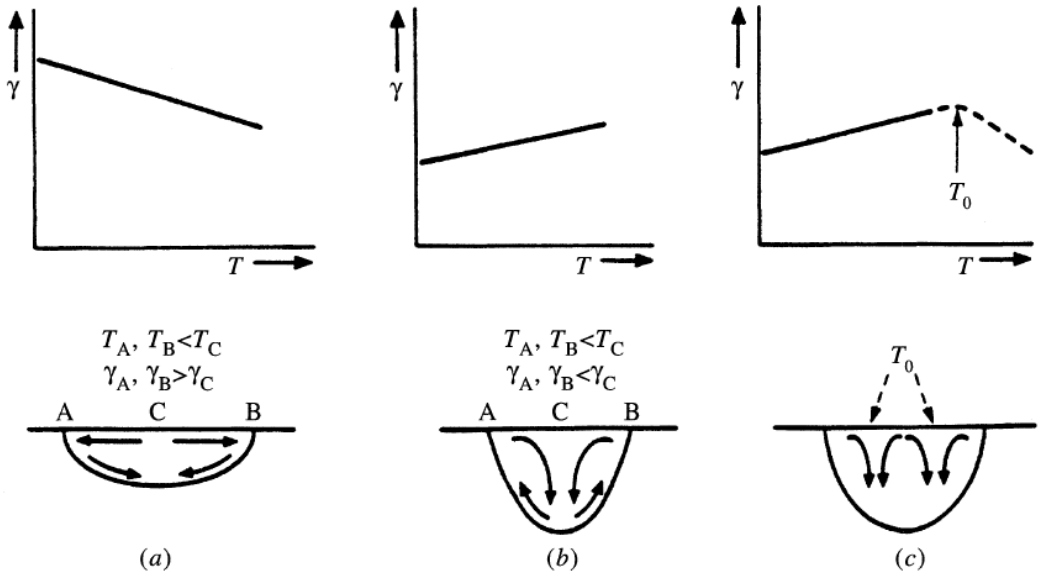

Figure 1.22: Schematic diagram illustrating the effect of surface tension gradient on the weld penetration [35].

low temperature, to a negative value at high temperature, has important consequences on the weld pool fluid flow and heat transfer, and the ultimate development of the weld [89]. Directly below the welding heat source, a hot zone exists where the temperature experienced by the molten weld metal is likely to be above the critical temperature, such that a negative $\partial\gamma/\partial T$ prevails in this region. This would cause two opposing surface tension gradients to exist on the weld pool surface: a positive surface tension gradient at the periphery of the weld pool, and a negative surface tension gradient at the center of the weld pool. Depending on the relative magnitude of these two driving forces, either a radially outward flow or a radially inward flow, or even a combination of both resulting in two opposing vertices, may develop as shown in figure 1.22 (c) [35].

A lot of research work has reported on the detailed heat flow and fluid flow resulting from the surface tensional gradient that exist in the weld pool surface [31, 35, 36, 53, 54, 56, 66, 68, 69, 90–93]. An improved understanding of the surface tension gradient effect was achieved by calculating $\partial\gamma/\partial T$ as a function of temperature and concentration of surface active elements. Sahoo et al. [94] proposed a semi-empirical relationship between the surface tension gradient, temperature and content of surface-active elements, for various binary alloys. For binary iron-sulfur systems, the relationship is as follows:

$$\frac{d\gamma}{dT} = -A_\gamma - R_g\Gamma_s ln(1+Ka_s) - \frac{Ka_s}{1+Ka_s}\frac{\Gamma_s\Delta H_0}{T} \tag{1.30a}$$

$$K(T) = k_1\, exp\left(-\frac{\Delta H_0}{R_g T}\right) \tag{1.30b}$$

Where a_s is the sulfur content of the workpiece material, A_γ is a constant (usually fixed at $4.3\times10^{-4}Nm^{-1}K^{-1}$), Γ_s is the surface excess at saturation ($1.3\times10^{-8}kmolm^{-2}$), R_g is gas constant($8314.3Jkmol^{-1}K^{-1}$), k_1 is the entropy factor (3.8×10^{-3}) and ΔH_0 is standard heat of adsorption, which is estimated from an empirical function of the difference in electronegativity between the solute and solvant atoms. For AISI 304L stainless steel

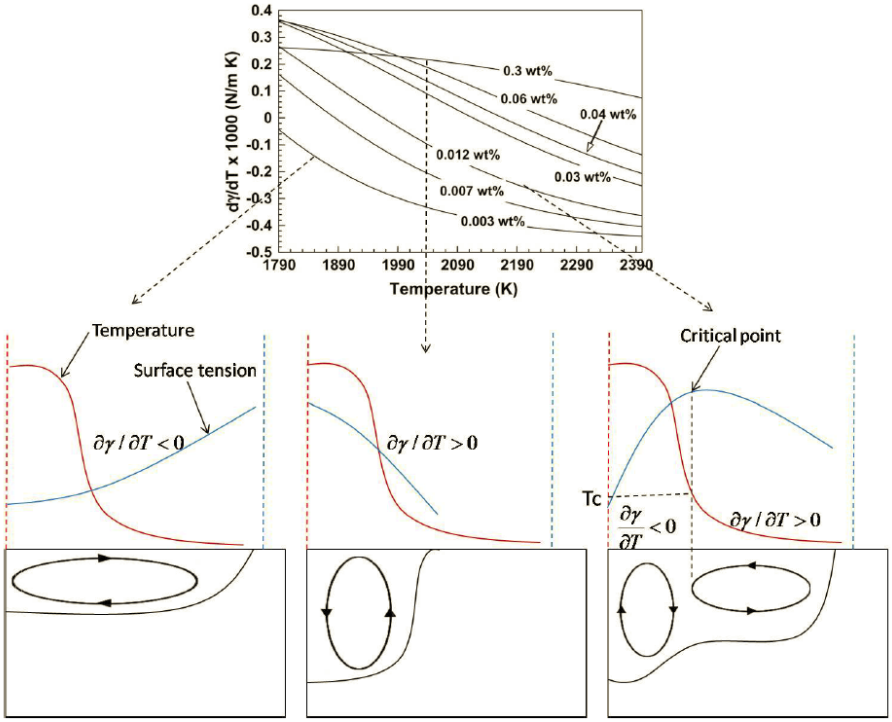

Figure 1.23: Surface tension gradient as a function of temperature and sulfur content for Fe-S alloys (top), and effect of sulfur content on the reversal flows in the weld pool (bottom) [18, 35].

alloy ΔH_0 is estimated to be $-1.88 \times 10^8 Jkmol^{-1}$ [91].

1.5.3.8 Arc drag force

The flow of the viscous plasma along the weld pool surface creates a shear stress directed towards the edges of the weld pool. This induces a outward flow as shown in figure 1.12(g) and (h), which increases the weld pool width. The gas shear stress is reported to be the third main important force in the weld pool, after the Marangoni shear stress and Lorentz forces. However, the intensity of gas shear stress is highly dependent on the welding current, the chemical composition of the shielding gas and the bevel angle of the electrode tip [73, 95]. Figure 1.24 shows the numerical results obtained for the radial distribution of the shear stress induced by the plasma jet for different shielding gas environment and for the constant welding current. For an addition of 9% hydrogen to argon produces a shear stress which is 2 times larger than that for pure Argon shielding [96]. Lee *et. al.* numerically modeled the effect of various factors that affect the intensity and distribution of the arc shear on the liquid weld pool. Figure 1.25 shows the variation of the maximum shear stress due to the arc plasma with different electrode bevel angle [95]. From their study they concluded that the electrode bevel angle and there by the arc drag force has a great influence on the fusion zone width.

1.6 Conclusion

With the availability of high computing facility and the sophisticated simulation tools enhances the more realistic modeling of the welding phenomena to understand the mech-

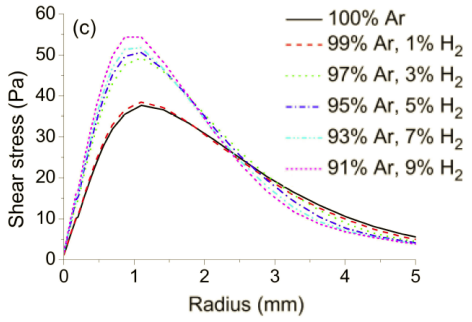

Figure 1.24: Radial evolution of the arc drag force for different argon-hydrogen mixtures. Welding current of 200 A with an arc length of 5 mm [96].

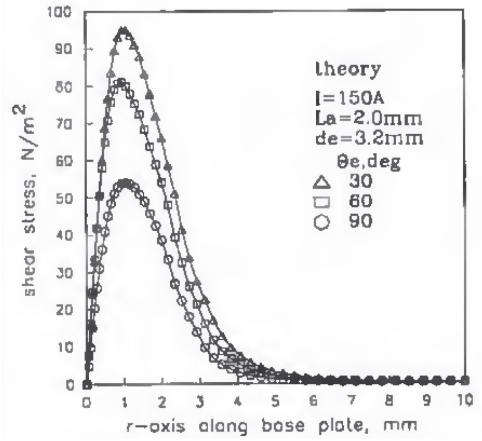

Figure 1.25: Effect of the electrode bevel angle on the arc drag distribution[95].

anism that drive the formation of weld pool.
A survey on the basic GTAW process fundamentals and the its parameters were carried out in the first section of this chapter. The effect and importance of some general process input parameters on the weld characteristics have been presented from a literature point of view.
An effort has been made to present the major physical and transport phenomena involved during the GTAW welding process. Each regions of the GTAW process were analyzed separately and discussed the basic physical coupling between them.
An introduction to the numerical modeling of welding has been presented in this chapter. The mathematical modeling of the two models considered in this thesis, such as heat conduction model and the magneto hydrodynamic model were presented in the last section. The boundary condition for heat flux and the various driving forces for the fluid flow are also detailed. A brief history on the numerical simulations on the GTAW process is carried out with latest unified model approach were discussed from literature point of view.

The proceeding chapter deals with the experimental work carried out for the current study. In view of the current research objective, preliminary experimental study is carried out to better understand and also come up with some useful assumptions for the fluid flow and heat transfer simulations.

Chapter 2

Static GTAW: Experimental Observations and Analysis

Contents

2.1 Introduction

This chapter presents the experimental work carried out during the research thesis. These experiments are necessary to better understand the effect of various welding parameters on the weld characteristics such as welding thermal cycles and the weld geometry. The first section of this chapter is dedicated to the presentation of the welding setup and associated acquisition devices for performing simultaneous measurements of temperature, welding parameters and weld pool observations. The second section presents the static GTA welding carried out and a discussion on the measured parameters such as process parameters (current and voltage), thermal history, transient evolution of weld pool (high speed camera measurements) and finally on the post processing data which includes the

macro structure study on the weld cross sections and the Electron Probe Micro Analysis (EPMA) for the sulfur concentration measurements. These experimental observations were used for the fluid flow and heat transfer study in the SS304L material for different material size and composition. The final section presents the experimental results obtained during static GTAW test for different set of input energy and material.

2.2 Experimental setup and context

2.2.1 Welding Bench- A multiphysics platform

An accurate, reliable and synchronized measurement system was used for the data aquisition from the highly noised environment of GTAW process [97]. Figure 2.1 shows an overview of the welding bench and some components of the data acquisition system. The welding traverse system comprises XY-table and a welding torch which can move in the z direction. Figure 2.1 shows the schematic of the experimental welding setup. The four major divisions of the welding bench are (1) the welding unit including generator and torch, (2) the XY-table, (3) Sensors (high speed camera and thermocouples) and (4) the data processing and controlling computers. An efficient analysis of welding and its char-

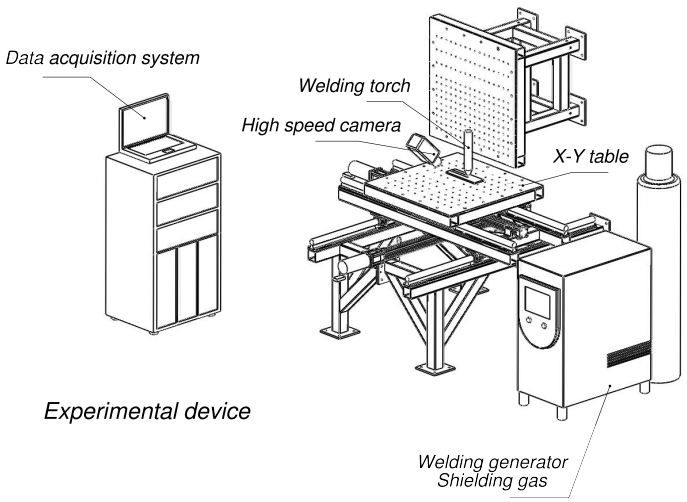

Figure 2.1: Experimental Platform and specific devices [29]

acteristic times is possible only by measuring signals of different kind simultaneously and synchronously. Due to the tremendous temperature gap between the arc plasma and the molten metal, the physical reactions in those regions (small area about one centimeter cubic space) include many unknown factors [98]. A high degree of perturbation is present in arc welding process due to the huge arc radiation and the electromagnetic noise. This leads to a hazardous situation to make any conventional measurements locally in the workpiece [4]. Also the time scale of the physical phenomena occurring in this region is very small (of the order of milliseconds). These are the main reasons why a high speed non-contact imaging technique is necessary for visual analysis of fusion welding processes. The global measurements such as current and voltage can also give information connecting the input and the output of welding process. As heat transfer is the major physical phenomena that occurs during the welding process, the measurement of the corresponding

field variable is important to analyze any major characteristics of weld pool.

By considering the different nature of data acquisition together needs a large number of experimental tests to characterize a welding phenomena. In order to manage, analyze and couple these data of different nature and acquisition frequency a library was designed during the PhD thesis of Chapuis [97] named BAME [99]. The developed data structure can quickly find information and values of different sensors during a welding test. The five main different data that can be measured using BAME during the welding process are as follows [29, 100]:

- Process : arc voltage - current - gas flow - wire speed;
- Thermal : temperature;
- Mechanic : strain gauge, displacement, force;
- Cameras : High speed camera and near infrared camera;
- Geometry : Geometrical characteristics of the specimen.

2.2.1.1 Welding unit

For the current study, the GTAW process utilizes a generator Sincosalt® AC/DC 400A and an associated automatic torch MEC4SAF-F RO® with water cooling. The tungsten electrode is used with a diameter of 2.4 mm.

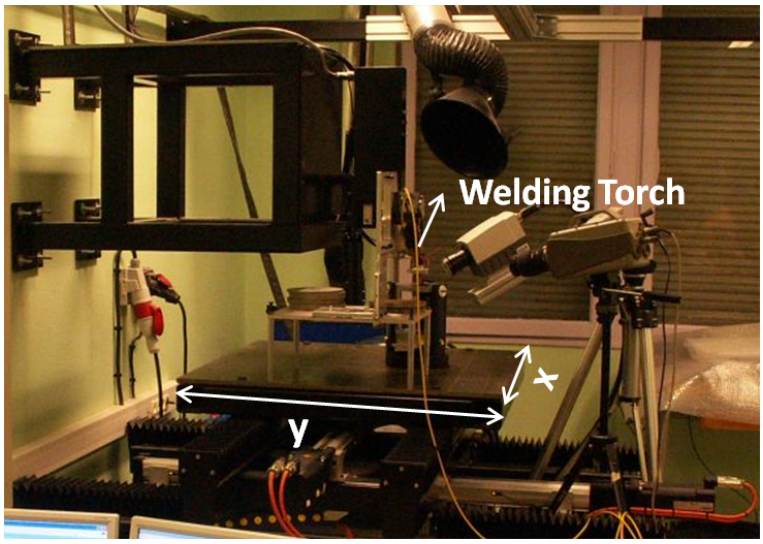

Figure 2.2: XY table

2.2.1.2 Process parameter acquisition

The major process parameters during the welding process are current (I) and voltage (U). The welding current is measured using the help of a high precision current transducer: LEM [101]. It measures the electron flow by Hall effect and gives an output voltage between 0 and 10 V proportional to the measured current. It can give a maximum

sampling frequency of 80 kHz. The welding voltage is measured in between the electrode and the work piece to avoid voltage drop across the welding power cables.

2.2.1.3 Thermocouple instrumentation on disc

Thermocouple is the most common method to measure temperature. It consists of two wires, of different metals, that are joined at one end. A change in temperature at the connection of the two wires will induce a change in the electromotive force (emf) between the other ends. As the temperature changes, the emf will change. Often the thermocouple wires are located inside a metal or ceramic shield that protects it. The most used thermocouple type is type K. It has one wire of nickel-chromium and one of nickel-aluminum. Thermocouples of type K of diameter 0.5 mm have been used in all experiments. The possible maximum temperature that the thermocouple K can measure is $1260°C$.

2.2.1.4 Weld pool visualization system

Monitoring of the weld pool behavior during welding was carried out by means of a high speed imaging technique. The monochrome digital high-speed video camera used for the weld pool visualization is *Phantom*® IR300, it has a maximum frequency of acquisition 10 kHz and with a sensor *CMOS(r)*®.

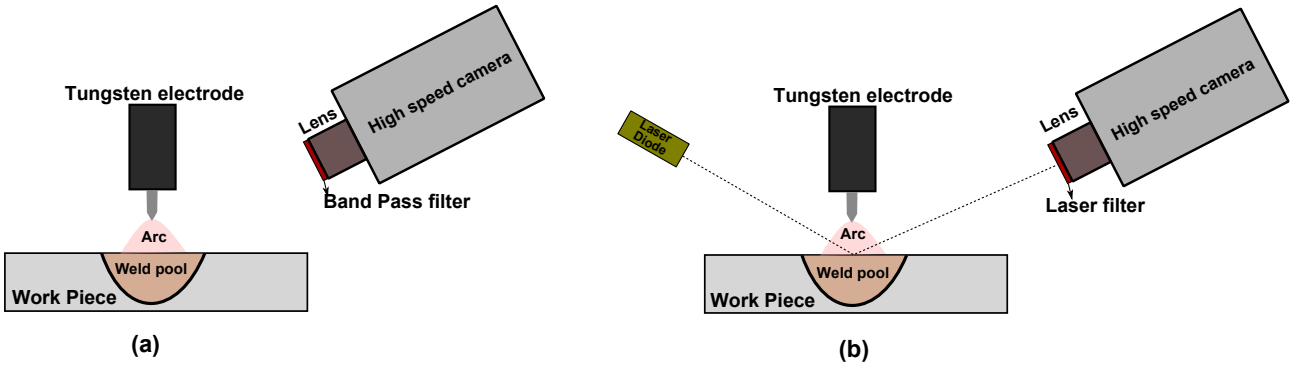

Figure 2.3: Schematic of high speed camera set up (not to scale) (a) Camera alone with band pass filter (b) Laser back light illumination with camera and laser filter

Two different settings were used for the weld pool visualization. Figure 2.3(a) shows the sketch of image capturing using the high speed camera with a band pass filter. The band pass filters were selected using a spectroscopic test, which gives the maximum emissions from the weld pool region. The 1100 nm wavelength band pass filter used for the present study. Figure 2.3(b) shows the sketch of second image capturing setup used. Here the laser diode illuminate the weld pool region and a filter with laser wavelength range (808 nm) is used in the high speed camera.

2.2.2 Post weld experimental analysis

2.2.2.1 Metallographic inspection

The examination of metallographic sections through welded joints is commonly carried out at two levels of inspection:- 1)**Macro**: Where magnifications up to 50x are employed with stereomicroscopes. 2) **Micro**: Where examination is at higher magnifications (up

to 1000x) using optical microscopes. The macrographic examination is commonly carried out on mounted cross sections through welded joints and simply involves cutting and coarse/fine grinding techniques. The resultant finish is adequate for etching, followed by an examination of the macro features of the weld joint. The macrographic observation permits to analyze the global shape and size of the weld pool, which also helps to identify different zones in the weld region due to the characteristic variation in the grain morphology. The macroscope used in the present study is *Leica*® Z16 APO.

The macro sections are cut through the center of the weld spot using a abrasive wet cutting process (water jet cutting), which minimizes the deformation from cutting and also there is no risk of thermal damage on the cut surface.

2.2.2.2 Electron probe microanalysis (EPMA)

Electron Probe Micro Analysis (also known as micro-probe) is a technique of in situ non-destructive analysis to detect elements in a volume of cubic micrometer with a sensitivity of about 100 ppm. The measurements were performed with a CAMECA SX 100 micro-probe employing five wavelength dispersive spectrometry (WDS) [102]. EPMA was used to measure the composition of the main alloying elements (Cr, Fe, Ni, Mn, and Si) and also the concentration profiles of sulfur in the base material and in the fusion zone on the cross-sections of the welds. The spot welded samples were cut in cross section through the center of the welding spot and the cross sections were well polished to get a finish of 1 μ m. The composition of the main alloying element and the measurement of sulfur were performed using an electron beam with an energy of 20 keV and beam current of 40 nA. The EPMA data was averaged over a spot size of 50 μm diameter.

2.3 Static gas tungsten arc welding experiments

The experimental sample arrangement is schematically shown in figure 2.4. The static gas tungsten arc was generated on the surface of the disc samples. The main objective

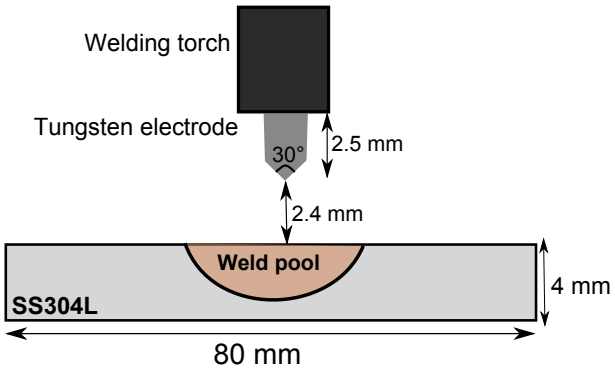

Figure 2.4: Geometric parameters for the torch and welding disc (not to scale)

of these experiments is to study the heat transfer and the transient evolution of the weld pool. Weld pool development with time was examined with emphasis on effect of input power which is varied by the welding current. For all experiments thermal measurements were carried out using thermocouples and video images of weld pool were produced in

order to validate the numerical modeling. A listing of static arc experiments can be found in table 2.5.

2.3.1 Methodology and Procedure

The Direct current Straight Polarity (negative cathode and positive anode) power setting was used for the GTAW process. The process parameters used and the welding conditions were presented in the table 2.1. The spot weld was made on 100 mm and 150 mm diameter structural steel S235 samples of 6 mm thickness and 80 mm and 40 mm diameter AISI304L low sulfur and high sulfur samples respectively of 4 mm thickness.A high-speed camera (Phantom IR300) was used with optical band pass filters to capture the weld pool evolution during static TIG welding. The images were recorded at 2000 frames per second so that which can give the weld pool dimensions. For the present set-up, the temperature

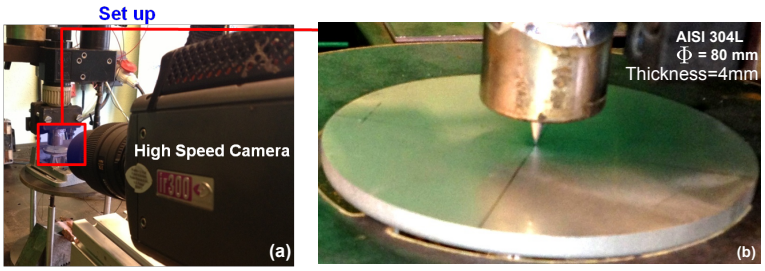

Figure 2.5: (a) Experimental setup for the Static GTAW Process (b) Close-up of the welding electrode and the AISI 304L stainless steel disc

were measured in five points with one at the center back side of the disc and two are at a distance of 4 mm and other 8 mm from the center back surface as shown in figure 2.6. The main objective of the temperature measurement is to understand the heat flow

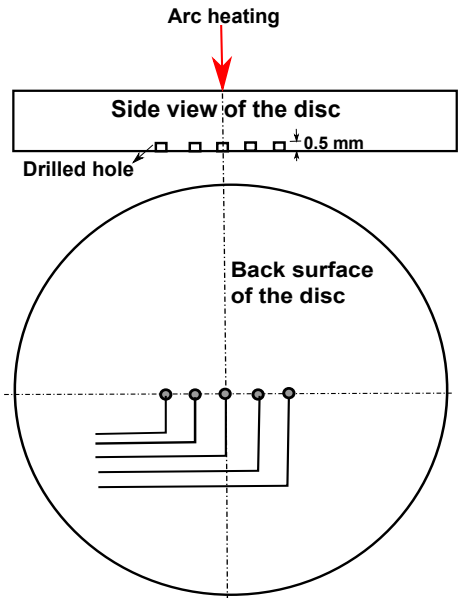

Figure 2.6: The locations of the thermocouples for temperature measurements when welding

and temperature distribution around the weld pool and also the nature of the heat source

from the arc plasma. The thermocouple measurement positions were selected in order to satisfy the following major requirements: 1) Get measurement close to the weld pool; 2) Avoid the electrical arc perturbation on the thermocouple measurement 3) Confirm the axial symmetry of the system without affecting the temperature field distribution in the material. The thermocouple contact points were placed in small drilled holes of diameter similar to the thermocouple (0.5 mm) and 0.5 mm depth as shown in figure 2.6. For the

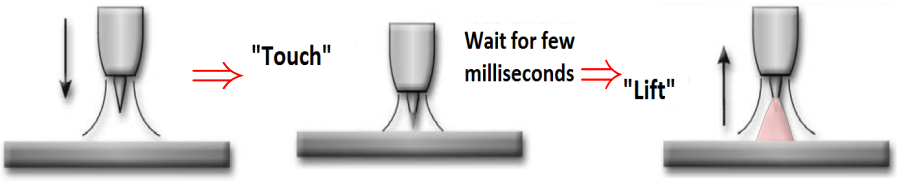

Figure 2.7: Lift Arc Technique

present study the high voltage high frequency arc starter method is not desirable because of the usage computers and the data acquisition systems, which can be interfered by the high frequency radiation. Welding where the use of high frequency for arc starting is not allowed or is not available may require a scratch or touch start technique. The scratch start technique creates an arc by scratching the tungsten lightly on the workpiece like a match. Or the tungsten may be touched to the workpiece and pulled away slightly to establish the arc as shown in figure 2.7. The high open circuit voltage of the power source is present as the tungsten touches the workpiece. This creates the tendency to stick or weld itself to the workpiece.

Table 2.1: Welding Parameters

Parameters	*Value*
Current	70 A
Arc length	2.4 mm
Voltage	9 V
Weld duration	5 s
Shielding gas (flow rate)	Argon (16 L/min)
Electrode tip angle	30°

2.3.2 Material Characteristics

For the present study stainless steel 304L material with two different sulfur content is used for the static GTAW process. The AISI 304L (austenitic) stainless steel is selected

Table 2.2: Chemical Composition of Low sulfur AISI 304 stainless steel (composition in wt.%)

SS304L	**Cr**	**Mn**	**Si**	**S**	**Ni**	**Fe**
Low sulfur	17.2	2.24	0.45	0.0024	7.63	66.9
High sulfur	17.89	2.04	0.302	0.0036	7.6	68.3

due to its wide range of applications and availability. Type 304 is a variation of the basic 18-8 grade, Type 302, with a higher chromium and lower carbon content. Lower carbon minimizes the chromium carbide precipitation due to welding and its susceptibility to inter granular corrosion [103].

Table 2.2 shows the results of EPMA, measured material composition of the two different AISI 304L samples with different concentrations of sulfur. Type 304L is an extra low carbon variation of Type 304 with a 0.03% maximum carbon content that eliminated the carbide precipitation due to welding. As a result this alloy can be used in the "as-welded" condition, even in severe corrosive conditions.

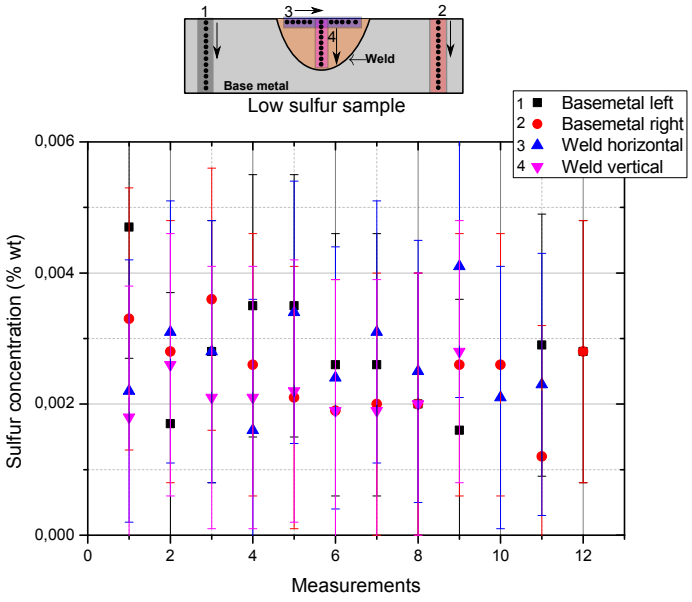

Figure 2.8: Measured sulfur content in the AISI 304L low sulfur sample using EPMA

Figure 2.8 shows the sulfur content distribution at different locations of the low sulfur sample measured using EPMA. The schematic shows the measurement points in the sample and the arrow nearby indicate the measurement number counting starting from the tail to the head. Four different locations were selected, two in the base material and two in the weld region.

Table 2.3: Sulfur content in base metal and weld region for AISI 304L samples

Material	*Weld*	*Base metal*
AISI304L Low sulfur	0.00265 ± 0.002 % wt	0.00245 ± 0.002 % wt
AISI304L High sulfur	0.00374 ± 0.002 % wt	0.00397 ± 0.002 % wt

A simple statistical data analysis is carried out in order to understand the distribution of sulfur concentration. Table 2.3 presents the mean and standard deviation of the sulfur content measured both in the base material and the weld zone. A mean of 0.00265 % wt

is obtained in the base material and 0.00245 % wt is obtained in the weld region for low sulfur 304L stainless steel sample.

Figure 2.9 shows the sulfur content distribution at different locations of the high sulfur content sample measured using EPMA. The schematic shows the corresponding locations and the arrow indicate the direction of measurement. Two locations on the base material and one location in the weld region is selected for the measurements.

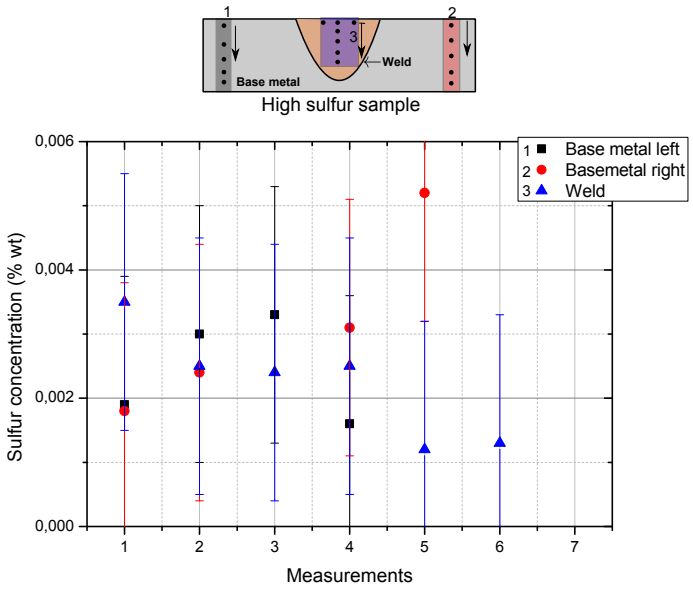

Figure 2.9: Measured sulfur content in the AISI 304L high sulfur sample using EPMA

Table 2.3 presents the mean and standard deviation of sulfur concentration in the base material and also in the weld region. A mean value of 0.00374 % wt is measured in the base material and 0.00397 % wt in the weld region.

The dimensions of the disc used are listed in the table 2.5 and the static gas tungsten arc spot were made at the center of each disc.

2.3.3 Process parameter measurement

Figure 2.10 shows the current and voltage signal measured during the static GTA welding process for current of 70 A and an arc height of 2.4 mm. During the arc initiation the current reaches a maximum value of 79 A and and then lower to 70 A and oscillate about a mean value of 70.7 A with noise measurements.

When the arc is switched on, the arc voltage increases and reaches a maximum value of 11.3 V and then gradually decreases and stabilizes with a mean value of 9.32 V. The arc is initiated using lift arc method as discussed in section 2.3.1. The initial peak corresponds to the arc initiation. The gradually increasing region thereafter corresponds to the lift arc, for a short time period of 0.5 s. As the electrode moves up, the potential between the electrodes increases and reaches a maximum value. There after the arc stabilizes and

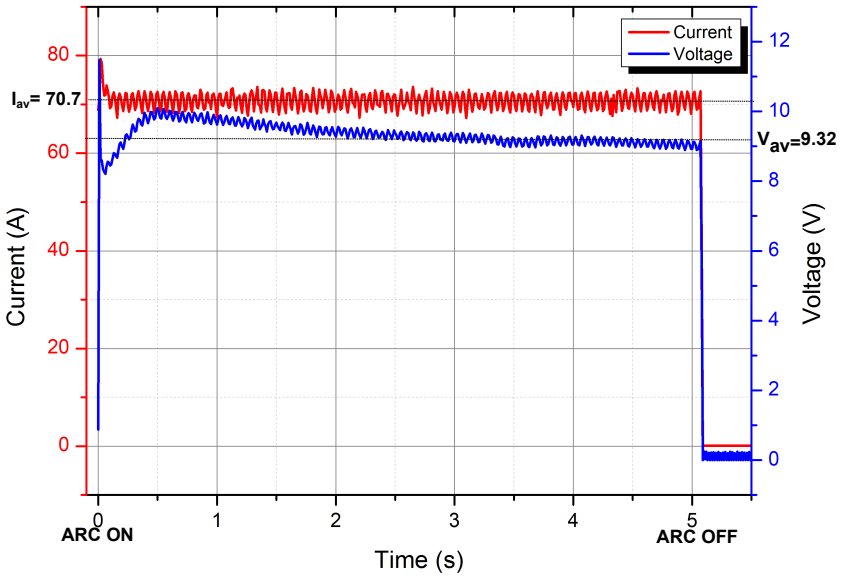

Figure 2.10: Measured process parameters for I= 70 A, Arc height= 2.4 mm

the potential decreases to a stable value with minor oscillations. From the voltage signal, due to the absence of any major fluctuations, it is believed that the oscillation due to the arc plasma on the weld pool is negligible. This means the weld pool top surface can be assumed as fixed boundary in the numerical modeling. However the majority of the small fluctuations occurring through out the signal are believed as noises originating from the electronic circuits with minor components of pool oscillation.

2.3.4 Temperature measurement

Figure 2.11(a) shows the measured temperature evolution at five selected points on the back surface of the welded sample. The points were located as one at the center back surface on a 0.5 mm drilled hole and the other four are 4 mm and 8 mm away from the center on each side as shown in schematic figure 2.11(b). But after the static welding on the disc, the macrographic images of welded sample's back surface revealed the relative deviation of the center position of the sensors with respect to the heat source center as shown in figure 2.11(c). The center of the heat source is altered by 0.3 mm. The maximum temperature reached from the back surface measurement is 789°C (1062 K) at the thermocouple measurement position T_1. The peak temperature occurs at time t = 5.467 s. Cooling rates were calculated after 10 s and 20 s after the arc heating. The temperature drops to 386°C and to 189°C at a rate of 88°C/s and 41°C/s after 10 and 20 s respectively. The maximum experimental temperature at measurement position T_2 is 619°C at a time step t = 5.63 s. The cooling rates calculated for T_2 are 59°C/s and 30°C/s respectively. Similarly the maximum experimental temperature for position T_3 and the corresponding cooling rates are 558°C at t = 5.8 s and 49°C/s and 26°C/s respectively.

There are several uncertainties that have to be considered in the interpretation of the thermocouple temperature measurements because of the high temperature gradients present. The change in the geometrical position of the thermocouple will change the measured temperature drastically. Furthermore, the thermocouple has some response

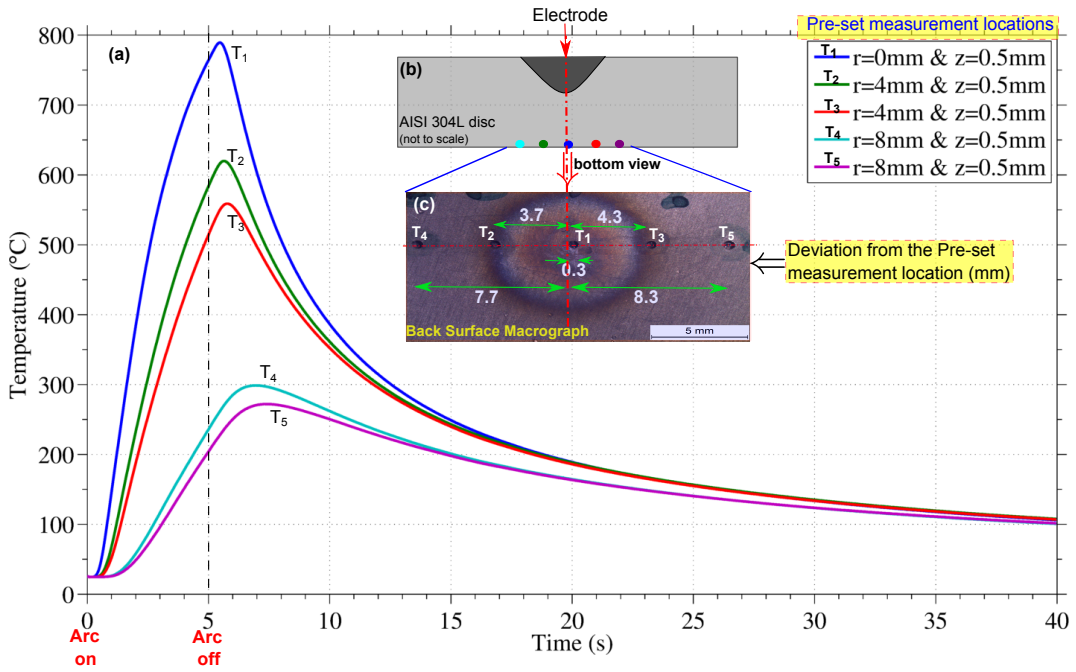

Figure 2.11: (a) Temperature history at back surface points (b) Schematic of the welded sample with pre-set sensor locations (c) Macrograph of the welded sample showing the deviation from the pre-set sensor locations

time and the thermal capacity of the thermocouple itself will affect the measurement. In addition to this, the drilled hole at the bottom surface in the disc for the placement of the thermocouple affects the development of the thermal fields in the disc. All these matters can have an impact on the near weld measurements. Whereas further away from the weld, the response of the thermal signal is slower with comparatively smaller temperature gradients. Consequently, the position of the thermocouple and its impact on the thermal field is relatively less affected.

Table 2.4: Calculation of temperature at a radius 3.7 mm on the right side from the heat source center; Temperatures in °C and temperature gradient in °C/mm and time in s.

time	T_1	T_2	T_3	dT_{13}/dr	T_{new}	T_{new}-T_2
1	145	67	51	23.5	65	2
2	383	232	187	49	216	16
3	563	378	314	62.25	351	27
4	683	494	424	64.75	462	32
5	763	583	514	62.25	551	32

The thermocouples T_2 (3.7 mm from the heat source center) and T_3 (4.3 mm from the heat source center) are placed at equal distance (4 mm) from the thermocouple T_1. In order to verify the axial symmetry of the heat source and the system, these two thermocouples (T_2 and T_3) have to be compared. For that a simple calculation based on the measurement is used and presented in table 2.4. The spatial temperature gradient

between the thermocouple T_1 and T_3 is calculated (dT_{13}/dr) for each time step. And used to find the temperature at a radius 3.7 mm on the right side by multiplying the gradient with the distance (0.6 mm) and added to the temperature at T_3. Then the calculated temperature at 3.7 mm on the right side and the measured temperature at 3.7 mm on the left side is compared in last column of the table 2.4. This study shows a maximum variation of 32°C corresponds to 5% occurs at time steps 4 s and 5 s. This variation of temperature at a radius 3.7 mm from the center of the heat source to each opposite side can be explained by two factors. The first factor is the measurement error that a thermocouple can make. Secondly, there exist another thermocouple at 0.3 mm on the right side in between the calculated point and the heat source center. This thermocouple is also positioned in a 0.5 mm drilled hole, this may be disturbing the diffusion of heat in this direction resulted in less calculated temperature at 3.7 mm on the right side (T_{new}). By taking into these factors the measured temperature is much closer to the calculated temperature at 3.7 mm (T_2 and T_{new}). From this we can conclude that the heat distribution system is axi-symmetric. Figure 2.12(a) presents the peak temperature

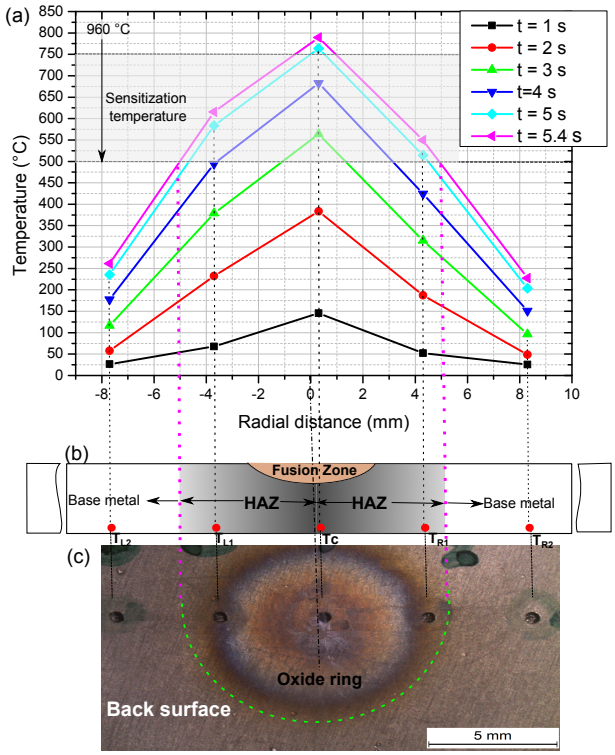

Figure 2.12: (a) Peak temperature profiles at different times (b) Schematic of the weldment with sensor locations (c) Macrograph of the welded sample showing the HAZ

profiles from the sensor positions corresponding to six different time steps. Figure 2.12(b) and 2.12(c) shows the corresponding sensor positions on schematic and from the macrographic image respectively. The maximum temperature profile has a peak at the center thermocouple position which is at 0.3 mm away from the heat source symmetry axis. The results are plotted for 5 s heating with step of 1 s starting from 1 s and an additional time taken where the center sensor location reaches maximum value. The back surface profiles reaches a maximum value after the arc switch off at t = 5.4 s. However these are the profiles connecting the peak temperature at the sensor locations, but in actual case the peak temperature may occur at the heat source center, which is 0.3 mm away from the center

thermocouple. It is also interesting to see the variation of temperature gradient between each sensor locations. A gradual increase from the initial time can be observed. At time t = 1 s the temperature gradient between T_C and T_{R1} is 93°C, and is the maximum at this time step. But in the final time step (t = 5.4 s), the temperature gradient is maximum between T_{L1} and T_{L2} and is 348°C. A marked variation in the microstructure occurs in the heat affected zone as shown by the dotted green circle.

2.3.5 Weld pool size measurements

2.3.5.1 Image analysis for the transient weld pool width evolution

Figure 2.13 shows the raw images acquired from the high speed camera for the static welding of SS304L low sulfur sample using the experimental setup as shown in figure 2.3(a). The welding conditions listed in table 2.1 are used. The first image at t=0.0005 s shows the arc initiation and the next four images till t=0.4 s shows the transient arc region because of the lift arc process which is explained in figure 2.7. The quantitative evolution of the weld pool size can be extracted from these images using an image processing algorithm as discussed later in this section.

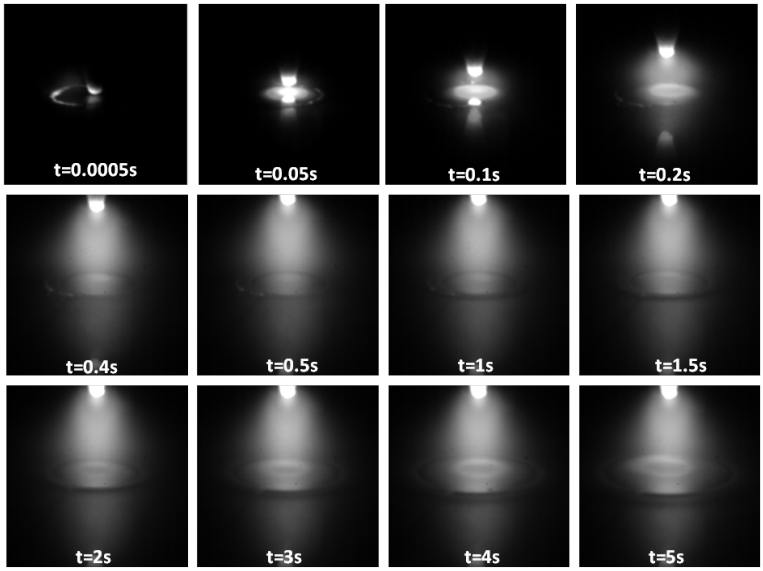

Figure 2.13: Images extracted for a static GTA welding of SS304L Low sulfur sample

Figure 2.14 presents the high speed camera images using laser back lighting for a static GTAW process for three different current setting. These images corresponds to the final time just before the arc switch off. The images were captured using a 808 nm band pass filter and the images are acquired at a frequency of 2000 frames/s.

Figure 2.15 shows the image analysis carried out on the raw data from the high speed camera. The filtering on the image has been carried out using a 5×5 high pass filter. The image grabbing and sampling process generates noise in the images. To reduce the noise a Gaussian smoothing function is used and is expressed as eq. 2.1.

$$G(x, y, \sigma_{im}) = \frac{1}{2\pi\sigma_{im}^2} exp\left[-\frac{1}{2\pi^2}(x^2 + y^2)\right] \tag{2.1}$$

Where σ_{im} is Gaussian distribution parameter, and it's value is selected as σ_{im}= 5.

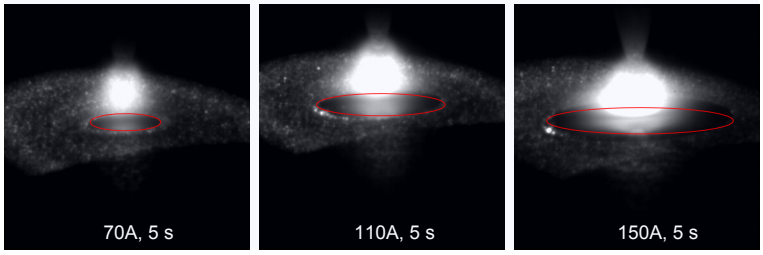

Figure 2.14: Images extracted for a static GTA welding of SS304L Low sulfur sample using laser back lighting

Figure 2.15 presents the different steps used in the image processing algorithm. Figure 2.15(a) shows the raw image from the high speed camera for a current of 70 A and 2.4 mm arc length. The images were captured using the first high speed camera setup as shown in figure. A band pass filter in the scope of 1000 nm was used for filtering the high arc emissions. The field of view include the tip of the tungsten electrode at the top, the plasma arc and the weld pool surface. The electrode reflection from the base metal is also present at the bottom of the image. Figure 2.15(b) shows the image after Gaussian filtering. The discretized 5×5 model of equation 2.1 is convolved with the raw image results in Gaussian filtering. In order to reduce the noise level in the image a denoising filter is used. Figure 2.15(c) shows the denoised image.

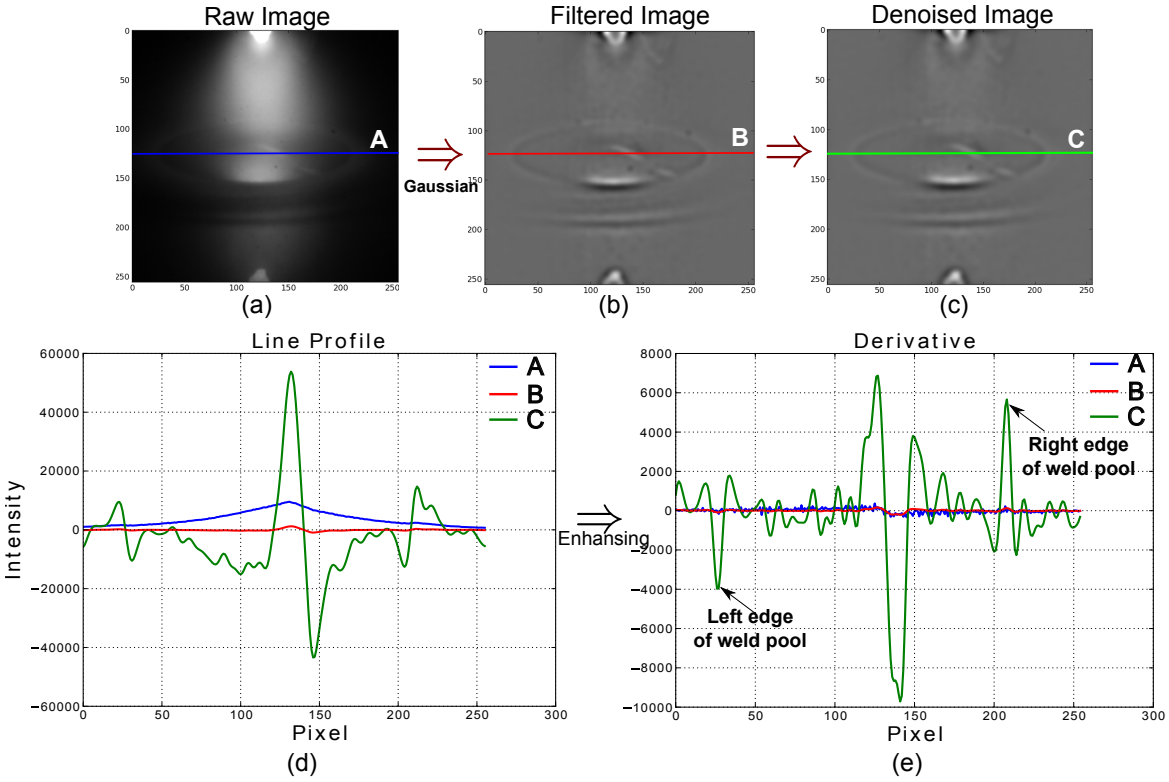

Figure 2.15: a)Raw image (70 A) b)Image convolved by Gaussian model c) Denoised image d)Line profile e) Enhancing along line A, B and C

In order to find the weld pool edges from the image a line profile is drawn across the three images A, B and C. Figure 2.15(d) presents the intensities measured along each line

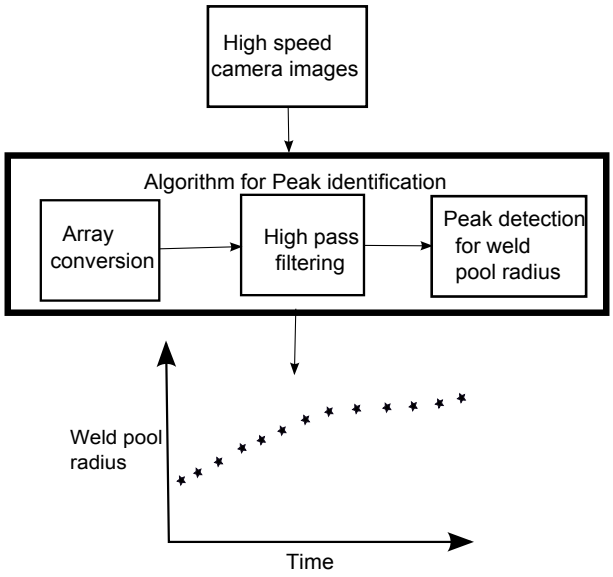

Figure 2.16: Schematic Pseudocode for weld pool width

profiles. The line profile C which corresponds to the filtered and denoised image shows clear indication of variation near the weld pool edge with a slope type edge. In order to precisely extract the edges of the weld pool, finite difference enhancement of each line profile has been done and plotted in figure 2.15(e). The left and right edges of the weld pool corresponds to the minimum and maximum point, respectively. Now the edges can be found out from these points.

Figure 2.16 shows the schematic pseudo code for the weld pool width calculation. An algorithm developed to automatically identify these peaks from all the images from the video file and plot the weld pool radius as a function of time. Figure 2.17 shows the

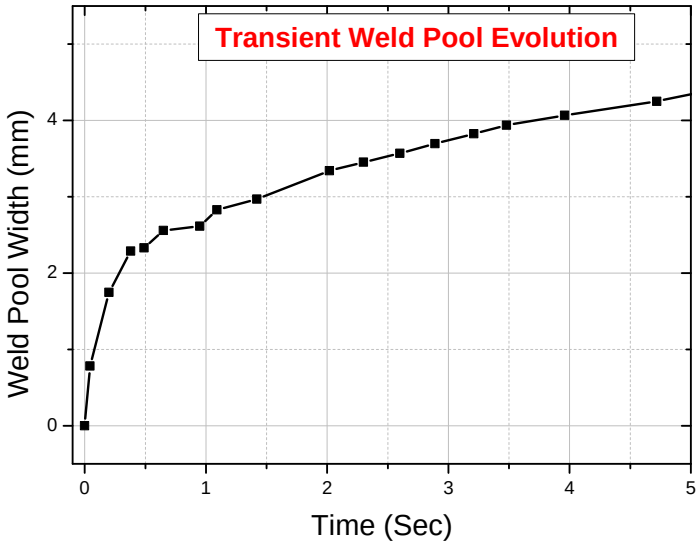

Figure 2.17: Weld pool width evolution measured for 70 A, 9 V

transient weld pool width evolution determined using the above mentioned algorithm. A rapid initial growth can be observed in this region till $t = 0.5s$. This is because of the high amount of arc strike on the solid metal results in rapid melting of the thin layer of solid. Later the arc get stabilized, the weld pool growth slows down and the gradual development of the weld pool size can be observed. After melting the top layer of solid, a small weld pool of certain radius will form there after the heating rate won't produce the same increment in weld pool radius.

2.3.5.2 Postmortem analysis of weld pool

Figure 2.18 shows the transverse section of a GTA weld after 5 s static heating with 70 A current and an arc length of 2.4 mm. The macrograph shows the relatively shallow weld pool with width 4.2 mm and depth 1.0 mm. This gives an aspect ratio (depth/width) of 0.238. The shape of the weld indicates that the weld pool experienced a radially outward flow. At the bottom curvature of the weld pool near to the center line, indicated by an arrow in the figure, shows a lack of symmetry about the axis of the electrode. This indicate the unsteady flow field in the weld pool.

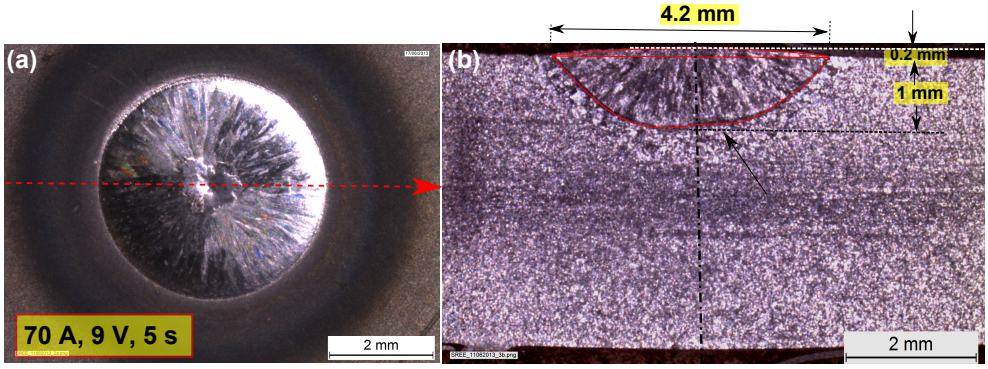

Figure 2.18: Transverse macrograph of the static GTA weld indicating the fusion zone size and shape for AISI304L material with 26 ppm sulfur content (a) Top view (b) cross sectional view

In literature Zacharia [92] observed similar behavior in the weld pool for a current of 150 A and 14 V after 2 s on 90 ppm 304L stainless steel. They concluded this behavior due to the presence of two strong opposing forces, namely, the electromagnetic and surface tension gradient forces. But for the present case the welding current used is not high enough to produce a significant force contribution from the electromagnetic effect. However this discrepancy may be explained by the occurrence of high weld pool surface temperature resulting in a negative $\frac{\partial \gamma}{\partial T}$ over a small area nearer to the electrode symmetry axis causing a reversal of flow. Apparently results in a low velocity flow near the symmetry axis and thereby comparatively less amount of heat transfer. It is inferred from the above discussion that the discrepancy occurred in the smooth liquid-solid interface is mainly because of the complex flow resulted from the variation of temperature coefficient of surface tension with temperature.

2.4 Experimental Campaign: Material and Energy Influence

Table 2.5 shows the experimental test cases and the corresponding welding conditions used. The experiments in table 2.5 were carried out several times to check the repeatability.

Table 2.5: The investigated welding conditions

Material	*Experimental test cases*	*Diameter (mm)*	*Thickness (mm)*	*Shielding gas*	*Arc length (mm)*	*Current*	*Voltage*
SS304L-LS	Test 1	80	4	Argon	2.4	150	11
	Test 2	80	4	Argon	2.4	110	10.6
	Test 3	80	4	Argon	2.4	70	9
SS304L-HS	Test 4	40	4	Argon	2.4	70	9

2.4.1 Temperature evolution

This section presents the thermal measurements for different energy and material experiments. Figure 2.19 presents the thermal cycles measured by the thermocouples for test 3 and test 4.

Table 2.6: Measurement Locations of the thermocouples from the bottom center (0,0)

	TC1	*TC2*	*TC3*
radius (mm)	0	4	8
height (mm)	0.5	0.5	0.5

Table 2.6 presents the thermocouple positions used for the temperature cycle measurements. For both cases the TC1 shows the maximum temperature as this thermocouple location is more close to the weld heat source center. The maximum temperature reached at the back side of the disc are 825 and 793 °C respectively for test 4 and test 3 at thermocouple TC1. For the two test cases, the thermocouples giving close results for the maximum temperature. A variation of 30 °C is observed for the TC1 measurements for the two test cases. This variation in the measurement is linked with the uncertainties of their locations. The close analysis of the heating rate for the two test cases is also presented in figure 2.19 as the material composition of the two cases are different. The transfer of heat from the weld pool to the base material are expected to be different due to the difference the weld pool convection. The thermocouple TC1 and TC2 showing slight variation in the heating rate. TC1 starts showing variation 0.5 s after the arc heating whereas for TC2, this variation is observed 1.5 s after the arc heating. A discrepancy in the cooling rate can be observed for the three thermocouple measurements, this constant deviation is expected due to the variation in the diameter of the samples. The larger diameter of the sample in test 3 conduct more heat and also the larger area for the boundary heat transfer.

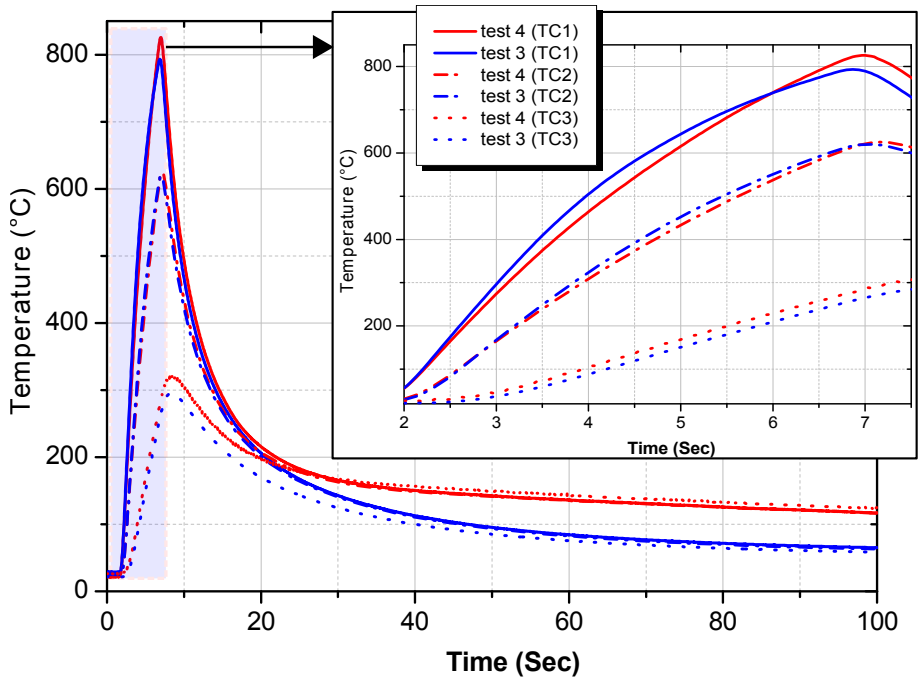

Figure 2.19: Thermocouple measurements for test 3 and test 4

2.4.2 Transient weld pool development

All the static arc experiments were carried out to study the weld pool development. The analysis of the bead on plate weld pool growth were done from the arc being struck to complete the weld pool development (0-5 seconds). As mentioned in the previous section, the recording speed of the high speed camera was 2000 frames per second.

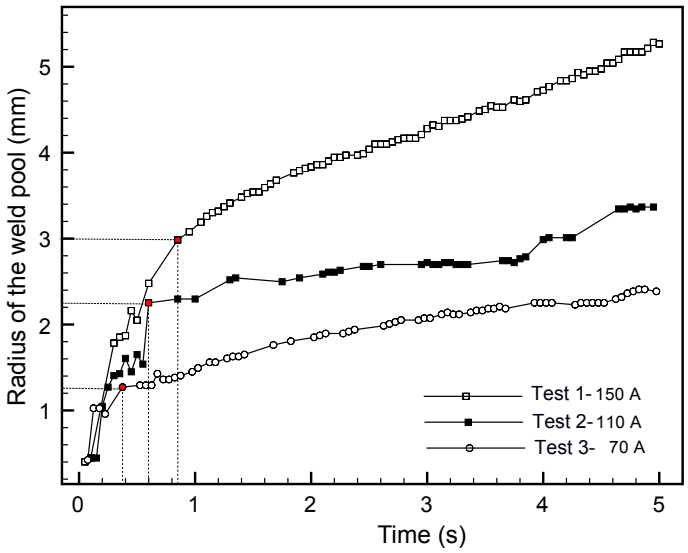

Figure 2.20: Transient weld pool development for the first three test cases as presented in table 2.5

Figure 2.20 shows the weld pool development for three first welding test cases as

presented in table 2.5. Two different trends can be observed from these results for different input energies. The first one is a rapid growing stage (within 1 s regime with in the coordinate marked with red color in figure 2.20 for each case) and the second one is a gradually developing stage (over 1 s - 5 s regime). A fewer points were unable to identify during the arc initiation stage due to the high intensity arc lighting. For test 1, the initial rapid development of the weld pool due to the direct arc melting on the top solid layer is obtained as 3.53 mm/s (a linear gradient calculated at the end of 0.85 s). Similarly for test 2 and test 3 gives 3.66 mm/s and 3.28 mm/s respectively at times 0.6 s and 0.38 s. Irrespective of the supplied arc power, a similar initial weld pool growth rate can be observed for the three cases. The second region after the red point in figure 2.20 for the three cases a gradual increase in the weld pool development can be observed for the rest of the arc heating. The rate at which the weld pool development takes place is calculated for the three cases and are 0.53 mm/s, 0.25 mm/s and 0.23 mm/s. These values implies that the static arc heating time (time for the arc is ON) is an important parameter to obtain a desired weld pool width. Also the gradient value is increasing with an increase in input power.

2.4.3 Macrostructure of Static GTA Welds

Figure 2.21 shows the top view of the weld bead formed (a, c, e) and the cross section of the spot weld cut through the bead center (b,d,f) for the three experimental test cases. The top weld surface profile is highlighted in figures b, d, and f. From the top view images, the fusion zone, heat affected zone and the base material can be distinguished each other with clear variation surfaces. The observed weld pool size and shape are comparable with the previous literature data [92]. The weld pool depth and width are also given in each cross sectional view.

For 70 A case a nearly hemispherical weld pool shape (“V” shape) with a penetration of 1 mm is obtained. The weld pool shape obtained for 110 A and 150 A case indicate that there occurred a complex weld pool motion due to the different interacting forces. In these two cases, the weld pool shape is “W”. These pool shapes observed here (“v” and “w”) are well known and experimentally observed in literature [36, 48, 57, 92]. For all the three test cases, the first common observation is their symmetry about the vertical center line. This symmetry is obtained because of the heating is symmetrical and the flat welding configuration resulted in a symmetrical gravitational effect. The average depth to width ratio obtained for the three cases is 20%. This low value is expected due to the low concentration of the sulfur content present in the AISI 304L stainless steel.

Additionally, it can be observed that test 1 and 2 are giving similar weld penetration at the weld center line with an increase in the weld half width by 2 mm. The major reason for this behavior is due to the complex Marangoni flow during the arc heating. Detailed explanation is given in the next chapter. The highlighted weld top surface profiles indicates that the weld bead height is negligible for all the three considered test cases. From this experimental observation, the important assumption of flat surface boundary condition can be utilized for the fluid flow numerical simulation.

Experimental results for the AISI 304L samples containing different sulfur content are presented in figure 2.22. Figure 2.22(a) and (c) shows the macrostructure of weld pool

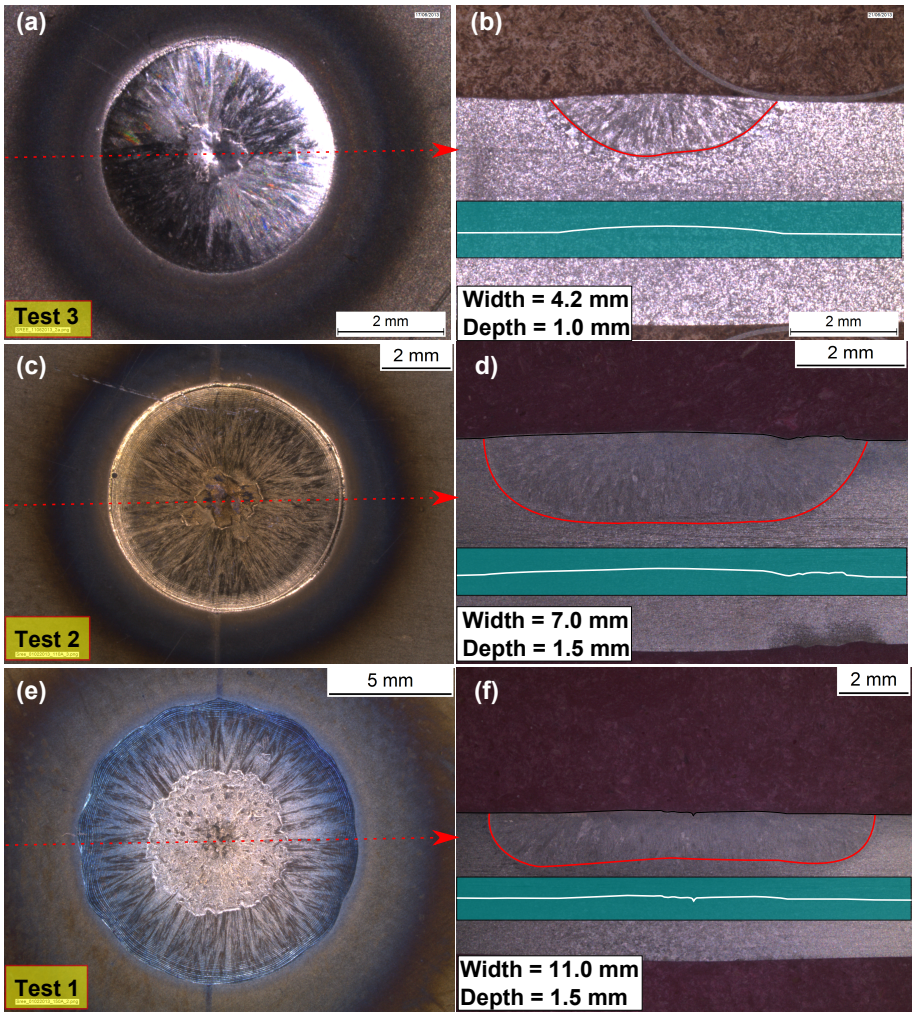

Figure 2.21: Weld pool shape Top view (a, c, e) and corresponding cross section cut through the bead center (b, d, f) for 70 A, 110 A and 150 A; heating for 5 s on AISI 304L samples; weld bead top surface profile is highlighted in figures b, d, f

Table 2.7: Measured weld pool dimensions

Experimental Test	*Average Power (kw)*	*Arc Duration (s)*	*Weld pool depth (mm)*	*Weld pool half width (mm)*
Test 1	1.65	5	1.5 ± 0.1	5.4 ± 0.1
Test 2	1.16	5	1.5 ± 0.1	3.4 ± 0.1
Test 3	0.63	5	1.0 ± 0.2	2.0 ± 0.15
Test 4	0.63	5	1.4 ± 0.1	2.0 ± 0.1

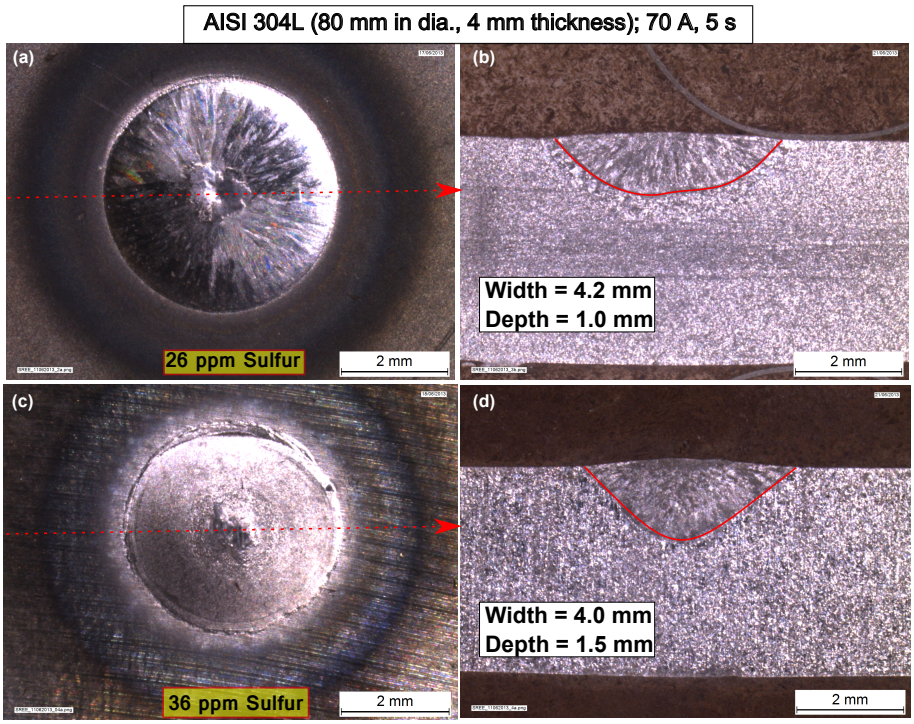

Figure 2.22: Weld pool shape Top view (a, c) and corresponding cross sections (b, d) for low sulfur and high sulfur sample for a current of $I = 70$ A and voltage of $U = 9$ V

top view for the two cases. The process parameters are 70 A current for 5 s with an arc length of 2.4 mm. The top view of the weld bead macrostructure pattern for 26 ppm sulfur content sample indicates that the weld pool experienced a radially outward flow. Where as the top surface macrostructure of the high sulfur weld with 36 ppm sulfur content sample shows indications of radially inward flow with a convex top surface profile. The surface instabilities such as waves and ripples can be visible in both cases and comparatively high in high sulfur sample near the weld pool periphery. Gas shear stress may be the reason for this instabilities [104]. The cross sectional results as shown in Figure 2.22(b) and (d) indicates the development of weld pool is essentially symmetrical about the axis of the electrode.

The weld dimensions (weld pool width and depth) for the different input energy and the different material investigated are presented in figure 2.23. From figure 2.21 and 2.23 it is clear that the weld pool width and penetration are increasing with increase in arc energy input. As presented in table 2.7, an increase of 0.53 kW welding power (Test 3 to Test 2) increases the weld pool width by 1.4 mm and depth of penetration by 0.5 mm. The calculated linear gradient of width is 2.64 mm/kW and that of depth is 0.94 mm/kW. Also these calculation for an energy increase of 0.49 kW (Test 2 to Test 1) gives linear gradient of width as 4 mm/kW and a zero linear gradient in depth. These results show that the increase in average arc power for the first case (Test 3 to Test 2) is 2.8 times more effective on the weld pool width than the penetration. For the second case with almost similar amount of increase in the welding power(Test 2 to Test 1) resulted in 1.36 mm/kW in the linear gradient of the width and no variation in the depth value. From this analysis it can be conclude that the increase in the arc power is a parameter to get a desired welding width for a static GTAW process of AISI 304L stainless steel material.

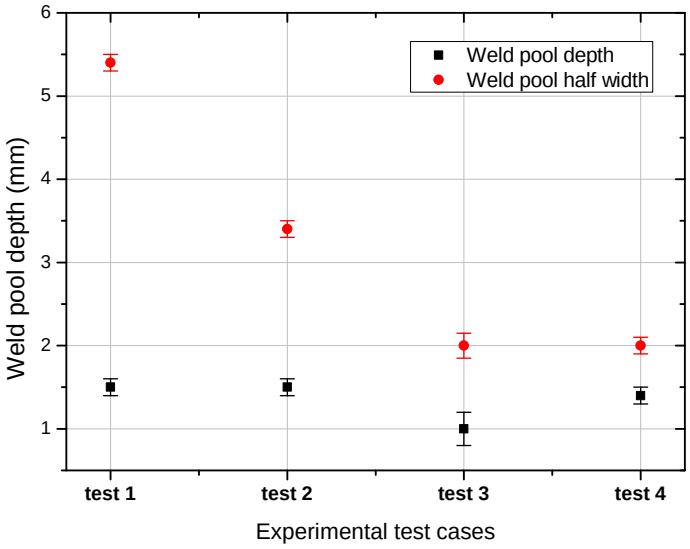

Figure 2.23: Characteristics of the spot weld dimensions for different energy input and material

From figure 2.22 and 2.23, it is clear that the increase in the percentage of sulfur content (26 ppm to 36 ppm) resulted in a 0.5 mm increase in penetration and 0.1 mm decrease in weld pool half width.

2.5 Conclusion

From the experimental results, the following conclusions were made.

1. Effect of sulfur
   The presence of sulfur in the stainless steel plays a major role in weld pool fluid motion and as a consequence on the weld pool shape. EPMA has been carried out to find the approximate concentration of sulfur content in the base material. The sulfur content measured in the weld pool also revealed some useful information regarding the motion in the molten metal. It is well known that at high temperature the sulfur element move to the surface because of their systems are characterized by very large negative enthalpy of segregation [90]. From the presented results it is clear that the presence of sulfur content in the weld center is comparatively less than the base material. And also in the case of high sulfur sample the presence of sulfur in the center region is comparatively higher than the weld base material. From these two observations, it can be concluded that the molten pool motion in the low sulfur sample caused the accumulated surface sulfur to move towards the periphery. In the case of high sulfur sample the inward motion leads to the accumulation of sulfur towards the center.

2. Process parameter measurement
   The instantaneous process parameters such as current and voltage were measured during the static GTA welding process. It is observed that the voltage value, which is a measure of the distance between tungsten electrode and base material shows

very little fluctuations other than electronic noise. This indicates the absence of any major weld pool oscillations. This fact means that the surface can be considered as flat (fixed) as an assumption for the numerical simulation.

3. Temperature distribution results
   The temperature distribution at the bottom surface of the welded disc has been measured using the thermocouple arrangement. The close results observed for thermocouples placed equally distant positions from the heat source center indicates that the axi-symmetric assumption can be made use for the numerical simulation. Also it is well known that the heat transfer in the weldment during welding process can affect the microstructre of the material thereby the mechanical properties of the material. It is visibly clear that the back surface measurement location's marked change in microstructure.

4. Weld pool size and final shape results
   The transient weld pool evolution and the final shape are obtained from the post-experimental data processing. This study reveals the unusual wavy weld pool boundary observed during the static arc heating of low sulfur samples. One of the major observations from the three currents analyzed such as 70 A, 110 A and the 150 A is the formation of negligible convex surface at the top (crown) of the weld bead. This gives the insight into the assumption of fixed surface simulations. The macrography, knowledge of the sulfur content and the literature can help us analyzing the fluid motion with in the weld pool. Moreover, the high growth rate of weld pool radius at 150 A can be attributed to the contribution of the arc drag force to the Marangoni force (Arc drag force is probably negligible at 110 A and null for 70A).

Chapter 3

Numerical simulation of static GTAW operation

Contents

3.1 Introduction

In this chapter, the numerical model used for the simulation of static GTAW experiment is detailed. The first part describes the simple heat conduction model for predicting the temperature distribution in the static GTAW. The second model studies the evolution of temperature and velocity fields during the static GTAW using a magneto-thermo-hydrodynamic simulation. A transient two-dimensional weld pool model is proposed to analyze the time dependent evolution of the weld pool under the static arc. The major purpose of the numerical study is listed below:

- A first approach in heat conduction alone is interesting in order to:
  - Try to define the global size of fluid and solid domain and thereby define the pseudo-fluid domain with fine meshing for more complex simulations with velocities and temperature using convection.
  - Constant vs temperature dependent thermophysical properties.
- Pros and cons of using a Magneto-thermo-hydrodynamic simulation; e.g better understand the temperature distribution due to the molten metal flow.
- The influence of various driving forces in the weld pool and to identify the dominant forces that govern the fluid flow.
- To quantify the weld pool geometry evolution with regards to welding energy, welding duration, amount of surface active elements etc.

Using this model, the effect of different parameters such as material properties, heat source parameters, temperature dependent thermo physical properties, space discretization and physical constants in the surface tension distribution on the temperature evolution, fluid velocity distribution and the weld pool size are also investigated.

3.2 GTAW Heat Conduction Simulation

3.2.1 Assumption

Due to the geometry of the studied domain (disc) and according to our experimental observation (see chapter 2) the physical problem can be reduced to an axisymmetric

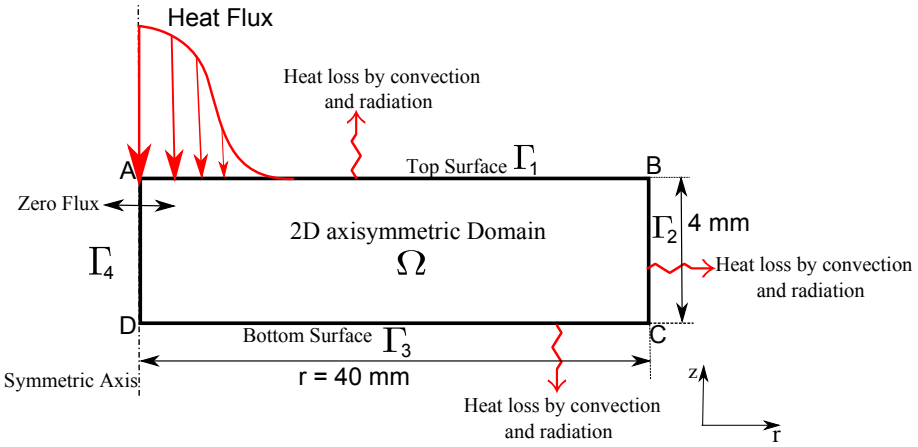

Figure 3.1: Schematic of the geometrical parameters (not to scale) and boundary conditions

problem as defined in figure 3.1.

The major assumptions used for this simple heat conduction model are as follows:

- 2D Axisymmetric heat conduction model is assumed;
- Temperature dependent thermophysical properties are considered;
- Gaussian heat distribution is assumed for the welding arc;
- All the exterior boundaries were given convection and radiation boundary condition.

3.2.2 Governing equations

The numerical solution of the transient 2D axisymmetric heat diffusion equation gives the thermal model of the problem. The thermophysical properties considered as temperature dependent with a initial temperature T_{room}.The 2D axi-symmetric heat conduction equation for the temperature field $T(r, z, t)$ can be written as

$$\rho C_p(T)\frac{\partial T}{\partial t} = \frac{1}{r}\frac{\partial}{\partial r}\left(k(T)r\frac{\partial T}{\partial r}\right) + \frac{\partial}{\partial z}\left(k(T)\frac{\partial T}{\partial z}\right) \quad in \;\; \Omega(t) \tag{3.1}$$

The associated boundary conditions are as follows with reference to figure 3.1:

Boundary AB:

$$-k_n\frac{\partial T}{\partial n} = Q(r,t) - h(T(r,z,t) - T_a) - \sigma\epsilon(T(r,z,t)^4 - T_a^4) \quad on \;\; \Gamma_1 \tag{3.2}$$

Boundary BC and CD:

$$-k_n\frac{\partial T}{\partial n} = h(T(r,z,t) - T_a) + \sigma\epsilon(T(r,z,t)^4 - T_a^4) \quad on \;\; \Gamma_2 \;\; and \;\; \Gamma_3 \tag{3.3}$$

Boundary AD:

$$-k_n\frac{\partial T}{\partial n} = 0 \quad on \;\; \Gamma_4 \tag{3.4}$$

With Initial condition

$$T(t=0) = T_{room} \quad in \ \ \Omega \tag{3.5}$$

Where the surface heat flux is modeled as a Gaussian distribution as discussed in section 1.5.3.1 of chapter 1 and is summarizing here as follows:

$$Q(r,t) = \frac{UI\eta}{2\pi r_H^2} exp\left(\frac{-r^2}{2r_H^2}\right) \tag{3.6}$$

The parameters used in equation 3.6 and the values used for the convective heat transfer coefficient and the radiation emissivity constants are given in the table 3.1. The geometrical parameters for the axi-symmetric computation domain is shown in figure 3.1. The static arc heating time is set to 5 s and the total simulation duration is set to 7 s. The temperature dependent thermophysical properties were used for the calculation and are presented in the next section.

Table 3.1: Simulation parameters

Parameter	**Value**
Welding voltage (U)	9 V
Welding Current (I)	70 A
Welding Process efficiency (η) [18]	68 %
Gaussian base radius (r_H) [42]	1.5 mm
Convective heat transfer coefficient (h) [18]	15 W/m^2K
Emissivity (ϵ) [18]	0.8
Ambient temperature (T_{room})	293.15

3.2.3 Thermophysical properties of AISI304L

It is obvious that accurate simulation of the welding operation can be achieved only with the use of correct description of material properties. For welding a steel alloy, it is necessary to reach its melting temperature that is around 1450°C. So its material properties must be known from ambient (25°C) to its melting temperature and above for the simulation of the molten metal. There are few data available over the melting temperature for steel. Several numerical studies considered only constant thermophysical properties such as the one presented in table 3.2 for AISI304L.

The transient heat transfer simulation of GTAW operation requires the knowledge of the thermal conductivity, specific heat and mass density over the temperature range. Furthermore any other phenomena such as phase transformation must be taken into account. The latent heat of fusion is not negligible during the welding operation especially during the solidification. Figure 3.2 shows the thermal conductivity as a function of temperature. At room temperature, the thermal conductivity is low about 14 W/(mK) as expected for an austenitic stainless steel. Then thermal conductivity increases steadily to 33 W/(mK) at the melting point then this value drops to 26 W/(mK) within a 50 K range. This narrow temperature window will affect the numerical simulation as small time steps are required to capture accurately the heat transfer phenomena occurring during the 50 K window (latent heat of fusion, material property values change drastically, etc.). Figure 3.3 shows the temperature dependent specific heat of stainless steel 304L material. The

Table 3.2: Material Properties of AISI 304 stainless steel [18]

symbol	**Material Property**	**value**
k_s	Thermal Conductivity of Solid	26 W/mK
c_{ps}	Specific heat of Solid	486 J/kgK
ρ_s	Density of Solid	7500 kg/m^3
T_s	Solidus Temperature	1673 K
T_l	Liquidus Temperature	1723 K
ΔH	Latent heat of fusion	2.47×10^5 J/kg

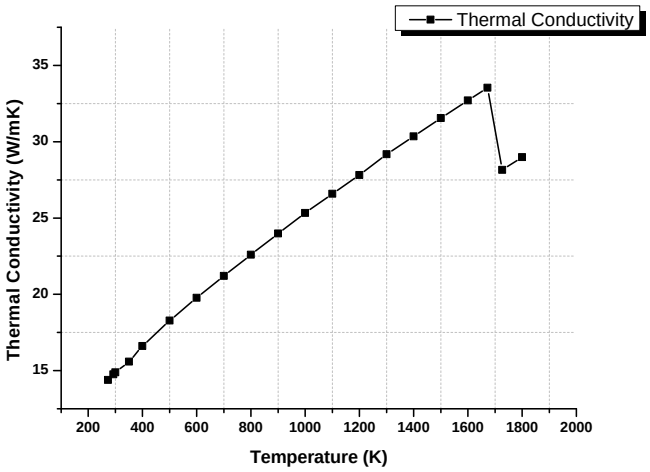

Figure 3.2: AISI 304L thermal conductivity as a function of temperature [105]

heat capacity of a substance is a measure of how well the substance stores heat. When heat is supplied to material, it will necessarily cause an increase in the material's temperature. The relationship between heat Q, and a temperature change T_1 to T_2, can be expressed

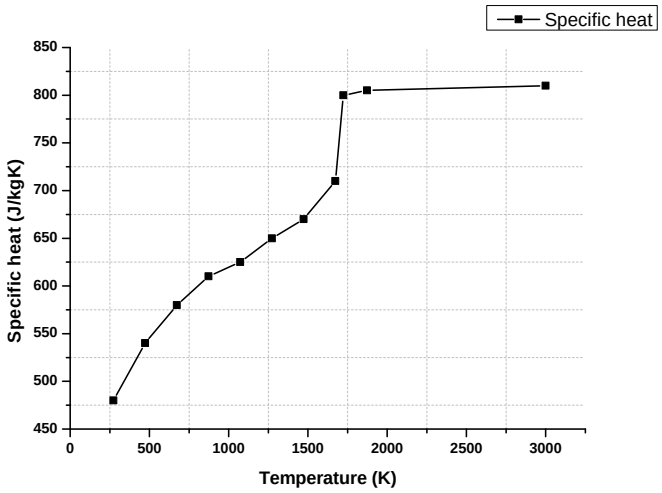

Figure 3.3: AISI 304L specific heat as a function of temperature [106]

in terms of the state variable enthalpy, H, which is defined as the sum of internal energy plus the product of the pressure and volume. The specific heat rises from 480 J/(kg.K) at the room temperature to 800 J/(kg.K) and then stabilizes over the melting temperature to 820 J(kg.K). The specific heat and mass density act on the temperature dynamic of the studied system and also on its capacity to store the heat inside the material whereas the thermal conductivity measures the ability of the material to transfer/propagate the heat faster or not.

Figure 3.4 shows mass density as a function of temperature.

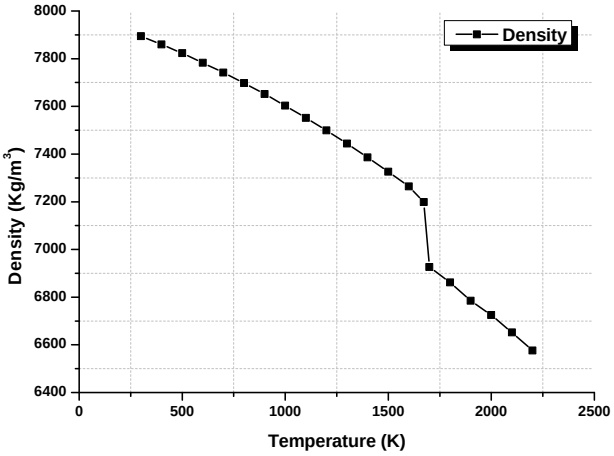

Figure 3.4: AISI 304L mass density as a function of temperature [106]

3.2.4 Finite element discretizations

The discretization of the two-dimensional axi-symmetric finite element domain for the static GTAW of disc is shown in Figure 3.5. A six node triangular element is used for the space discretization with the option of quadratic Lagrange interpolation. Further details about the selected element may be found in [107]. High temperature and flux gradients are anticipated in and around the fusion zone (FZ), therefore a relatively fine mesh is used within a distance of 5 mm from the symmetry axis or the heat source center (disc center). Away from this region, the element size increases with an element growth rate of 1.2. The anticipated high temperature gradient region was discretized with a minimum mesh size of 150 μm. Which resulted in a mesh with 2741 number of elements and with 5628 degrees of freedom.

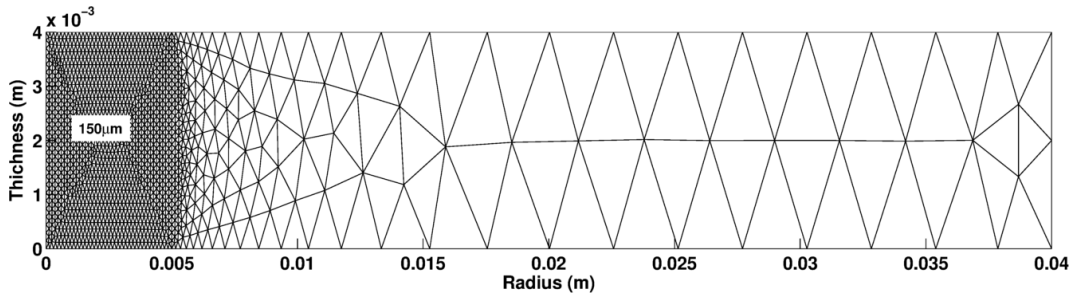

Figure 3.5: Finite element mesh for transient thermal conduction model

A sensitivity analysis is carried out by successive mesh refinement in order to find the optimum mesh size that gives a stable temperature field. The analysis is mainly based on the maximum temperature reached at r= 0 mm and z= 4 mm. The maximum time step for this analysis is fix to 0.001 s. Figure 3.6 shows the results obtained from the sensitivity analysis. From this study it is clear that the maximum temperature is stabilized for a mesh size of 150 μm, further refinement in the mesh size results in a negligible variation in the maximum temperature value. Also the computational time increases drastically for mesh size less than 100 μm. A simulation with 100 μm is solved after 150 s while a 50 μm mesh takes 600 s. So the optimum mesh size is selected as 150 μm by considering the stabilized maximum temperature and the optimum computational time.

The time discretization is performed with a Backward Differentiation Formula scheme of 5th order (BDF 5) associated with adaptive time stepping algorithm which has a constraint on the time step that can not exceed 0.001 s. The maximum time step was set to 0.001 s. Heat conduction calculations were performed in matter of seconds on a 2.5GHz CPU speed and 4GB RAM memory computer.

3.2.5 Numerical results

Figure 3.7 shows the temperature field at the end of the arc heating (5 s) for a current of 70 A and a arc height of 2.4 mm. This shows the classical heat wave characteristics of an isotropic thermal conductivity material. This is the reason for the hemispherical isothermal contour lines from the heat source. It can be noticed that the back surface of the disc along the symmetry axis reaches a temperature of around 1100 K at the end of the

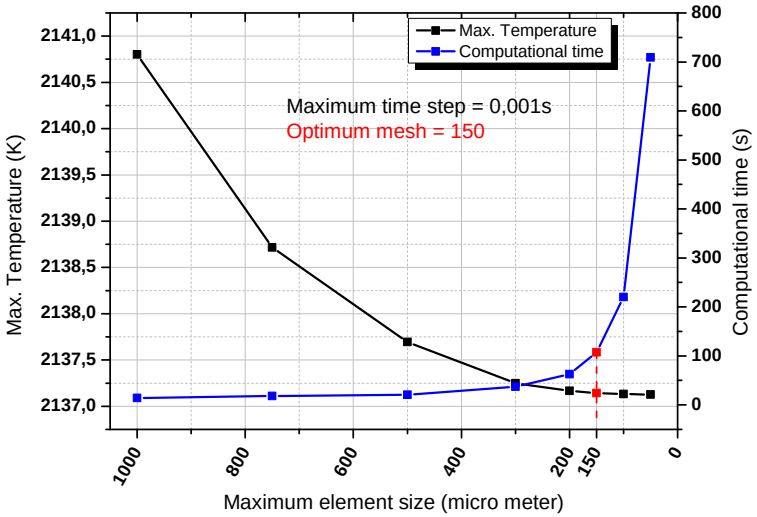

Figure 3.6: Mesh sensitivity analysis based on maximum temperature and optimum computational time

arc heating while the top surface at the center showing a maximum temperature of 2136 K. So through the center of the disc a temperature gradient of 250 K/mm can be observed for this case. Again if we consider the temperature at a radial distance of 5 mm from the center, around 900 K this gives a gradient of around 250 K/mm along the radial direction. From this analysis it can be concluded that, most of the heat is localized within a region of 5 mm radius during the formation of the weld pool (arc heating on). The temperature contours are also plotted for the solidus (1673 K) and liquidus temperature (1723 K).

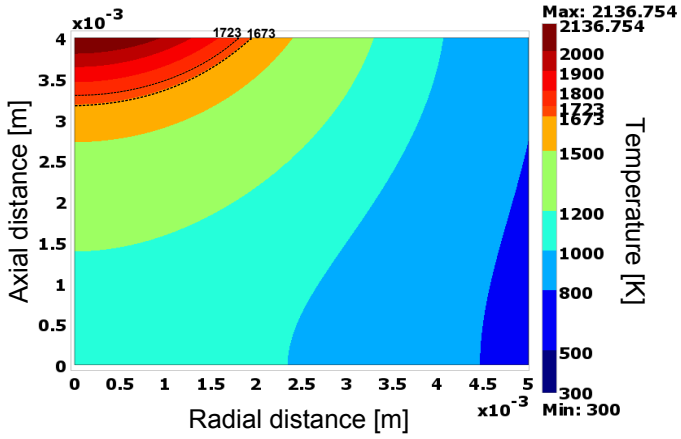

Figure 3.7: Surface and thermal contour plot for static GTAW of 5 seconds

Figure 3.8 shows the temperature field for six different times (0.5 s, 1 s, 2 s, 3 s, 4 s and 5 s) during the static arc heating for a region of radius 5 mm of the disc. The maximum temperature is observed at top center of the disc as expected. The orange color corresponds to the solidus temperature (1673 K).

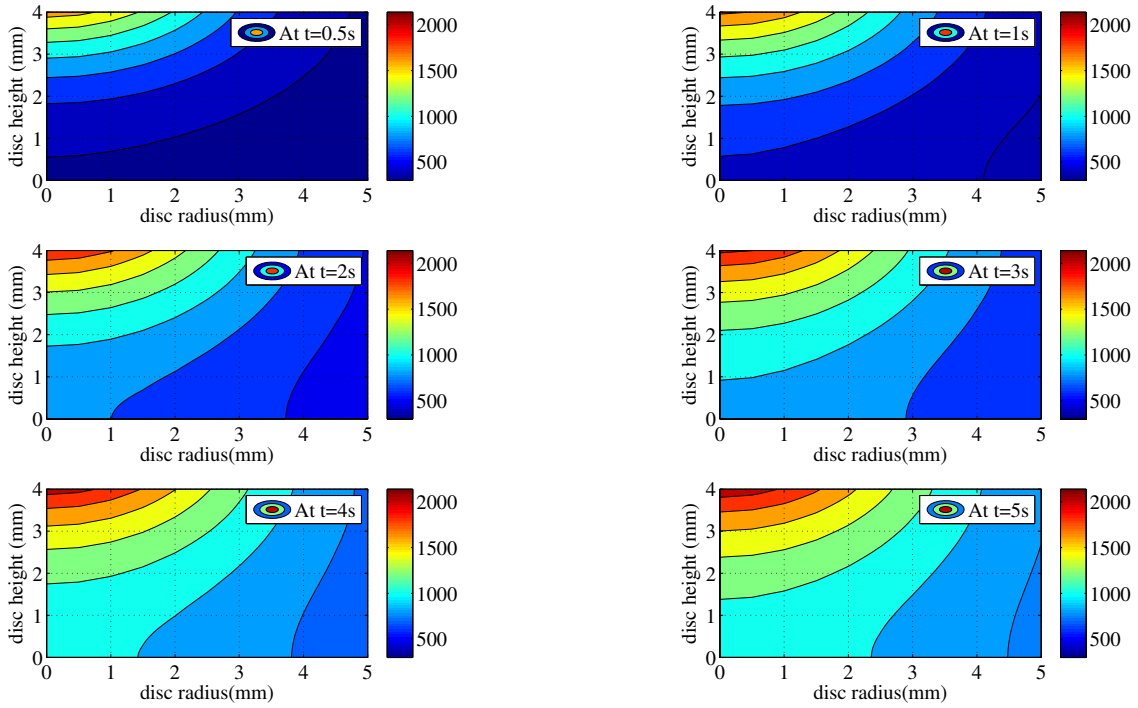

Figure 3.8: Temperature profiles at 6 different time steps during the welding process

Figure 3.9 shows the temperature evolution at eight different points in the computational domain. The locations where the temperatures are plotted is also schematically represented on the solution domain at the end of the arc heating. The maximum temperature attained at the end of the arc heating is 2136 K at the center of the disc (curve 1). The curves 1 to 4 indicate the temperature distribution inside the weld pool. Curve 1 exihibits the highest temperature evolution as it is recorded on top center surface where the Gaussian heat flux is maximum. Temperature evolution at points 2 (r=0.5 mm), 3 (r=1 mm) and 4 (r=1.6 mm) admit lower values as the radius increases, heat flux distribution decreases. Curves 5, 6, 7, and 8 show the temperature distribution in the solid material, first three are located at the bottom and the last one is at the top surface 10 mm away from the weld pool center. The maximum temperature of (1111 K) occurs for the point at the bottom center point (point 5). A rise in temperature of 558 K and 246 K were reached at the locations 6 and 7 respectively. As shown in figure 3.9 the last point is 10 mm away from the weld center and the response at this point is low. After the arc switch off at 5 s the temperature dropped quickly and the temperature after 2 second at the center of the pool and the nearby points reach to 780 K, at a cooling rate of 677 K/s. It is important to identify the temperature distribution and the cooling rate in and around the weld pool because it affects the final micro structure in the weld and the HAZ regions.

Figure 3.10 presents the time dependent evolution of weld pool half width and the weld pool depth. Due to the Gaussian distributed heat over the boundary gives a sudden increase in the weld pool half width and depth around 1 s, thereafter a gradual increase.

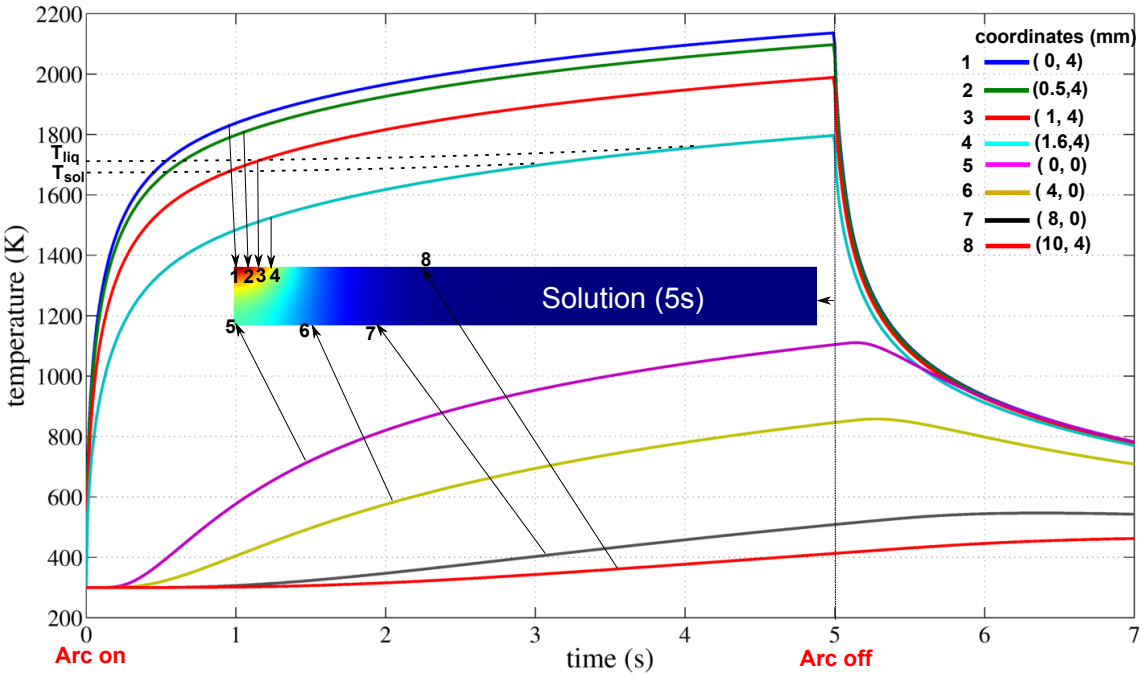

Figure 3.9: Transient temperature evolution at different locations

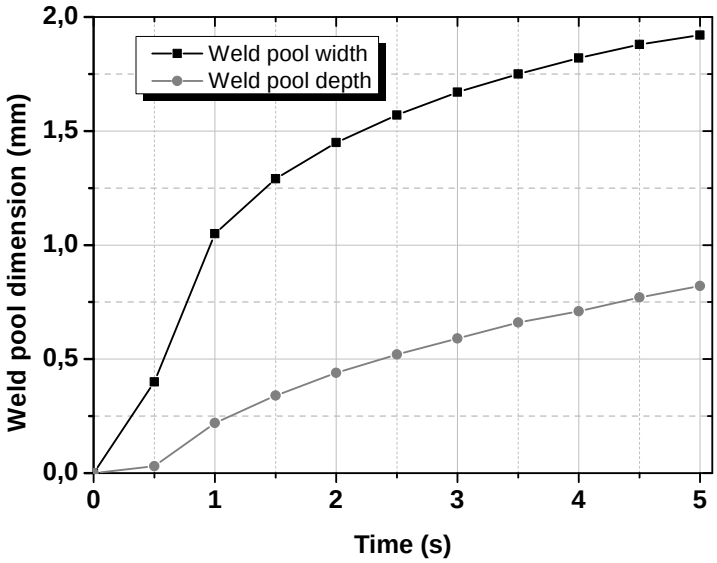

Figure 3.10: Transient weld pool evolution

3.2.6 Summary

The heat conduction model for the prediction of temperature during the welding process is presented in this session. The simple thermal problem considered a surface welding arc as a Gaussian distribution on the boundary. The weld pool shape and the temperature fields were obtained using the model. The major conclusions from this study are listed below.

- The heat conduction model is useful to get the approximate temperature distribution with in the weld pool and the solid base metal.
- Heat conduction model is also useful to determine the enhanced thermal conductivity of the material.
- The approximate weld pool dimensions identified from thermal conduction is made use for the definition of fine mesh region of the thermo convective problem which is explained in the next section.
- Major lacks of Heat Conduction Models are listed below with comparison to the literature
  - Different shapes of the weld pool
    The heat conduction model always predict the classical hemispherical weld pool shape. But in many real cases the weld pool shape are far different in behavior as shown in Figure 3.11.

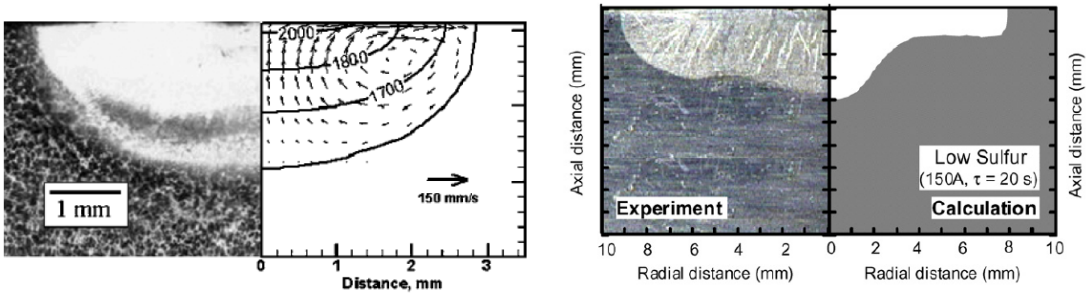

(a) Classical hemispherical weld pool[108] (b) GTA welding of mild steel Material[57]

Figure 3.11: Non-Classical weld Pools

  - Effect of minor alloying elements
    The addition of minor alloying elements such as sulfur, selenium, telurium etc... in steel can result in a very different weld shape as shown in Figure 3.12(a) and 3.12(b). Because these elements in group VI of the periodic table are 'surface active' in iron based alloys and can have a dramatic effect on liquid surface tension even when present in low concentrations. When in solution, these elements have the propensity to go to the weld pool boundary where they are responsible for a significant lowering of the surface tension. This effect of minor alloying element cannot be explained ignoring convection [90–92].

From the literature it is clear that the weld pool shape is driven by the convective phenomena within the molten metal. Therefore it is compulsory to take into account the fluid phase by solving Navier-Stokes equations as well as energy equation.

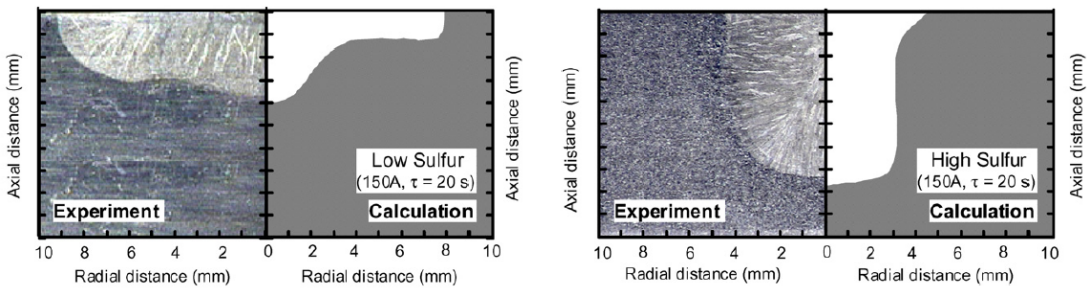

(a) GTA welding of Low Sulfur stainless steel [57]

(b) GTA welding of High Sulfur stainless steel [57]

Figure 3.12: Effect of minor alloying elements: Important influence on weld pool shape

3.3 Magneto-Thermo-Hydrodynamic Model

Figure 3.13 shows the schematic of the physics involved in GTAW process. By applying an electrical potential difference between the cathode (tungsten electrode) and the anode (workpiece), an electric arc can be established between the two poles. This electric arc is the energy source in the process. The amount of heat that is absorbed by the workpiece is high enough to melt it and develop a molten metal pool. This pool will grow until the heat

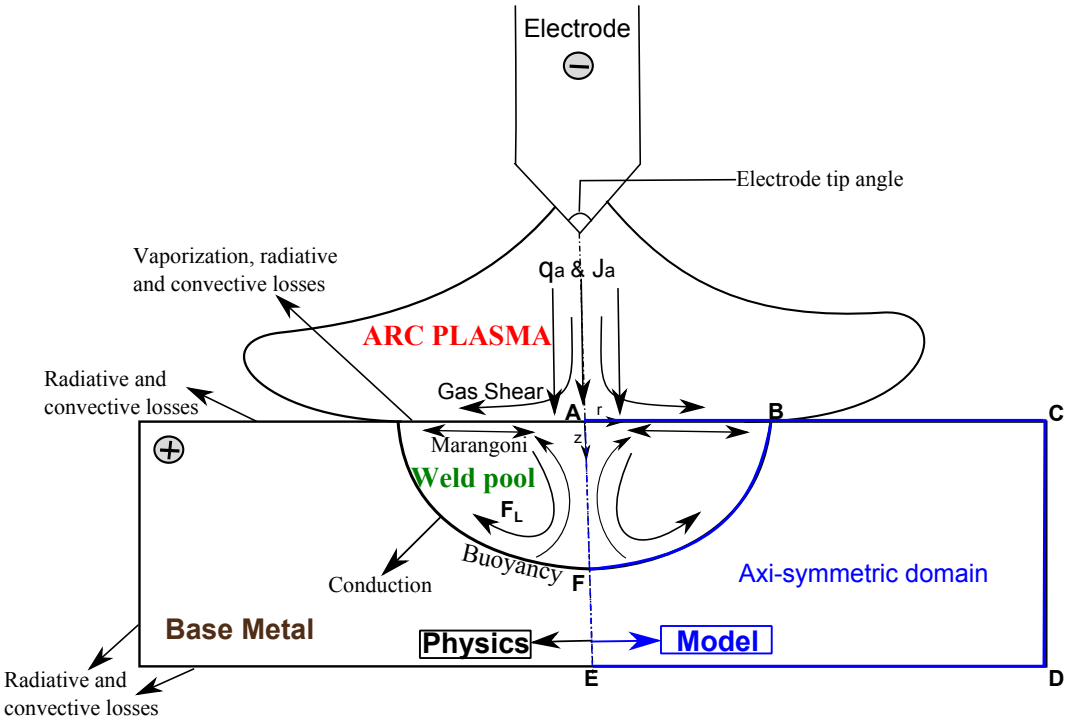

Figure 3.13: Left half shows the schematic representation of various physical phenomena occurring in GTAW Process and right half shows the axi-symmetric computational domain

gained by the workpiece equals the heat loss by conduction, convection, radiation and vaporization. Flows in the pool are driven by a combination of forces mentioned (Buoyancy, Marangoni, Lorentz and arc drag forces) in the first chapter and shown schematically in Figure 3.13. From the previous studies, for low welding currents (less than 200 A), the arc pressure acting normally on the weld pool is negligible [109] and is not taken into

account in the present study and that leads to a flat weld pool surface. Therefore, the forces in the weld pool are the Buoyancy, Marangoni, Lorentz and the arc drag forces.

Figure 3.14 shows the considered physical coupling and the corresponding coupling variables between different physics.

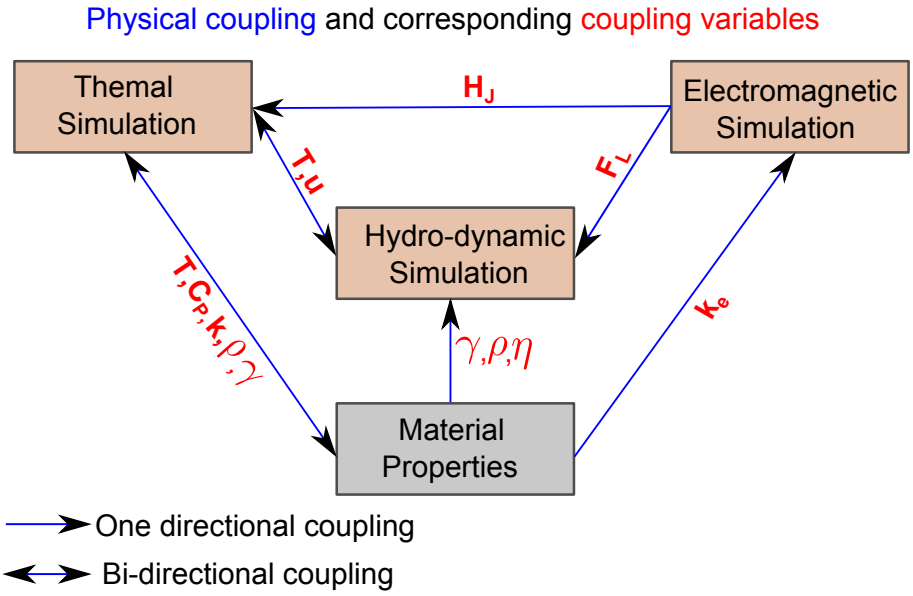

Figure 3.14: Simulation Approach used for the present study

Where

- $\boldsymbol{u}$ - Flow velocity
- $\boldsymbol{T}$ - Temperature
- $\boldsymbol{F_L}$ - Lorentz force
- k - Thermal conductivity
- c_p - Specific heat
- η - Dynamic viscosity
- γ - Surface tension
- k_e - Electric conductivity
- H_J - Joule heating

The mathematical model used in this study is presented here.

3.3.1 Assumption

The general model presented in chapter 1 can be simplified according to the following assumptions:

- Static TIG welding is carried out so a 2D axi-symmetric model is assumed (Experimentally verified from the temperature measurements see chapter 2).
- Molten metal flow is Newtonian and incompressible, in view of the relatively small size of the weld pools expected [63, 110].
- Liquid metal flow in the weld pool is considered as laminar, since this assumption permit to get quite good results with reduced computing times [111].
- A spatially distributed heat flux and current density falling on the surface are Gaussian in characteristics.
- The latent heat of fusion is taken into account by equivalent heat capacity formulation see section 1.5.3.2 of chapter 1.
- The surface tension gradient is dependent on both temperature and sulfur content of the alloy using the Sahoo et al. relationship [94].
- The weld pool surface is considered as fixed (experimentally observed for the welding currents 70A-150A)

The driving forces considered for the fluid flow in the current model are as follows:

- Electromagnetic force arising from the interaction of divergent current and its own magnetic field;
- The buoyancy force due to variation of density is taken into account using the Boussinesq approximation;
- The surface tension force due to temperature gradient (Marangoni effect);
- The shear stress on the surface of the weld pool by the gas flow.

The model presented takes into account the Joule heating into the workpiece and the melting/solidification phenomenon into the weld pool. The mechanisms that govern the heat loss from the free surface of the workpiece such as radiation and convection are also taken into account. It has been reported that the vaporization in GTAW of stainless steel does not play a critical role in determining the temperature of the weld pool surface [112]. So the vaporization phenomena is not taken into account for the present modeling.

Figure 3.15 shows the computational domain for analyzing the electrical potential, molten pool convection and heat transfer, which has a dimension of 40 mm(r) $\times$ 4 mm(z). The geometry is divided into two subdomains (Ω_1 and Ω_2). This partition is done to minimize the computational time. In subdomain Ω_1 (i.e. BCDEF), solves the electrical potential and temperature field with a relatively coarse mesh. On the other hand, in subdomain Ω_2 (i.e. ABF), solves electrical potential, temperature and velocity fields with a very fine mesh. Also, the top boundary of the subdomain Ω_2 (AB) has to be refined further to accurately approximate the results due to the presence of high temperature

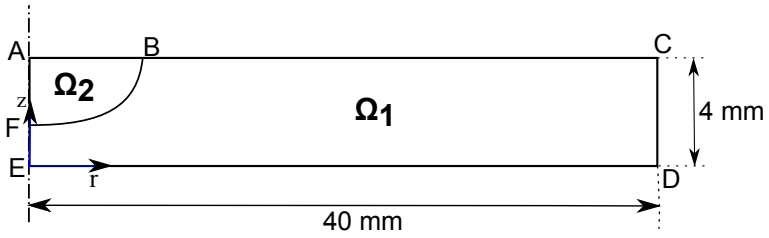

Figure 3.15: Schematic of the geometrical parameters (not to scale)

and velocity gradients. The subdomain Ω_2, where the weld pool is expected to generate, is named as pseudo-fluid domain. The size of the pseudo-fluid domain is different for different input energy. For each simulation with different energy the pseudo-fluid domain is defined using the approximate weld pool dimensions obtained from heat conduction simulation and also using the analysis of weld macrograph.

3.3.2 Governing equations

By considering the above assumptions, the governing equations in 2D axi-symmetry are summarized below:

The mass-continuity equation is

$$\frac{\partial u}{\partial r} + \frac{u}{r} + \frac{\partial w}{\partial z} = 0 \tag{3.7}$$

The radial-momentum conservation equation is

$$\frac{\partial u}{\partial t} + u\frac{\partial u}{\partial r} + w\frac{\partial u}{\partial z} = -\frac{1}{\rho}\frac{\partial P}{\partial r} + \nu\left[\frac{\partial^2 u}{\partial r^2} + \frac{1}{r}\frac{\partial u}{\partial r} - \frac{u}{r^2} + \frac{\partial^2 u}{\partial z^2}\right] - \frac{1}{\rho}(J_z B_\theta) - \frac{1}{\rho}Ku \tag{3.8}$$

The axial-momentum conservation equation is

$$\frac{\partial w}{\partial t} + u\frac{\partial w}{\partial r} + w\frac{\partial w}{\partial z} = -\frac{1}{\rho}\frac{\partial P}{\partial z} + \nu\left[\frac{\partial^2 w}{\partial r^2} + \frac{1}{r}\frac{\partial w}{\partial r} + \frac{\partial^2 w}{\partial z^2}\right] - \frac{1}{\rho}(J_r B_\theta) - \frac{1}{\rho}Kw + g\beta(T - T_r) \tag{3.9}$$

The energy-conservation equation is

$$\rho C_p^{eq}\left[\frac{\partial T}{\partial t} + u\frac{\partial T}{\partial r} + w\frac{\partial T}{\partial z}\right] = \frac{1}{r}\frac{\partial}{\partial r}\left(k(T)r\frac{\partial T}{\partial r}\right) + \frac{\partial}{\partial z}\left(k(T)\frac{\partial T}{\partial z}\right) + Q_{joule} \tag{3.10}$$

In momentum conservation equations 3.8 and 3.9, u and w are the radial and axial velocity components in the weld pool. The source terms include Lorentz force term and the drag term due to the mushy zone for radial momentum equation. In case of axial momentum there exists an additional buoyancy force term. The drag term serves to simulate the reduction of velocity in the mushy zone.

In the energy conservation equation 3.10, T is temperature, $C_p^{eq} = C_p + \Delta H_f \frac{df_L}{dT}$ is an equivalent specific heat which takes into account the latent heat of fusion ΔH_f, f_L is the liquid fraction and Q_{joule} is the volumetric heat generation due to joule effect. The

joule effect is expressed using the well known relationship $\vec{Q}_{joule} = \vec{j} \cdot \vec{E}$ and it has been reported in literature that this heating effect is negligible in the weld pool [18].

Using cylindrical co-ordinate system the current continuity equation, equation 1.15 in chapter 1, is written as

$$\nabla^2 \phi = \frac{1}{r}\frac{\partial}{\partial r}\left(r\sigma\frac{\partial \phi}{\partial r}\right) + \frac{\partial}{\partial z}\left(\sigma\frac{\partial \phi}{\partial z}\right) = 0 \tag{3.11}$$

The current density is calculated from Ohm's law

$$j_r = -\sigma_e \frac{\partial \phi}{\partial r} \tag{3.12}$$

$$j_z = -\sigma_e \frac{\partial \phi}{\partial z} \tag{3.13}$$

while the self-induced azimuthal magnetic field is then obtained from

$$B_\theta = \frac{\mu_0}{r}\int_0^r j_z r \partial r \tag{3.14}$$

Where σ_e is electrical conductivity, ϕ is the electrical potential, j_r and j_z are radial and axial current density respectively, B_θ is the self induced magnetic field intensity and $\mu_0 = 4\pi \times 10^{-7} H/m$ the permeability of vacuum. The integration constant is assumed zero. The **Lorentz force**, $\mathbf{J} \times \mathbf{B}$, is then given by:

$$(\mathbf{J} \times \mathbf{B})_r = -J_z B_\theta \tag{3.15}$$

$$(\mathbf{J} \times \mathbf{B})_z = -J_r B_\theta \tag{3.16}$$

3.3.3 Boundary conditions

Figure 3.15 shows the computational domain used for the numerical study. The geometry includes two sub-domains such as a solid domain (BCDEF) and a fluid domain (ABF). The different boundary conditions are discussed below.

1. Momentum Boundary Conditions:

   A flat top surface (AB) is assumed for the weld pool region in the present study. So the continuity of shear stress is assumed at the free surface. The fluid flow boundary condition for top surface AB is

   $$-\mu\frac{\partial u}{\partial z} = \tau_a + f_L \frac{d\gamma}{dT}\frac{\partial T}{\partial s} \tag{3.17}$$

   Where u and w are the velocity components along r and z directions, respectively, and $\partial\gamma/\partial T$ is the temperature coefficient of surface tension. From the above equation, velocity u is determined from the Marangoni effect. The w velocity is equal to zero since there is no outward flow at the pool top surface. τ_a is the additional plasma drag shear stress detailed in section 1.5.3.8. The temperature-dependent

surface tension is obtained from a semi-empirical relationship given by Sahoo *et al.* [94].

$$\frac{d\gamma}{dT} = -A_\gamma - R_g\Gamma_s ln(1+Ka_s) - \frac{Ka_s}{1+Ka_s}\frac{\Gamma_s\Delta H_0}{T}$$
$$K(T) = k_1 exp\left(-\frac{\Delta H_0}{R_g T}\right) \tag{3.18}$$

Where a_s is the sulfur content of the workpiece material, A_γ is a constant, Γ_s is the surface excess at saturation, R_g is gas constant, k_1 is the entropy factor and ΔH_0 is standard heat of adsorption, which is estimated from an empirical function of the difference in electronegativity between the solute and solvant atoms. More details given in section 1.5.3.7.

2. Thermal Energy Boundary Conditions

The axi-symmetric surface heat input from the arc was modeled as a fixed Gaussian density function [83]

$$q_n(r) = \frac{dQ}{\pi r_H^2} exp\left(\frac{-d\,r^2}{r_H^2}\right) \tag{3.19}$$

Where Q is the actual heat input directly from the arc to the workpiece, it can be written as $Q = U\,I\,\eta$. Where d is the heat power distribution factor. Also r_H is the base radius of the Gaussian heat distribution. The Gaussian heat distribution parameters are the main factor to adjust the heat input distribution on the free surface of the weld pool. The heat distribution factor $d = 0.5$ (for GTAW [18]), the efficiency η=0.68 [18] and the base radius r_H used for the different currents are listed in table 3.7.

Additionally, convection (q_{conv}) and radiation (q_{rad}) are applied on the free surface. Therefore, the heat input on the free surface is expressed as:

$$-k\frac{\partial T}{\partial n} = \frac{dQ}{\pi r_H^2} exp\left(\frac{-d\,r^2}{r_H^2}\right) - h_c(T-T_0) - \sigma\epsilon(T^4 - T_0^4) \tag{3.20}$$

Where, h is the convective heat transfer coefficient, ϵ is the emissivity, σ Stefan-Boltzmann constant ($5.67 \times 10^{-8} W/m^2K^4$) and T_0 the ambient temperature.

The convection radiation boundary condition is applied on the side (CD) and bottom (DE) boundaries as follows:

$$-k\frac{\partial T}{\partial n} = -h_c(T-T_0) - \sigma\epsilon(T^4 - T_0^4) \tag{3.21}$$

And a zero flux transfer is considered across the symmetric boundary (AF and FE)

$$\frac{\partial T}{\partial n} = 0 \tag{3.22}$$

3. Electric Potential Boundary Conditions

On the top surface

$$j_n(r) = -\sigma_e \frac{\partial \phi}{\partial n} = \frac{gcc \cdot I}{\pi r_J^2} exp\left(\frac{-gcc \cdot r^2}{r_J^2}\right) \tag{3.23}$$

Where $j_n(r)$ is the current density. gcc is Gaussian current coefficient, σ_e is the electrical conductivity of the material, r_H is Gaussian current parameter and I is current (A). The Gaussian distribution is varied as a function of Gaussian current coefficient and Gaussian current parameter. In literature, the Gaussian current coefficient, which is a important factor for the current distribution on the weld pool surface, is selected as 0.5 [113] and 3 [65]. In the present work, Gaussian current coefficient is explicitly selected as 0.5 for Lorentz force calculation. The bottom boundary is electrically ground and hence the current density in this boundary is zero.

Table 3.3: Boundary Conditions

Boundary	u	w	T	ϕ
AB	$\tau = \tau_{st} + \tau_{gas}$	0	$-k\frac{\partial T}{\partial n} = q_n(r) - q_{conv} - q_{rad}$	$-\sigma\frac{\partial \phi}{\partial n} = J_n(r)$
BC	0	0	$-k\frac{\partial T}{\partial n} = q_n(r) - q_{conv} - q_{rad}$	$-\sigma\frac{\partial \phi}{\partial n} = J_n(r)$
DE	0	0	$-k\frac{\partial T}{\partial z} = -q_{conv} - q_{rad}$	$\frac{\partial \phi}{\partial z} = 0$
CD	0	0	$-k\frac{\partial T}{\partial r} = -q_{conv} - q_{rad}$	$\frac{\partial \phi}{\partial r} = 0$
AF	0	$\frac{\partial w}{\partial r} = 0$	$\frac{\partial T}{\partial r} = 0$	$\frac{\partial \phi}{\partial r} = 0$
EF	0	0	$\frac{\partial T}{\partial r} = 0$	$\frac{\partial \phi}{\partial r} = 0$

3.3.4 Material Properties

Table 3.4 shows the thermal and physical properties of AISI-304L stainless steel material for the weld pool calculations performed in this study and are obtained from Traidia [18]. The sulfur content which plays a major role in weld pool shape formation [88] is taken into account for the weld pool fluid flow study. The sulfur content value ($0.0026 \pm 0.002\% wt$) used for the model was identified using Electron probe micro analysis (EPMA) technique as mentioned in the previous chapter. The standard heat of adsorption, the empirical constant value used in the temperature dependent surface tension gradient was taken from Zacharia *et. al.*[91].

Table 3.4: Material Properties of AISI 304 stainless steel [18, 114]

symbol	Material Property	value
Physical properties		
a_s	Activity of sulfur	0.0026 $wt\%$
A_γ	Constant in surface tension gradient	$3 \times 10^{-4}\ Nm^{-1}K^{-1}$
R_g	Gas constant	8314.3 $Jkg^{-1}mol_{-1}K^{-1}$
ΔH_0	Standard heat of adsorption	$-1.88 \times 10^{8}\ Jkg^{-1}mol^{-1}$
Γ_s	Surface excess at saturation	$1.3 \times 10^{-8}\ Jkg^{-1}mol^{-1}m^{-2}$
γ_m	Surface tension of pure metal	1.943 Nm^{-1}
ρ_s	Density of Solid	7500 kg/m^3
ρ_l	Density of Liquid	6350 kg/m^3
μ	Dynamic Viscosity	$2.5 \times 10^{-3}\ kgm^{-1}s^{-1}$
β_0	Volumetric expansion coefficient	$1 \times 10^{-4}\ K^{-1}$
Thermal properties		
k_s	Thermal Conductivity of Solid	26 W/mK
k_l	Thermal Conductivity of Liquid	20 W/mK
c_{ps}	Specific heat of Solid	486 J/kgK
c_{pl}	Specific heat of Liquid	650 J/kgK
ΔH	Latent heat of fusion	$2.47 \times 10^{5}\ J/kg$
T_s	Solidus Temperature	1673 K
T_l	Liquidus Temperature	1723 K
h	Convective heat transfer coefficient	15 W/m^2K
ϵ	Emissivity	0.8[95]
Electrical properties		
K_e	Electrical conductivity	7.7×10^{5}

3.3.5 Simulation approach and Settings

Comsol Multiphysics® was used to solve the coupled multiphysics equations. The direct solver UMFPACK was used for solving the matrix system. Backward Differentiation Formula (BDF) has been used for the time integration. As illustrated in figure 3.14 the electric potential equation is solved solely in order to compute Lorentz force and Joule heating as it is assumed that the welding intensity do not vary during the welding operation. The computed Lorentz force and the Joule heating are then reused in the coupled heat transfer-fluid flow problem. Finally the computed solution gives the electromagnetic, velocity and temperature fields in the domain.

3.3.5.1 Space discretization

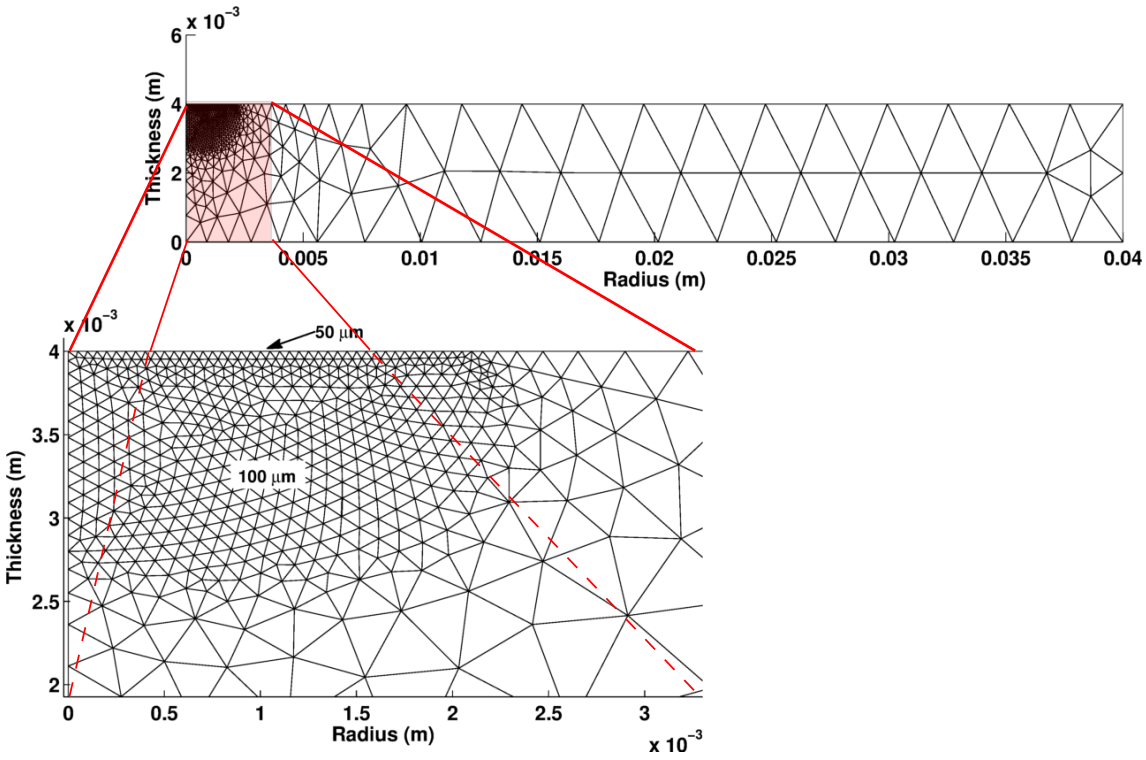

Figure 3.16: Meshed computational domain and zoomed pseudo-fluid domain with fine meshing

Figure 3.16 shows the meshed geometry used for the computation. The mesh size used

Table 3.5: Meshing parameters

Domain/Boundary	*Maximum mesh size (µm)*
Subdomain Ω_1 (BCDEF)	1000
Pseudo-fluid domain Ω_2 (ABF)	100
Top boundary (AB)	50
Symmetry axis (AF)	100
Other boundaries	1000

are different for the two subdomains as discussed in the previous section. The subdomain Ω_1 has a coarse mesh and the subdomain Ω_2 has a very fine mesh. The zoomed projection shows the very finer grid spacing in the pseudo-fluid domain (100 μm) and a spacing of 50 μm is used on the top boundary where the high gradient of temperature and velocity occurs. Table 3.5 gives the mesh parameters used for the simulation.

3.3.6 Weld Pool Results and Analysis

This section presents a general behavior of the simulation results for a 70 A case with particular attention given on the temperature and velocity field associated with weld pool and the weld pool dimensions. The welding parameters used for the numerical calculation are presented in table 3.6. All the simulations in this section are using the parameters as shown in table 3.6 with temperature dependent thermophysical properties and temperature coefficient of surface tension is varying with temperature unless otherwise stated.

Table 3.6: Simulation parameters

Parameters	*Value*
Welding Current, I (A)	70
Welding voltage, U (V)	9
Welding duration (s)	5
Pseudo-fluid domain width (mm)	2
Pseudo-fluid domain depth (mm)	1.2
Gaussian current coefficient (gcc)	0.5
Gaussian current distribution parameter, r_J (mm)	1.5
Gaussian heat distribution parameter, r_H (mm)	1.5
Power distribution factor, d	0.5
Efficiency, η	0.68
Maximum arc shear (Pa)	10
Arc drag force distribution (mm)	2
Simulation duration (s)	7
Time step (s)	0.05
Ambient temperature (K)	293
Convective heat transfer coefficient, h (W/m^2K)	15

3.3.6.1 Temperature evolution

Figure 3.17 shows the simulation results for a region of 8 mm diameter from the symmetry axis at six different time steps, these results show the temperature distribution in and around the weld pool region. The solidus temperature is also shown in each figure to identify the weld pool. Maximum temperature reached at each of this time steps is also indicated. Most of the heat from the arc is located near the weld pool region, indicated as yellow color in figure that represents temperature above 1500 K. The temperature reached

above the melting temperature appears at times around 0.6 s, and this initiates the formation of the weld pool from the center as shown in the first figure at t=0.6 s. Figure

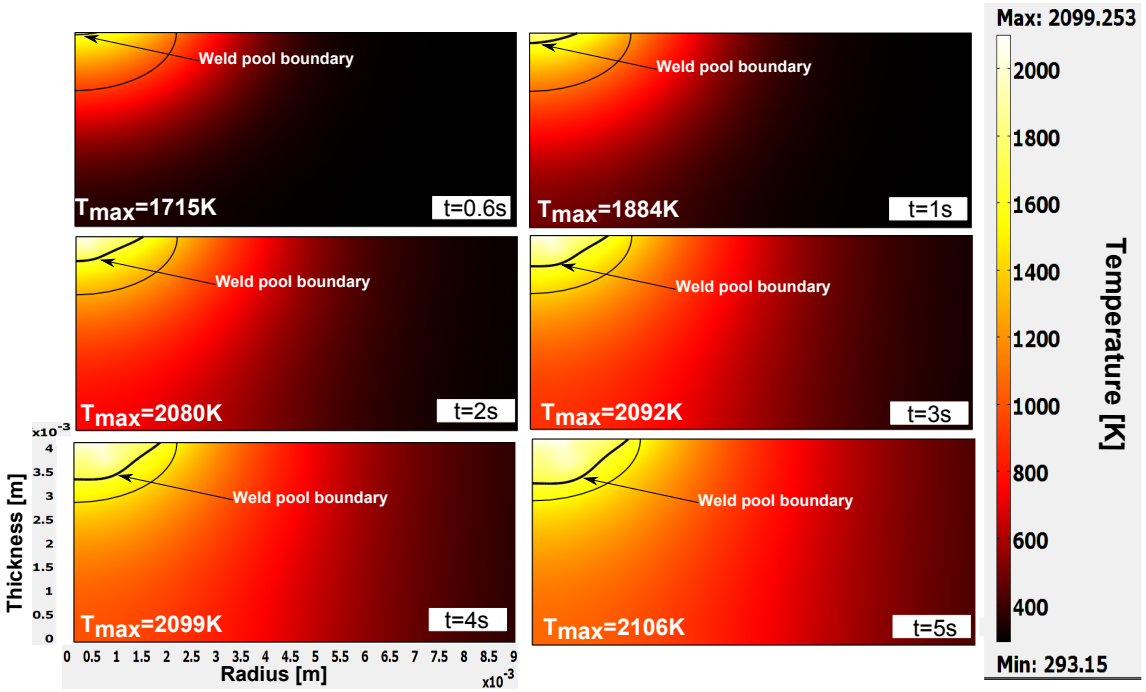

Figure 3.17: Temperature distribution, weld pool development and maximum temperature at different time steps during the arc heating.

3.18 shows the radial temperature distribution on the weld pool top surface at different times. This figure shows the shift in the peak temperature location from the center of the weld pool. At 1 s, the maximum temperature occurred at the weld pool center. At the end

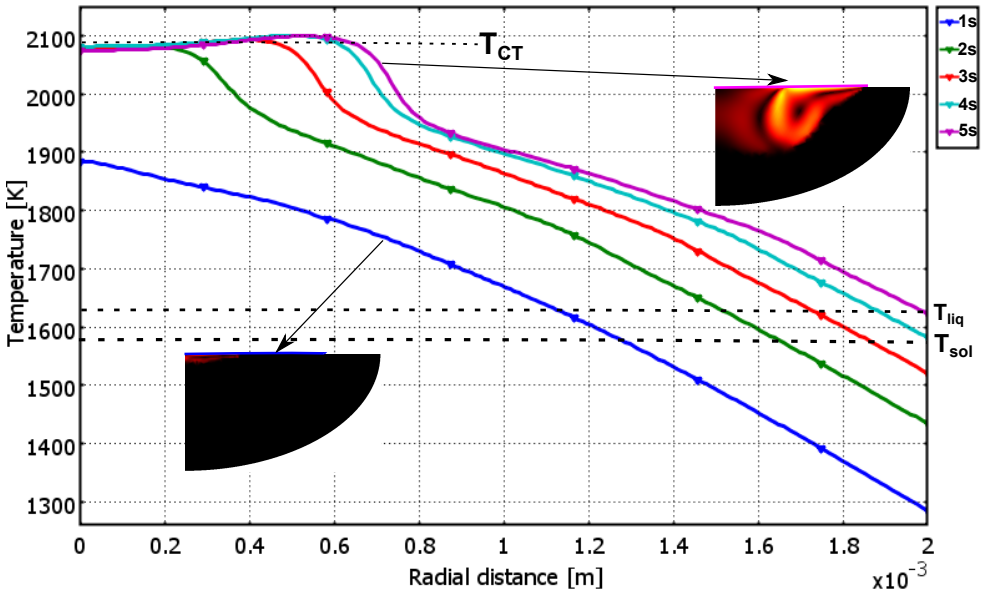

Figure 3.18: Temperature distribution on the weld pool surface at different time steps.

of the arc heating (5 s) the peak temperature location is shifted to 0.54 mm away from the

center. This peak temperature location shift in the weld pool surface is due to the variation of the surface tension coefficient with the temperature and the accompanying convective heat transfer. The weld pool surface reaches a critical temperature (where the temperature coefficient of surface tension change sign and which results in change in direction of the Marangoni force and the corresponding fluid flow see section 1.5.3.7 of chapter 1) at T_{CT}=2095 K. For the four cases $(2s, 3s, 4s, 5s)$, where the temperature reaches the T_{CT}, a common trend in the surface temperature distribution can be observed. The first region near to the disc top center, the temperature gradually increases from the center and reaches a peak temperature. In the second region, a sudden drop in temperature with steep slope is observed. In the third region, a gradually decreasing slope is observed. The rise of temperature in the first zone is probably due to the positive radial velocity distribution in this region as shown in figure 3.22. Due to the surface tension effect, the fluid motion is outward (from the center to the weld pool edge) transferring the heat away from the center. At T_{CT}, the surface tension coefficient changes, and the fluid motion is inward (from the weld pool edge to the center). These two opposed flows occur where T=T_{CT} is reached. This movement of fluid from the center to radially outward direction transferred the heat from the center in the flow direction and would resulted in an increase in temperature. The sudden drop of temperature in the second region can be explained using the occurrence of maximum resultant velocity at this region causing an increase in the liquid convection, and this inward flow of molten metal would transport heat more rapidly into the weld pool. In the third region the direction of flow is inward, these heat and mass flows from the comparatively low temperature boundary to the center direction resulted in the slowing down of the cooling rate. Figure 3.19 shows the temperature

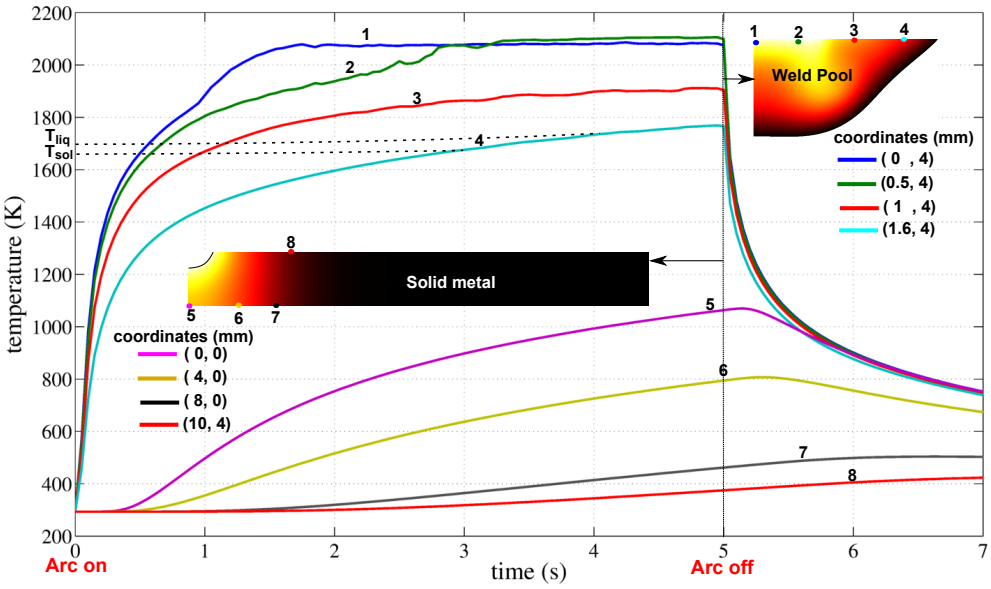

Figure 3.19: Temperature history at different locations of weld pool and the solid metal, which is indicated on the computational solution domain at the end of arc heating.

history of eight selected points from the computational domain. The first four points are on the weld pool and the rest on the solid metal boundary. All the four points on the surface of the weld pool show sudden increase in the first second due to the application of the welding arc. Point 1 at the center of the weld pool reaches its final temperature after 1.5 s. As discussed in the previous paragraph, due to the molten metal circulation,

the point 2 which is 0.5 mm away from the center shows a rise in temperature as the arc heating progresses and at time t=3 s, the temperature at this point is slightly greater than the center point. The sudden decay takes place once the arc switched off at t=5 s.

The curves 5 to 8 in figure 3.19 shows the temperature of four points on the solid metal. Points 5,6 and 7 for back surface and 8 on the top surface. The maximum temperature observed at the bottom center of the pool is 1070 K.

3.3.6.2 Velocity field

Figure 3.20 shows fluid flow velocity within a region 1 mm × 2 mm in the pseudo-fluid domain at the end of the arc heating. The arrows are proportional with a scale factor of 0.6. The isotherms for solidus (1673 K) and liquidus (1723 K) temperature are also

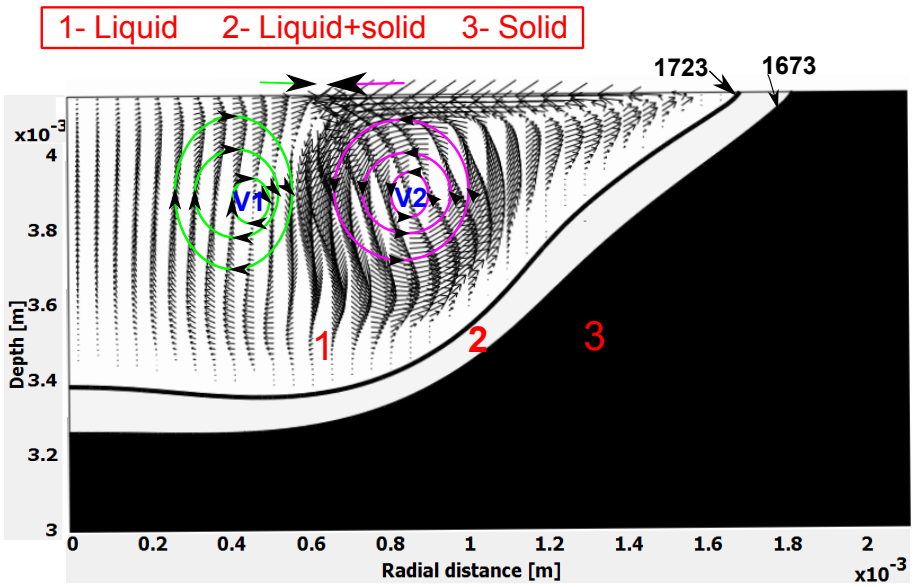

Figure 3.20: Velocity distribution in weld pool

plotted. In region 1, the temperature is above liquidus temperature and the material is in the liquid state. The region 2, where the temperature is in between solidus and liquidus temperature is known as mushy zone. In this region both solid and liquid states coexist. The region 3, where the temperature is below the solidus temperature, the material is in the solid state. The maximum temperature and absolute velocity at the end of the static arc heating are 2099.25 K and 36.07 cm/s respectively. Two vortex (V1 and V2) are formed in the weld pool due to the complex convection phenomena. V1 is from the bottom to the surface near the symmetrical axis with a relatively weak velocity distribution. And V2 is from the edge of the weld pool towards the center with a high velocity distribution. This flow occurs because of the high temperature gradient across the fluid surface, which generates a stronger surface tension driven flow. The forces opposing to this flow are the arc drag force and buoyancy force. For low current welding the effect of Lorentz force and arc drag force are low. The maximum velocity is occurred at the fluid top boundary at a radius of 1.24 mm from the symmetry axis.

Figure 3.21 shows the evolution of the velocity field at different step time within a 2 mm wide and 1.2 mm deep region of the fluid domain. At time t=0.8 s the maximum

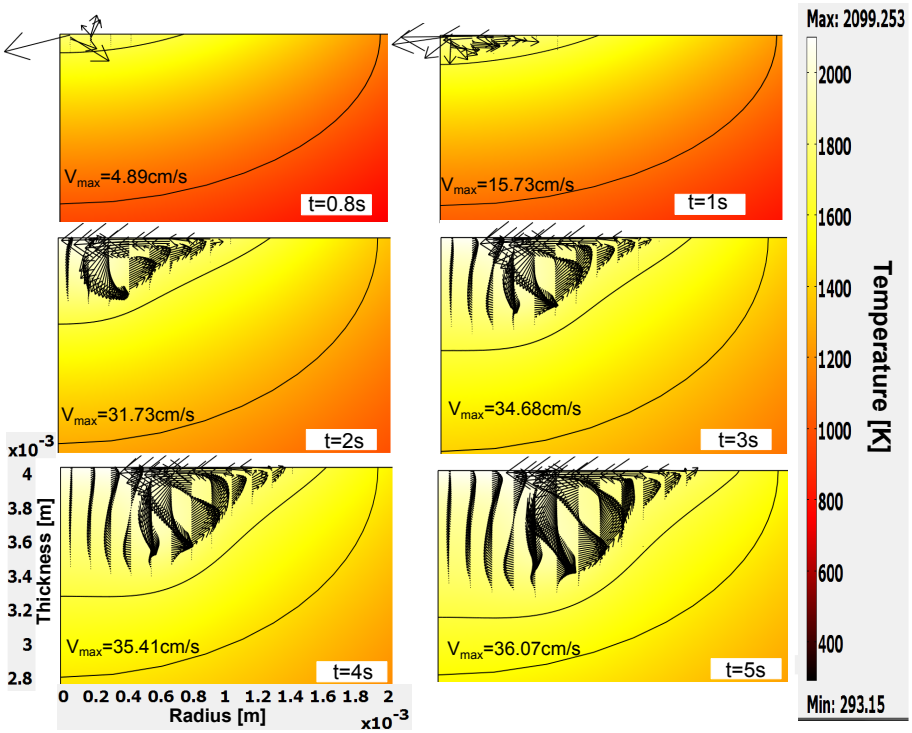

Figure 3.21: Velocity distribution, weld pool development and maximum velocity at different time steps during the arc heating.

fluid flow is 4.89 cm/s. After 0.2 s the maximum velocity becomes three times higher (i.e. 15.73 cm/s) with same direction of flow. After 2 s two vortex are formed due to the

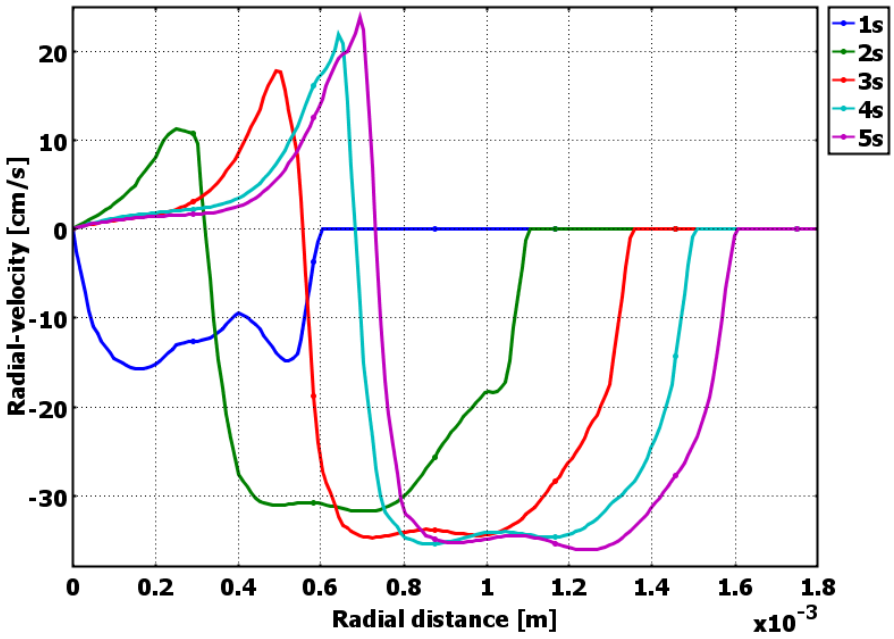

Figure 3.22: Radial velocity distribution at the top surface of the weld pool at different time steps during the arc heating.

change in the surface tension because of the thermal gradient on the weld pool surface. As a result of this change in flow direction, there is a geometrical effect in the weld pool formation. The maximum depth region in the weld pool get shifted to the weld edge direction. The profiles at t=2 s and t=3 s show the flattening of the curved bottom area. At t=4 s and t=5 s, the liquid-solid boundary gets more flattened and start shift towards a maximum depth point. This is occurring because of the downward flow during liquid convection with high velocity that causes the shift in concentration of heat flow due to the complicated Marangoni flow.

Figure 3.22 shows the radial velocity distribution at the top surface of the weld pool for different time steps during the arc heating. At 1 s the negative value of the surface velocity means that the flow is inward (from the edge to the center) because the temperature surface tension coefficient is positive. In the later times a reverse of fluid flow direction occurs when the surface temperature reaches the critical temperature (T_{CT}). This critical temperature corresponds to the temperature at which the temperature dependent surface tension changes sign. A sharp peak is observed for the last three curves, respectively for 3s, 4s and 5s, it would be interesting to investigate this behavior with a finer mesh on the top weld pool boundary.

3.3.6.3 Weld pool evolution

Figure 3.23 shows the weld pool evolution during the static GTAW process for different time steps. The size of the weld pool is identified using the solidus isotherm (1673 K). The weld pool formation starts 0.5 s after the arc sparking. For the first two cases (0.6 s

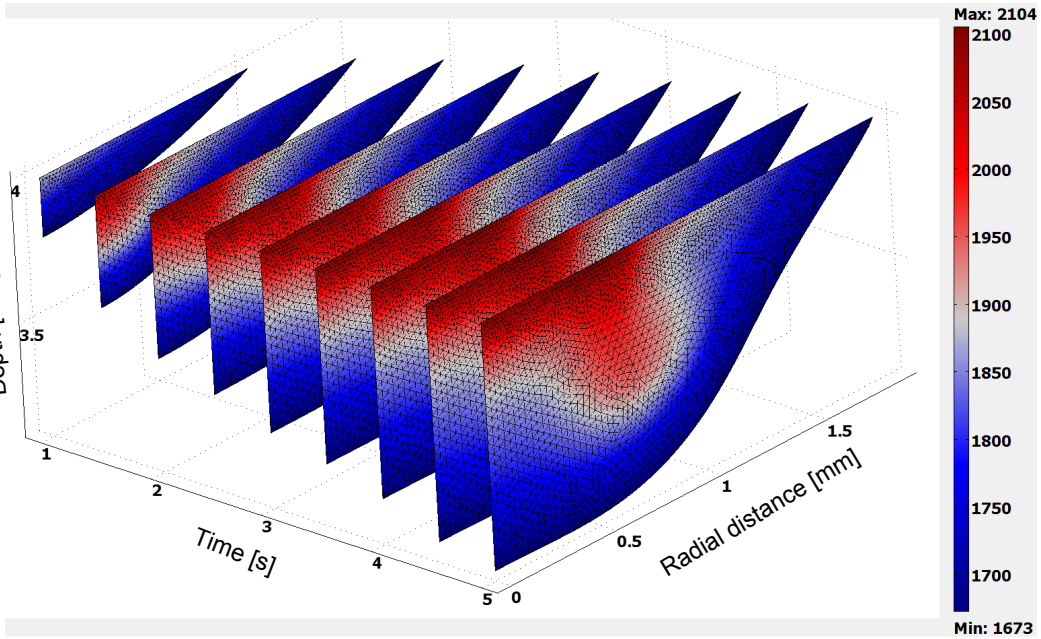

Figure 3.23: Transient weld pool evolution and the temperature distribution.

and 1 s) the weld pool was similar to the classical hemispherical shape, then as mentioned earlier, the critical temperature is reached for the surface tension and a counterclockwise flow appears and the weld pool shape starts to be deformed and tends to a shallow weld pool. The weld pool width seems to grow faster than the depth. At the end of arc heating

(5 s) the weld pool width and depth are 1.85 mm and 0.86 mm respectively. That gives a aspect ratio (depth to width) of 0.46. Figure 3.23 shows the temperature distribution in the pseudo-fluid domain with lower limit of solidus temperature during the 5 s static arc heating. This temperature distribution indicates the domination of convection over conduction in the weld pool heat distribution. The "hot zone" transports the heat in to the depth of the weld pool due to the encounter of the clockwise and anticlockwise flows under the radius where the critical temperature is reached.

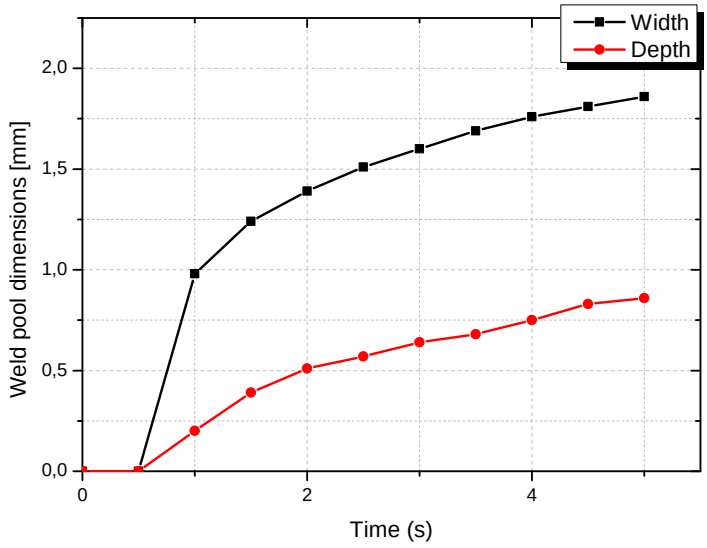

Figure 3.24: Evolution of weld pool dimensions.

Figure 3.24 shows the evolution of the weld pool width and radius with time. The weld pool starts around t=0.5 s and quickly grows to 1 mm at t=1 s while the depth is about 0.2 mm. The growth of the weld pool is important within t=0.5 s and t=1 s. At t=5 s, the width (actually half width) is about 1.85 mm for a depth of 0.86 mm as said previously. It can be seen from the evolution of this curves that the steady state is not yet reached. The growth of the weld pool after t=1 s seems to be linear (till 5 s) with a rate of 0.21 mm/s for the width and 0.16 mm/s for the depth.

3.3.7 Study on the effect of welding energy

Three cases are considered for the influence of the welding energy on the weld pool generation. Table 3.7 presents the simulation parameters for the three cases.

Figure 3.25 shows the temperature and velocity distribution at the end of a 5 s arc for the different welding energy considered with currents 70 A, 110 A and 150 A. The solution shows velocity distribution on the right side and six isothermal contours starting from the solidus temperature (1673 K). The maximum observed velocity and temperature is also presented. First of all, a clear indication of the effect of energy can be identified from the volume of melted material. As the energy increases the amount of metal melted is also increased. The fusion zone boundary evolved for the three cases are different. The

Table 3.7: Parameters

Parameters	*Case 1*	*Case 2*	*Case 3*
Welding Current, I (A)	70	110	150
Welding voltage, U (V)	9	10.6	11
Welding duration, (s)	5	5	5
Welding Energy, (s)	2142	3740	7140
Pseudo-fluid domain width (mm)	2	3.4	4.2
Pseudo-fluid domain depth (mm)	1.2	2	2.5
Current density distribution parameter, r_J (mm)	1.5	1.8	2.1
Gaussian current coefficient	0.5	0.5	0.5
Heat distribution parameter, r_H (mm)	1.5	1.8	2.1
Power distribution factor, d	0.5	0.5	0.5
Efficiency, η	0.68	0.68	0.68
Maximum arc shear (Pa)	10	40	65
Arc drag force distribution (mm)	2	2	2

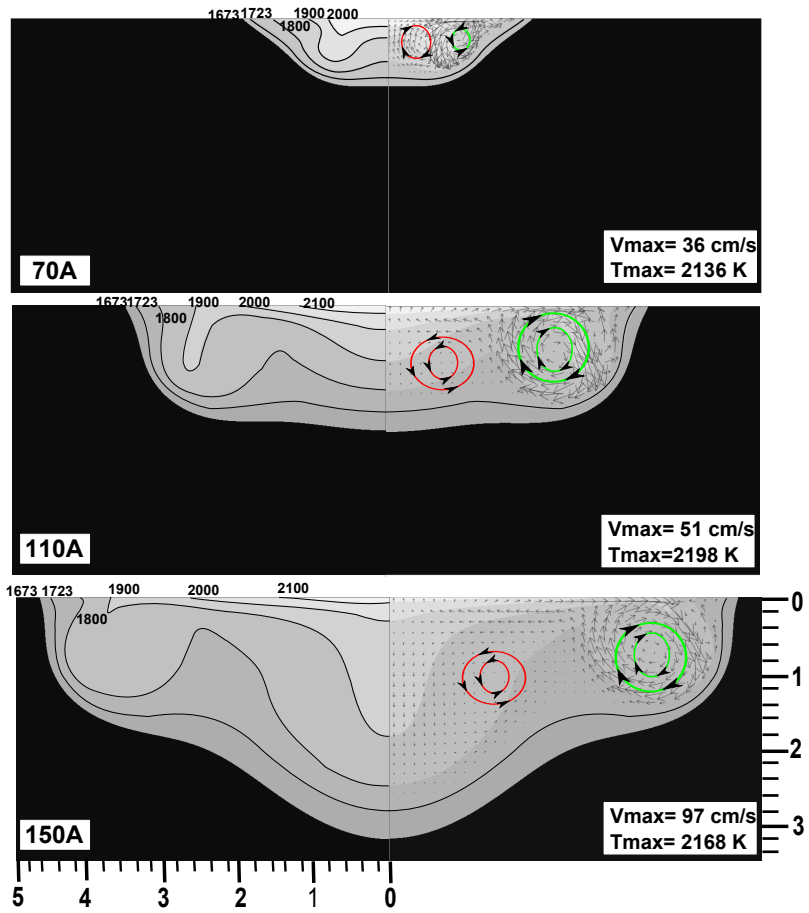

Figure 3.25: Temperature and Velocity distribution. The welding conditions are presented in table 3.7

fusion front development is clearly affected by the weld pool convection. The dynamic effect of the weld pool are responsible for the final pool dimensions. As seen from the 70 A weld pool velocity distribution, the 110 A and 150 A cases also showing two vortices. The velocity field at the top surface of the weld pool plays an important role for the heat transfer inside the molten pool. So it is interesting to see the top surface velocity profile for the three cases.

Figure 3.26 shows the top weld pool surface radial velocity distribution at the end of arc heating for the three cases. Here two regions, one with positive and other with negative velocity fields can be observed. For 70 A case, as discussed earlier, the radial velocity is predominantly negative with a maximum value of 36 cm/s. On the contrary, for 110 A and 150 A the velocity become predominantly positive with maximum values of 51 cm/s and 97 cm/s respectively. The positive maximum radial velocity at the top surface of the weld pool, transfer the most of the heat with the molten pool in the radial direction and is responsible for the larger width compared to the 70 A case. Due to the

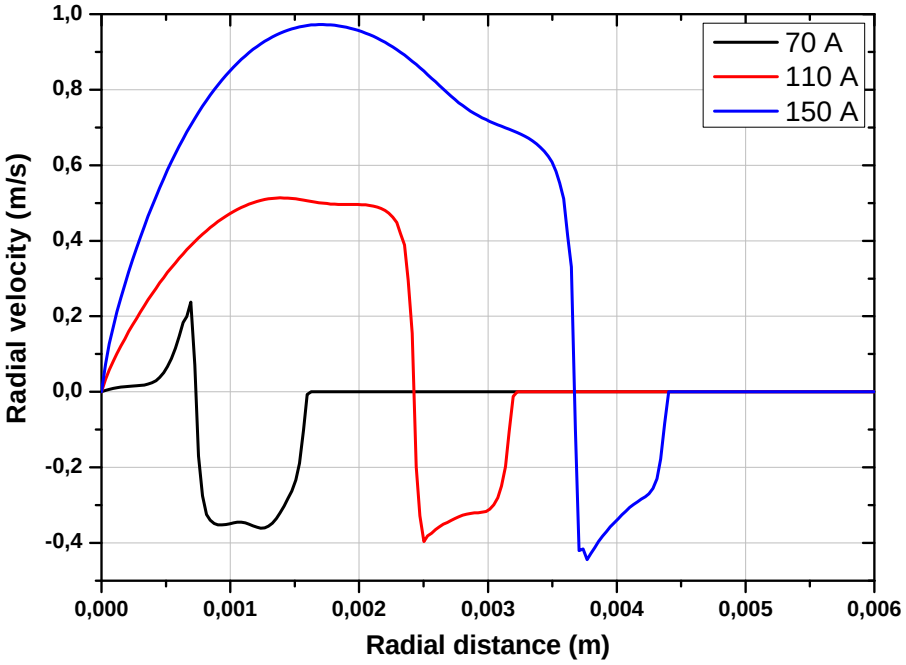

Figure 3.26: Radial velocity distribution at the end of arc heating (5 s)for the three studied energy. The welding conditions are presented in table 3.7

two recirculation loops present in the weld pool for the above three cases, a wavy fusion boundary formed. The shallow upper loop formed generated due to the high velocity driven flow by Marangoni force and arc drag force. The deeper second loop is generated as a result of Marangoni flow and Lorentz flow (in the case of 110 A and 150 A).

3.3.7.1 Comparison with literature

It could be interesting to recall some of the earlier work in order to provide a realistic perspective regarding the calculated results. We did not carry out a one to one matching with others work instead we found some previous works that matches closely with the presently studied cases. Also we compared quantitatively the most important observations of the study such as maximum velocity.

Lee *et. al.* [95]

Lee *et. al.* [95] analyzed the weld pool convection caused by the stationary GTA welding arc by considering the electromagnetic force, surface tension force and the arc shear stress. The heat source boundary conditions were found out using a electric arc model. They

Table 3.8: Comparison between the major parameters used by Lee et al. for 150 A case for 2 s and 3 s

Parameters	*Lee et al.*	*Our model*
Heat source parameters	Arc model	Gaussian assumption
Arc length (mm)	2	2.4
Electrode bevel angle	30°	30°
Current density	Arc model	Gaussian distribution
Arc shear stress	Arc model	Same as Lee et al.
Surface tension gradient	Sahoo et al. [94]	Sahoo et al. [94]
Weld pool surface	Free	Fixed

carried out calculations on type 304L stainless steel sample which has a 30 ppm sulfur content with a welding current of 150 A, arc length of 2 mm and electrode bevel angle of 30°. A comparison between the parameters used in Lee et al. configuration is presented in table 3.8.

Figure 3.27 shows the comparison between our model and the Lee et al. model for the weld pool formed after 2 s and 3 s of arc heating. The predicted weld pool shape and the size are in good agreement with the Lee et al. calculations. Moreover, the small discrepancies in the prediction of weld pool width are probably arose from the differences in the boundary conditions and the small variations material properties used.

The weld pool profiles obtained are similar to the calculated results of Tanaka *et. al.* [48]. They used stainless steel 304 anode with welding a current of 150 A, argon shielding is used at 15 L/min flow rate, an arc length of 5 mm, and electrode tip angle 60 °. The

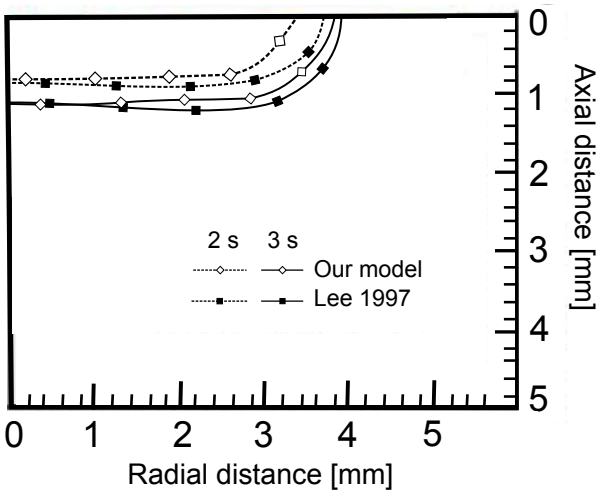

Figure 3.27: Comparison of weld pool size for 150A with literature data. The welding conditions for our model 150A current, 11V Voltage, efficiency 0.68 and Gaussian base radius of 0.0021 m, Lee et. al. [95] is given in table

weld pool profiles obtained for Tanaka *et. al.* are comparable with our results. Choo et al. [114] modeled welding arc and weld pool for GTAW spot welding operation. The maximum velocity calculated for a current of 100 A is reported as 72 cm/s.

3.3.7.2 Dimensionless heat input

In order to study the formation of the observed wavy weld pool boundary a dimensionless heat input Q* is defined similar to Arora et al. [115] work. The dimensionless number Q*, which is the ratio of heat supply rate and the conduction heat transfer rate, is defined as follows

$$Q^* = \frac{Q}{RkT_m} \tag{3.24}$$

Where Q is the heat supply rate, R is the radius of heat source, k is the thermal conductivity and T_m is the melting temperature. Table 3.9 shows the parameters used, the calculated Q*, and Marangoni number (see section 3.3.8.5 for the three studied cases Interestingly the Q* calculated for the three cases are same and is 10. According to Arora

Table 3.9: Calculated dimensionless heat input

Welding Current	*Heat input rate (W)*	*Radius of heat source (mm)*	Q*	Ma
70 A	630	1.5	12	24705
110 A	1166	1.8	19	33544
150 A	1650	2.1	23	36916

at al. [115] the wavy fusion zone boundary forms at a Marangoni number greater than 26000 and a Prandtl number less than 0.06 and dimensionless heat input greater than 20. Among the three investigated cases, from figure 3.25, the 70 A and 110 A cases do not exhibit a wavy fusion boundary. On the contrary 150 A case shows the wavy fusion

boundary. The condition for Marangoni number and Q* to get a wavy boundary is validating with our numerical model (Ma less than 26000 for 70 A and greater for 110 A and 150 A cases and Q* is less than 20 for 70 A and 110 A cases and is more than 20 for 150 A case) with the exception of Prandtl number, which is obtained as 0.08, see section 3.4.3, and is calculated using a dynamic viscosity of μ= 0.006 kg/m.s.

3.3.8 Study on the effect of various forces acting in the weld pool

Simulations were carried out by considering each individual forces alone to understand their effect on velocity and temperature field. Also this analysis allows us to verify the effect of each forces by comparing with literature results. The focus of this study will be on the magnitude of velocity, direction of flow and heat transfer in the weld pool. The results are plotted in a region of 2 mm wide and 1 mm deep from the symmetric axis and the weld pool top surface respectively. All the simulations presented hereafter were carried out with the parameters in table 3.4, 3.6, 3.5. Temperature dependent thermophysical properties were employed as discussed in section 3.2.3 and $\partial\gamma/\partial T$ was also assumed as temperature dependent unless otherwise stated.

3.3.8.1 Buoyancy force

Variation of temperature of the molten metal causes variation in the density of the metal which produces flow into the weld pool due to buoyancy. The current model takes this effect into account by use of Boussinesq approximation. The weld pool developed due to the effect of buoyancy alone is plotted in Figure 3.28. Despite the low values of the fluid velocity (0.046 cm/s), a clockwise flow is developed transferring the "cold molten metal" from the bottom weld pool to the "top surface" and transferring the "hotter molten metal" from the top center surface to the edge of the weld pool. Due to the low fluid velocity, most of the heat is transferred by conduction that is why the weld pool shape is more or less hemispherical. The maximum velocity attained by the liquid metal is 0.046 cm/s and it can be conclude that for this welding condition the force and there by the velocity field generated due to buoyancy effect is negligible. The maximum temperature obtained is 2223 K at the top center of the weld pool.

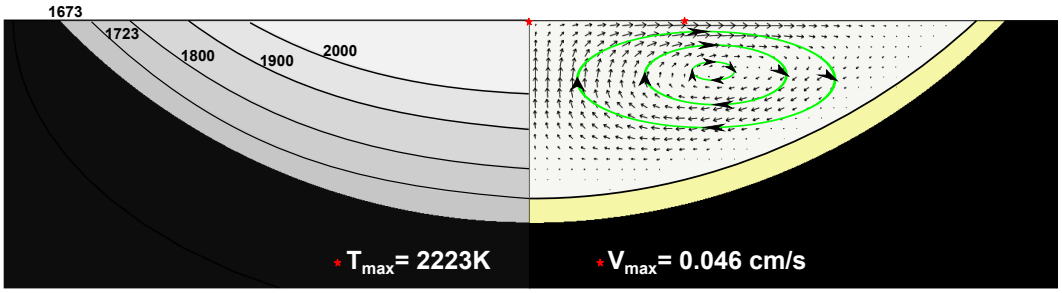

Figure 3.28: Temperature and Velocity distribution; Weld pool shape and size under buoyancy force alone.

3.3.8.2 Lorentz force

Figure 3.29 shows the liquid metal velocity field and the temperature field in the weld pool when Lorentz force acts alone at t=5 s when the arc is switched off. The interaction between current flow and the self induced azimuthal magnetic field generates an electromagnetic force (Lorentz force) in the weld pool. This body force drives the liquid metal towards the center of the pool and towards the weld pool bottom that results in an increase in weld pool depth. This will accumulate the heat to the center and results in a deeper weld pool. The maximum velocity attained is 0.117 cm/s. This low velocity field is due to the low input current. It has been reported in the literature that the electromagnetic force play a major role in the weld pool convection for currents higher than 200 A [109]. The maximum temperature in the weld pool is 2226 K.

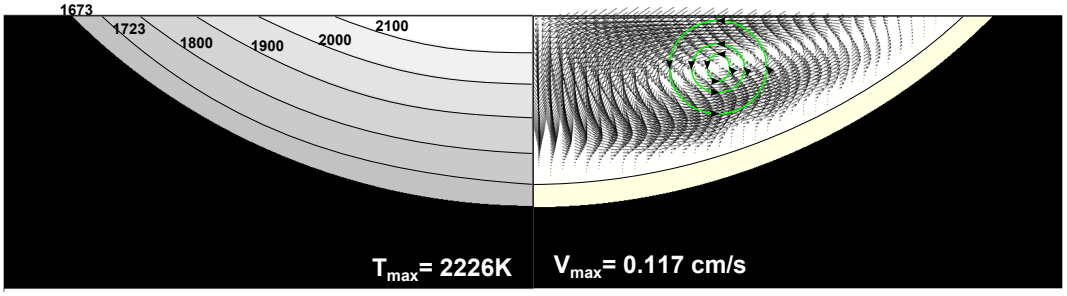

Figure 3.29: Temperature and Velocity distribution; Weld pool shape and size under Electromagnetic force alone.

3.3.8.3 Surface tension force

Figure 3.30 shows the velocity and temperature field distribution in the weld pool by considering the surface tension force alone. Because of the high gradient of temperature in the weld pool surface results in a high surface tension at the center and a low surface tension at the edge of the pool. The surface tension force also called Marangoni force is defined, in chapter 1 section 1.5.3.7, as the product of temperature surface tension coefficient and temperature gradient as follows:

$$F_{MA} = \frac{\partial \gamma}{\partial T}\frac{\partial T}{\partial r} \tag{3.25}$$

Generally the temperature surface tension coefficient for pure metal is negative which results in the positive Marangoni force and resultant flow is from center to the edge of the pool. For alloys, due to the presence of minor alloying elements, the surface tensional gradient changes sign at a particular temperature. This generates a negative Marangoni force. This is the reason for reversal of flow direction in the weld pool as shown in figure 3.30. This surface tension shear force, which acts at the boundary of the weld pool is responsible for the fluid motion. The maximum velocity attained by the liquid metal flow is 36.67 cm/s. The temperature dependency of the surface tension gradient results in the shifting of the maximum depth of penetration in the weld pool from the symmetry axis toward the edge. This results in the formation of "W" shaped weld cross section [36]. The maximum depth occurs at the location where the reversal of flow takes place. The temperature corresponding for this flow reversal is known as critical temperature. At this

temperature the surface tension gradient change its sign. The maximum temperature reached at the end of the arc heating is 2117 K at a radius of 0.43 mm on the top surface of the weld pool as shown in the left part of figure 3.30. Compared to buoyancy force and Lorentz force, Marangoni force dominated the fluid flow with a maximum velocity of 800 times higher than that of buoyancy force and 300 times higher than that of Lorentz force for a welding intensity of 70 A.

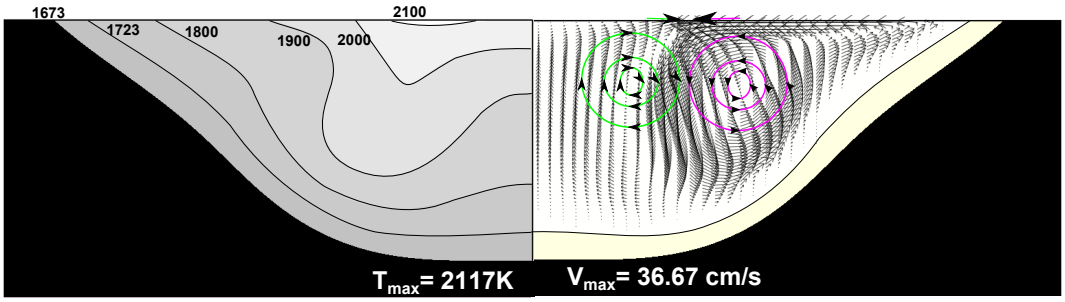

Figure 3.30: Temperature and Velocity distribution; Weld pool shape and size under surface tension force alone.

3.3.8.4 Arc drag force

Arc drag force is considered as the third most important driving force in the weld pool convection [18, 28]. Choo *et. al.* concluded in their study that, if the magnitude of the aerodynamic shear stress approaches that of the Marangoni shear in the weld pool increases the importance of arc gas shear force [104]. The arc shear on the weld pool is very much dependent on current, the composition of the shielding gas, and also on the tip angle of the electrode [18, 95] see section 1.5.3.8 of chapter 1. For the present study the effect of arc drag force is considered as a spatial boundary distribution. The following function represents the arc drag force distribution:

$$P_{Drag}(r) = P_{Max}\sqrt{\frac{r}{r_{Shear}}}exp - \left(\frac{r}{r_{Shear}}\right)^2 \tag{3.26}$$

Figure 3.31 shows the velocity and temperature distribution in the weld pool by considering arc drag force alone. The aerodynamic shear force results in an anti-clockwise

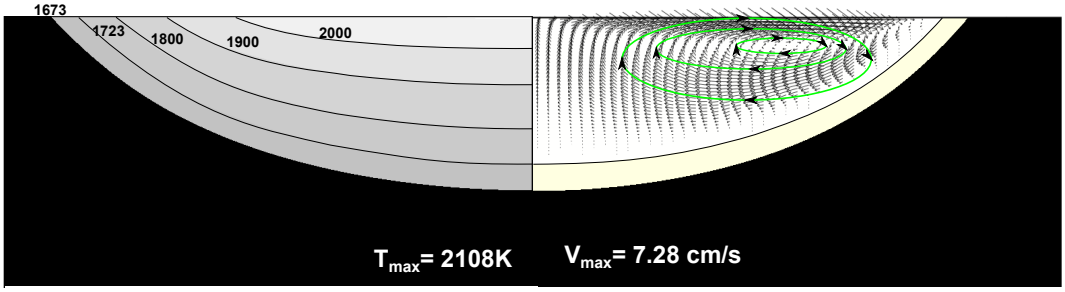

Figure 3.31: Velocity and temperature distribution; Weld pool shape and size under arc drag force alone.

flow in side the weld pool. It enhances the flow of liquid metal from center to the edges

resulting in wider weld pool and shallow penetration. The maximum velocity attained by the molten metal is 7.28 cm/s, which is 150 times higher than buoyancy force, 60 times higher than Lorentz force and 5 times lower than Marangoni force. The maximum temperature in the weld pool is 2108 K at the top center point of the domain.

The arc drag force distribution for the numerical simulation is fixed using the literature data. The parameters of the arc drag force function were estimated by fitting as much as possible available data from the literature [53, 57, 62, 95].

3.3.8.5 Summary

Table 3.10 illustrates the direction of flow at the top and symmetrical axis boundaries of the computational domain. Table 3.11 presents the comparison between different forces

Table 3.10: Direction of flow in the weld pool top surface and the center symmetry axis; The arrows $\longrightarrow$ and $\uparrow$ corresponds to clockwise motion where as $\longleftarrow$ and $\downarrow$ indicate the anti-clockwise motion

Force	*Top surface flow direction*	*Symmetry axis flow direction*
Buoyancy	$\longrightarrow$	$\uparrow$
Electromagnetic	$\longleftarrow$	$\downarrow$
Surface tension	$\longrightarrow\longleftarrow$	$\uparrow$
Arc drag	$\longrightarrow$	$\uparrow$
All together	$\longrightarrow\longleftarrow$	$\uparrow$

and the combined effects on the maximum temperature (T_{max}), maximum velocity (v_{max}) and the weld pool dimensions. Among the four driving forces, surface tension force dominated in the liquid convection for the present welding parameters. The contributions in the fluid velocity from buoyancy force and Lorentz force were negligible. Because of the minor role of these body forces in liquid convection, the conduction dominated in these cases and resulted in a comparatively high maximum temperature in the weld pool. In the case of surface forces, both enhanced the convection in the liquid phase and a small decrease in the maximum temperature was observed. The calculated maximum weld pool

Table 3.11: Comparison of weld pool forces

Force	$T_{max}(K)$	$v_{max}(cm/s)$	*half width (mm)*	*depth (mm)*
Buoyancy	2223	0.046	1.91	0.791
Electromagnetic	2226	0.117	1.91	0.793
Surface tension	2117	36.67	1.865	0.921
Arc drag	2108	7.28	1.931	0.703
All together	2106	36.07	1.86	0.86

velocities are 0.046, 0.117, 36.67, 7.28, 36.07 cm/s for Buoyancy, Lorentz, Marangoni, arc drag and all the forces together respectively for a 70 A current. Similarly, the maximum

velocity calculated for 150 A current with all the driving forces is 97.25 cm/s. In literature, Tanaka et al. [48] carried out similar predictions for static GTAW process. They used 150 A current with an arc length of 5 mm. The electrode conical angle was 60° and used argon shielding gas. Their model did not consider the temperature dependent surface tension coefficient. Figure 3.33 shows the importance of considering the temperature dependent surface tension coefficient. The maximum velocities from their calculations are 1.4, 4.9, 18 and 47 cm/s for buoyancy, Lorentz, Marangoni and arc drag force respectively. The maximum velocity obtained for all the force together is 54 cm/s. Where as our calculations for 150 A case predicted a maximum velocity of 97.25 cm/s. The variation is mainly due to the low arc length (2.4 mm) for our calculation.

Dimensionless parameters are useful to understand the relative importance of the driving forces. It could be interesting to evaluate the magnitude of different characteristic dimensionless number as Arora *et. al.* [115] did.

The Marangoni number, Ma presents the relative importance of surface tension force to viscous force and indicate the strength of the Marangoni flow. It is given as follows

$$Ma = \frac{\rho c_p R \frac{d\gamma}{dT}}{k\mu} \tag{3.27}$$

Where R is the radius of the heat source. Since the surface tension force depends on the temperature gradient on the surface, $(T_p - T_s)$ is more meaningful than the solidus temperature T_s, where T_p represents the peak temperature. The calculated values of Marangoni numbers are 24705, 33544 and 36916 respectively for welding currents 70 A, 110 A and 150 A. Arora et al. [115] studied the formation of wavy weld pool boundary using dimensionless numbers derived from Buckingham π-theorem. Their calculations shows that the wavy fusion zone boundary forms at a Marangoni number greater than 26000. This wavy boundary originates from the interaction of counter-rotating liquid metal loops at high Marangoni numbers. The calculated values of Marangoni number for the three currents and the corresponding fusion zone boundary observed more or less validating this criteria. The fusion boundary for 70 A is not so wavy in the present case. But for 110 A and 150 A case showing a wavy fusion boundary.

3.3.9 Study on the dependence of sulfur content

3.3.9.1 Constant temperature coefficient of surface tension

Figure 3.32 shows the velocity field and the weld pool shape at the end of arc heating when considering constant positive (left side) and negative (right side) values of temperature dependent surface tension coefficient. If the surface tension γ reduces with increase of temperature T, i.e. $\partial\gamma/\partial T < 0$, distribution of surface tension will be small at the center and large at the edge of the weld pool. This creates a flow from the center to the periphery which means the flow from high temperature to low temperature region. This flow of liquid metal provokes the convective heat transport from center to the edge of the pool which will form a shallow and wide weld pool as shown on the right side of figure 3.32. If the surface tension increases with temperature, i.e. $\partial\gamma/\partial T > 0$, the surface tension distribution will be large at the center and small at the edges. This create a flow from periphery to the center which means the flow from low temperature to high

temperature region. This flow of molten metal from periphery to the center leads to the convective heat transport to the center which will form a narrow and deep weld pool as shown on the left side of figure 3.32.

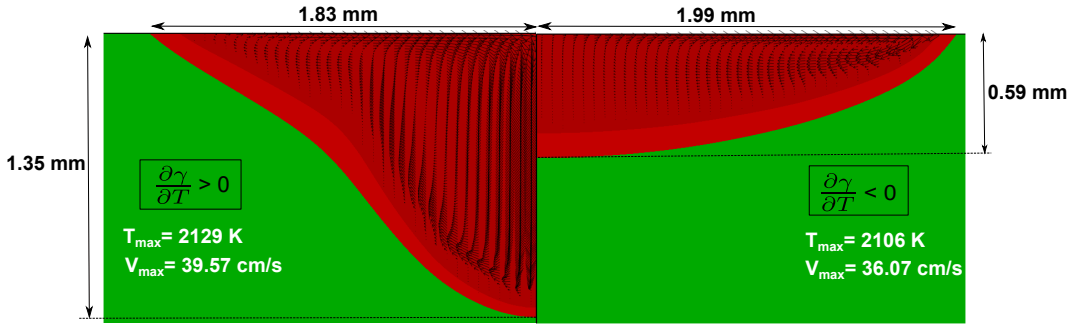

Figure 3.32: Velocity distribution and the weld pool size at the end of static arc heating for positive and negative temperature coefficient of surface tension. The welding conditions are 70 A current, 9 V Voltage, efficiency 0.68 and Gaussian base radius of 0.0015 m, temperature dependent thermophysical properties and surface tension gradient is constant.

3.3.9.2 Temperature coefficient of surface tension varying with temperature

In order to understand the effect of temperature coefficient of surface tension on temperature and sulfur content, simulations were carried on stainless steel 304L material with two different sulfur contents 0.0026%wt and 0.0036%wt. These values are obtained for materials that are currently available for experiments. These %wt of sulfur are obtained from the EPMA experiment which is already explained in the section 2.3.2. Figure 3.33

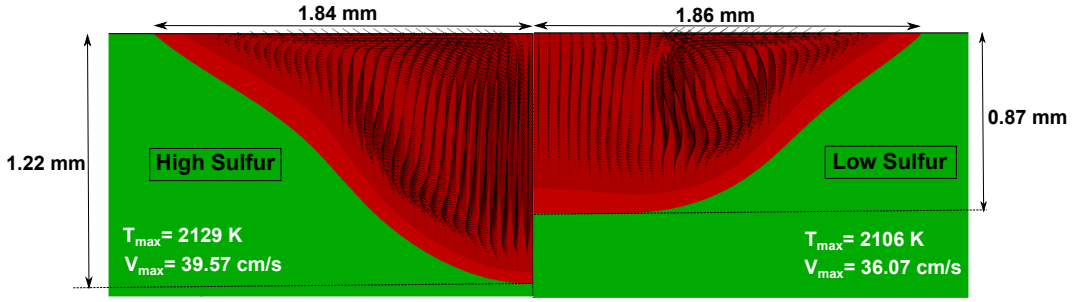

Figure 3.33: Velocity distribution and the weld pool size at the end of static arc heating for high sulfur and low sulfur stainless steel 304L. The welding conditions are 70 A current, 9 V Voltage, efficiency 0.68 and gaussian base radius of 0.0015 m, temperature dependent thermophysical properties and surface tension gradient is varying with temperature.

shows the velocity field distribution and the weld pool shape and dimensions obtained for high sulfur (left side) and low sulfur (right side)stainless steel 304L samples for a current of 70 A and voltage 9 V. The flow direction is observed to be different for both cases. For low sulfur sample the flow at the center of the weld pool is in the upward direction and for high sulfur sample it is in the downward direction. Low sulfur case shows a comparatively wider weld pool and shallow penetration. But the high sulfur case produced

a deeper weld pool penetration. In order to explain the effect of the sulfur concentration the equation governing the temperature coefficient of surface tension (also known as Marangoni coefficient) is remembered and summarized as follows:

$$\frac{d\gamma}{dT} = -A_\gamma - R_g\Gamma_s ln(1+Ka_s) - \frac{Ka_s}{1+Ka_s}\frac{\Gamma_s \Delta H_0}{T} \tag{3.28a}$$

$$K(T) = k_1\, exp\left(-\frac{\Delta H_0}{R_g T}\right) \tag{3.28b}$$

From the literature, two cases are presented in figure 3.34, which shows the variation of temperature coefficient of surface tension as a function of temperature, sulfur content and standard heat of adsorption in the alloy steel. For the first case the value of ΔH_0 was given by Sahoo *et. al.* [94] as $-1.66 \times 10^8 J/kg.mol$. The second case ΔH_0 uses the value $-1.88 \times 10^8\ J/kg.mol$ proposed by Zacharia *et. al.* [91, 92] for AISI 304 material. It is well established that the amount of surface active elements and the standard heat of adsorption ΔH_0 have a great influence on the value of the Marangoni coefficient [18, 36, 114]. For each curves, the critical temperature is given on the temperature axis (where the surface tension coefficient goes from a positive to negative value). It is clear that the value of the standard heat of adsorption must be known accurately otherwise the prediction of fluid flow reversal (counterclockwise flow) will not be accurate as well as the position where the reversal occurs. As shown by Choo *et. al.* [114] it is clear that the variation of 10 % of standard heat of adsorption (from $-1.66 \times 10^8\ J/kg.mol$ to $-1.88 \times 10^8\ J/kg.mol$) varied the critical temperature value by 250 K.

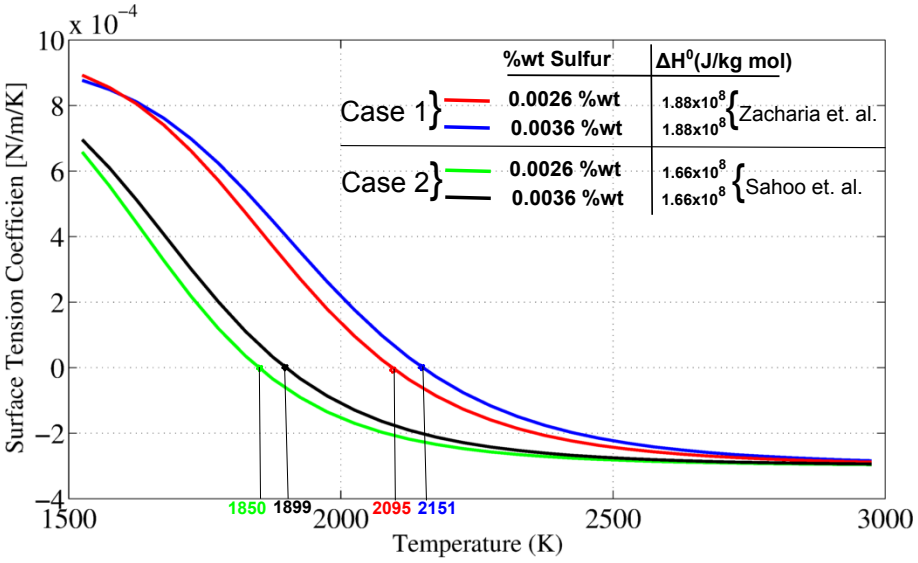

Figure 3.34: Variation of temperature coefficient of surface tension as a function of temperature, Sulfur content and standard heat of adsorption. Evaluated from equation 3.28b

3.4 Conduction versus Convection

The energy supplied from the arc is transported through the base material by both convection and conduction. The rate of heat flow with in the weld pool is responsible for the

temperature distribution (both in weld pool and HAZ) and the evolution of the weld pool shape. Therefore it is important to understand the effect of conduction and convection on the heat distribution. In order to better understand the effect of convection in the weld pool, a comparison of the conduction model and the convection model is carried out. In this section the conductive model is compared with the corresponding convective model for stainless steel 304L material containing two different sulfur concentrations (26 ppm and 36 ppm). The welding parameters used for the simulation are given in table 3.6. The simulation results used for the comparison are temperature distribution at the end of the arc heating and the transient weld pool dimensions. Also a dimensionless analysis is carried out using Peclet number to study the effect of convection over conduction.

3.4.1 Temperature distribution

Figure 3.35 shows the comparison of isothermal profiles at the end of 70 A arc heating for cases with and without considering convection for 70 A. The convective case presents the isotherm profiles for low and high sulfur content materials. In figure 3.35, seven isothermal contours were plotted with a maximum of 2000 K and minimum of 800 K in which dotted red lines corresponds to the conduction model, solid black line represents the convection model for low sulfur content material and blue line with dot represents the high sulfur content material. The line 3 corresponds to the solidus temperature (1673 K) and it represents the weld pool boundary. A close analysis of isotherms 1 and 2 with in

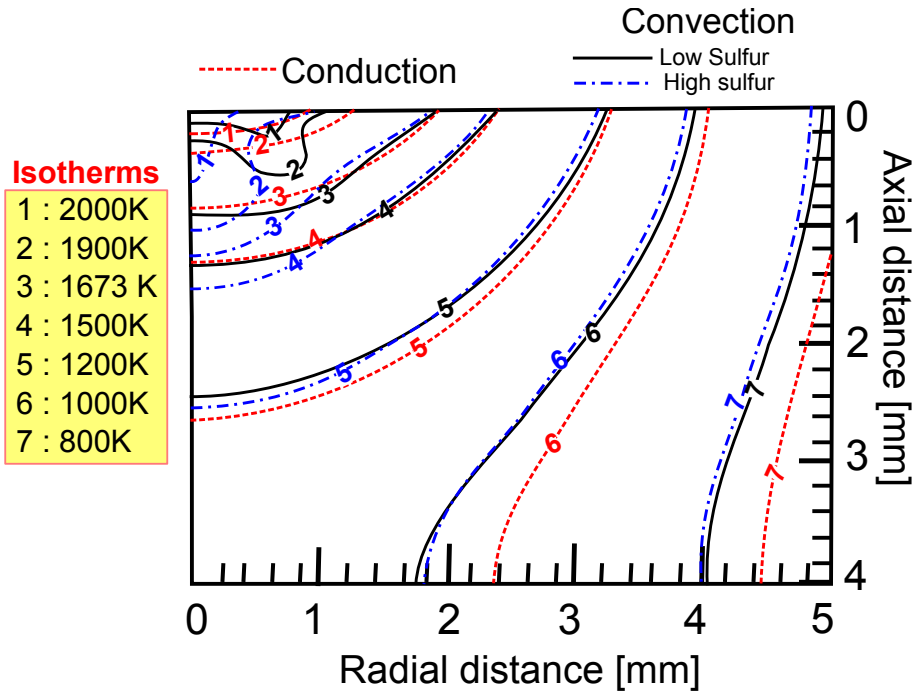

Figure 3.35: Comparison of isothermal contours for cases without (heat conduction) and with (heat transfer and fluid flow) considering convection. The welding conditions used are given in table 3.6

the weld pool indicates that the isotherms predicted with convection is showing greater variation from the conduction solution model. In the case of isotherm 1 and 2, top edge of the isotherms (edge touching the weld pool top surface) predicted from the conduction model are slightly leading than the corresponding convective prediction of low sulfur case

and a comparatively larger distance compared to high sulfur convective prediction. This gives insight into the fluid flow direction within the weld pool. From curvature of the isotherms it is clear that the low sulfur convective prediction the fluid velocity is towards the direction where the maximum depth occurred and similarly for high sulfur convection the fluid velocity is maximum along the center line of the weld pool. A similar analysis on the bottom edge (edge at the weld pool center line) shows that there occurred a upward motion for low sulfur case (shallow penetration) and a strong downward motion in the case of high sulfur.

The weld pool top width predictions with convection is exactly matching with the conduction for each cases (isotherm 3). This finding is quite important as this count out any possibility of radially outward motion at the surface of the pool near the periphery. In other words, if there would have been a radially outward motion on the surface; then the resulting top width would have been much larger than the pure conduction predictions. Hence, from this analysis we can conclude that the internal motion of the weldment has to be radially inward at the top surface close to the periphery. A similar observation can be seen for the isotherm boundary at the center line for low sulfur convection case. That means their occurred a upward flow for low sulfur convection case. On the contrary, the high sulfur convection case showing a deeper penetration (around 0.5 mm) compared to the predicted conduction model. This indicates the heat conduction model underestimated the heat flow through the center of the weld pool. The convection is dominated in this region for high sulfur convection case.

In the solid region the difference in the isotherms 4 and 5 are less. But interestingly for the isotherms 5 and 7 showing slight difference, this happens due to the faster removal of heat from the weld pool due to convection resulted in faster propagation of heat through the solid.

Two important features are identified from the figure 3.35 are as follows:

- The pure conduction model underestimates the depth of the weld pool (Comparatively high for high sulfur convection case)
- The conduction solution is almost predicting the correct weld width.

3.4.2 Weld pool characteristics

Figure 3.36 shows the comparison of transient weld pool characteristics for conduction and convection models. Here, the conduction model is slightly over predicting the weld pool width than the convective simulations. The low sulfur and high sulfur gives the same weld pool width dimensions. The comparison of weld pool depth evolution is very interesting, it shows that we can get different weld penetration using the same welding energy, with a slight variation in the sulfur content of the sample. The heat conduction model is able to predict the weld pool width and depth for low sulfur content sample. But in the case of high sulfur content sample the heat conduction model is under predicting the depth of penetration.

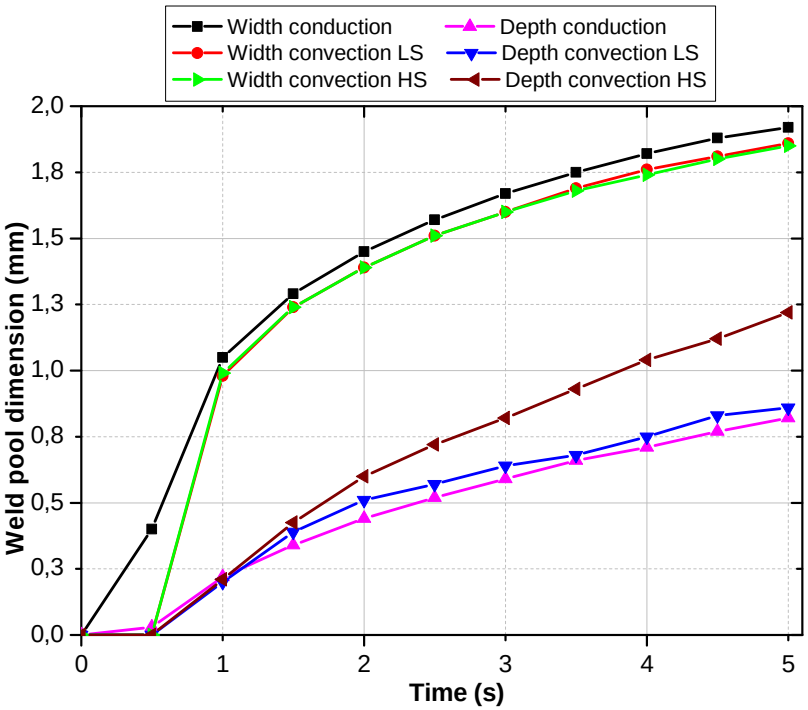

Figure 3.36: Comparison of weld pool dimensions for cases without (heat conduction) and with (heat transfer and fluid flow) considering convection. The welding conditions used are given in table 3.6

3.4.3 Dimensionless analysis

The relative importance of heat transfer mode within the weld pool can be evaluated using Peclet number [15]. The Peclet number, Pe, is defined as as the ratio of convective heat transfer to conduction and is given in equation 3.29

$$P_e = \frac{heat_{convection}}{heat_{conduction}} = \frac{u\rho c_p \Delta T}{k\Delta T/R_L} = \frac{R_L \rho c_p u}{k} \tag{3.29}$$

where u is the typical fluid velocity, ρ is the density, c_p is the specific heat, R_L is the characteristic length, and k is the thermal conductivity. The heat is transported mainly by convection for $Pe >> 1$. The average value of weld pool radius is taken as R_L and an maximum value of velocity in the weld pool is taken as u. For static arc welding, the Peclet number is a function of time because both u and R_L depend on time [64]. The dimensionless time t_1^* is defined as

$$t_1^* = \frac{t}{t_h} \tag{3.30}$$

Where t_h is the arc duration. t_1^* represents the ratio between actual time and the heating time. Figure 3.37 shows the calculated Peclet number as a function of the dimensionless time. Here, the Peclet number is gradually increasing with the growth in weld pool radius and suddenly drop at the end of arc heating. This indicates that at the initial times the heat transferred by conduction is comparable with the convective heat transfer. Once the weld pool get established, the convective heat transfer become important than conduction and play a role in modifying the final weld pool shape. Secondly, it is interesting to notice that in high sulfur content sample the Peclet number is high at beginning of arc

heating and gradually the difference is reducing with the arc duration. This can be explained by the increased level of molecular agitation with in the liquid with the increase in temperature may promote the greater involvement of the surface active elements with the bulk, *i.e.* their concentration at the surface is reduced [90]. The Prandtl number,

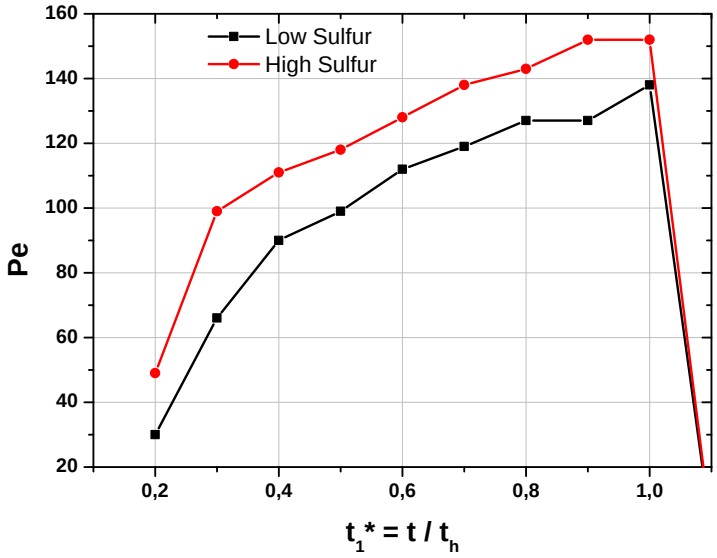

Figure 3.37: Peclet number as a function of dimensionless time. The welding conditions used are given in table 3.6

Pr, represents the relative rates of viscous momentum transfer to heat conduction. It is defined as follows:

$$P_r = \frac{\mu c_p}{k} \tag{3.31}$$

Where μ is viscosity, c_p is specific heat and k is thermal conductivity. This number is important in convective heat transfer problems in fluids since the viscosity can be regarded as the diffusion coefficient of momentum, while the thermal conductivity deals with the diffusion of heat. According to the values of physical parameters presented in table 3.4, $Pr = 0.08$ in all the studied case. From the study of Robert and DebRoy [116], for materials with high Prandtl number, Pe (Peclet) and Ma (Marangoni number) were high, heat transported primarily by convection with in the weld pool. The resulting welds were shallow and wide. In the current case The calculated high Pe and Ma (calculated in section 3.3.8.5) conforms the importance of convective heat transfer over conduction in the weld pool.

3.5 Parametric study

A parametric study on the different parameters used in the model have been carried out in this section. The main aim is to understand the effect of each individual parameters on temperature evolution, fluid velocity distribution and weld pool width and depth. The second goal of this study is to evaluate the most influential parameters of the mathematical model. These most influential parameters will be treated carefully as the accuracy of the

numerical results will rely on the accuracy of these influential parameters. In order to assess the effect of the investigated parameters, the following data were analyzed.

- Temperature history at the bottom center point with coordinates (0,0)
- Resultant velocity distribution at the top boundary of the fluid domain
- Time dependent evolution of weld pool depth and width

In this section three sorts of investigations have been done as follows:

(a) Material properties such as thermal conductivity, mass density, specific heat and viscosity.

(b) The heat flow parameters: Efficiency and Gaussian distribution

(c) The effect of temperature dependent thermophysical properties vs temperature constant properties.

Two more investigations have been done, one on the mesh grid size and another about the parameter composing the Sahoo's law for the surface tension. These results are presented in Appendix B.

3.5.1 Reference model

First of all a reference set of parameters for the mathematical model is defined. The numerical results of this reference simulation will be used for the analysis. The parametric study consisted of applying a small variation to one parameter at each time in order to observe its effect on the above mentioned output data. The thermophysical properties used for the reference simulation are assumed temperature independent as it simplifies the study.

Table 3.12: Material Properties

Thermal conductivity (W/mK) Solid/Liquid	*Density (kg/m^3) Solid/Liquid*	*Specific heat (W/mK) Solid/Liquid*	*Coefficient of thermal expansion [CTE] (m/K)*	*viscosity (Pa.s)*
26/20	7500/6350	486/650	10^{-4}	0.0025

Table 3.13: Simulation parameters

Maximum mesh size of top fluid domain surface (μm)	*Maximum mesh size of fluid domain (μm)*	*Time step (s)*	*Spot duration (s)*	*Simulation duration (s)*
60	100	0.05	5	5

The reference parameters used in the mathematical model are presented in tables 3.12, 3.13, 3.14 and 3.15. These reference parameters are respectively the material properties,

simulation parameters (time step, mesh size, duration), the heat flux parameters/welding condition and surface tension parameters. It was decided to apply a variation of 5% to each investigated parameters. Then the new numerical results are compared to the reference results.

The parameters such as efficieny (η) and Gaussian base radius (r_b) are reportedly playing major role in the numerical model. So these parameters were varied 5% and compared with the reference simulation.

Table 3.14: Parameters describing the Gaussian heat flux

gcc coefficient	*Welding current (A)*	*Welding voltage (V)*	*Gaussian Radius (m)*	*Process efficiency*
0.5	70	9	0.0015	0.68

Table 3.15: Other fluid and solid properties for the 304L material

Sulfur content (%wt	*Constant in surface tension gradient $[A_\gamma]$ (N/mK)*	*Sulfur tension of pure metal $[\gamma_m]$ (N/m)*	*Standard heat of adsorption ΔH° $(J/kg.mole)$*	*Surface excess at saturation Γ_s $(Kg.mole/m^2)$*
0.003	3×10^{-4}	1.943	-1.66×10^8	1.3×10^{-8}

3.5.2 Effect of Material properties

A variation of 5% was made on the constant thermophysical properties in order to study the dependency of each parameters on the different weld characteristics such as temperature evolution, weld pool velocities, weld pool width and depth. The material properties

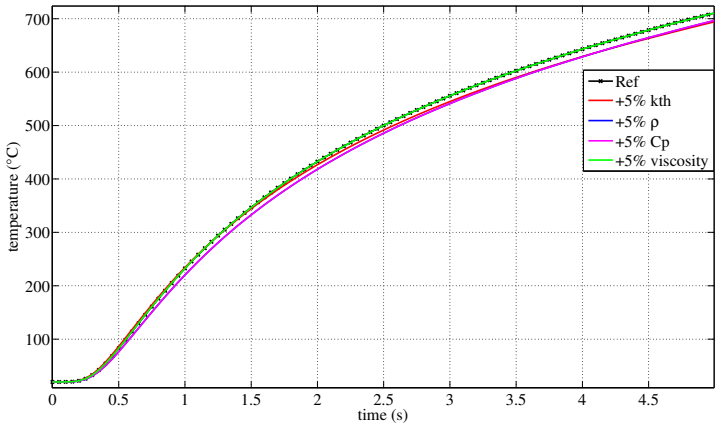

Figure 3.38: Variation of temperature history at center back surface of the disc for a 5% variation in material properties

that are taken into account for the parametric analysis are thermal conductivity (k_{th}), density (ρ), specific heat C_p and viscosity.

Figure 3.38 shows the temperature history at a point on the center back surface of the disc. This point was chosen as it is easily recorded with a thermocouple. A 5% variation in the material properties didn't make any noticeable change in the temperature distribution at the center back surface of the disc. A decrease in the peak temperature about $10°C - 20°C$ is observed for the change in thermal conductivity, specific heat and density values. This temperature variation is less than 2% and can be considered as negligible.

Figure 3.39 shows the variation of resultant velocity distribution along the top surface for a 5% variation in the material property. Velocity distribution also didn't show any major noticeable difference from the reference numerical simulation data except for thermal conductivity at the edge of the weld pool the velocity distribution is slightly lower than the reference model. This is due to the increase in thermal conductivity that increases the conduction through the material that traduces by a decrease of weld pool size.

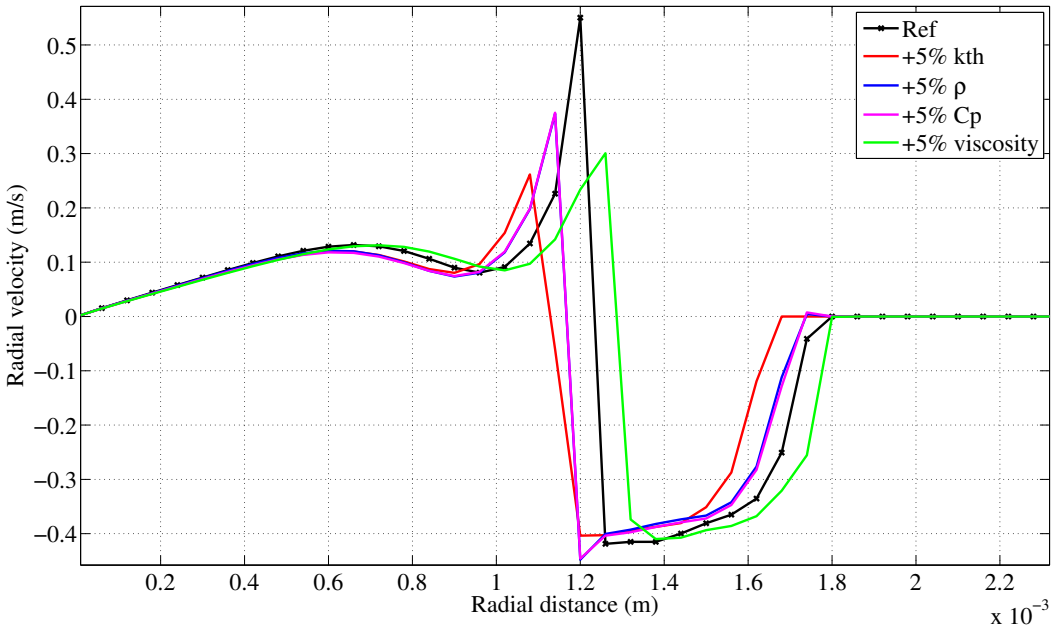

Figure 3.39: Variation of resultant velocity along the top surface at the end of arc heating (5 s) for a 5% variation in material properties

Figure 3.40(a) and 3.40(b) shows the weld pool depth and width variation respectively during the arc heating. The specific heat change is giving a maximum variation in the weld pool depth which is of 20% less compared to the reference model. From the basic definition of specific heat, it is the energy required for increasing the temperature of a 1Kg material by 1 °C. So the 5% increase in specific heat means that more heating is required to get the same reference weld pool. As the heating is identical to the reference case, the current weld pool is smaller in depth but also in volume. So specific heat is found to be more sensitive to the weld pool penetration. The density is also giving a 12% decrease in the weld pool depth. While thermal conductivity and the viscosity values are giving

a 5% decrease in the weld pool depth value. The weld pool width is hardly affected by the variation in most of the material properties. A variation near to 2% in the weld pool width is observed for the changes in thermal conductivity, density and specific heat.

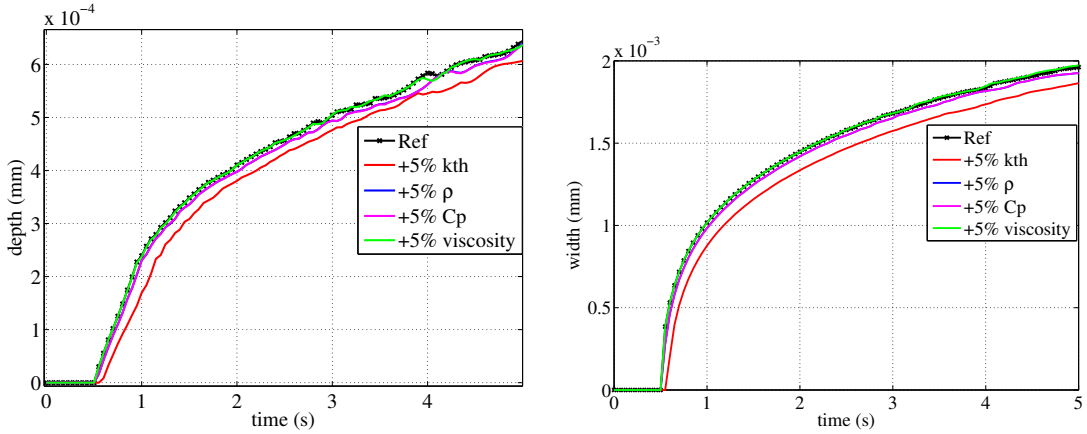

(a) Variation of weld pool depth during the arc heating

(b) Variation of weld pool width during the arc heating

Figure 3.40: Evolution of weld pool size for a 5% variation in material properties

3.5.3 Effect of heat flux parameters

This study investigates the effect of a small variation of the efficiency and Gaussian distribution parameters on the simulation results (temperature, fluid velocity and weld pool dimensions). Figure 3.41 shows the temperature evolution at the center back point of

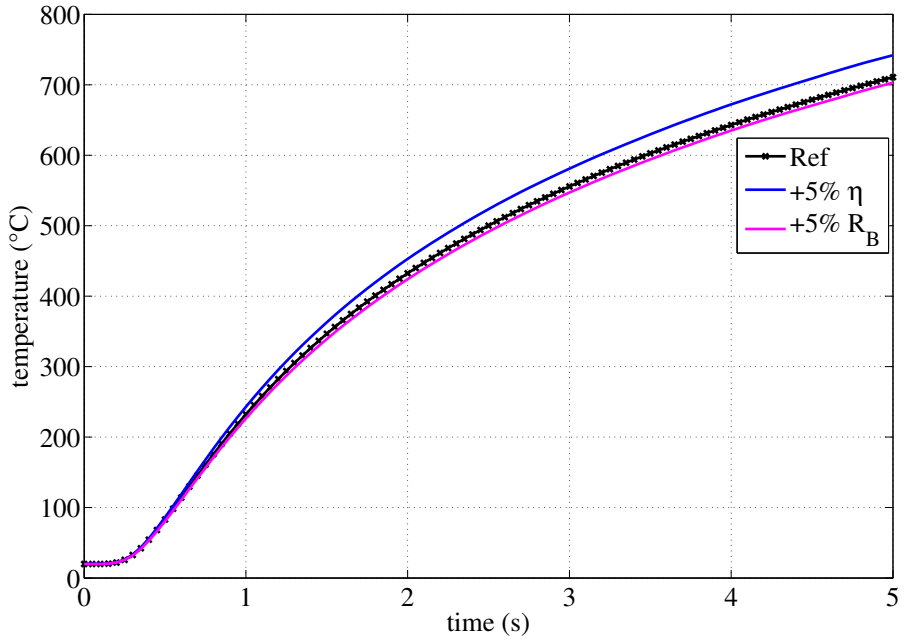

Figure 3.41: Variation of temperature history at center back surface of the disc for 5% variation in the different heat flux parameters

the disc for a variation of +5% from the reference heat source parameters. The efficiency

variation resulted in 32°C difference in maximum temperature, which is about 4.5% difference from the reference simulation. The increase in efficiency resulted in the supply of more energy to the workpiece and this is why we observed a temperature rise compared to the reference simulation. On the other hand increased Gaussian base radius resulted in a more distributed energy input to the system and caused a decrease in temperature, about 7°C.

Figure 3.42 shows the radial surface velocity distribution at the end of the arc heating for a +5% variation in the heat source parameters from the reference values. In the case of +5% increase in efficiency, a decrease in the maximum positive velocity (movement of fluid from center of the weld pool to the edge- clockwise) is observed with a slight increase in the negative velocity (flow from edge to center- counterclockwise). The increased energy into the weld pool resulted in the shifting of critical temperature position, that means the position where the flow reversal occurs (v_{radial}=0). An increase in the final weld pool width can be observed. The increase of +5% gaussian base radius leads to spreading of energy and reduction in the maximum positive velocity. Conversely, the spreading of energy resulted in the low temperature gradient along the surface and shifting of the critical temperature position towards the center and a reduced weld pool width. Figure

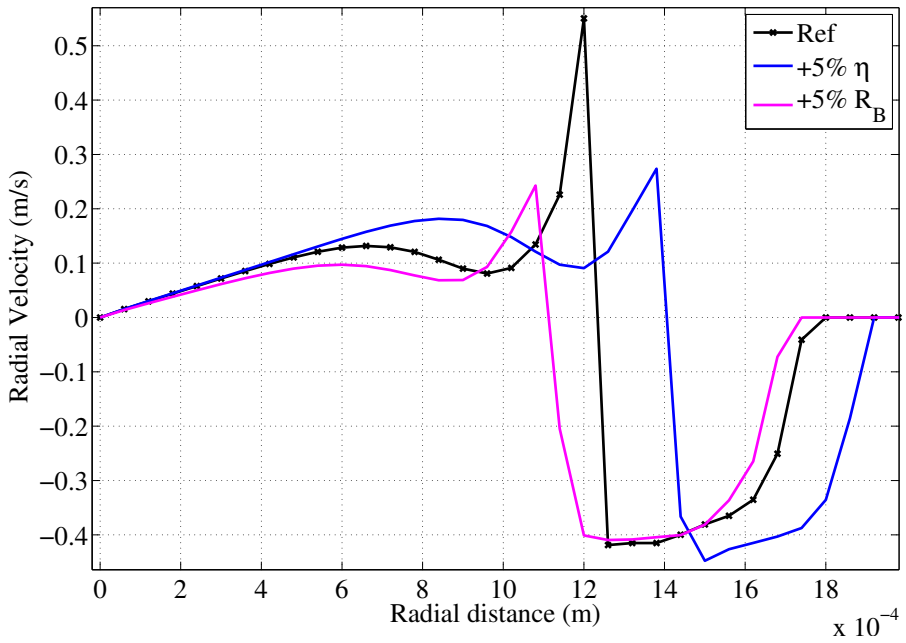

Figure 3.42: Variation of resultant velocity along the top surface for 5% *variation in the different heat flux parameters*

3.43(a) shows the weld pool depth evolution during the static heating at the center of the disc for a +5% variation in the heat source parameters from the reference data. An increase of about 5% in the weld pool depth is resulted for the +5% increase in efficiency. Similarly for the +5% increase in Gaussian base radius resulted in 5% reduction in the weld pool depth. Figure 3.43(b) shows the weld pool width evolution during the static arc heating for a +5% variation in the heat source parameters from the reference value. The weld pool width is increased by 7% for a +5% increase in the efficiency value. In the case of +5% increase in the gaussian base radius led to 2.5% reduction in weld pool

width compared to the reference simulation.

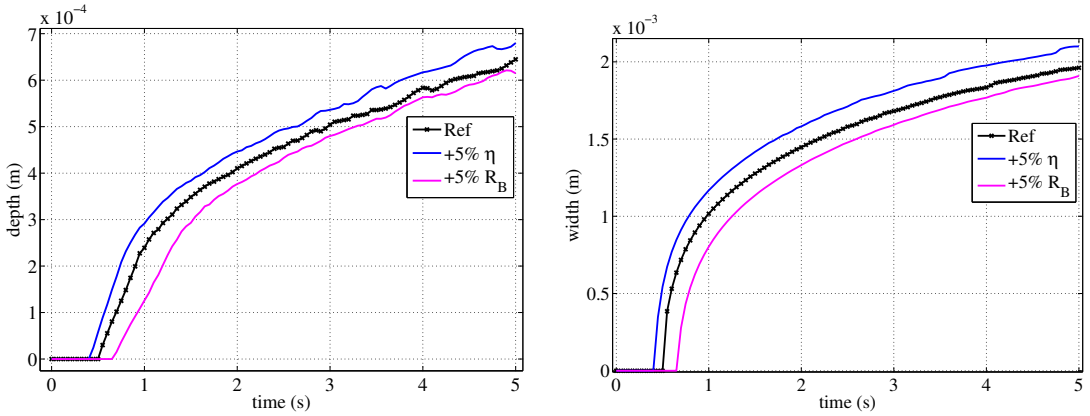

(a) Variation of weld pool depth during the arc heating

(b) Variation of weld pool width during the arc heating

Figure 3.43: Evolution of weld pool size for 5% variation in the different heat flux parameters

3.5.4 Effect of temperature dependent properties

The aim of this section is to validate or not validate the assumption of temperature constant thermophysical material properties. Here the reference simulation was obtained with temperature constant mass density, thermal conductivity and specific heat. A simulation considering these three material properties as temperature dependent is done. Figure 3.44 shows the variation in the temperature history at the bottom center of the disc for the two cases. In this figure, it is clearly noticeable that temperature dependent thermophysical properties led to increase temperatures (about 92°C) which is about 12% higher and the temperature dynamic is also higher in comparison to the reference temperature. Figure

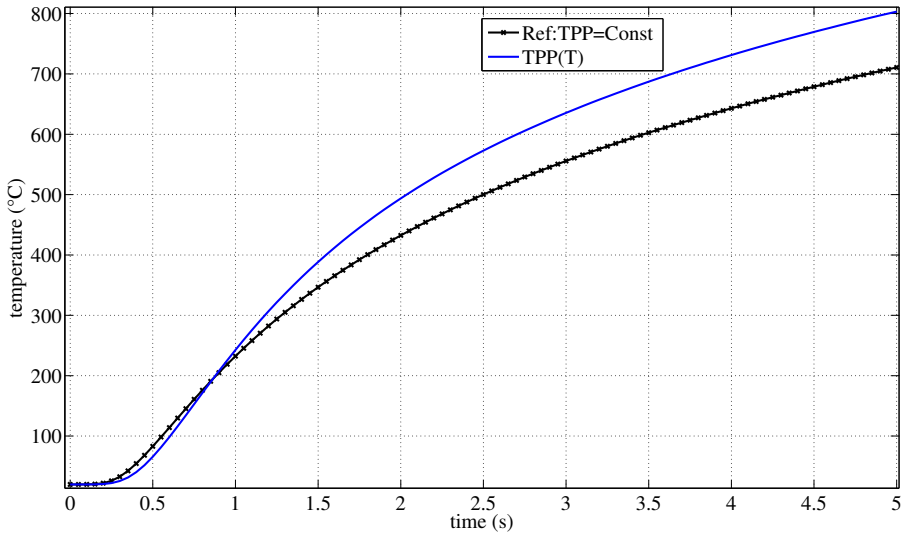

Figure 3.44: Variation of temperature history at center back surface of the disc when considering the temperature dependent thermophysical properties

3.45 shows the velocity distribution on the top surface of the weld pool for the above men-

tioned test cases. The effect of the temperature dependent thermophysical properties is important on the fluid velocity field. A decrease of 50% of the positive radial velocity and 15% negative radial velocity were observed. The position where the critical temperature occurs is also affected by the temperature dependent thermophysical properties. A slight reduction in the weld pool width is also occured. Figure 3.46(a) shows variation in the

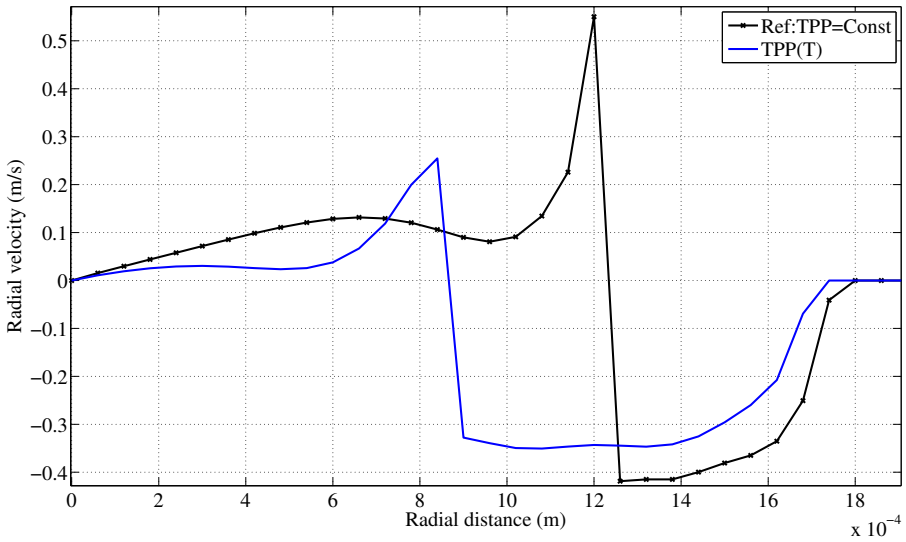

Figure 3.45: Variation of resultant velocity along the top surface when considering the temperature dependent thermophysical properties

evolution of weld pool depth at the disc center during the arc heating for the two cases. The use of temperature dependent thermophysical properties resulted in an increase of about 30% of the weld pool penetration. Figure 3.46(b) shows the variation of weld pool width evolution during the static arc heating for the two cases. A negligible (about 1%) in width is occurred.

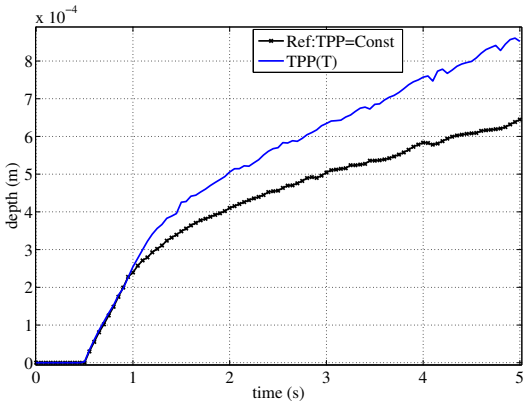

(a) Variation of weld pool depth during the arc heating

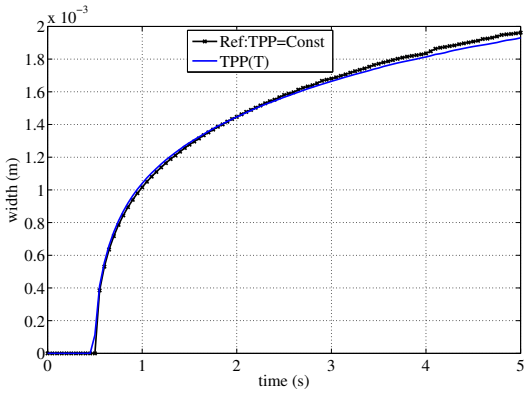

(b) Variation of weld pool width during the arc heating

Figure 3.46: Evolution of weld pool size when considering the temperature dependent thermophysical properties

3.5.5 Summary of parametric analysis

From the material properties investigation, it appears that the specific heat and mass density affects strongly the penetration. Actually an increase in these parameters leads to a slight decrease of the weld pool size (or volume) as more energy is required to melt the material (specific heat and mass density have been increased).
From the heat source parameter investigation, it is very clear from the results that all the simulation results has a great influence on the very small changes in the efficiency and the Gaussian base radius. Among the two efficiency playing a major role, this is mainly because efficiency directly reducing the energy input while Gaussian base radius affecting the distribution of the energy. Effect on temperature field, velocity field and weld pool width are moderated in comparison to the effect on the penetration.
The last investigation showed that it is compulsory to use the temperature dependent thermophysical properties in order to get reliable GTAW thermoconvective simulations. So the problem is to get accurate values for these thermophysical properties especially for such high temperatures.

3.6 Validation of transient magneto thermo hydrodynamic model

In order to validate the numerical simulations a comparison has been carried out with the experimentally measured data. The comparison is based on the three measured parameters from experiment such as transient temperature evolution at the bottom of the welded disc at different locations (see table 3.16), the transient evolution of the weld pool radius (measured using high speed camera) and the final weld pool shape (measured using the cross sectional postmortem of the welded sample) see chapter 2. The welding parameters used for the simulation are given in table 3.6.

3.6.1 Evolution of temperature

Figure 3.47 presents the comparison between experimentally measured and calculated temperature history at five locations on the disc bottom surface. The measurement locations were already discussed in chapter 2 and is summarized in table 3.16. The error bars are also added to the experimental measurements in order to consider the error due to measurement location in a 0.5 mm drilled hole. These error values were estimated from the spatial thermal gradients between thermocouples which is calculated and presented in table 2.4 of chapter 2.

Table 3.16: Measurement Locations of the temperature sensors

	TC1	*TC2*	*TC3*	*TC4*	*TC5*
radius (mm)	0.3	3.7	4.3	7.7	8.3
height (mm)	0.5	0.5	0.5	0.5	0.5

As seen from figure 3.47, the temperature profile TC1 which is located close to the weld pool is showing similar trend as that of experiment but are not matching with the experimental measurements. The maximum temperature reached during the simulation

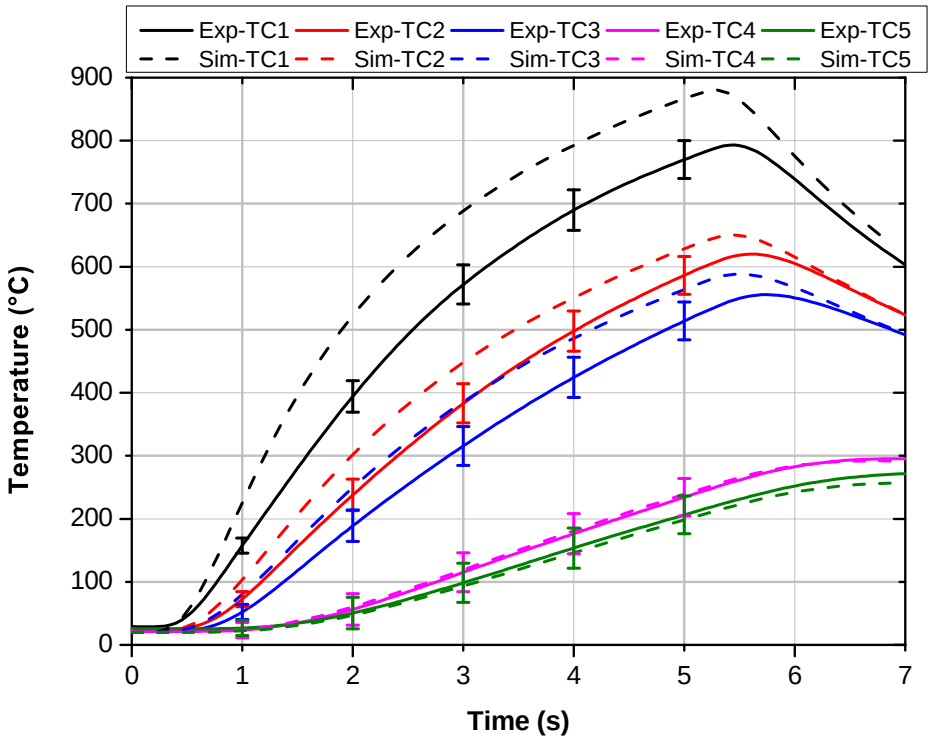

Figure 3.47: Comparison of experimentally measured temperature history with simulation for 70 A current case

at TC1 is 880°C which is of about 109°C higher than that of the corresponding experimental measurement. Similarly, the difference is calculated for the TC2 and TC3 are respectively 30°C and 33°C. The maximum temperatures are less well predicted in case of thermocouples TC1, TC2 and TC3. But for thermocouples TC4 and TC5 the maximum reached temperatures are well predicted. This comparison shows that the trend of heating rate (slope of the curve during the heating phase) is well predicted by the numerical model. This indicate the validity of the assumed heat flux distribution with some minor corrections needed to get good comparison. The discrepancy in the heating rate is believed to be attributed to four different errors. Those are numerical errors (mesh densities), temperature dependent thermophysical material properties chosen for the stainless steel material (different values observed in other literature), errors corresponding to the experimental temperature measurement (uncertainties related to the thermocouple position and the disturbances caused by the drilled hole in heat propagation) and prescribed surface heat flux parameters. Besides the first two errors, the main source of explanation could be experimental errors and the assumed parameters in the heat flux distribution such as efficiency (η) and Gaussian base radius (r_H), which is detailed later in chapter 4. The experimental error corresponds to the uncertainty due to thermocouple positioning is taken into account by the temperature gradient corrections as discussed in chapter 2 and is added to the data as stated before and shown in figure 3.47. The cooling rates (slopes of the curve during the cooling phase) for the first three thermal sensor's (TC1, TC2 and TC3) were calculated at the end of 7 s, and are respectively 28°C/s, 10°C/s and 18°C/s higher than that of the corresponding experimental cooling rates. This variation in cooling rates corresponds to the over estimation of energy losses from the boundary and also

it could be related to the first two errors mentioned in the case of heating discrepancy.

3.6.2 Evolution of Weld pool radius

Figure 3.48 shows the comparison of time varying diameter from high speed camera measurement and the simulation predictions. It is remarkable to see that the experimental weld pool predictions are well matching with the predicted values. The initial growth rate is well picked up by the simulation model. But initial stages of the gradually developing second region is over predicted slightly by the numerical model. The simulation results show a gradual increase in the weld pool diameter and it is closely matching to the experimental results at the later times. An identical match is observed in the overall trend of the spreading behavior. At the starting of the weld pool it is difficult to measure the weld pool size from the high speed camera data due to the high arc illumination and it becomes difficult to differentiate between the arc boundary and the weld pool boundary. Also the effect of the lift arc method is not completely modeled in the simulation that is the high concentration of the current density distribution. This is the reason for the mis-predictions of weld pool size observed in the initial times.

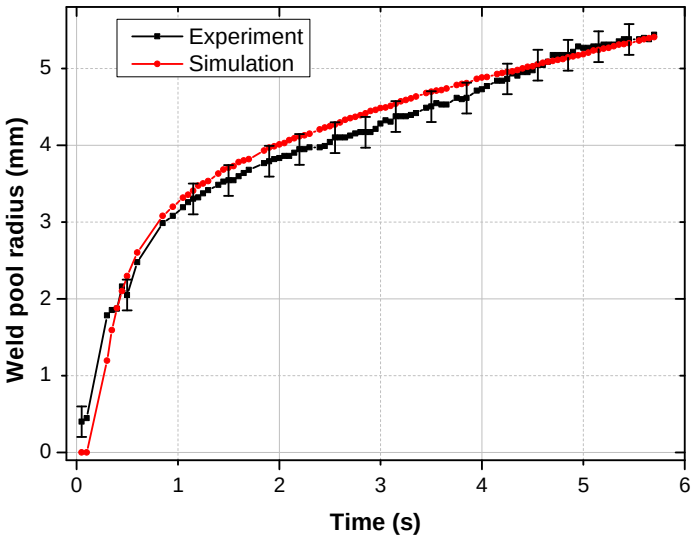

Figure 3.48: Weld pool diameter evolution comparison of experimental and simulation data for 150 A current

3.6.3 Weld pool size

Figure 3.49 shows the weld pool shape comparison between the experimental macrograph and the numerical simulations for the three energy inputs. The macrograph represents the shape of the weld pool for a static electrical arc duration of 5 s. Globally, a satisfying agreement is obtained for all the studied cases. Particularly for the 70 A case the weld pool penetration is almost similar to the experimental data with a negligible difference. But the calculated width is showing a difference of 0.23 mm less from the experimental results. In case of 110 A case, the calculated depth of penetration is showing very less

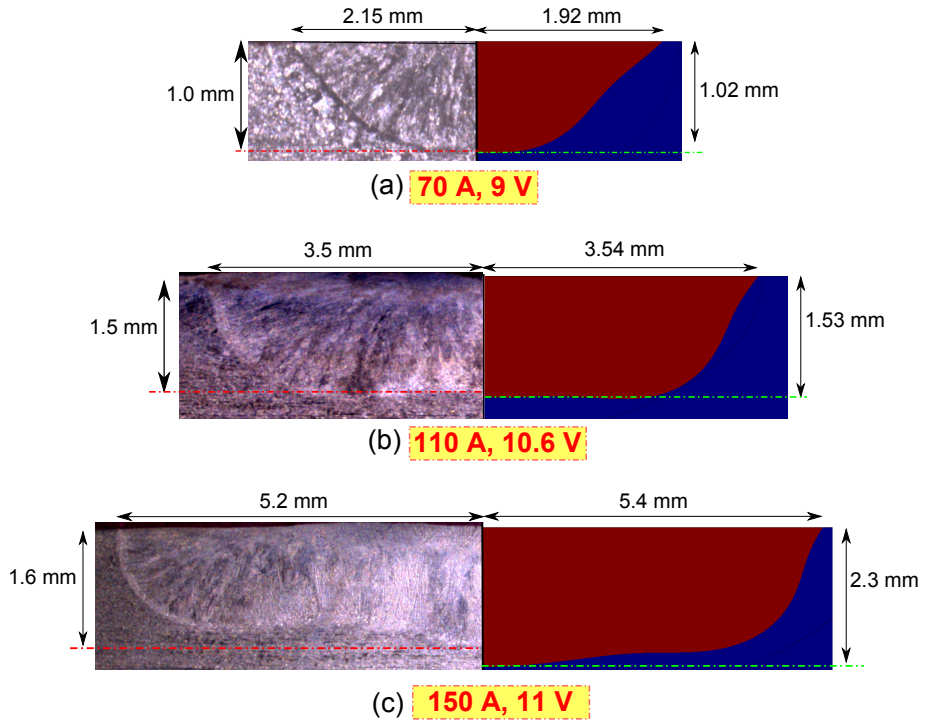

Figure 3.49: Comparison of weld pool size at the end of static arc heating for the three cases; 70 A, 110 A, and 150 A

deviation from the experimental value. The calculated width is slightly higher in this case by 0.04 mm. In the experimental case, the maximum penetration occurred at a location away from the symmetry axis. Simulation also shows the similar behavior. It should be noted that these discrepancies can be reduced either by modeling the arc plasma or by adjusting the Gaussian heat source parameters in the prescribed heat flux distribution (Which is carried out in the next chapter).

Figure 3.50 shows the comparison of weld pool size and shape between the calculated and experimental results for two stainless steel 304L samples having different sulfur concentrations (26 ppm and 36 ppm). The simulation results show good agreement with the measured weld pool width and depth. The quantitative assessment of the weld pool dimensions are presented in table 3.17.

Table 3.17: Comparison between experimentally measured and numerically calculated weld pool dimensions

Material and Process parameters	*Weld pool depth (mm)*		*Weld pool half width (mm)*	
	Experimental	*Numerical*	*Experimental*	*Numerical*
AISI 304L, 70A, 9V, Low sulfur	1.0 ± 0.2	1.02	2.0 ± 0.15	1.92
AISI 304L, 70A, 9V, High sulfur	1.4 ± 0.1	1.37	2.0 ± 0.1	2.0
AISI 304L, 110A, 10.6V	1.5 ± 0.1	1.53	3.4 ± 0.1	3.54
AISI 304L, 150A, 9V	1.5 ± 0.1	2.3	5.2 ± 0.1	5.4

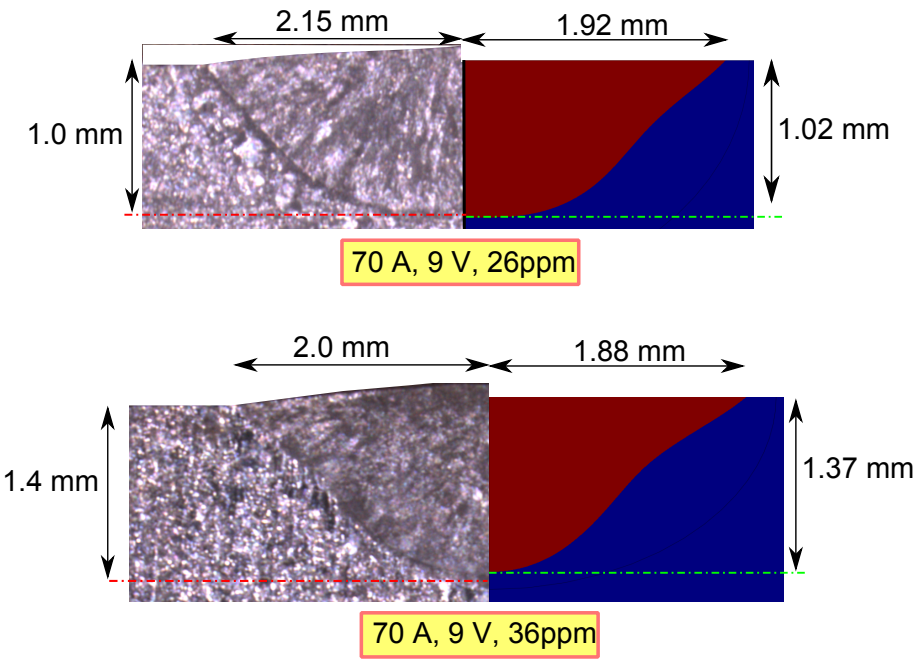

Figure 3.50: Comparison of weld pool size at the end of static arc heating for high and low sulfur content samples

3.7 Conclusion

In this chapter, the numerical simulation of the static GTAW process is studied using a heat conduction and magneto-thermo-hydrodynamic (MTHD) models. First a simple heat conduction model is used with prescribed surface Gaussian heat flux. The second model solves heat transfer, fluid flow and electromagnetic fields in transient mode by assuming the surface heat and current density distribution. The temperature cycles, velocity fields and weld pool width and depth were quantitatively calculated using the MTHD model. A parametric study is carried out to identify the major influencing parameters in the numerical model. The numerical simulations were validated using the experimentally observed temperature history, transient weld pool evolution and weld pool macrographs. Following are the major conclusion from the investigation.

(a) The heat conduction model developed is able to predict the temperature cycles in welding process. The heat conduction model always produces the classical hemispherical weld pool which is not the case for stainless steel 304L material containing minor alloying element such as sulfur. However, the heat conduction model is useful in determining the thermal gradient in and around the weld zone and HAZ. Also the calculated approximate information on the weld pool size were used later in the MTHD simulation to define the pseudo fluid domain.

(b) The magneto-thermo-hydrodynamic model is able to predict the temperature and velocity field in the weld pool. The simulation results were able to present the transient temperature, velocity and weld pool evolution. The simulation results were also able to predict the double vortex velocity loop formed due to the Marangoni effect by considering the temperature gradient of surface tension as a function of both temperature and sulfur content.

(c) The convection is identified as the dominant mechanism of heat transfer in the weld pool compared to conduction. However at low current such as 70 A, the conduction model is able to predict the weld pool depth and width with reasonable accuracy for low sulfur content samples. But for high sulfur content sample heat conduction under predict the weld pool depth. But for both cases the final weld pool shape is mis-predicted by heat conduction model. In this chapter, we also carried out some dimensionless analysis using Peclet number to identify the effect of convective heat transfer. This study shows that the convection is more dominant transfer mode for high sulfur content steel than low sulfur content steel for the same amount of input energy.

(d) A study is carried out to identify the dominant forces in the weld pool convection. The calculated maximum velocities are 0.046, 0.117, 36.67, and 7.28 cm/s for buoyancy, Lorentz, Marangoni and arc drag force respectively for 70 A and 9 V static arc. The Marangoni force is identified as dominant force at low currents (70 A). The arc drag force is identified as playing a major role in the fluid flow at higher currents (110 A and 150 A) giving maximum values respectively 52 and 58.19 cm/s. The obtained fluid velocities for each forces are comparable with the previous studies.

(e) Simulation results for constant temperature coefficient of surface tension ($\partial\gamma/\partial T$) explains the occurrence of a clockwise flow when $\partial\gamma/\partial T < 0$ resulting in a wider and shallow weld pool. Where as for $\partial\gamma/\partial T > 0$ a counterclockwise flow is created and produces deeper and narrow weld pool. When $\partial\gamma/\partial T$ is considered as both dependent on temperature and sulfur concentration, which resulted in a unusual wavy weld pool boundary for low sulfur sample with a double vortex loop formed with maximum penetration occurring at radius other than the weld pool center. However, for high sulfur case produced a much deeper weld pool with a anticlockwise flow with similar width as that of low sulfur sample.

(f) From the parametric study, the thermal conductivity and specific heat are identified as the major influencing material properties on the temperature cycle, velocity fields and the weld pool dimensions. Moreover the heat flux parameters such as arc efficiency and Gaussian base radius are also exhibit significant influence on the final weld pool shape. Additionally parametric study concluded that the thermophysical properties should be considered as temperature dependent because of its major influence in the final weld pool characteristics.

(g) In the case of welding currents of 70 A and 110 A, the calculated results were relatively consistent with experimental results. For welding current 150 A, the experimental results showed a wider weld pool shape than the calculated one.

From the experimental measurements (EPMA) and the available literature data we hope that the thermophysical parameters and the surface tension parameters are well defined. So the question is how to estimate the Gaussian heat flux parameters correctly. In next chapter an inverse heat transfer problem is defined in order to estimate the efficiency and Gaussian base radius by comparing the simulation results and the experimentally observed results.

Chapter 4

Estimation of heat flux parameters

Contents

4.1 Introduction

In the previous chapter, the comparison between measured and calculated temperatures exhibited some differences. These differences are mainly due to the values used for the efficiency and Gaussian radius in the simulations and also the experimental measurement errors. Inverse heat conduction problem represents an alternative approach for estimating the efficiency and Gaussian radius. This methodology is justified when temperature

measurements in vicinity of the weld pool area are impossible. As it has been explained in chapter 2, temperature measurements are difficult to record due to the severe welding conditions. It is very difficult to measure the temperature into the pool with a thermocouple or close to it (e.g. electrical phenomena, high radiation...). However, temperature measurements must be done in relevant thermal zone of the work piece e.g. in the Heat Affected Zone (HAZ) closer to the Fusion Zone (FZ) in order to estimate accurately the heat flux parameters [117]. Many other authors have dealt with inverse heat transfer problems in welding in the last decades [51, 108, 118, 119].

Then, this chapter is dedicated to the estimation of GTAW efficiency and Gaussian radius (model's parameter of the heat flux due to the arc plasma and absorbed by the metal work-piece). This chapter is divided in 5 sections. The first part is a general introduction to inverse heat transfer problems where some keywords are defined such as direct heat transfer problem (or direct problem). Then the inverse heat transfer problem under consideration is stated. The iterative regularization technique used for solving the stated inverse problem is presented. The fourth section entitled "sensitivity analysis" investigates the feasibility to estimate the unknown parameters. The last section deals with the resolution of the stated inverse heat transfer problem through numerical test cases before using experimental data.

4.2 Generalities about Inverse heat transfer problem

In what follows, the generalities will be based on heat conduction problem only in order to simplify the discussion.

4.2.1 Direct Heat Transfer Problem (DHTP) definition

Heat conduction problem is often modeled with a system of partial differential equations (PDEs) which can be linear or not. In what follows, the heat conduction problem is assumed non linear (because a welding operation involves fusion of the material over a wide range of temperature). The thermophysical properties of the material are considered temperature dependent in the present case.

The heat conduction equation (or energy governing equation) for an immobile rigid body with no internal heat source, see figure 4.1, can be expressed as follows: (with the domain $\Omega \in R^3$ (3D Cartesian coordinates) and the time variable $t \in I$):

$$C(T)\frac{\partial T}{\partial t} - \nabla \cdot (k(T)\nabla T) = 0 \;\; in \;\; \Omega \times I \tag{4.1}$$

with $T = T(x,t)$,$C(T) = \rho(T) \cdot C_p(T)$ is the product of mass density with specific heat, $k(T)$ is the thermal conductivity. An initial condition is associated to the heat conduction equation 4.1:

$$T(x, t = 0) = T_0(x) \;\; in \;\; \Omega \tag{4.2}$$

Conditions are required on the domain's boundary denoted as $\Gamma = \Gamma_1 \cup \Gamma_2$, see figure 4.1. These boundary conditions can be of different types:

- Dirichlet condition: $T(x,t)=T_{imposed}$ on $\Gamma_1 \times I$

- Non homogenous Neuman condition:

$$-k(T)\frac{\partial T}{\partial n_2} = -h(T)(T-T_{room})-\epsilon(T)\sigma(T^4-T_{room}^4)+Q(T,x,t)+g(T,x,t) \quad on \quad \Gamma_2 \times I \tag{4.3}$$

With h(T) is the convective heat transfer coefficient, T_{room} is the surrounding temperature, ϵ(T) is the emissivity coefficient, σ is the Stefan-Boltzmann constant, Q is an incident heat flux and g is a surface heat source.

These equations 4.1 to 4.3 can be completed with an observation equation which is, for example, temperature measurements at points x_i= 1,...,n_s with n_s is the total number of sensors: $Y_{meas}(t) = T(x=x_i,t)$. The direct heat transfer problem (DHTP) consists in

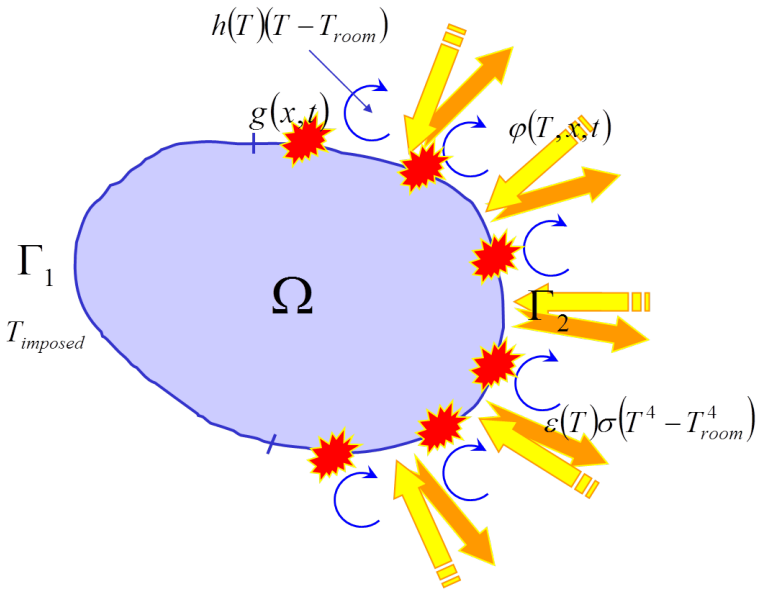

Figure 4.1: Considered heat conduction problem with different heat transfer exchanges

solving equations 4.1 to 4.3 in order to get the temperature field in the domain Ω for any time t. The DHTP can be solved only if all the model's parameters (thermophysical properties, boundary conditions...) are known. If one or more parameters are unknown, the observation equation can be used to estimate the unknown parameter(s). This method is called Inverse Heat Transfer Problem (IHTP). The resolution of the IHTP leads to the estimation of the unknown parameter(s). Then the estimated parameter(s) are used in the DHTP in order to give to the mathematical model its predictive function.

4.2.2 Inverse Heat Transfer Problem (IHTP) definition

Let's $Y_{meas}(x_i, t_j)$, i=1, n_S, j= 1, n_I the measured temperatures at n_S sensors and n_I times. Let's be $\overline{p}$ = p_1, p_2, ..., p_u the unknown vector of parameters to estimate. The Inverse Heat Transfer Problem formulation is:
Find the unknown $\overline{p} \in$ P such as the calculated temperatures of the DHTP match the measured temperatures of the investigated physical processes:

$$T_{cal}(x = x_i, t = t_j, p) = Y_{meas}(x_i, t_j), i = 1, n_S, j = 1, n_I \tag{4.4}$$

The IHTP is difficult to solve under this form. A criterion must be defined in order to minimize it and to get the unknown $\overline{p}$. So a quadratic criterion is defined (or least squares method). Quadratic criterion are often better to minimize especially when the inverse technique is based on the computation of the criterion gradient. So, it comes the second formulation of the IHTP in least squares sense:

Find the unknown function $\overline{p} \in \mathrm{P}$ that minimizes the following objective function (or also called cost function or criterion function):

$$J(T,P) = \frac{1}{2} \int_T \int_\Omega \sum_{i=1}^{n_S} \left[T_{cal}(x,t,p) - Y_{meas}(x,t)\right]^2 \delta(x - x_i)\, d\Omega\, dt \tag{4.5}$$

where $\delta(.)$ is the Dirac function. The coefficient 1/2 is merely added to simplify the computation of the criterion gradient. The space definition P depends of the nature of the parameter(s) to estimate.

4.2.3 Classification of inverse heat transfer problems

The IHTP can be classified in four classes according to Alifanov [120]:

- IHTP dedicated to the estimation of the initial temperature field or at a given time within the domain [121, 122]. These IHTP are often called "inverse backwards heat conduction problems". These problems are often investigated in aeronautics [121] or for the estimation of temperature field in a flow [123, 124].
- The IHTP dedicated to the estimation of boundary conditions only. It consists in estimating a heat flux applied on a surface as a function of time and / or space [125, 126] or the estimation of heat transfer coefficient during a casting operation between the casting / mold interface [127].
- The IHTP dedicated to the estimation of volumic parameters such as material characteristics (thermal conductivity and specific heat) [128–131] or heat source terms [132–134].
- IHTP of design. These problems are of great interests in casting process for controlling the cooling rate and the solid / liquid interface [51, 135, 136].

4.2.4 Regularization techniques

Despite the formulation of the IHTP in least squares sense, the solution is neither unique nor stable. Hadamard proposed in 1902 the definition of a well posed problem and therefore an ill posed problem by the way [137]. In general, an inverse problem can be written as follows: $Au = f$, $u \in U$,$f \in F$ with u is the vector of unknown parameters and f are the measured data which belongs to the respective normed spaces U and F. The Operand $A : U \to F$ is assumed to be defined within the domain $D(A) \subseteq U$ with value in $R(A) \subseteq F$. So the problem $Au = f$ is well posed in Hadamard sense if and only if:

- Whatever $f \in R(A) = F$, it exists one solution $u \in U$ (existence)
- The solution is unique in U (uniqueness)

- The solution depends continuously on f (stability).

If one of these three conditions is not verified then the problem $Au = f$ is said ill-posed. It is often the case of inverse heat transfer problems. IHTP are ill-posed especially due to the measurement errors which can disturb the solution and lead to several solutions. In order to attenuate the sensibility of the solution with regards to the measurement errors, model errors and numerical errors, it is required to use a regularization technique. The most used regularization techniques in IHTP are the Tikhonov regularization [138], the singular value decomposition regularization, the Beck's specification method [139, 140] and the iterative regularization methods [141] based on the computation of criterion gradient.

4.2.4.1 Tikhonov's regularization

This technique [138] consists in adding a penalization term to the quadratic criterion as follows:

$$J(U, R, \mu) = \|AU - f\|^2 + \mu \|R_n U\|^2 \tag{4.6}$$

Associated to the matricial system $Au = f$ with A is a matrix, U is the temperature vector and f is the measurement vector. μ is the regularization parameter and R_n is a regularization matrix. The main difficulties are the choice of the regularisation parameter. If its value is important, the penalization term $\|R_n U\|^2$ will be predominant and the estimated solution will have a bias. If its value is small, the solution will be still unstable. Gejadze et al. will be predominant and the estimated solution will have a bias. If its value is small, the solution will be still unstable. Gejadze *et. al.* [123] proposed a method for chosing the regularization parameter.

4.2.4.2 Singular Value Decomposition (SVD) regularization

The SVD regularization consist in decomposing a matrix A_{nm} into three matrices U_{nn} and V_{mm} and W_{nm}. The SVD regularization consists in decomposing a matrix: W is a diagonal matrix built with the singular values w_i while U and V are orthogonal matrices. The inverse of the matrix A can be easily obtained from the following formula: $A = UWV^T \Rightarrow A^{-1} = UW^{-1}U^T$. As a consequence, the solution of the matrix system: $Ax = f$, the solution x is: $x = A^{-1}f = VW^{-1}U^T f$ or $x = \sum_{i=1}^{min(n,m)} \frac{\{u_i\}\{f_i\}}{w_i} \{v_i\}$ with $\{u_i\}$ and $\{v_i\}$ are respectively the vector of the orthogonal base for the matrices U and V. The solution x is dominated by the small w_i terms when the numerator values are not small. The regularization technique consists in choosing a truncation order for the values of the previous inversion: $x = \sum_{i=1}^{n_T} \frac{\{u_i\}\{f_i\}}{w_i} \{v_i\}$. n_T is the truncation order. The difficulty of this method resides in the choice of this parameter as the stability relies on it. The SVD regularization is only used for linear problems whatever is the space dimension.

4.2.4.3 Beck's specification function

Beck *et. al.* [140] developed this method for the estimation of heat flux or surface temperature in aeronautics applications. Lefévre *et. al.* used this approach for the simultaneous estimation of power and position of a heat source [133]. The unknown parameters are estimated sequentially at each step time by using some future values. The minimized quadratic criterion is written as follows:

$$J(T, p^{k+1}) = \frac{1}{2} \sum_{i=1}^{n_S} \sum_{j=0}^{r} \left[T_i^{k+j}(p^{k+1}) - Y_i^{k+j} \right]^2 \tag{4.7}$$

With r the number of future steps. The function specification consists in decomposing p on function basis according to the time. The minimization of $J(T, p^{k+1})$ means that $\partial J(T, p^{k+1})/\partial p^{p+1} = 0$. The derivative of the criterion comes:

$$\sum_{i=1}^{n_S} \sum_{j=0}^{r} \left[T_i^{k+j}(p^{k+1}) - Y_i^{k+j} \right] \frac{\partial T_i^{k+j}(p^{k+1})}{\partial p^{k+1}} = 0 \tag{4.8}$$

As the function p^{k+1} is not known, a first order Taylor expansion is made:

$$T_i^{k+j}(p^{k+1}) = T_i^{k+j}(p^k) + \frac{\partial T_i^{k+j}(p^{k+1})}{\partial p^{k+1}} \left(p^{k+1} - p^k \right) \tag{4.9}$$

The linearized expression of $T_i^{k+j}(p^{k+1})$ is replaced in the criterion gradient equations in order to establish the next expression in order to get the computation of the new estimated parameter p^{k+1}:

$$p^{k+1} = p^k + \frac{\sum_{i=1}^{n_S} \sum_{j=0}^{r} \left[T_i^{k+j}(p^{k+1}) - Y_i^{k+j} \right] \frac{\partial T_i^{k+j}(p^{k+1})}{\partial p^{k+1}}}{\sum_{i=1}^{n_S} \sum_{j=0}^{r} \left[\frac{\partial T_i^{k+j}(p^{k+1})}{\partial p^{k+1}} \right]^2} \tag{4.10}$$

The major difficulty of this technique resides in the choice of the parameter r for the number of future steps to take into account. If this parameter is too small or too large, the solution is unstable. This parameter is often set manually after testing few values for r. Moreover, another term of spatial regularization (Tikhonov one) can be added introducing another difficulty.

4.2.4.4 Iterative Regularization Method (IRM)

Most of the iterative regularization methods are based on the computation of the gradient of the quadratic criterion with regards to each parameter to estimate. The iterative regularization method does not require a regularization term because the solution is implicitly regularized iteration after iteration. The "regularization parameter" is the number of iteration required before stopping the iterative process. This parameter depends generally of the measurement noise. The main difficulty resides in the computation of criterion gradient.

4.2.5 Initialization of the unknown parameters and stopping criterion

The four presented regularization techniques are not the only ones but the most used in the literature. Whatever the adopted regularization approach, the influence of the initial unknown parameters and the stopping criterion on the solution should always be investigated before solving the IHTP with experimental data. Generally speaking, few initialization values for $\overline{p}$ (describing the whole space of definition of $\overline{p}$) should be used to verify that the solution converges towards the same value.

A stopping criterion or threshold should be defined every time that an iterative regularization method is used. There are numerous stopping conditions. One of the easiest is to define the stopping criterion as the sum of the measurement noise over the time range

and the sensor number such as: $J(\hat{\overline{p}}) \leq n_S \times (\sum \sigma_i^2)_{i=1}^{n_I}$ with $y_S(t_i) = y_m(t_i, \hat{\overline{p}}) + b(t_i)$. As $y_S(t_i) \approx y_m(t_i, \hat{\overline{p}})$, $e_0(t_i, \hat{\overline{p}}) \approx b(t)$ where $b(t)$ is normal noise, of null mean and standard deviation $\sigma(t)$. Where i = 1,....,n_I. This stopping criterion requires to know the measurement noise.

Another criterion consist in comparing the previous quadratic criterion with the current one and define a small value η as stopping criterion: $J(\hat{\overline{p}}^{k+1}) - J(\hat{\overline{p}}^{k}) \leq \eta$. The last computed criterion must be inferior to the previous iteration as well. This criterion can be used when the measurement noise is not known.

4.3 The Inverse Heat Transfer Problem (IHTP) for the estimation of GTAW efficiency and Gaussian radius

In what follow the Gaussian radius R_B is chosen to vary linearly with time variable t. So :

$$R_B(t) = \frac{R_B(t_f) - R_B(t_0)}{\Delta t} \cdot t + R_B(t_0) \tag{4.11}$$

Finally the unknown vector $\overline{p} = \left\{\eta, R_B^{t_0}, R_B^{t_f}\right\}$. Hence 3 unknown parameters need to be estimated. It is assumed that the Gaussian radius is smaller at the beginning electric arc due to its stabilization (even if it is faster in comparison to the other investigated phenomena).

The formulation of the considered IHTP in least squares sense is as follows:

Find the unknown vector $\overline{p} = \left\{\eta, R_B^{t_0}, R_B^{t_f}\right\}$ which minimizes the objective function $S(\overline{p})$ defined as the quadratic difference between the calculated $T_{cal}(x, t, \overline{p})$ and measured $Y_{meas}(x_i, t)$ temperatures. The expression of the objective function is:

$$S(\overline{p}) = \frac{1}{2} \left[Y_i - T_i\right]^T W \left[Y_i - T_i\right] \quad or \tag{4.12a}$$

$$S(\overline{p}) = \frac{1}{2} \int_{t_0}^{t_f} \int_{\Omega} \sum_{i=1}^{n_S} \left[Y_{meas}(x_i, t) - T_{cal}(x_i, t; \overline{p})\right]^2 \, d\Omega \, dt \tag{4.12b}$$

with x_i the position of sensors, $i = 1, ..., n_S$.

The inverse heat transfer process can be represented as follows, see figure 4.2. The iterative regularization loop is represented in Grey color and the minimization technique is included in this loop. The Levenberg-Marquardt (LM) technique is used for the minimization of the stated objective function, equation 4.12b. The LM is well adapted to solve IHTP with few parameters to estimate and the defined objective function (quadratic criterion). Furthermore the method is not too complicate to program.

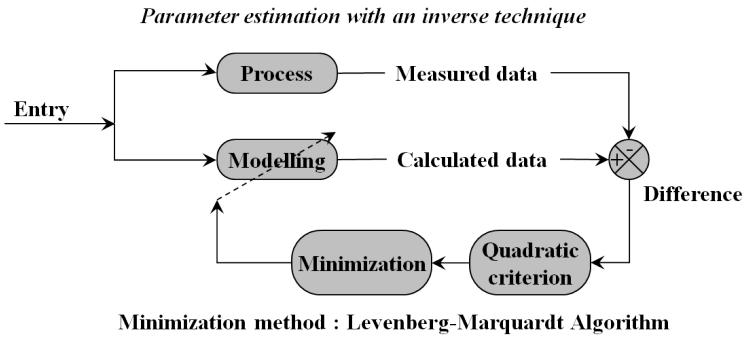

Figure 4.2: Representation of the parameter estimation

4.4 Minimization of the objective function with the Levenberg-Marquardt method

The minimization of the cost function $S(\overline{p})$ is obtained by equating to zero its derivatives with respect to the unknown parameters $\overline{p}$, so:

$$\frac{\partial S(\overline{p})}{\partial \overline{p}} = 0 \tag{4.13}$$

This condition can be represented in matrix format as follows:

$$\nabla S(\overline{p}) = 2\left[\frac{\partial T_i(\overline{p})}{\partial p}\right]^T [Y_i - T_i(\overline{p})] = 0, \quad i \in I \tag{4.14}$$

The term $\left[\frac{\partial T_i(\overline{p})}{\partial p}\right]^T$ is called transpose of sensitivity matrix $J(\overline{p})$. I is the total number of temporal measurements. The elements of the sensitivity matrix are named the sensitivity coefficients. The sensitivity coefficients are the first derivative of the estimated temperature at position x_i with respect to the unknown parameters $\overline{p} = \{\eta, R_{B1}, R_{B2}\}$. By using the definition of the sensitivity matrix in the equation 4.14, gives :

$$\nabla S(\overline{p}) = 2J^T(\overline{p})\,[Y_i - T_i(\overline{p})] = 0 \tag{4.15}$$

Let's develop the term $T(\overline{p})$ with a first order Taylor expansion around the current solution $\overline{p}^k$ at iteration k:

$$T(\overline{p}) = T(\overline{p}^k) + \frac{\partial T(\overline{p}^k)}{\partial \overline{p}}\left(\overline{p} - \overline{p}^k\right) = T(\overline{p}^k) + J^k\left(\overline{p} - \overline{p}^k\right) \tag{4.16}$$

with $T(\overline{p}^k)$ and $J^k = J(\overline{p}^k)$ are the estimated temperatures and the sensitivity matrix evaluated at iteration k respectively. Equation 4.16 is substituted into equation 4.15 in sort of the new parameters $\overline{p}^{k+1}$ is expressed from its previous value $\overline{p}^k$, sensitivity matrix J^k and output error $(T_i(\overline{p}^k) - Y_i)$:

$$\overline{p}^{k+1} = \overline{p}^k + \left[(J^k)^T J^k\right]^{-1}\left[(J^k)^T\left(T_i(\overline{p}^k) - Y_i\right)\right] \tag{4.17}$$

Furthermore the matrix $J^T J \approx 0$ is ill-conditioned especially around the initialization of parameters p^0. The Levenberg-Marquardt method alleviates such difficulties by adding a scalar parameter λ^k:

$$\overline{p}^{k+1} = \overline{p}^k + \left[(J^k)^T W J^k + \lambda^k \Omega^k\right]^{-1}\left[(J^k)^T W\left(T_i(\overline{p}^k) - Y_i\right)\right] \tag{4.18}$$

Ω^k is a diagonal matrix. The term $\lambda^k\Omega^k$ damps oscillations and instabilities due to the ill-conditioned character of the matrix. This parameter is large at the beginning of the iterative procedure (and the method is like the steepest descent method) then it decreases when the procedure advances to the solution (and the method tends to the Gauss method). W is a diagonal matrix which can be either equal to unity matrix or to the inverse of the standard deviation of the measurement errors if known.

The Levenberg-Marquardt algorithm is summarized below. Let's Y_i measured data at the following sensors location x_i, $i = 1, ..., n_S$. Let's choose an initial set of parameters $\overline{p}^0 = \{\eta^0, R^0_{B1}, R^0_{B2}\}$ and the initial value for the damping parameter equals to $\lambda^0 = 0.001$. The iteration number is also initialized ($k = 0$).

- Step 1: Solve the direct problem with the available estimate $\overline{p}^k$ in order to obtain the temperature vector $T_j(\overline{p}^k) = (T_{1,0}, ..., T_{M,t_f})$.
- Step 2: Compute $S(\overline{p}^k)$.
- Step 3: Compute the sensitivity matrix $J(\overline{p}^k)$ and then set the matrix $\Omega^k = I$ (Unity matrix).
- Step 4: Calculate the new set of estimate $\overline{p}^{k+1}$ from equation 4.18.
- Step 5: Solve the direct problem with the new estimate $\overline{p}^{k+1}$ in order to find $T_j(\overline{p}^k)$. Then compute $S(\overline{p}^k + 1)$, as defined in step 2.
- Step 6: if $S(\overline{p}^{k+1}) \geq S(\overline{p}^k)$, replace λ^k by $\lambda^{k+1} = 10 \cdot \lambda^k$ and return to step 4.
- Step 7: if $S(\overline{p}^{k+1}) < S(\overline{p}^k)$, accept the new set of estimate $\overline{p}^{k+1}$ and replace λ^k by $\lambda^{k+1} = \lambda^k/10$. Check the stopping criteria. Stop the iterative procedure if it is satisfied; Otherwise, replace k by $k + 1$ and go to step 3.

This algorithm is also depicted in figure 4.3 for more clarity. The difficulty of the LM resides in the building of the sensitivity matrix $J(\overline{p}^k)$. The sensitivity matrix must verify some criteria:

- Its determinant must be different to zero;
- Columns must be linearly independent of each other. If not, it means that a parameter of the unknown vector $\overline{p}^k$ is linked to another parameter.

4.5 Sensitivity of temperature field and weld pool width to efficiency and Gaussian radii

The inverse heat transfer procedure requires that both temperature and weld pool width (the available experiment data) are relevant to get a correct estimation of the parameters. That means the measured temperatures and weld pool width have to be sensitive to a small variation of the parameter to estimate: efficiency and Gaussian radius.

This study can be done by analyzing the sensitivity of both temperature and weld pool width with regards to each parameter to estimate. In what follow, the approach

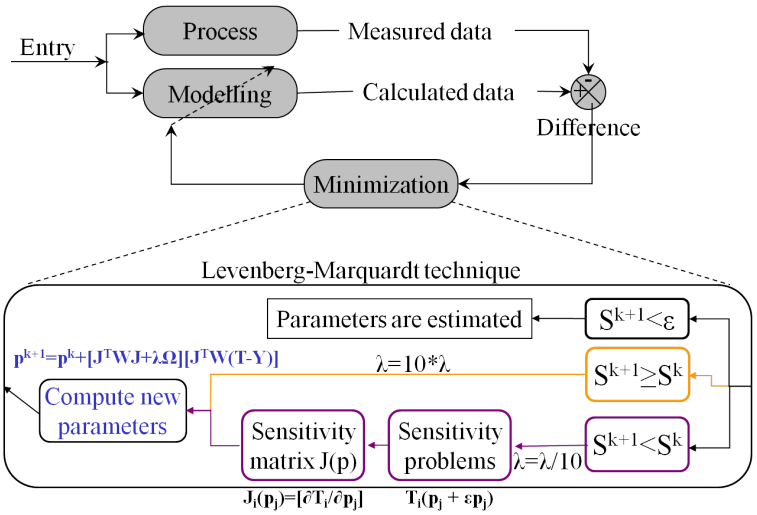

Figure 4.3: The Levenberg-Marquardt optimization technique

used for computing this temperature and weld pool with sensitivity is explained. These temperature and weld pool width sensitivity are analyzed in order to:

- Locate the best position for the thermal sensors;
- Define when to start and end the data acquisition;
- Check that the parameters to estimate are linearly independent.

4.5.1 Computation of the sensitivity coefficients

Let's consider the parameter η of the unknown vector $\overline{p} = \{\eta, R_{B1}, R_{B2}\}$. The sensitivity coefficients for η are obtained by differentiating the equations of the stated direct problem with regards to η: $\delta T_\eta = \frac{\partial T}{\partial \eta}$. The resulting system of PDE is very complex because it involves the temperature sensitivity function δT_η and velocity sensitivity functions δu_η and δw_η.

An alternative method consists in approximating the temperature sensitivity function with a forward difference scheme [142] as follows:

$$\delta T_{\overline{p}} = \frac{T_i(\overline{p} + \epsilon\overline{p}) - T_i(\overline{p})}{\epsilon\overline{p}} \tag{4.19}$$

Where $T_i(\overline{p} + \epsilon\overline{p})$ is the calculated temperatures following with a small variation $\epsilon\overline{p}$. The difficulty resides only in the choice of the ϵ parameter. It must be small but not too small or the temperature sensitivity coefficient will be equal to zero all the time. That means the stated forward problem is only used and repeated three times, one time for each parameter to estimate: $\overline{p} = \{\eta, R_{B1}, R_{B2}\}$.

4.5.2 Numerical results

Instead of dealing directly with temperature sensitivity coefficients, let's define "normalized" sensitivity (NS) coefficients: $\chi_{\overline{p}}$. It is defined as follows:

$$\chi_{\overline{p}} = \overline{p} \cdot \delta T_{\overline{p}} \tag{4.20}$$

Then all the normalized sensitivities are expressed in the same unit that simplifies the sensitivity analysis. Furthermore, due to the severe welding conditions on the top side

Table 4.1: Reference and varied parameters for the sensitivity analysis

Parameter	η	$R_{B1}(mm)$	$R_{B2}(mm)$
Initial value	0.68	2.5	3.5
Variation (+5%)	0.714	2.625	3.675

(especially in and upon the weld pool), the current analysis is made on the back side where it is easier to probe the temperature with thermocouples. Nevertheless, a temperature is observed on the top side close to the weld pool where the metal never melts. A number of 5 points (where are located the K- type thermocouple) are selected and they are given in table 4.2.

Table 4.2: Locations of the temperature sensors

	Point 1 top side	*Point 2 back side*	*Point 3 back side*	*Point 4 back side*	*Point 5 back side*
radius (mm)	10	0	3	5	7
height (mm)	4	0	0	0	0

Remarks:

- The reference point is the center of the disc back side (r=0 mm and z=0 mm);
- The backside is referenced as z=0 mm and the topside is referenced z=4 mm.

4.5.2.1 Normalized temperature sensitivity evolution: $\chi_\eta(t)$

Calculated NTS evolutions, with respect to η, are reported in figure 4.4. The sensors located at the backside of the plate reached values between 600°C (sensor 2) and 750°C (sensor 4) while the sensor on the top surface rised to a maximum value of 400°C at the final time. Sensors located at positions 2 and 3 reached their final value after 2 s and 3 s respectively, see figure 4. These NTS values remained stable until the end of the simulation (tf=5 s). According to the formula used for the computation of these NTS values $\left(\overline{p}\delta T_{\overline{p}} = \overline{p}\frac{T_i(\overline{p}+\epsilon\overline{p})-T_i(\overline{p})}{\epsilon\overline{p}}\right)$, these positive values mean that a small increase of the efficiency results in a general increase of the temperature. These NTS values look relevant after 0.5s/1s with values over 50°C for all the studied sensors located on the backside. Relevant NTS values means that the noise measurement is lower in comparison. Let's assume that the noise measurement is about 5% of the current measured what leads to a maximum noise measurement of 40°C. Let's consider 40°C as a limit for the present study. All the NTS values must be higher (in absolute) to this limit: 40°C. Greater are the NTS values and better it will be for the estimation of the heat flux parameters. According to

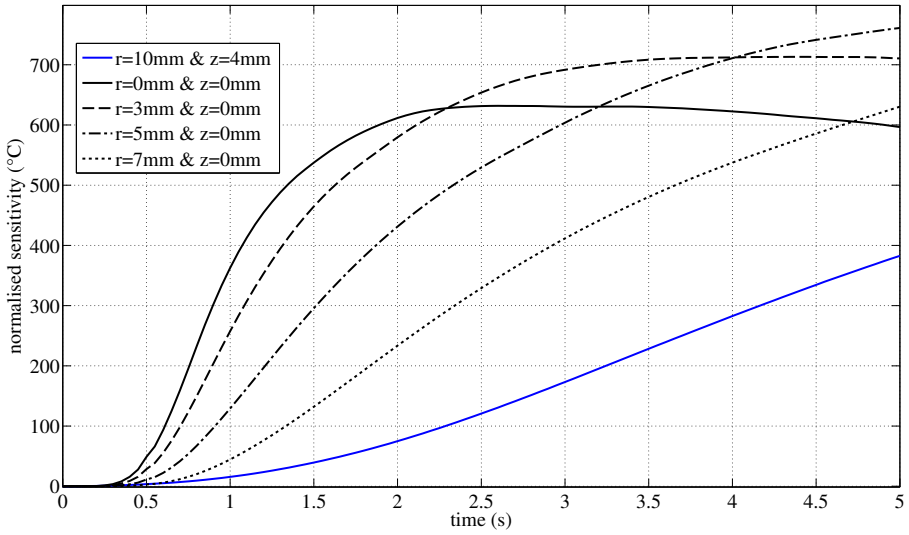

Figure 4.4: Normalized temperature sensitivity coefficient $\chi_\eta(t)$

this, it seems that the temperature data recorded on the disc backside are useful for the estimation of the efficiency.

4.5.2.2 Normalized temperature sensitivity evolution: $\chi_{RB1}(t)$

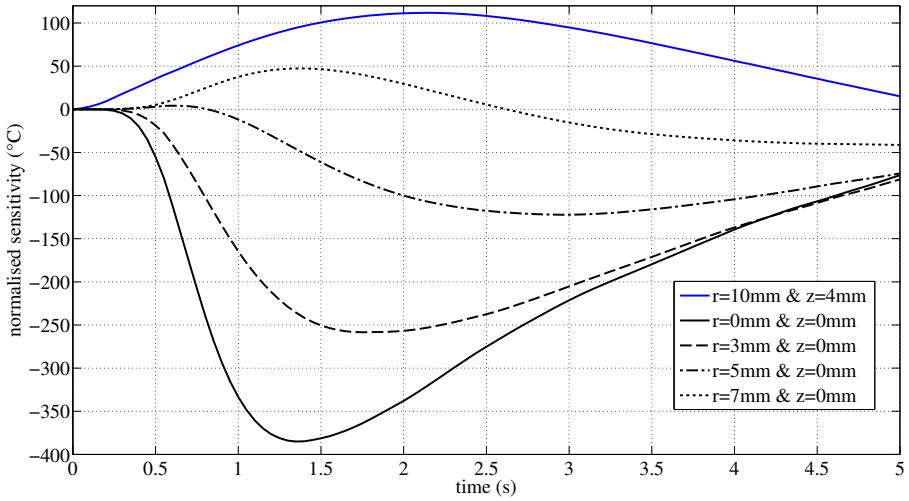

Figure 4.5: Normalized temperature sensitivity coefficient $\chi_{RB1}(t)$

NTS values with regards to R_{B1} are presented in figure 4.5. The five investigated locations exhibit different NTS evolutions. On the disc backside, within a radius of 5 mm, these evolutions are almost negatives over the studied time. Sensors 2, 3 and 4 admit a peak value of ≈ -400°C, -250°C and -120°C respectively at different times: 1.4 s, 1.7 s and 2.8 s respectively. The sensor 5 (r=7 mm) on the backside presents positive values over the range [0.5 s - 2.5 s] and then negative values. Sensor 5 reaches the maximum value of +50°C (at t ≈ 1.4 s) and decreased to a minimum value of -50°C at t=5 s. Sensor 1 always exhibits positive values over the studied time range with a maximum value of

+110°C at time 2.2 s. The increase of R_{B1} (5%) means that the welding energy is spread over a larger area what results in lower temperature on the backside (negative NTS) and higher temperature on top side. Nevertheless these NTS are quite important: greater to 50°C in absolute sense and never admit any stabilized values (as observed previously).

4.5.2.3 Normalized temperature sensitivity evolution: $\chi_{RB2}(t)$

NTS evolutions with regards to R_{B2} are depicted in figure 4.6. All the the NTS values start to be relevant (in absolute sense) after 1 s for sensors 2 to 4, after 2 s for sensor 1. The evolution of sensors 2 to 4 decrease almost linearly to values around -200°C from t=0.5 s to t=5 s. The evolution of sensor 5 is very low, with values almost close to zero till t<3.5 s and then it decreases almost linearly to -50°C at t=5 s. Conversely, sensor 1 has positive values and evolves linearly between t=0.5 s and t=5 s with a final value around 200°C. These NTS values for R_{B2} are relevant for sensors 1 to 4. Moreover these NTS values do not reach any stabilized values over the time interval as R_{B1}-NTS values. This last remark is especially interesting for the next study: are the three parameters linearly independent? One way to carry on this study is to compute the ratio of each NTS values for each sensor position.

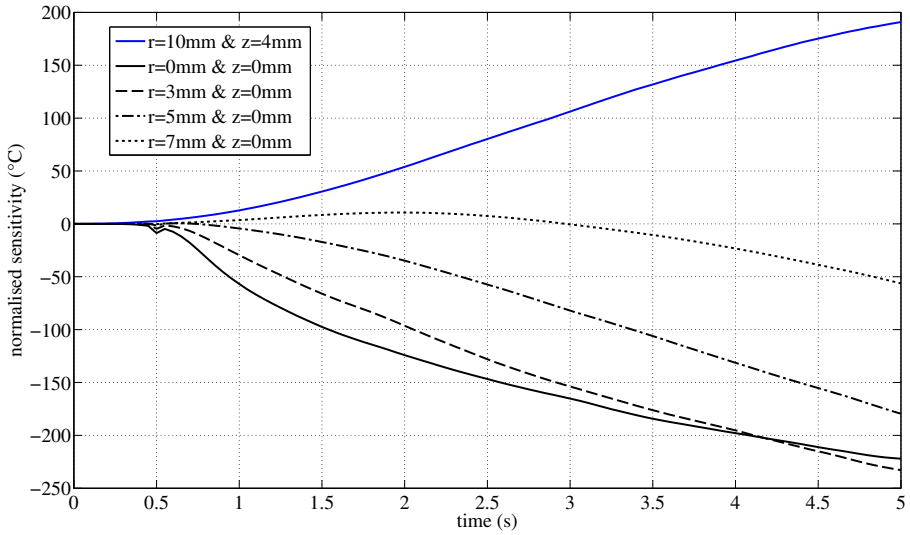

Figure 4.6: Normalized temperature sensitivity coefficient $\chi_{RB2}(t)$

4.5.2.4 Ratio of normalized sensitivity evolutions

In this section, we are verifying that the sensitivity of parameter χ_η is independent of the sensitivity of parameter χ_{RB1} for example (the same work has to be done with χ_{RB2} and between χ_{RB1} and χ_{RB2}). The method consists in computing the ratio of the NTS for each sensor location such as: $X_{\eta RB1} = X_\eta / X_{RB1}$. If this ratio is constant over the time interval that means the studied parameters are constant (these parameters can be constant over a short time interval). As a consequence the estimation of the two parameters is not possible over the time interval where the NTS ratio is constant. These ratios evolutions are presented in figures 4.7 and 4.8.

Figure 4.7 reports the three ratios for sensor located at r=10 mm on top surface. it is clear that parameters η and R_{B2} are quite linearly dependent (or proportional) as their NTS ratio χ_η/χ_{RB2} (full black curve) is almost constant over the time interval [0.5 s-5 s]. The two other NTS ratios are varying over 2/3 of the time interval: the ratio χ_{RB1}/χ_{RB2}

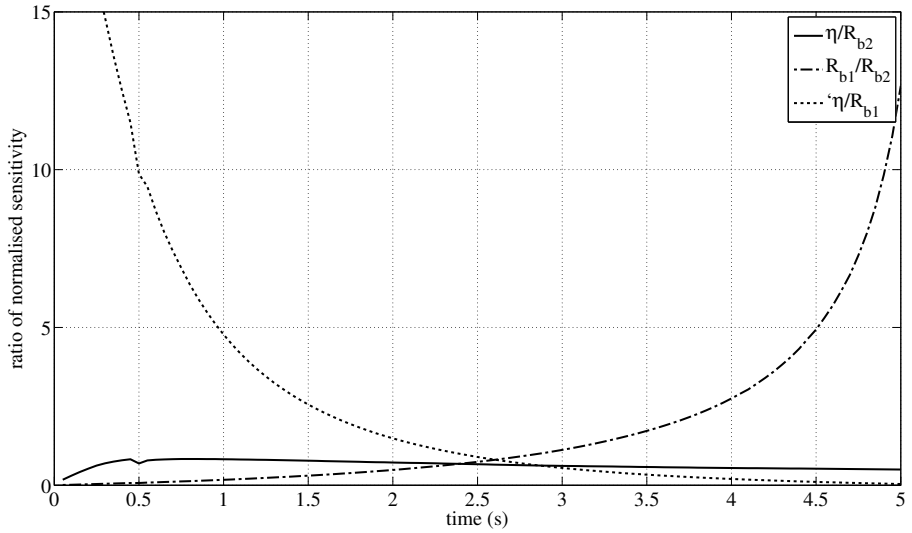

Figure 4.7: Ratio of the normalized temperature sensitivity coefficients at r=10 mm and z=4 mm (on top side)

(dashed black curve) is varying strongly in the time interval [0.5 s-4 s] while χ_η/χ_{RB1} is varying in the time interval [1.5 s-5 s]. That means that R_{B1} and R_{B2} are independent (or not proportional) in [0.5 s-4 s] and η and R_{B1} are independent in [1.5 s-5 s].

Because the two parameters η and R_{B2} are quite proportional over the time interval, the temperature recorded at this sensor may prevent the resolution of the inverse heat transfer problem. Figure 4.8(a) and 4.8(b) present the same evolutions for the three ratios. Figure 4.8(a) reports these ratio evolutions at the center of the back side of the disc while figure 4.8(b) exhibits these ratio evolutions at r=3 mm on the same side. The ratios χ_η/χ_{RB2} and χ_{RB2}/χ_{RB1} seems to be independent in the interval [0.5s-4s] while χ_η/χ_{RB1} is rather independent in [1s-5s]. From figures 4.4, 4.5 and 4.6, it was noticed that the NTS for the three parameters was quite important over the two time interval identified from figure 4.8(a) and 4.8(b).

Figure 4.8(c) shows the three ratio evolutions at sensor 4 (r=5 mm on back side). The three ratios exhibit a vertical asymptote at t$\approx$ 0.7 s. Therefore, the three ratios are strongly varying around this time before stabilizing after 1s except for the ratio χ_η/χ_{RB2}. That means that the three ratios are quite independent in the time interval [0.3-1.2 s]. In addition, the NTS values of the three parameters are quite low in this stated time interval then the data given by the sensor 4 are not useful.

The evolution of the three ratios at sensor 5 (r=7mm on disc back side) is displayed in figure 4.8(d). The ratios exhibit again a vertical asymptote at $t \approx 3s$ for ratios χ_η/χ_{RB2} and χ_{RB2}/χ_{RB1} while it is at t=2.6 s for ratio χ_η/χ_{RB1}. Astonishingly, the time evolutions of the three ratios are quite important in the time interval [1.5 s-4 s] for ratios χ_η/χ_{RB2} and

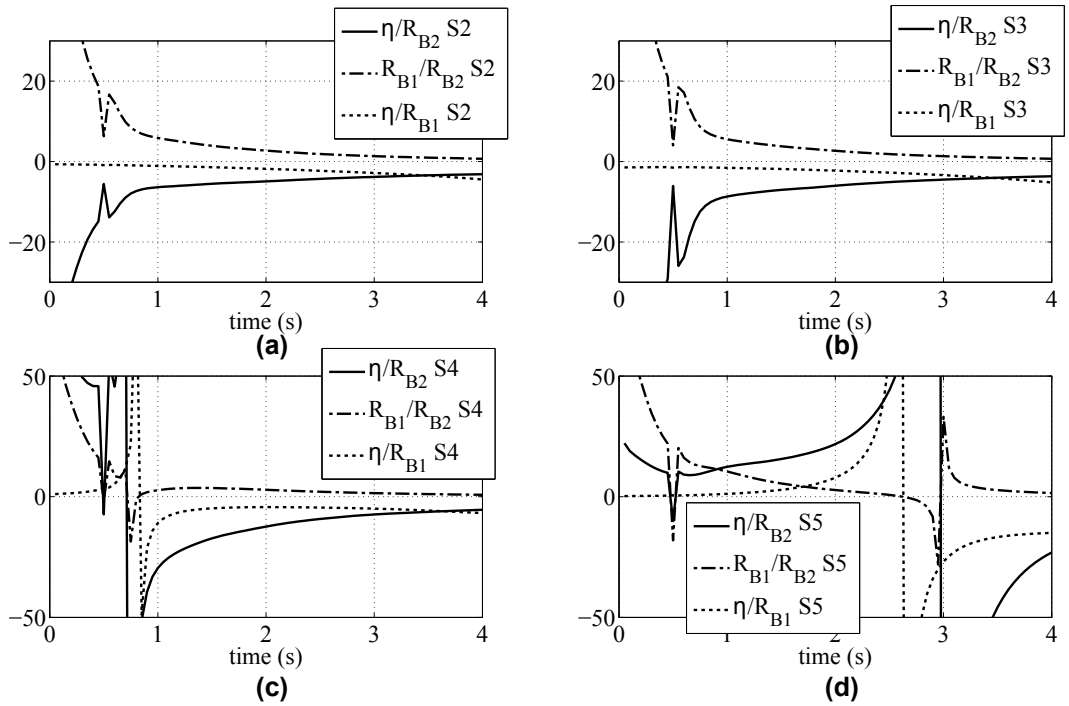

Figure 4.8: Ratio of the normalized temperature sensitivity coefficients. a) At point r=0mm and z=0mm (back side). b) At point r=3mm and z=0mm (back side). c) At point r=5 mm and z=0 mm (back side). d) At point r=7 mm and z=0 mm (back side)

χ_{RB2}/χ_{RB1} and the time interval [0 s-4 s] for the last χ_η/χ_{RB1}. This sensor is located far away than the previous (r=5mm) but this sensor location (r=7 mm) looks quite relevant for measuring temperature. But the NTS values for the two Gaussian radius R_{B1} and R_{B2} are quite low over all the time interval of the simulation. This sensor 5 is interesting if the noise measurement on the measured temperatures is quite low (less than 1%). Let's remark that this sensor location is interesting due to the size of the weld pool (4.3 mm half-width and 1.1 mm depth) under the investigated welding conditions: $\widetilde{I}$=150 A and $\widetilde{U}$=10.4 V. Lower welding power will lead to smaller weld pool and sensor 5 may become less relevant while sensor 4 may become relevant.

From the five sensors positions, it can be stated that sensors 1 and 4 can not be used for the estimation of the parameters. Sensors 2 and 3 are useful but sensor 5 is probably the best one. The problem of sensor 5 is that the NTS values of the Gaussian radii are low. It seems that the temperature measurements should be recorded within a radius lower than and also around 7 mm$\leq r \leq$ 8 mm for a weld pool size of 4.3 mm and 1.1 depth. This conclusion is closely related to the geometry of the weld pool obtained under the studied welding conditions ($\widetilde{I} = 150A$). For different welding conditions, for example: lower welding energy the weld pool will be smaller, so the sensor locations (especially sensors 3, 4 and 5) should be adjusted. The time interval [1 s-4 s] is the more relevant for temperature measurements according to the previous analysis.

4.5.2.5 Normalized weld pool width sensitivity evolution

Figures 4.9(a) and 4.9(b) represent respectively the Normalized Weld pool width Sensitivity (NWS) coefficients for each parameter and the ratio of these NWS coefficients. The two ratios η/R_{B1} and η/R_{B2} are quite independent for t>2 s. The NWS ratio R_{B1}/R_{B2} is constant over all the time interval what means there is a strong dependence between the two parameters. Therefore this data is still useful for estimating the GTAW efficiency η.

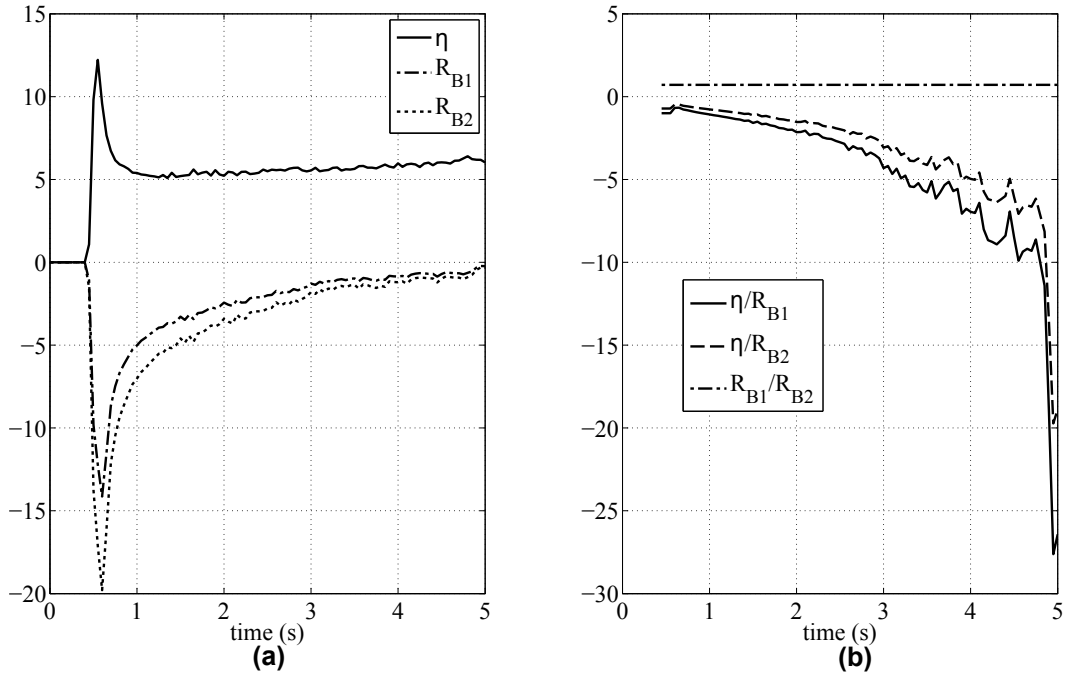

Figure 4.9: a) Normalized Weld pool width Sensitivity coefficients for each parameter. b) Ratios of Normalized Weld pool width Sensitivity coefficients

4.5.3 Conclusion

The aim of this sensitivity analysis was, firstly, to define where and when measuring relevant temperatures and, secondly, what are the linearly independent parameters to estimate. It appears:

- Temperature measurements must be done on the back side of the plate (it is mainly an experimental constraint)
- The estimation of GTAW efficiency η will be easier than the two Gaussian radii. The best position for the sensors is close to the center and another position around r=7mm from the disc center.
- The weld pool width data is complementary and provides relevant data for GTAW efficiency parameter only (as the two Gaussian radii are linked together).

4.6 Numerical resolution of inverse heat transfer problem

The aim of this section is to demonstrate that the temperature measurements on disc back side and weld pool width data are relevant for solving the inverse heat transfer problem (ihtp). Five test cases are investigated in what follows. The first part of this section is dedicated to validate the uniqueness of the solution (the three parameters) by solving the inverse heat transfer problem with two sets of initial parameters. Then the effect of various sources of errors on the input data (noise measurement, error on sensor position and error on material properties) are investigated to better understand their effect on the final estimation of the parameters.

4.6.1 Numerical tests with exact data

The goal of this study is quite straightforward: check that the ihtp converges and leads to the exact values of the three parameters when the input data are exacts. Exact data means that the stated GTAW modeling is solved with the following values: η=0.68, R_{B1}= 2.5 mm and R_{B2}=3.5 mm (with $\widetilde{I}$=150 A and $\widetilde{U}$=10.4 V). This simulation gives both temperatures and weld pool width to use as input in the ihtp. As the ihtp is based on the same GTAW modeling (called forward problem) and initialized with different values for the three parameters (which are: η=0.1, R_{B1}= 20 mm and R_{B2}=20 mm), at the end of the iterative process, the estimated parameters should be equal to the one used for getting the exact data. As it is a numerical study, the initial values are chosen far away from the exact values in order to show that the ihtp is able to manage it.

Two cases have been carried out in this section. In the first case, the ihtp was solved with two thermal sensors located on the back side at r=0 mm and r=7 mm. In the second case, the ihtp was solved with thermal sensors at the positions: r=6 mm and r=8 mm of the back side. Figure 4.10 presents the evolution of the cost functions with the iteration

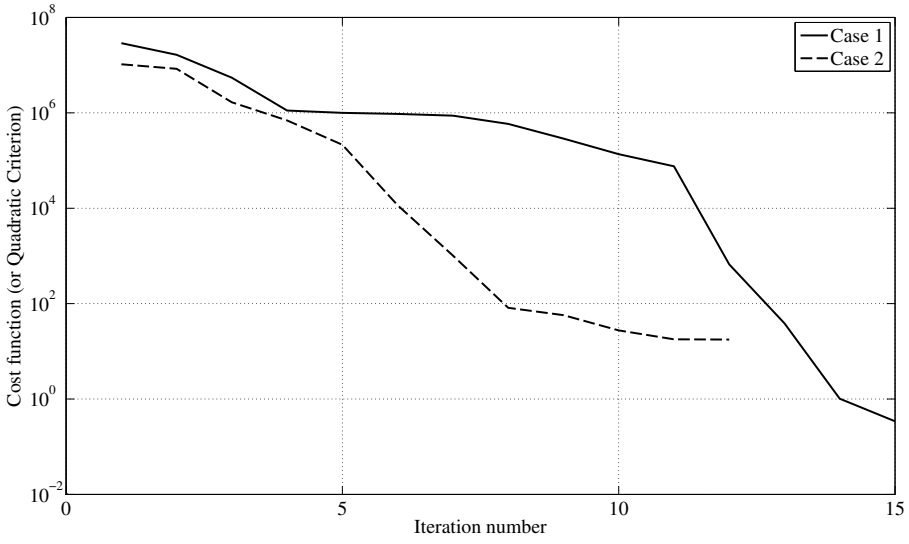

Figure 4.10: Evolution of the cost functions with regards to the iteration number

number. Both cost functions decrease towards a value close to zero as expected. The case

2 converged faster towards zero. The computation case 1 ran for about 39 hours before stopping it while computation case 2 ran about 25 hours (The forward multi-physics problem run takes about half an hour).

Figures 4.11(a) and 4.11(b) show respectively the calculated and reference temperatures for case 1 and their temperature difference also called temperature residual at iteration 15. The calculated temperatures match perfectly the reference temperatures. The temperature residual is lower than 0.1°C for the sensor located at the center and lower than 0.02°C for the sensor located at r=7 mm, figure 4.11(b). Figures 4.12(a) and

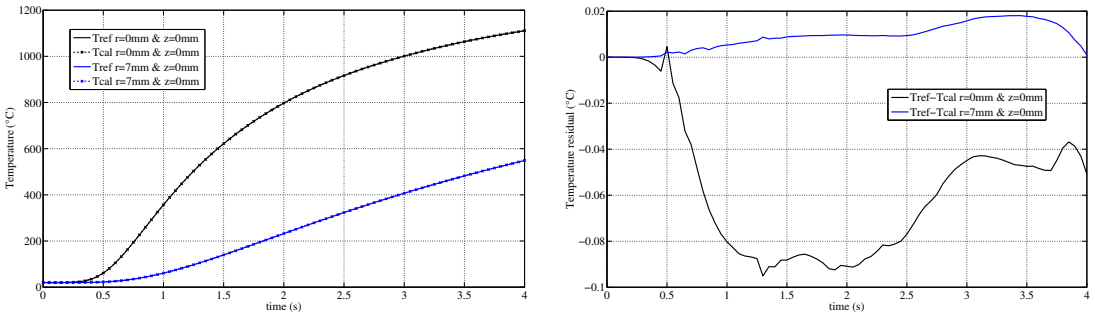

(a) Comparison between the input data (Tref) and the calculated ones (Tcal) at the end of the 15th iteration.

(b) Temperature residual (Tref-Tcal) at the end of ihtp computation (iteration 15)

Figure 4.11: Temperature and temperature residual

4.12(b) show respectively the calculated and reference temperatures for case 2 and temperature residual (Tref - Tcal) at iteration 11. For the two cases, the temperature residual is lower than 0.1°C in absolute value. The calculated temperatures fit correctly with the input data. Figures 4.13 and 4.14 present the estimated parameters with regards to the

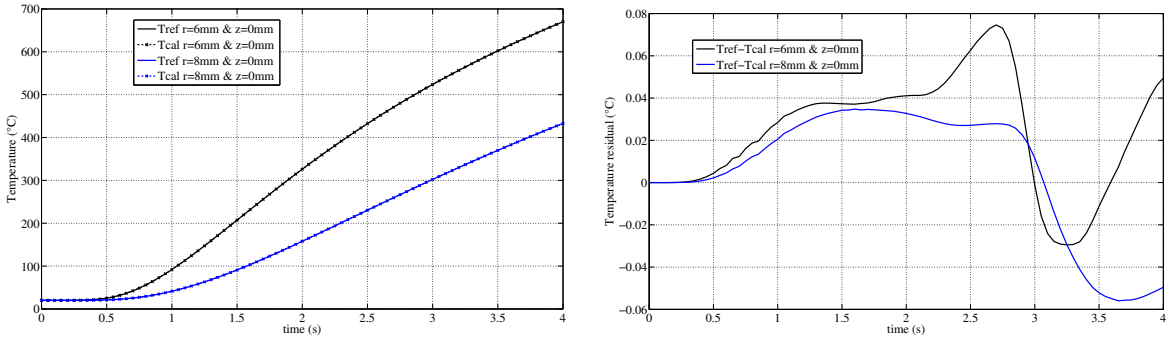

(a) Comparison between the input data (Tref) and the calculated ones (Tcal) at the final iteration.

(b) Temperature residual between the input data (Tref) and the calculated ones (Tcal) at the final iteration

Figure 4.12: Temperature and temperature residual for case 2

iterative number. The three parameters are quite well estimated after 6 iterations for case 2 and after 11 iterations for case 1. These iteration numbers 6 and 11 correspond to a cost function value below 10^4.

Figures 4.15(a) and 4.15(b) present respectively the comparison between the reference weld pool width with the calculated one and their residual for case 1. The same results

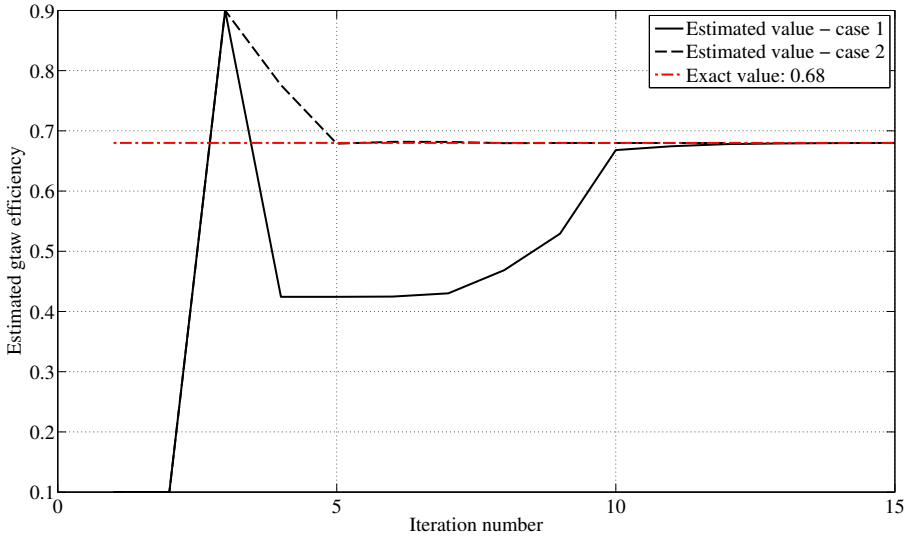

Figure 4.13: Evolution of the estimated efficiency with regards to the iteration number.

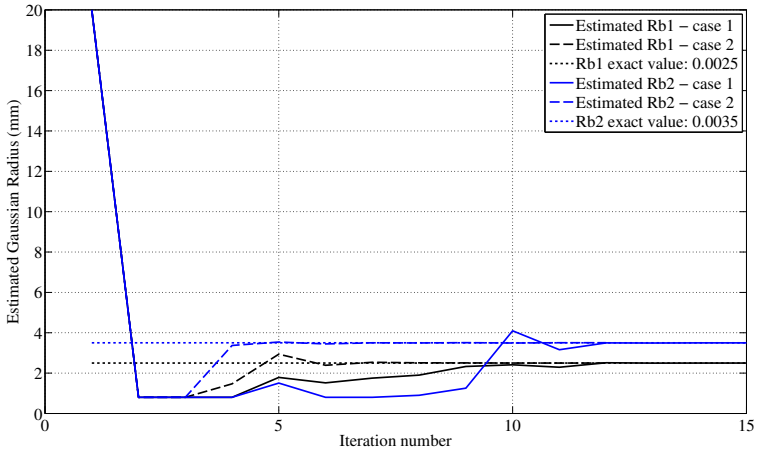

Figure 4.14: Evolution of the estimated gaussian radii with regards to the iteration number.

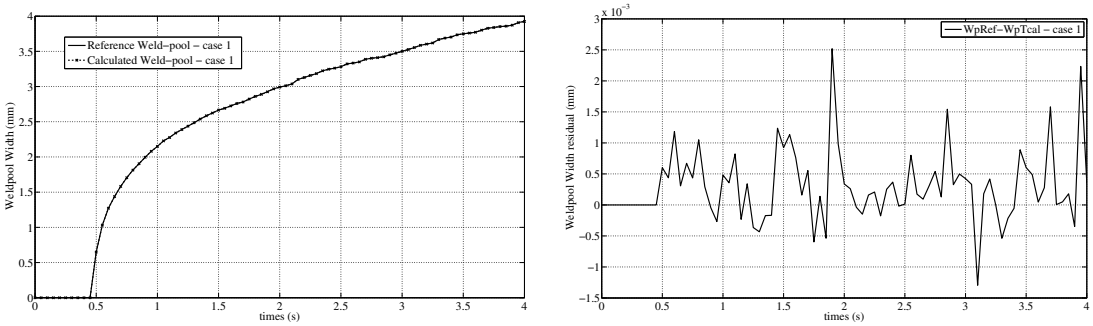

(a) Comparison between reference weld pool width and the calculated one at the last iteration

(b) Residual of weld pool width and the calculated one at the last iteration for case 1

Figure 4.15: Weld pool comparison between reference and calculated

are shown in figures 4.16(a) and 4.16(b) for case 2. The reference and calculated weld pool half-width match very well as it can be seen in figures 4.15(a) and 4.16(a). Their difference is lower than 0.03 mm so less than 0.8%. This residual is probably due to to the numerical simulation (mesh grid used). Let's discuss now about the accuracy of the $\sigma(p_i)$ estimated

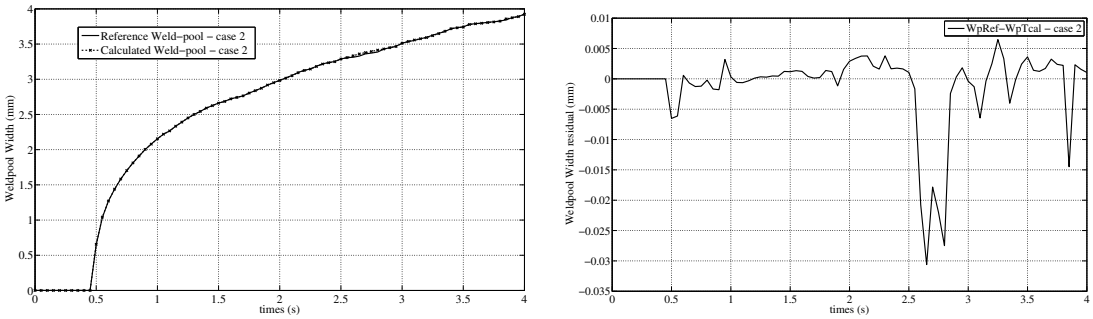

(a) Comparison between reference weld pool width and the calculated one at the last iteration

(b) Residual of weld pool width and the calculated one at the last iteration for case 2

Figure 4.16: Weld pool comparison between reference and calculated

parameters. It is well known that the sensitivity matrix can be also used for evaluating the confidence interval for each estimated parameters. Let's explain, the Hessian matrix $H(\overline{p})$ is approximately equal to the sensitivity matrix $J^T(\overline{p})J(\overline{p})$. The covariance matrix is itself related to the Hessian matrix as follow: $cov(\overline{p}) = H^{-1}(\overline{p})$ then the accuracy $\sigma(p_i)$ on each estimated parameter can be evaluated from the covariance matrix by applying the next formula: $[\sigma(p_i)]^2 = cov(p)_{ii}$. All these steps can be summarized by the following formula:

$$[\sigma(p_i)]^2 = cov(p)_{ii} = H_{ii}^{-1}(\overline{p}) \approx \left[J^T J\right]_{ii}^{-1} \tag{4.21}$$

The accuracies for each estimated parameters are reported in the next table 4.3. As we can see, these three parameters are estimated with an excellent accuracy as expected. The accuracy is slightly better for the case 1 but the error done on the estimated parameters is of the same order of magnitude. Finally both choice of sensor position: one on the disc center and one at r=7 mm or both located around r=7 mm led to excellent estimation of the parameters. The second set of sensor location just converged faster to the exact parameters. In the next paragraph, the robustness of the ihtp with regards to different

Table 4.3: Estimated parameters for both studied cases after solving ITCP

Parameters	*Exact Values*	*Case 1 (after 15 iterations)*			*Case 2 (after 11 iterations)*		
		Estimated	*Accuracy*	*% error*	*Estimated*	*Accuracy*	*% error*
Efficiency	0.68	0.6799	± 0.00027	≤ 0.015	0.6799	± 0.0003	≤ 0.015
R_{B1}	2.5	2.499	± 0.0018	≤ 0.04	2.498	± 0.01	≤ 0.08
R_{B2}	3.5	3.499	± 0.0049	≤ 0.028	3.503	± 0.017	≤ 0.085
Computation time (hours)			39			22.5	

sort of errors is investigated. The aim is to check that the three parameters are estimated with a correct accuracy with some reasonable measurement errors.

4.6.2 Numerical tests with noised input data

The following three sort of errors are investigated:

- Noise measurement: a random error is added to the reference temperature with a maximum standard deviation $\sigma(t)$ of 5% of the actual temperature ($|\sigma(t)| \leq 5\% \times T_{REF}(t)$) so the new noised input are: $T_{NOISE}(t) = T_{REF}(t) + \sigma(t)$. The reference and noised temperatures are plotted in figure 4.17(a).
- Error on thermo-physical properties: a 5% error is assumed on thermal conductivity, mass density and specific heat. The new set of data with slightly different thermo-physical properties is presented in figure 4.17(b) (dashed curves).
- Error on the position of the thermal sensors. It is assumed that the sensor position is known within a confidence interval of ± 0.5 mm.

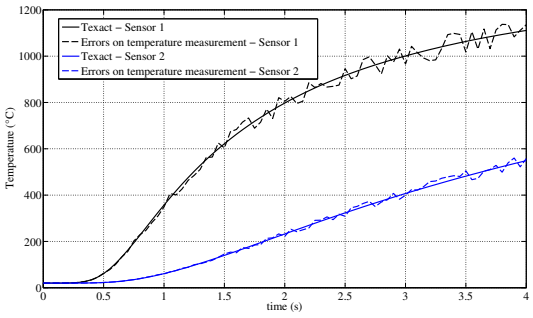

(a) Reference temperatures (with no noise) and new input temperatures including noise measurement.

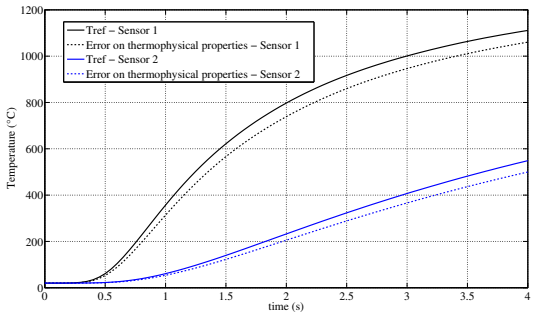

(b) Reference temperatures (with no noise) and new input temperatures with errors on the thermo-physical properties.

Figure 4.17: Comparison of noised and reference data

The evolution of the cost functions are presented in figure 4.18. The three cost functions converged to a stabilized value after 7 iterations. Then the ihtp was stopped because the cost function did not decrease enough between two iterations. This final cost function can be evaluated as it is connected to the error added to the input data. This final value can be assessed from the cost function formula:

$$S_{THRESHOLD} = \frac{1}{2}\int_{t_0}^{t_f}\int_{\Omega}\sum_{i=1}^{n_S}\left[Y_{mes}(t) - T_{cal}(x_i, t; \overline{p})\right]^2 d\Omega dt + \frac{1}{2}\int_{t_0}^{t_f}\int_{\Gamma}\left[W_{mes}(t) - w_{cal}(t; \overline{p})\right] d\Gamma\, dt \tag{4.22}$$

by substituting $Y_{mes}(t)$ with $T_{REF}(t)$ and $T_{cal}(t)$ with $T_{NOISED}(t)$. $W_{mes}(t)$ and $w_{cal}(t)$ are respectively the reference and calculated weld pool width. So, the final value for the 1st case is about 6.7×10^4. The cost function stabilized finally to a value of 4×10^4 for the case with measurement errors. The two others cost functions stabilized to 10^4 and 9×10^3 for the ihtps solved respectively with errors on the sensors location and errors on the thermo-physical properties. These estimated cost function thresholds can be used

as stopping criterion when the errors on the input data are known. If the errors are not known, the cost function should be stopped when its value between two iterations is slowly improved such as 0.1% for example.

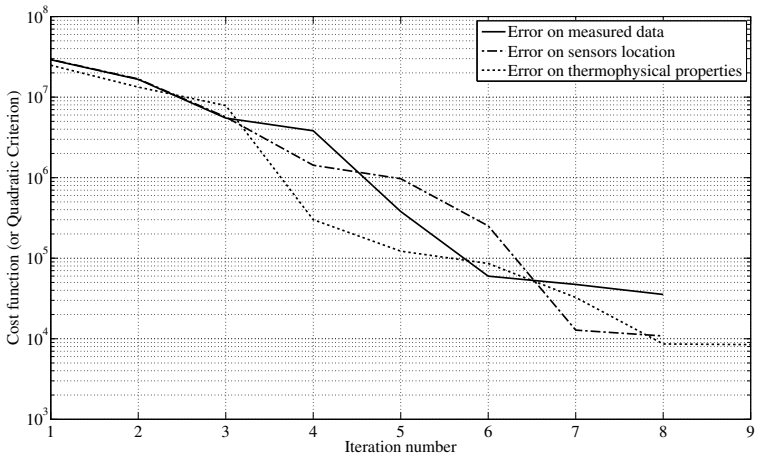

Figure 4.18: Evolution of the cost functions with regards to the iteration number

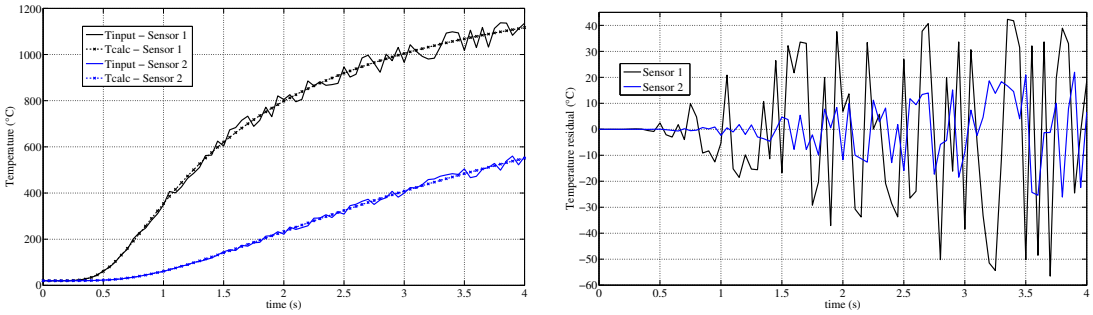

(a) Comparison between input and calculated temperatures at the last iteration. Case with noised temperatures

(b) Temperature residual at the last iteration. Case with noised temperatures

Figure 4.19: Noised temperature case

Figure 4.19(a) compares the calculated temperatures with the input data used (data with noise measurements) at the last iteration. The calculated temperatures evolutions are smooth in comparison to the input data. The Levenberg-Marquardt algorithm has filtered out the noise from the input data. Figure 4.19(b) presents the temperature residual so the difference between the noised input and calculated temperatures after solving the ihtp. The filtering effect of the ihtp is here highlighted and the normal distribution of the noise is also verified. Figures 4.20(a) and 4.20(b) show respectively the comparison between input and calculated data and their temperature residual for the second studied case: error on the sensors position. The input data were taken at point r=0.5 mm and r=6.7 mm while the ihtp was solved at the following locations: r=0 mm and r=7 mm on the back side. The calculated temperature matches very well the input temperature for sensor 1 (r=0.5 mm, back side) while there is some temperature difference at sensor 2 (r=6.7 mm). Nevertheless this temperature difference does not exceed 6°C, figure 4.20(b).

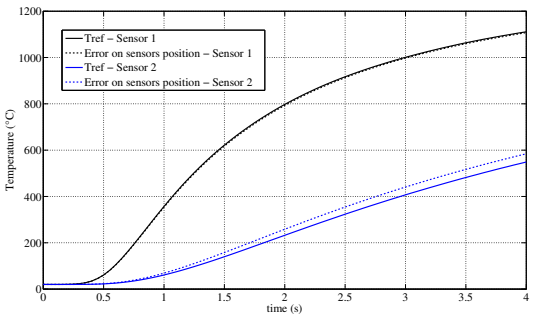

(a) Reference temperatures (input) and calculated temperatures at the last iteration. Case with changes on sensor position

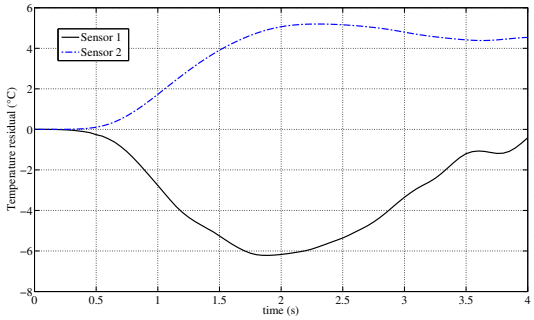

(b) Temperature residual at the last iteration. Case with changes on sensor position

Figure 4.20: Case with changes in sensor position

Figure 4.21(a) displays the temperature residual for the last case with errors on the thermophysical properties. Let's remember that a 5% error was assumed on these thermophysical parameters. The final temperature residual is lower than 6°C what is quite low in comparison to a maximum temperature of 1100°C for sensor 1 and 550°C for sensor 2. This low temperature residual means that the calculated temperatures and input ones are fitting very well.

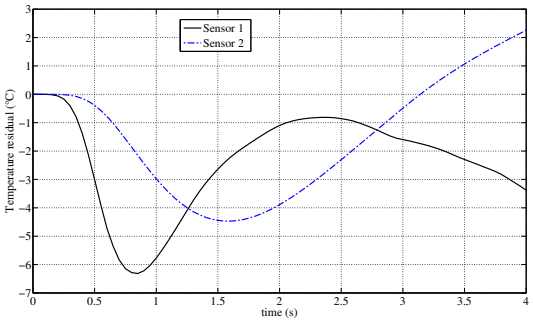

(a) Temperature residual at the last iteration. Case with 5% error on thermophysical properties

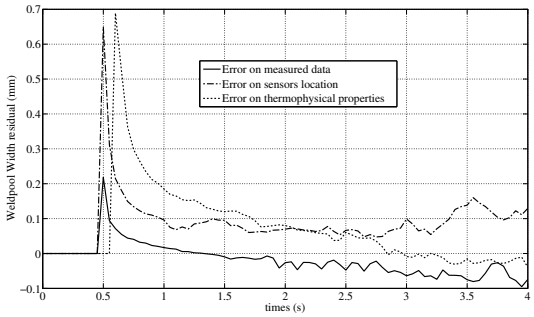

(b) Residual of weld pool width at the end of ihtp computation for the 3 cases

Figure 4.21: Case with 5% error in thermophysical properties

Figure 4.21(b) shows the weld pool residual at the last iteration for the three studied cases. These residuals are quite important (≈ 0.6 mm) at the beginning of the formation of the weld pool ($t \approx 0.5s$) then this residual stabilized below 0.1 mm. A 0.1 mm residual represents 2.5% of the final weld pool radius (about 4 mm).

The evolutions of the three estimated parameters along the iteration number are presented in figures 4.22, 4.23 and 4.24. The final values for each parameter are also reported in table 4.4.

The first studied case of error: temperature with noise measurement (as defined previously: within 5% of actual read temperature) did not prevent a good estimation of the

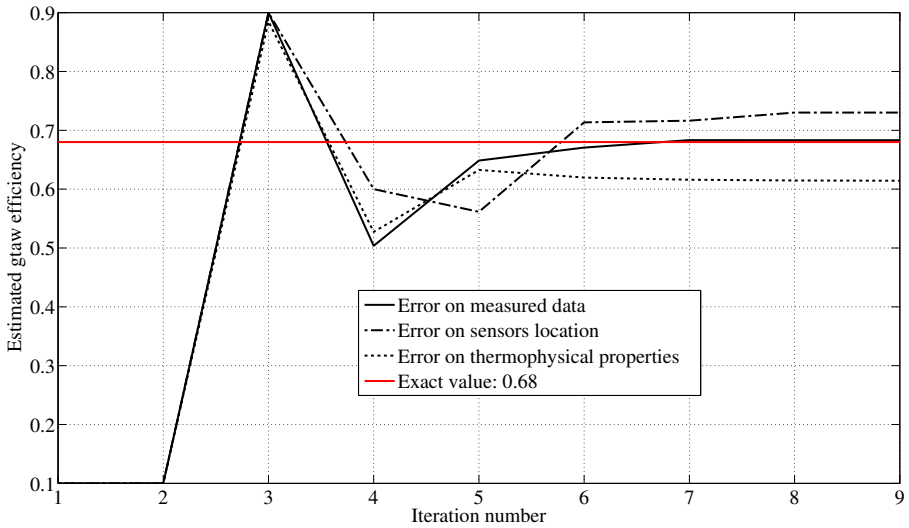

Figure 4.22: Evolution of the estimated efficiency with regards to the iteration number

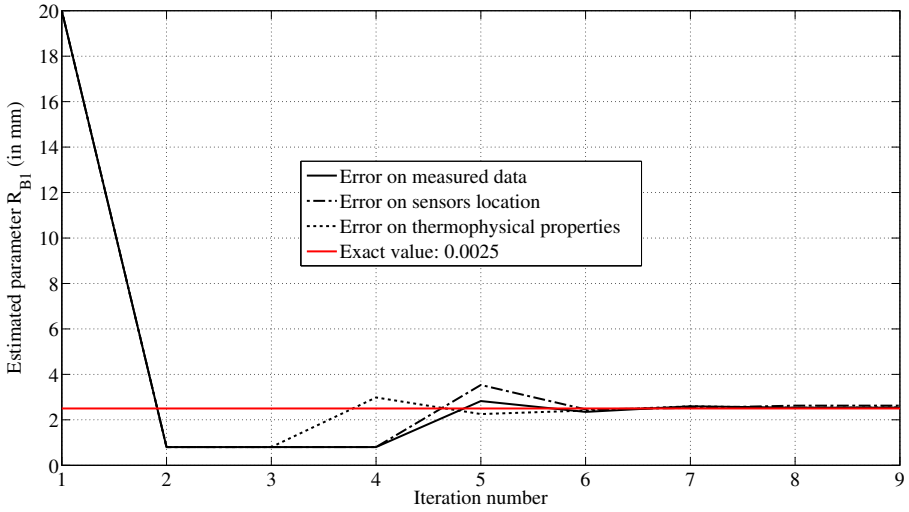

Figure 4.23: Evolution of the estimated R_{B1} parameter with regards to the iteration number

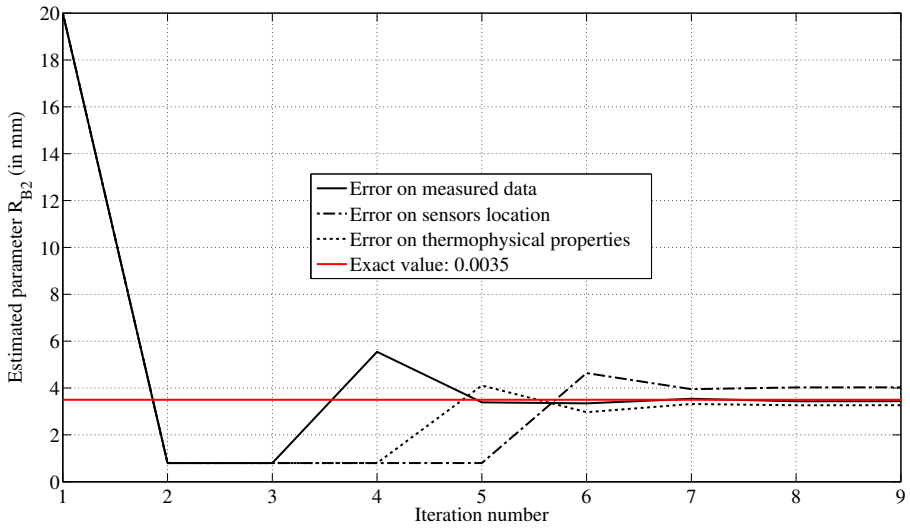

Figure 4.24: Evolution of the estimated R_{B2} parameter with regards to the iteration number

three parameters. For this case, the accuracy on the efficiency is less than 0.5% while it is less than 1.8% for the two Gaussian radii, see table 4.4. It took 7 iterations before getting an accurate set of estimated parameters.

The second case, error on sensors position led up to 15% error on the R_{B2} parameter (case with error on sensors position), see table 4.4, despite low temperature residuals as seen in figure 31. R_{B2} is overestimated as well as the efficiency. In this test case, the sensors positions were r=0.5 mm and 6.7 mm for getting the input while it was set to r=0 mm and r=7 mm for the ihtp. At position r=0 mm, temperature measurement are very sensitive to the efficiency than to the Gaussian radii as it was observed along the sensitivity analysis on the efficiency. As a consequence the ihtp estimated easier the efficiency than the Gaussian radii. From the sensitivity analysis, it was observed that R_{B2} is more sensitive than R_{B1}. Finally this parameter was overestimated because the efficiency was also overestimated in order to keep the same amount of absorbed heat flux (a larger radius will spread the energy over a large area what decrease the heating). In table 4.4, the integral of energy (so the heat flux on the top side) was calculated. This integral energy is almost close to the reference one and its error is less than 2.7% that is quite low in comparison to the respective errors of 7.4% and 15.1% on GTAW efficiency and R_{B2} parameter.

For the third case (error on thermo-physical properties), the introduced error is mostly absorbed by the GTAW efficiency parameter. This parameter is underestimated (10%) in comparison to the exact value. The RB2 is then underestimated by 6.5% in order to get higher heat flux values. The computation of the energy integral shows that there is a loss of energy of 7.2%. Finally this sort of error gives inaccurate estimation for two parameters out of three but also an inaccurate estimation of the energy absorbed by the disc.

Table 4.4: Parameters estimated for the three studied cases of error

Parameters	*Exact Values*	*Case 1 (9^{th} iteration)*		*Case 2 (9^{th} iteration)*		*Case 3 (9^{th} iteration)*	
		Estimated	*Error (%)*	*Estimated*	*Error (%)*	*Estimated*	*Error (%)*
GTAW Efficiency	0.68	0.683	≤ 0.44	0.73	≤ 7.4	0.614	≤ 9.7
$R_{B1}(mm)$	2.5	2.538	≤ 1.5	2.623	≤ 4.9	2.549	≤ 2
$R_{B2}(mm)$	3.5	3.438	≤ 1.78	4.028	≤ 15.1	3.267	≤ 6.5
Heat flux integral	1.425×10^5	1.434×10^5	≤ 0.63	1.386×10^5	≤ 2.7	1.322×10^5	≤ 7.2
Computation time (hours)		23		19		18	

4.7 Estimation of parameters using experimental measurements

The inverse thermo-convective problem was solved with the temperature data obtained from the following experimental conditions as given in table 4.5. The radius of the low sulfur 304L steel disc is 40 mm. The sulfur content was evaluated to be closer to 39 ppm instead of the 36 ppm measured during the EPMA experiments. After welding, the steel disc has been cut in two parts in order to observe the resulting weld pool shape. The weld pool radius and depth for this experiment were respectively 2 mm and 1.4 mm, see table 4.6.

Table 4.5: Experimental conditions for high sulfur sample

Average current I_w	*Average voltage U_w*	*Arc length*	*Argon & flow rate*	*Sulfur content*	*Arc duration*	*radius*	*thickness*
71.3 A	8.7 V	2.4 mm	16 l/min	39 ppm	5 s	40 mm	4 mm

The three unknown parameters $\{\eta, R_{B1}, R_{B2}\}$ were initialized respectively to 0.85, 10 mm and 10 mm as it can be seen in figures 4.26(a) and 4.26(b) at the 1^{st} iteration. The time step is set to 0.05 s and the duration of the simulation (forward problem) is set to 5 s. The fluid domain is reduced to one fourth of an elliptic domain with a radius of 3 mm by 2 mm depth (along the major axis of the ellipse domain). The fluid domain was defined after observation of the experimental weld pool shape from the macrograph analysis. The inverse problem was stopped at the 6^{th} iteration as there was no more important decrease of the objective function as shown in figure 4.25(a). The final value of the objective function is about 27600 what corresponds to an average standard deviation of $\overline{\sigma} \pm 18°C$, see table 4.7. The average standard deviation was calculated as follows: $\overline{\sigma} = \sqrt{\frac{2J_{final}}{n_t n_s}}$ with J_{final} the objective function at the last iteration, n_t is the number of time step and n_s is the number of sensors. The comparison between the experimental temperatures

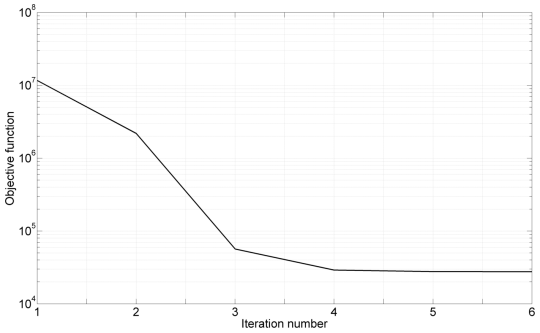

(a) Evolution of the objective function with iteration number

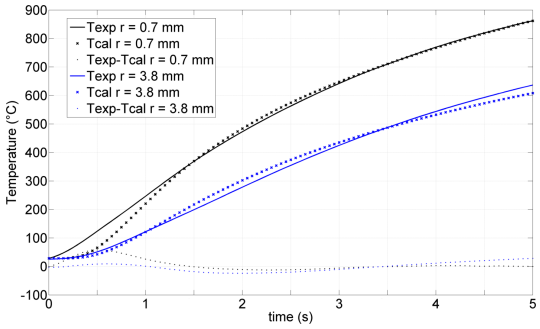

(b) Experimental, calculated and residual of temperatures at last iteration

Figure 4.25: Results obtained for high sulfur sample case

and calculated one at the 6_{th} iteration are presented in figure 4.25(b). The calculated temperatures match quite well the experimental what was obvious due to the low average standard deviation ($\overline{\sigma} \approx 18°C$). The locations of the sensors were 0.7 mm and 3.8 mm from the center on the backside. The temperature calculated at r = 0.7 mm does not match well the experimental one between 0 s and 1.3 s. Most of the differences between the experimental and calculated temperatures are at the beginning of the simulation (for time inferior to 1.5 s). The evolutions of three estimated parameters with regards to the

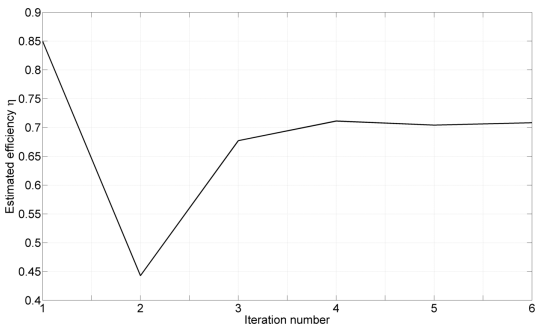

(a) Evolution of the estimated efficiency with the iteration number

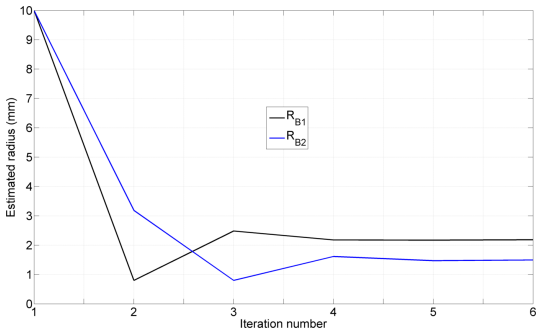

(b) Evolution of the estimated radii with iteration number

Figure 4.26: Evaluated heat source parameters for high sulfur sample

iteration number are shown in figures 4.26(a) and 4.26(b). As mentioned previously, these values did not change a lot since the 4^{th} iteration (as the objective function did not change from the 4^{th} iteration). The estimated values at the last iteration are 0.71, 2.18 mm and 1.5 mm respectively for the efficiency, first and second Gaussian radii. Let's remember that the first Gaussian radius corresponds to the initial time and the second one to the final time. The estimated value for the R_{B1} Gaussian radius was unexpected whereas the values obtained for the efficiency and R_{B2} look coherent. Let's perform a statistical analysis on the accuracy of the estimated parameters. According to some statistical assumptions, the standard deviation for each estimated parameters can be calculated from the covariance matrix [143]. The covariance matrix is derived from the sensitivity matrix as follows: $Cov(p) = (J^T J)^{-1}\overline{\sigma}$ where J is the sensitivity matrix ($p = \{\eta, R_{B1}, R_{B2}\}$) and $\overline{\sigma}$ is the average standard deviation that we suppose to be equal to the one at the final iteration

of the inverse problem. Finally the standard deviation for each parameter is given by:

$$\sigma_p = \overline{\sigma}\sqrt{[J^T J]^{-1}} \tag{4.23}$$

The corresponding standard deviations for each parameter are reported in table 4.7. These low values mean that the parameters are estimated with a good accuracy.

In section 4.6.2, several numerical cases have been studied with noised input data. It has been shown that the error on the sensor location was the worst case. A small error on the sensor position ±0.25 mm led to high errors on the estimation of the parameters, up to 15% on the 2nd Gaussian radius. This error is difficult to evaluate due to the size of the employed thermocouples: 0.5 mm which is quite large with regards to the temperature gradient on the back side of the steel disc. Furthermore, it is well known that a thermocouple introduces a thermal contact resistance. This thermal contact resistance results in a delay of the thermocouple response as well as lower measured temperature [144, 145]. If the recorded temperature is lower (because of this thermal contact resistance), it means that either the efficiency should be higher or the Gaussian radii should be smaller than the current estimated values presented in table 4.7.

Table 4.6: Final weld pool dimensions (calculated at the final iteration) for high sulfur sample

Weld pool	*Experimental*	*Calculated*
Radius (mm)	2.0	2.05
Depth (mm)	1.4	1.32

Table 4.7: Estimated heat source parameters at the last iteration for high sulfur sample

Parameters	*Estimated value*	*Estimated standard deviation*
Efficiency η	0.708	± 0.0065
R_{B1}(mm)	2.18	± 0.045
R_{B2}(mm)	1.5	± 0.057
Final averaged standard deviation σ ($^\circ C$)	± 17.7	

The values estimated for the GTAW efficiency and Gaussian radii are in good agreement with the one found in the literature. Nonetheless, a question on the choice of assumed constant efficiency along the studied time interval is probably wrong. It is maybe the reason of the difference of temperature (between experimental and calculated) within the first 1.5 s of the simulation. It has been shown in the sensitivity analysis section that the efficiency and Gaussian radii (especially the 1^{st} Gaussian radius) were sometimes lowly independent which can prevent an accurate estimation. The use of another optimization method must be explored.

4.8 Conclusion

In this chapter, some definitions have been explained such as direct problem, regularization method, quadratic criterion and the general definition of an inverse heat transfer problem. Then, the inverse heat transfer problem was stated to our problem: the estimation of efficiency and Gaussian radii. The Levenberg-Marquardt method was used for the minimization of the stated cost function. Before carrying out any resolution of the ihtp, a sensitivity analysis was performed in order to guarantee that the temperatures measured at some sensors locations were relevant. Indeed the measured temperatures must be sensitive to the estimated parameters in order to get relevant values for the efficiency and gaussian radii. Some sensor locations have been identified as more interesting than others. From the sensitivity analysis, it was concluded that:

- The temperature measurement must be done closer to the center of the disc back side and closer to a point r=7mm for our welding conditions (when the weld pool half-width is about 4mm).
- The time interval for recording the data should not exceed 4/5s.
- The weld pool half-width (measured with the high speed camera) is relevant for the estimation of the efficiency only.

Then, few numerical cases were investigated to confirm that the stated ihtp worked well with exact input data and behaved robustly with noised data. Through the five different numerical cases, it was shown that

- The inverse method is robust to noise measurement and provided excellent estimated parameters and estimation of the energy absorbed in the work-piece;
- The position of the sensors must be carefully checked every time and marked on the disc (for later measurement once the experiment has been finished and the center of the weld pool is used as reference point for sensors position) as it may lead to a bad estimation of efficiency and R_{B2}. The energy integral is lowly affected by this error.
- The values of the thermo-physical properties and especially the thermal conductivity must be known quite accurately over the whole temperature range. This can lead to a bad estimation of efficiency and R_{B2} parameters.

At least the chapter ends with the estimation of the efficiency and gaussian radii with experimental data (temperatures only). The value of the efficiency (0.7) is in good agreement with the one found in the literature for the GTAW process. The values for the Gaussian radii are respectively 2.1 mm and 1.5 mm for the Gaussian radius at t=0s and the one at t=5 s. It was expected a similar value for the both radii or a smaller value for the 1st radius due to the stabilization of the electric arc. Due to the size of the thermocouple (0.5 mm) and to the introduced thermal contact resistance, the value of the 1st Gaussian radius is probably not well estimated. Another assumption is probably that the efficiency is not the same at the beginning (t=0s) than at the final time.

Conclusions and Perspectives

In the present study a fluid flow and heat transfer model was developed to understand the basic mechanisms during static GTAW process. Numerical model was used to predict the temperature, weld pool growth and final weld geometry.

Experimental investigations have consisted in the static GTA welds on stainless steel 304L samples. This experimental setup carried out synchronized measurements of temperature history and transient weld pool radius. Experiments were carried out with different welding currents (70 A, 110A and 150 A) and for different material composition. The measured voltage between the fixed electrode and the weld pool free surface indicate very little fluctuations other than electronic noise. This can justify the fixed surface assumption used for the numerical simulation. Postmortem analysis revealed the final weld cross section with unusual wavy boundary for low sulfur content sample with different welding energy. This indicates the complex fluid flow experienced with in the weld pool. On the contrary, the high sulfur sample produced deep penetrated weld pools. This indicates the flow occurred from the weld pool edge to the center resulting the transfer of heat into the depth. The penetration was 1.5 mm for the high sulfur case while it was 1 mm for the low sulfur. The weld pool radius was respectively 2 mm and 2.15 mm. The measured temperatures confirmed that the depth of the weld pool was deeper for the high sulfur than the sample with low sulfur. Indeed, in the same welding conditions, the thermocouples close to the disc center reported a maximum temperature of 860°C against 790°C for the low sulfur case. For the three studied cases, the negligible convex surface is observed at the top boundary (crown), this ruled out the possibility of any outward fluid flow from the boundary. This observation also underlines the fixed surface assumption for numerical model. The image processing algorithm used for the analysis of high speed camera results provided the weld pool growth rate for the three different case studied. The high growth rate of the weld pool radius produced by 150 A current indicates the added effect of arc drag force to the Marangoni force, while for 70 A and 110 A this growth rate is lower.

Then, a 2D axi-symmetric magneto thermo hydrodynamic numerical is studied in chapter 3. First, a simple heat conduction model is studied using a Gaussian heat distribution. The heat conduction model is useful in determining the thermal gradients around the fusion zone and HAZ. Afterward, the heat transfer and fluid flow numerical model is developed by assuming a fixed weld pool boundary. The results of the developed model gives an idea of how the variation of parameters such as welding power, welding duration or the amount of surface active elements such as sulfur can influence the static GTAW process results. The results presents the transient temperature, velocity, weld pool evolution and the final weld shape. The double vortex circulation in the weld pool is observed for 70 A current case with a maximum penetration occurring at a radius where the peak surface

temperature reaches a critical value. This change in flow direction of the liquid metal with in the weld pool is mainly due to the temperature dependance of surface tension coefficient. The established numerical model for the static GTAW process, systematically investigate the effects of individual driving forces in the weld pool, effect of the percentage of surface active element present in the material and the physical parameters that govern the Marangoni convection on the weld pool characteristics.
The convection in the weld pool is identified as the dominant mechanism for heat transport. A comparison between the conduction and convection showed that at low welding current (70 A), conduction model predicted the weld pool depth and width similar to convection for low sulfur content sample. However, for high sulfur sample the heat conduction underestimated the weld pool penetration. The dimensionless Peclet number calculation showed that the convection is the dominant heat transfer mechanism.

The dominant driving force in the weld pool was evaluated by taking the effect of each individual force at a time. For 70 A case, the Marangoni force dominated the fluid flow in the weld pool with a maximum velocity 5 times higher than the arc drag force and 60 and 150 times higher than the Lorentz and Buoyancy force. The calculated maximum velocity in the weld pool are in the range of values that are available in literature (36 cm/s).

The last chapter of this work focused in the development of an inverse thermo-convection problem in the aim to estimate the GTAW efficiency and the Gaussian distribution. Indeed, the heat flux exchanged between the arc plasma and the steel 304L disc was modeled with a Gaussian function. The comparison between the experimental data and the simulation results showed a good agreement of the final weld pool shape but the simulated temperatures were higher to the measured ones. These differences are certainly due to the presence of the 0.5 mm diameter thermocouples. It is well known that thermocouples introduce temperature distortion due mainly to the bad thermal contact between the thermocouple tip and sample to measure. Nevertheless, a set of experimental data has been used for the estimation of the parameters: efficiency and Gaussian radius. The inverse thermo-convective problem was solved with the Levenberg-Marquardt method associated to an iterative regularization procedure. The efficiency was estimated to 0.71 while the initial Gaussian radius ($t=t_0$) and final Gaussian radius ($t=t_{fin}$) were evaluated to 2.15 mm and 1.5 mm. The important difference between the two radii was not expected. This is probably due to the underestimation of the local temperature because of the presence of the thermocouple. The use of smaller thermocouple and measurement closer to the weld pool should improve the results.

I conclude this work with some perspectives in order to improve the results of this present research work and to future research works. From an experimental point of view, the use of non intrusive measurement such as an infrared camera would be a great tool to either measure the temperature on the back side without complicating the settings (because the radiation of the arc is hidden by the steel disc). This should avoid any temperature distortion due to the presence of the thermocouple. Of course, the infrared camera must be correctly calibrated. The other advantage of thermal camera is also the measure of the temperature on the weld pool surface. This will be an important insight on the temperature distribution on the weld pool surface and it may be closely related to the flow of the molten metal. Such thermal data will be extremely pertinent for the estimation

of parameters such as process efficiency and heat flux spatial distribution with an inverse technique. About the resolution of the inverse problem with the proposed method, a 3D heat transfer and fluid flow approach including the presence of the thermocouples would have improved the estimated parameters. The problem resides only in the computation time of such inverse problem that may take weeks to converge the values. It is also though that the efficiency, supposed to be constant along the time interval, was probably time varying. It would be interesting to consider the process efficiency as temperature dependent with a constant or time varying Gaussian radius. This approach means lots of unknown parameters to estimate and the Levenberg-Marquardt method is not well adapted to this sort of problem. The Gradient conjugate technique associated to an adjoint problem (related to the heat transfer and fluid flow forward problem) is one amongst all the available approaches. Nevertheless the experimental data must be free of errors as much as possible. Once the inverse approach and the experimental measurements will be correctly handled, this can be used for the characterization of heat flux with various gaseous mixtures. Helium can be added to the Argon shielding gas as well as some tension-active gas like Oxygen (in lowest quantity to avoid any oxidation). Effect of electrode tungsten alloy can be studied as well in order to observe any effect on the heat flux at the arc plasma – steel sample interface. It is known that some alloyed tungsten electrodes are used because of their ability to release electrons.

Appendix A

Normalised temperature sensitivity coefficient

Normalised temperature sensitivity coefficient with regards to efficiency

The normalised temperature sensitivity (NTS) coefficients are presented in figure A.1 for different times (these NTS values resulted of a 5% variation of η). NTS coefficients reaches high values (>1500°C) on the top surface of the disc for 3 mm $\leq$ r $\leq$ 6 mm. As the efficiency was increased, more heat flux was absorbed within the disc what leads to a larger weld pool than the reference simulation. *High NTS values (in absolute meaning) are an indicator about where and when should be made the thermal measurement. These measured data are full of relevant information about the efficiency parameter. Low NTS values (in absolute meaning) are insensitive to a variation of efficiency parameter so useless.* Hence the disc top side (3 mm $\leq$ r $\leq$ 6 mm) is interesting because a small variation of will be observable in the temperature measurements. However this interesting zone is difficult to probe because of the severe experimental conditions (arc radiation, electromagnetic field ...). The disc backside is also interesting for simulation time between 1.5s and 5s (within 8mm radius), see figure A.1. The NTS reaches values between 400°C and 800°C which is enough important. Moreover, the disc backside is easier to probe in comparison to the disc top side. So temperature measurements must be made on the bottom side within 8mm radius from the center for getting relevant data for the estimation of η parameter.

Normalised temperature sensitivity coefficient with regards to R_{B1} parameter

Let's analyze the NTS fields with regards to a variation of R_{B1} (+5%), see figure A.2. It is noticed that a 5% increase of R_{B1} parameter leads to a general decrease of the temperature through the whole disc (because NTS values are negatives). An increase of the Gaussian radius leads to a larger spread of the energy over the disc top surface. Then the heat flux reaches lower values (in W/m^2) as $\eta\frac{U_S \cdot I_S}{\pi(R+\epsilon R)^2} < \eta\frac{U_S \cdot I_S}{\pi R^2}$. The highest NTS values (in absolute value) are located on the top surface of the weld pool, nearby the solid/liquid frontier of the weld pool (till t< 4s). Unfortunately this part of the disc can not be used for measuring temperatures due to the severe welding conditions. The disc back side

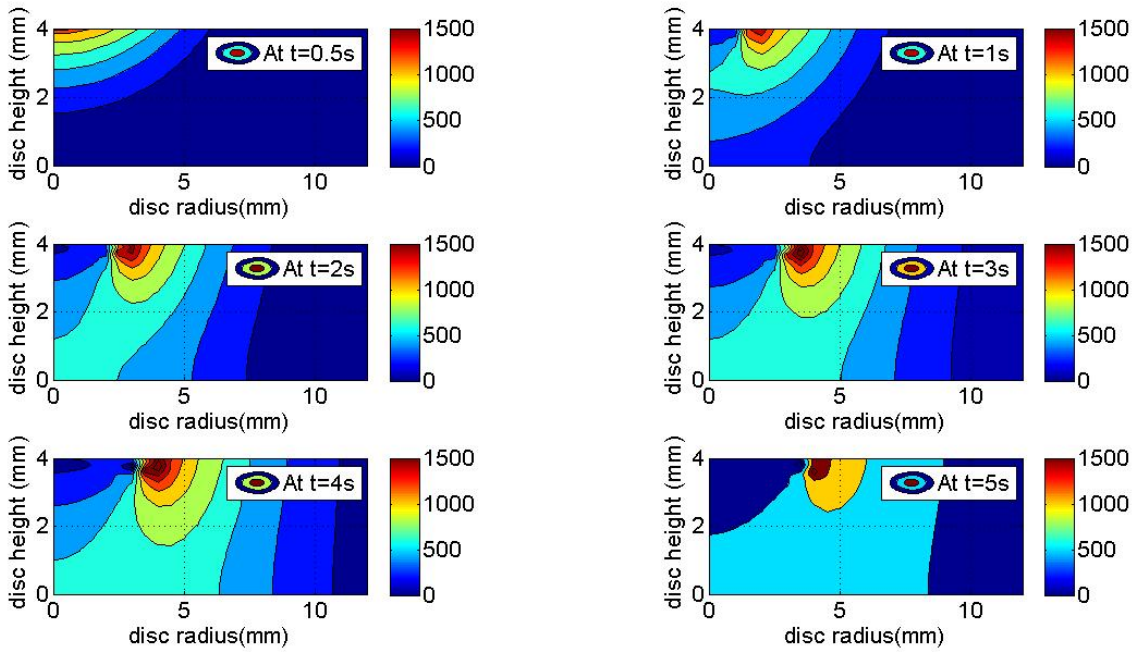

Figure A.1: Normalized temperature sensitivity field at different times with regards to efficiency

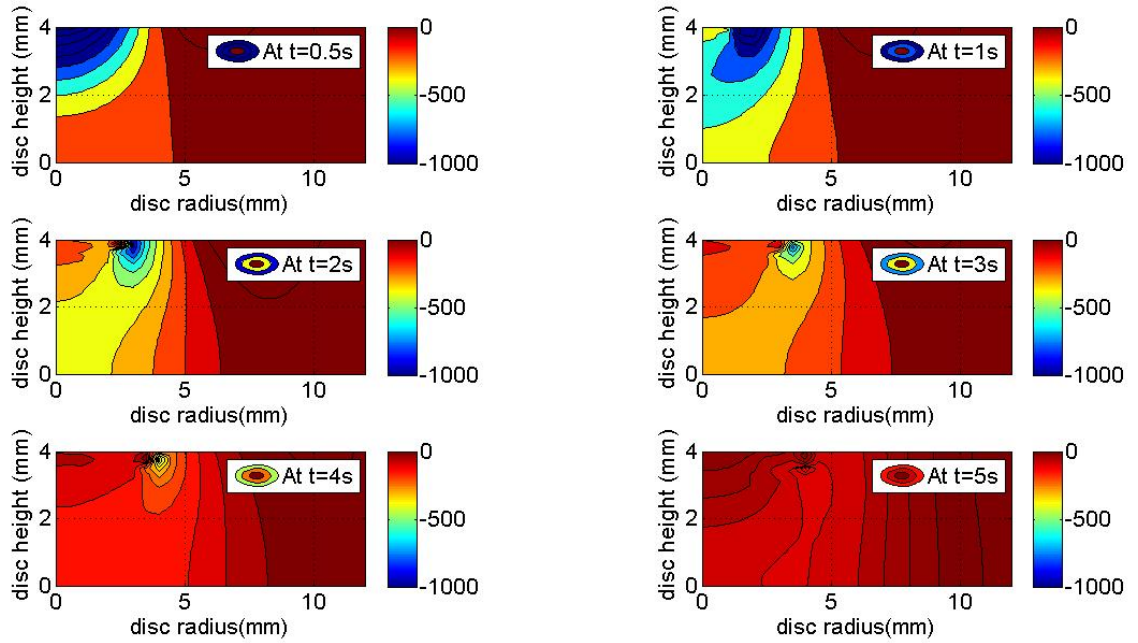

Figure A.2: Normalized temperature sensitivity field at different times with regards to R_{B1} parameter

looks interesting for getting some useful temperature measurements which are sensitive to R_{B1} parameter. On disc back side, NTS reach values between 150°C and 400°C within 5-6mm radius for 0.5s$\leq$ t $\leq$ 3.5s. Then the NTS values decrease quickly towards zero. The disc back side can be used for getting relevant temperature measurement in order to estimate this parameter: R_{B1}. These values are 4 times lower than the ones obtained for the efficiency parameter.

Normalised temperature sensitivity coefficient with regards to R_{B2} parameter

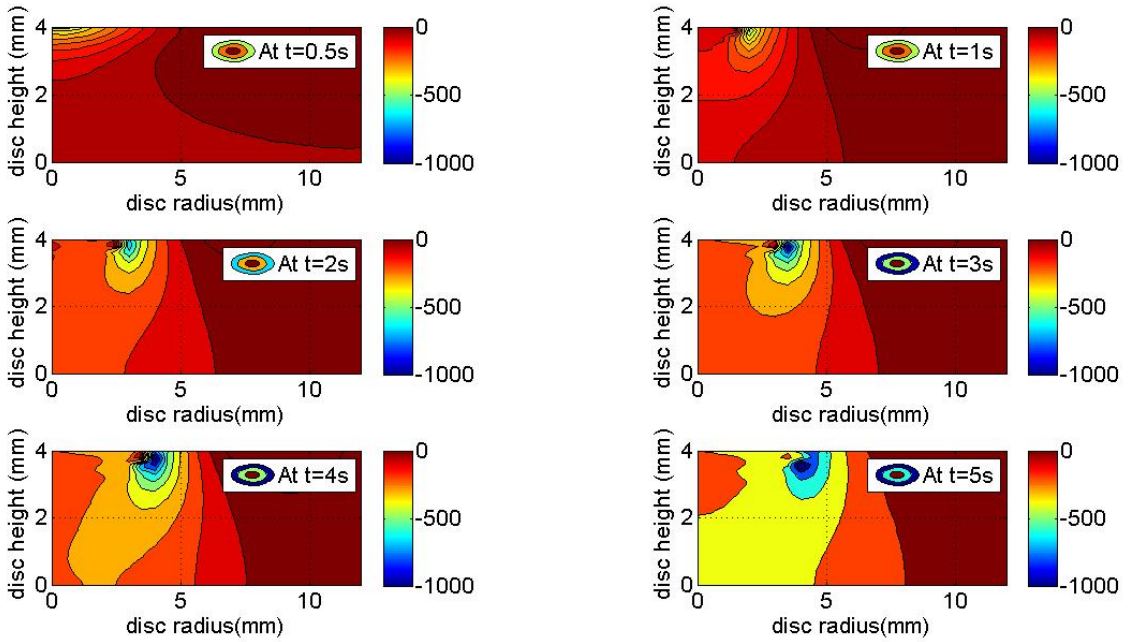

Figure A.3: Normalized temperature sensitivity field at different times with regards to R_{B2} parameter

NTS fields with regards to a variation of R_{B2} (+5%) are presented in figures A.3. As noticed for R_{B1}, the increase of R_{B2} also generates a decrease of the overall temperature in the disc (NTS values are negatives). This general decrease of temperature appears for time greater than 1.5s-2s. Let's remember that R_{B2} is the value of the Gaussian radius at time t=5s. The fomula used for computing the Gaussian radius is: $R_B(t) = \frac{R_{B2}(t_f)-R_{B1}(t_0)}{\Delta t} \cdot t + R_{B1}(t_0)$. That is why NTS values with regards to R_{B2} are higher towards the final time of the simulation whereas the R_{B1} values were higher at the beginning of the simulation. As explained for the two first parameters (η and R_{B1}), the NTS highest values (absolute value) are located on the disc top surface at the edge of the weld pool. Indeed, an increase of 5% of R_{B2}, at the final simulation time, leads to a spread of the heat flux distribution, so lower heat flux values and as a consequence a lower heating of the top surface and finally a smaller weld pool. On disc backside, NTS has quite relevant values understood between 200°C and 400°C between 2s $\leq$ t $\leq$ t_f = 5s and within 8mm radius (from disc center).
The three normalised temperature sensitivity presented ($\aleph_\eta$, $\aleph_{R_{B1}}$, $\aleph_{R_{B2}}$) exhibited rele-

vant values on the backside of the plate (the top side can not be used for temperature measurements because of the arc welding operation). Moreover, the temperature measurement should be made within 8mm radius on the back side. Regarding to the time or when these temperature measurements have to be made, it seems that the time range [1s - 5s] is suitable.

Appendix B

Extended Parametric study

B.1 Effect of mesh grid

In this section, two other mesh grid sizes were investigated: a coarse mesh grid (two times larger than the reference mesh grid) and a finer one (two times smaller than the reference one). The reference mesh grid details are presented in table 3.13. Figure B.1 shows the variation of temperature evolution at the back center of the disc for different mesh settings. The finer mesh settings shows a 2°C increase in the maximum temperature compared to the reference model. The coarse mesh settings produces 16°C less maximum temperature than the reference model. The variation between reference model and the fine mesh is 0.3% that can be neglected for such a high temperature range. Figure B.2 shows the

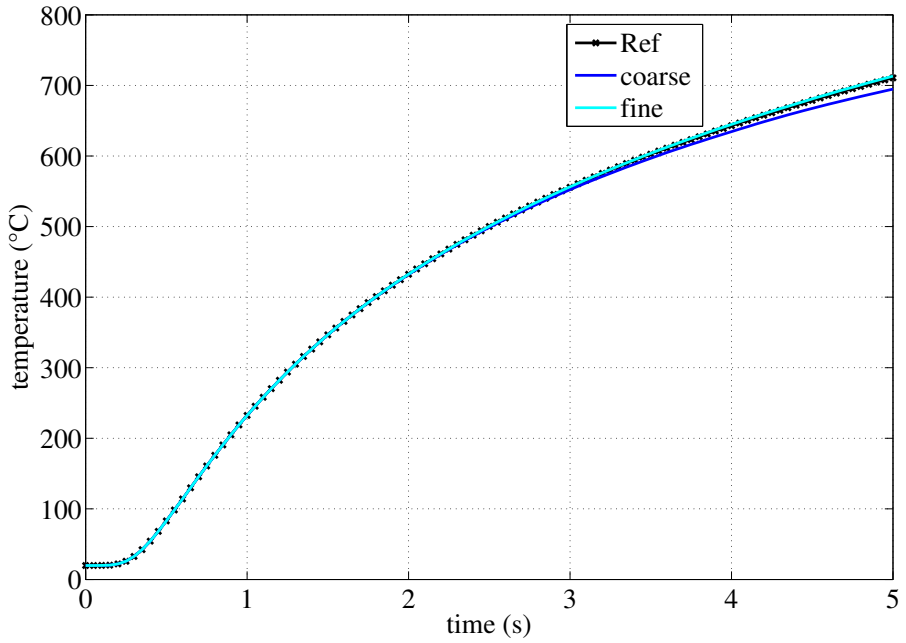

Figure B.1: Variation of temperature history at center back surface of the disc for different mesh settings

resultant surface velocity distribution along the radius for different mesh settings.

Figure B.3(a) shows the weld penetration at the center of the disc during the welding process for the three mesh setting. The finer mesh setting resulted in 1.4% more deeper

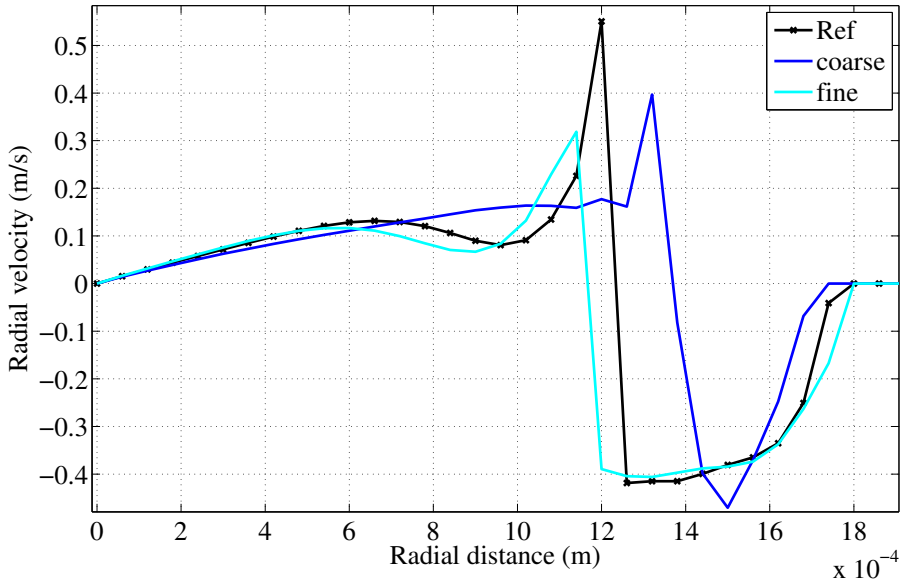

Figure B.2: Variation of resultant velocity along the top surface for different mesh settings

weld pool while the coarse mesh gives a 6% decrease in weld pool depth. Figure B.3(b) shows the weld pool width evolution during the static arc heating for the three mesh setting. The fine meshing didn't show a noticable variation in width compared to the reference numerical model but the coarse meshing give a 2% less wider weld pool than the reference model.

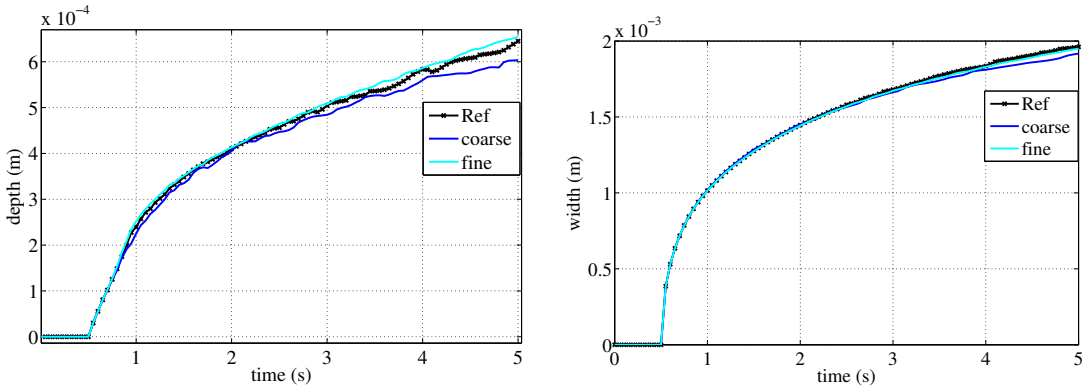

(a) Variation of weld pool depth during the arc heating

(b) Variation of weld pool width during the arc heating

Figure B.3: Evolution of weld pool size for different mesh settings

From this study, which is not showing any remarkable variation in any of the simulation output, it can be conclude that the mesh setting that is using for the reference model is suffiecient to predict the weld pool dimensions accurately.

B.2 Effect of surface tension parameters

Table 3.15 gives the major constant parameters used in the empirical relationship of $\partial\gamma/\partial T$ for a binary system defined by Sahoo et al. [94]. Sahoo et al. showed that the

critical parameter that controls $\partial\gamma/\partial T$ is the heat of adsorption, ΔH°, and suggested an empirical relationship for estimating ΔH°. In literature two values were suggested for ΔH°, $-1.66\times10^{8} J/kg.mole$ and $-1.88\times10^{8} J/kg.mole$. In order to better understand the effect of ΔH°, simulations were done for the two values and compared. Choo et al. [112] conducted numerical simulations and showed the sensitivity of the weld pool to ΔH°, and concluded that there occur a large change in the surface temperature, velocity profile and weld shape for a 10% change in ΔH°. The different constant values were found from the literature for the empirical formulation of the temperature dependent surface tension force. An analysis was carried out in order to identify the importance of these constant values. Figure B.4 shows the variation in temperature evolution when using a different value compared to the reference model. Figure B.5 shows the top surface resultant velocity

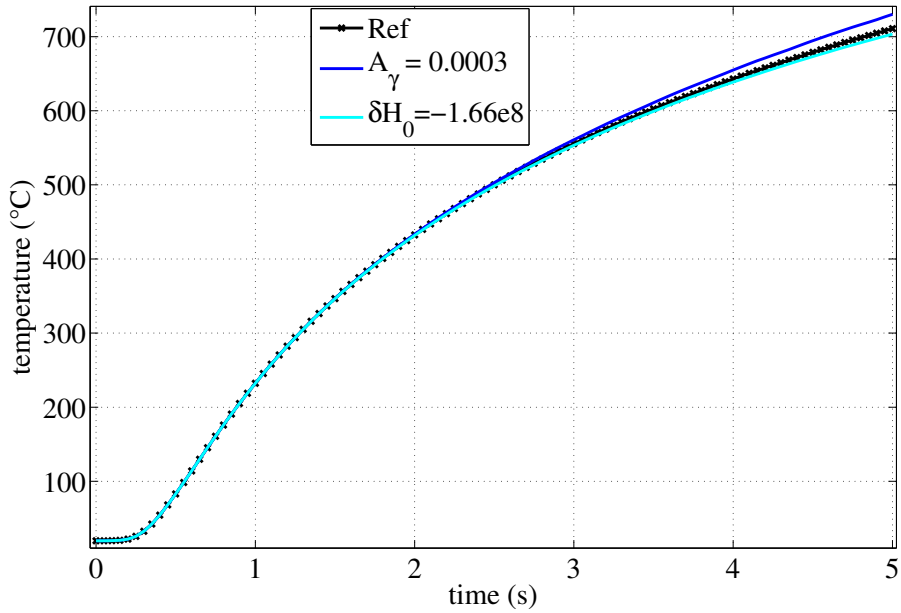

Figure B.4: Variation of temperature history at center back surface for different constant parameters in the surface tensional force

distributiuon at the end of arc heating for the three different cases. Figure B.6(a) shows the variation in weld pool depth evolution at the center of the disc for the three different cases. Figure B.6(b) shows the variation in the weld pool width evolution during the arc heating for the three different cases.

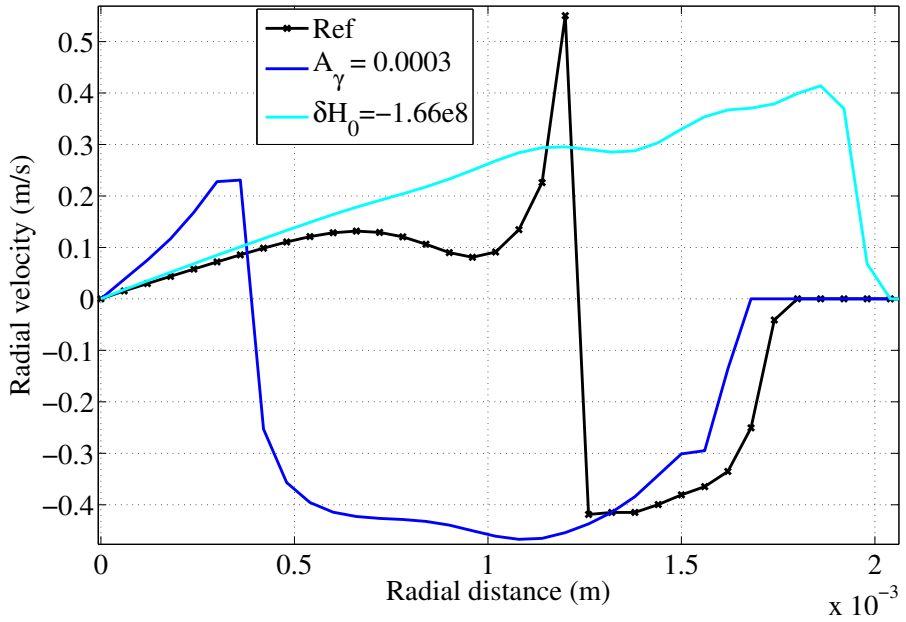

Figure B.5: Variation of resultant velocity along the top surface for different constant parameters in the surface tensional force

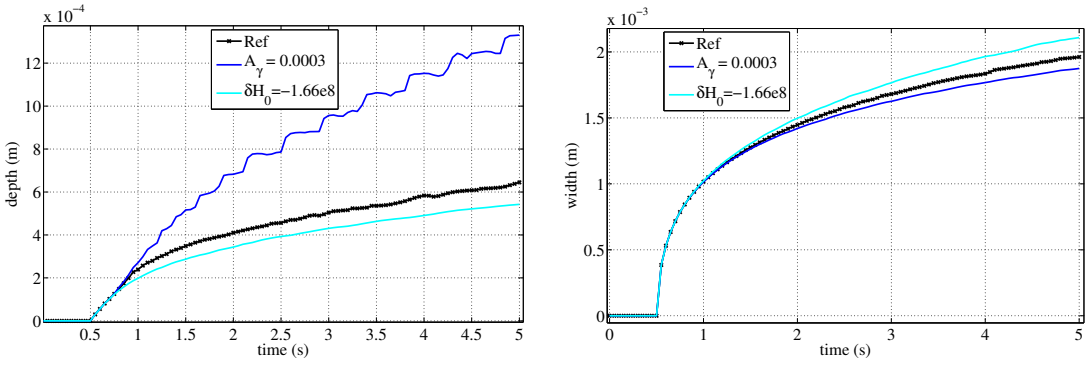

(a) Variation of weld pool depth during the arc heating

(b) Variation of weld pool width during the arc heating

Figure B.6: Evolution of weld pool size for different constant parameters in the surface tensional force

Bibliography

[1] LEE E Allgood. Gas tungsten arc welding. In T Lienert, T Siewert, S Babu, and V Acoff, editors, *ASM Handbook, Volume 6A, Welding Fundamentals and Processes*, pages 344–354. ASM International, 2011.

[2] L Tsai. Heat flow in fusion welding. In T Lienert, T Siewert, S Babu, and V Acoff, editors, *ASM Handbook, Volume 6A, Welding Fundamentals and Processes*, pages 55–66. ASM International, 2011.

[3] Aurélie Niel. *Étude et modélisation du phénomène de fissuration à chaud en soudage à l'arc: Application à l'alliage d'aluminium 6061*. PhD thesis, University of Montpellier 2, 2011.

[4] Sudarsanam Suresh Babu. Introduction to integrated weld modeling. In T Lienert, T Siewert, S Babu, and V Acoff, editors, *ASM Handbook, Volume 6A, Welding Fundamentals and Processes*, pages 745–765. ASM International, 2011.

[5] Robert W Messler. An overview of joining processes. In T Lienert, T Siewert, S Babu, and V Acoff, editors, *ASM Handbook, Volume 6A, Welding Fundamentals and Processes*, pages 3–12. ASM International, 2011.

[6] Robert W Messler. Overview of welding processes. In T Lienert, T Siewert, S Babu, and V Acoff, editors, *ASM Handbook, Volume 6A, Welding Fundamentals and Processes*, pages 13–26. ASM International, 2011.

[7] W H Kielhorn, Y Adonyi, R L Holdren, R C Horrocks, and N E Nissley. Survey of joining, cutting, and allied processes. In *Welding Handbook*, chapter 1. American Welding Society, New York, 9th edition, 2001.

[8] S. Kou. *Welding Metallurgy*. John Wiley & Sons, Hoboken, New Jersey, 2003. ISBN 1-85233-953-5.

[9] http://www.stellite.co.uk/WeldingProcesses/TIGOxyAcetylene/tabid/70/Default.aspx, Online; accessed 15-Oct-2013.

[10] T. W. Eagar. Physics of arc welding. In *Proceedings,AIP/AISI 1981 Conf. Physics in the steel industry*, pages 272–285, New York, 1982.

[11] Thomas W. Eagar. The physics of welding processes. In *Proceedings, 5th JWS International Symposium, Tokyo, 17-19 Apr. 1990*, pages 11–16, Tokyo, 1990. Japan Welding Society.

[12] Altino Loureiro J. Norberto Pires and Gunnar Bolmsjo. *Welding Robots*. Springer-Verlag London Limited, London, 2006. ISBN 1-85233-953-5. doi: 10.1007/1-84628-191-1. URL http://www.springerlink.com/index/10.1007/1-84628-191-1.

[13] Robert W Messler Jr. *Principles of welding: processes, physics, chemistry, and metallurgy*. Wiley-VCH, 2004.

[14] T Debroy and S Kou. Heat flow in welding. In *Welding Handbook*, chapter 3. American Welding Society, New York, 9th edition, 2001.

[15] Wei Zhang. *Probing heat transfer, fluid flow and microstructural evolution during fusion welding of alloys*. PhD thesis, The Pennsylvania State University, 2004.

[16] Nils Stenbacka, Isabelle Choquet, and Hurting Kjell. Review of arc efficiency values for gas tungsten arc welding. Technical Report XII-2070-12/212-1229-12, University West, Trollhattan, Sweden, February 2012. IIW Commission IV-XII-SG212, Intermediate Meeting, BAM, Berlin, Germany.

[17] Gokhan Goktug. *On the effect of environmental pressure on gas tungsten arc welding process*. PhD thesis, Massachusetts Institute of Technology, 1994.

[18] Abderrazak Traidia. *Multiphysics modelling and numerical simulation of GTA weld pools*. PhD thesis, Ecole Polytechnique, 2011.

[19] AWS. Welding handbook. American Welding Society, Volume 2, 1987.

[20] A A Shirali and K C Mills. The effect of welding parameters on penetration in gta welds. *Welding Journal*, 72:347s–353s, 1993.

[21] Pires J Norberto, Loureiro Altino, and Bolmsjo Gunnar. *Welding robots technology, system issues and applications*. Springer, 2006.

[22] R R Ambriz and V Mayagoitia. Welding of aluminum alloys. In Ahmad Zaki, editor, *Recent trends in processing and degradation of aluminium alloys*, chapter 4, pages 63–86. InTech, Janeza Trdine 9, 51000 Rijeka, Croatia, November 2011.

[23] Ogawa Yoji. Visual analysis of welding processes. In Kovacevic Radovan, editor, *Welding Processes*, chapter 12, pages 277–304. InTech, Janeza Trdine 9, 51000 Rijeka, Croatia, November 2012.

[24] Jan Langkjaer Hansen. *Numerical modelling of welding induced stresses*. PhD thesis, Technical University of Denmark, 2003.

[25] Muhammad Ejaz Qureshi. *Analysis of residual stresses and distortions in circumferentially welded thin-walled cylinders*. PhD thesis, College of Electrcal and Mechanical Engineering National University of Science and Technology, 2008.

[26] R W Richardson, J N Dupont, D F Farson, K A Lyttle, and D W Meyer. Physics of welding and cutting. In *Welding Handbook*, chapter 2. American Welding Society, New York, 9th edition, 2001.

[27] C W Chang, J Szekely, and T W Eagar. The analysis of magnetohydrodynamics and plasma dynamics in metal processing operations. In *Advances in Metal Processing, Proceedings, 25th Sagamore Army Materials Research Conference*, pages 319–343, Bolton Landing, New York, 1981.

[28] Massoud Goodarzi. *Mathematical modelling of gas tungsten atc welding (GTAW) and gas metal arc welding (GMAW) processes.* PhD thesis, University of Toronto, 1997.

[29] J Chapuis, E Romero, C Bordreuil, F souile, and G Fras. Structuration et archivage de donnees lors d'une campagne d'essais en soudage a l'arc. *Soudage et techniques connexes*, 65(7):29–33, 2011.

[30] T DebRoy and S A David. Physical processes in fusion welding. *Reviews of Modern Physics*, 67:85–112, 1995.

[31] G M Oreper, T W Eagar, and J Szekely. Convection in arc weld pools. *Welding Research Suppliment*, pages 307s–312s, 1983.

[32] G M Oreper, J Szekely, and T W Eagar. The role of transient convection in the melting and solidification in arc weld pools. *Metallurgical Transactions B*, 17B: 735–744, 1986.

[33] M L Lin and T W Eagar. Pressure produced by the Gas Tungsten Arcs. *Metallurgical Transactions B*, 17B:601–607, 1986.

[34] A Traidia, F Roger, and E Guyot. Optimal parameters for pulsed gas tungsten arc welding in partially and fully penetrated weld pools. *International Journal of Thermal Sciences*, 49:1197–1208, 2010.

[35] K C Mills, B J Keene, R F Brooks, and A Shirali. Marangoni effects in welding. *Philosophical Transactions: Mathematical, Physical and Engineering Science*, 356 (1739):911–925, 1998.

[36] Georg Ehlen, Andreas Ludwig, and R Peter Sahm. Simulation of time-dependent pool shape during laser spot welding: Transient effect. *Metallurgical And Materials Transactions A*, 34A:2947–2961, 2003.

[37] Wei Zhang, Rohit Rai, and Amit Kumar. Modeling of heat and mass transfer in fusion welding. In T Lienert, T Siewert, S Babu, and V Acoff, editors, *ASM Handbook, Volume 6A, Welding Fundamentals and Processes*, pages 766–788. ASM International, 2011.

[38] Kenneth Easterling. *Introduction to the physical metallurgy of welding.* Butterworth-Heinemann Ltd, 1992.

[39] Mehran Maalekian. Solid-state transformations in weldments. In T Lienert, T Siewert, S Babu, and V Acoff, editors, *ASM Handbook, Volume 6A, Welding Fundamentals and Processes*, pages 122–145. ASM International, 2011.

[40] D Rosenthal. Mathematical theory of heat distribution during welding and cutting. *Welding Journal*, 20:220–234, 1941.

[41] T W Eagar and N Tsai. Temperature fields produced by traveling distributed heat sources. *Welding Journal*, 62(12):346–355, 1983.

[42] N S "Tsai and T W" Eagar. Changes of weld pool shape by variation in the distribution of heat source in arc welding. In *in Modelling of casting and welding process II*, AIME, New York, 1984.

[43] R Komanduri and Z B Hou. Thermal analysis of arc welding process: Part 1. general solutions. *Metallurgical and Materials Transactions B*, 31B:1353–1370, 2000.

[44] Z B Hou and R Komanduri. General solutions for stationary/moving plane heat source problems in manufacturing and tribology. *International journal of heat and mass transfer*, 43:1679–1698, 2000.

[45] N R Roshyara. Correct modeling for gaussian distributed heat source on a finite thin rod. *Heat Mass Transfer*, 45:1253–1260, 2009.

[46] D B Darmadi, John Norrish, and A K Tieu. Analytical and finite element solutions for temperature profiles in welding using varied heat source models. *World Academy of Science, Engineering and Technology*, 57:154–162, 2011.

[47] O R Myhr and O Grong. Factors influencing heat flow in fusion welding. In T Lienert, T Siewert, S Babu, and V Acoff, editors, *ASM Handbook, Volume 6A, Welding Fundamentals and Processes*, pages 67–81. ASM International, 2011.

[48] M Tanaka, H Terasaki, M Ushio, and J J Lowke. A unified numerical modeling of stationary tungdten-inert-gas welding process. *Metallurgical and Materials Transactions A*, 33A:2043–2052, 2002.

[49] Michel Brochard. *Modèle couplé cathode-plasma-pièce en vue de la simulation du procédé de soudage à l'arc TIG*. PhD thesis, Université de Provence (Aix-Marseille I), 2009.

[50] Zaki Saptari Saldi. *Marangoni driven free surface flows in liquid weld pools*. PhD thesis, Delft University of Technology, 2013.

[51] Morgan Dal, Philippe Le Masson, and Muriel Carin. Estimation of fusion front in 2D axisymmetric welding using inverse method. *International Journal of Thermal Sciences*, 55:60–68, 2012.

[52] J A Goldak, A P Chakravarti, and M Bibby. Modeling of fundametal phenomena in welds. *Modelling Simul. Mater. Sci. Eng.*, 3:265–288, 1995.

[53] H G Fan, H L Tsai, and S J Na. Heat transfer and fluid flow in a partially or fully penetrated weld pool in gas tungsten arc welding. *International Journal of Heat and Mass Transfer*, 44:417–428, 2001.

[54] Fenggui Lu, Shun Yao, Songnian Lou, and Yongbing Li. Modeling and finite element analysis on GTAW arc and weld pool. *Computational Material Science*, 29:371–378, 2004.

[55] C S Wu, P C Zhao, and Y M Zhang. Numerical simulation of 3-d surface deformation of a completely penetrated gta weld - an analytical model that explores the dynamic behaviour of a weld pool will help in the development of a sensor that detects complete joint penetration in gas tungsten arc welding. *Welding Journal*, 83:330S–335S, 2004.

[56] Muriel Carin and Eric Favre. Numerical simulation of fluid flow during arc welding. In *Proceedings of the COMSOL Multiphysics User's Conference*, Paris, 2005.

[57] M Tanaka and J J Lowke. Topical Review: Predictions of weld pool profiles using plasma physics. *Journal of Physics D: Applied Physics*, 40:R1–R23, 2007.

[58] B Ribic, R Rai, and T Debroy. Numerical simulation of heat transfer and fluid flow in gta/laser hybrid welding. *Science and Technology of Welding and Joining*, 13(8): 683–693, 2008.

[59] Wenchao Dong, Shanping Lu, Dianzhong Li, and Yiyi Li. Gtaw liquid pool convections and the weld shape variations under helium gas shielding. *International Journal of Heat and Mass Transfer*, 54:1420–1431, 2011.

[60] A Traidia and F Roger. Numerical and experimental study of arc and weld pool behaviour for pulsed current gta welding. *International Journal of Heat and Mass Transfer*, 54:2163–2179, 2011.

[61] A Traidia, F Roger, E Guyot, J Schroeder, and G Lubineau. Hybrid 2d-3d modelling of gta welding with filler wire addition. *International Journal of Heat and Mass Transfer*, 55:3946–3963, 2012.

[62] X Kong, O Asserin, S Gounand, P Gilles, J M Bergheau, and M Medale. 3d finite element simulation of tig weld pool. *IOP Conf. Series: Materials Science and Engineering*, 33:1–18, 2012.

[63] H G Fan and R Kovacevic. Three-dimensional model for gas tungsten arc welding with filler metal. In *Proceedings of the Institution of Mechanical Engineers, Part B: Journal of Engineering Manufacture*, pages 1107–1115, 2006.

[64] W Zhang, G G Roy, J W Elmer, and T Debroy. Modeling of heat transfer and fluid flow during gas tungsten arc spot welding of low carbon steel. *Journal of Applied Physics*, 93(5):3022–3033, 2003.

[65] Sindo Kou and D K Sun. Fluid flow and weld penetration in stationary arc welds. *Metallurgical Transactions A*, 16A:203–213, 1985.

[66] Akira Matsunawa, Shinichiro Yokoya, and Yutaka Asako. Convection in weld pool and its effects on penetration shape in stationary arc welds. In *Transactions of JWRI*, Osaka 567, Japan, 1987. Welding Research Institute of Osaka University.

[67] Natarajan Ramanan and A Seppo Korpela. Fluid dynamics of stationary weld pool. *Metallurgical Transactions A*, 21A:45–57, 1990.

[68] T Zacharia and S A David. Computational modeling of gta welding with emphasis on surface tension effects. In *Proceedings of the 3rd ASME-JSME Thermal Engineering Joint Conference*, page 18 pages, Reno, NV (USA), 1991.

[69] R Mclay and G F Carey. Coupled heat transfer and viscous flow, and magnetic effects in weld pool analysis. *International Journal for Numerical Methods in Fluids*, 9:713–730, 1989.

[70] G G Roy, J W Elmer, and T Debroy. Mathematical modeling of heat transfer, fluid flow, and solidification during linear welding with a pulsed laser beam. *Journal of Applied Physics*, 100:034903–034903–7, 2006.

[71] R Rai, G G Roy, and T Debroy. A computationally efficient model of convective heat transfer and solidification characterestics during keyhole mode laser welding. *Journal of Applied Physics*, 101:054909–054909–11, 2007.

[72] S Mishra, T J Lienert, M Q Johnson, and T Debroy. An experimental and theoretical study of gas tungsten arc welding of stainless steel plates with different sulfur concentrations. *Acta Materialia*, 56:2133–2146, 2008.

[73] S P Lu, W C Dong, and Y Y Li. Numerical simulation for welding pool and welding arc with variable active element and welding parameters. *Science and Technology of Welding and Joining*, 14(6):509–516, 2009.

[74] A Traidia, F Roger, and E Guyot. Numerical simulation of pulsed tig welding partial and full penetration. In *COMSOL Conference*, Milan, 2009.

[75] A Berthier, P Paillard, M Carin, F Valensi, and S Pellerin. TIG and A-TIG welding experimental investigations and comparison to simulation Part 1: Identification of Marangoni effect. *Science and Technology of Welding and Joining*, 17(8):609–615, 2012.

[76] A Berthier, P Paillard, M Carin, F Valensi, and S Pellerin. TIG and A-TIG welding experimental investigations and comparison to simulation Part 2: arc constriction and arc temperature. *Science and Technology of Welding and Joining*, 17(8):616–620, 2012.

[77] V Kamala and J Goldak. Error due to two-dimensional approximations in heat transfer analysis of welds. *Welding Journal*, 72(9):440s–446s, 1993.

[78] J A Goldak, A P Chakravarti, and M Bibby. A new finite element model for welding heat sources. *Metallurgical Transactions B*, 15:299–305, 1984.

[79] A D Brent, V R Voller, and K J Reid. Enthalpy-Porosity technique for modeling convection-diffusion phase change: Application to the melting of pure metal. *Numerical Heat Transfer*, 38:297–318, 1988.

[80] Hamid Reza Saedi. *Transient response of plasma arc and weld pool geometry for GTAW process*. PhD thesis, Massachusetts Institute of Technology, 1986.

[81] D Rosenthal. The theory of moving source of heat and its application to metal treatments. *Transactions of the A.S.M.E.*, pages 849–866, 1946.

[82] V Pavelic. Experimental and computed temperature histories in gas tungsten arc welding. *Welding Journal Research Supplement*, 48:295s–305s, 1969.

[83] N S Tsai and T W Eagar. Distribution of heat and current fluxes in Gas Tungsten Arcs. *Metallurgical Transactions B*, 16B:841–846, 1985.

[84] Jung-Ho Cho, Dave F Faarson, John O Milewski, and Kendall J Hollis. Weld pool flows during initial stages of keyhole formation in laser welding. *Journal of Physics D: Applied Physics*, 42(17):175502(11pp), 2009.

[85] C S Wu and J Q Gao. Analysis of the heat flux distribution at the anode of a TIG welding arc. *Computational Materials Science*, 24:323–327, 2002.

[86] W H Kim and S J Na. Heat and fluid flow in pulsed current GTA weld pool. *International Journal of Heat and Mass Transfer*, 41:3213–3227, 1998.

[87] Manabu Tanaka, Masao Ushio, and John James Lowke. Numerical analysis for weld formation using free-burning helium arc at atmosheric pressure. *JSME International Journal*, 48(3):397–404, 2005.

[88] C R Heiple and J R Roper. Mechanism for minor element effect on gta fusion zone geometry. *Welding Research Supplement*, 61:97s–102s, 1982.

[89] B Pollard. The effect of minor elements on the welding characteristics of stainless steel- sulfur, oxygen and deoxidant contents determine penetration, while the silicon-to-aluminum ratio controls slagging characteristics. *Welding Research Supplement*, pages 202s–214s, 1988.

[90] Mark Rodwell. Surface tension effects in welding. *TWI Bulletin*, page 10pages, 1985.

[91] T Zacharia, S A David, J M Vitek, and T Debroy. Weld pool development during gta and laser beam welding of type 304 stainless steel, part-1 theoretical analysis. *Welding Journal*, 12:499s–509s, 1989.

[92] T Zacharia, S A David, J M Vitek, and T Debroy. Weld pool development during gta and laser beam welding of type 304 stainless steel, part-2 experimental correlation. *Welding Journal*, 12:510s–520s, 1989.

[93] N EI-Kaddah, M Arenas, and V L Acoff. Heat transfer and fluid flow in stationary gta welding of γ-tial based alloys: Effect of thermocapillary flow. In *Second International conference on CFD in the materials and process industries*, pages 417–422, CSIRO, Melbourne, Australia, 1999.

[94] P Sahoo, T Debroy, and M J Mcnallan. Surface tension of binary metal-Surface active solute systems under conditions relevent to welding metallurgy. *Metallurgical Transactions B*, 19B:483–491, 1988.

[95] S Y Lee and S J Na. A numerical analysis of molten pool convection considering geometric parameters of cathode and anode. *Welding Research Suppliment*, pages 484S–497S, 1997.

[96] A B Murphy, M Tanaka, S Tashiro, T Sato, and J J Lowke. A computational investigation of the effectiveness of different shielding gas mixtures for arc welding. *Journal of Physics D: Applied Physics*, 42:115205(14pp), 2009.

[97] Julien Chapuis. *Une approche pour l'optimisation des operations de soudage a l'arc*. PhD thesis, University of Montpellier 2, 2011.

[98] S A David and T Debroy. Current issues and problems in welding science. *Science*, 257:497–502, 1992.

[99] Numerical library open source:. http://subver.lmgc.univ-montp2.fr/BAME, Developed by welded assemblies team, LMGC UMR 5508 - UM2 - CNRS.

[100] J "Chapuis, E Romero, C Bordreuil, F Soulie, and G" Fras. Dynamic behaviour of weld pool in stationary gmaw. In *EPJ Web of Conferences 6*. EDP Sciences, 2010.

[101] http://www.lem.com/hq/fr, Online; accessed 15-Oct-2013.

[102] Presentation de la microsonde electronique (epma). http://www.gm.univ-montp2.fr/spip/IMG/pdf/EPMA.pdf, Service Microsonde Sud, Geo sciences Montpellier UMR 5243 - UM2 - CNRS.

[103] N Parvathavarthini and R K Dayal. Time-temperature-sensitization diagrams and critical cooling rates of different nitrogen containing austenitic stainless steels. *Journal of Nuclear Materials*, 399:62–67, 2010.

[104] R T C Choo and J Szekely. The effect of gas shear stress on marangoni flows in arc welding : Gas shear has little effect in low-current operations, but high-current operations require further study. *Welding Journal*, 9:223s–233s, 1991.

[105] C. Y. Ho and T. K. Chu. Electrical resistivity and thermal conductivity of nine selected aisi stainless steel. Prepared for American Iron and Steel Institute, September 1977.

[106] Argonne National Laboratory. Properties for lmfbr safety analysis. Prepared for the U. S. Energy Research and Development Administration, March 1976.

[107] Comsol multiphysics. http://www.comsol.com, Online; accessed 15-Oct-2013.

[108] A De and T DebRoy. Improving reliability of heat and fluid flow calculation during conduction mode laser spot welding by multivariable optimization. *Science and Technology of Welding and Joining*, 11(2):143–153, 2006.

[109] Lu Zhenyang and Huang Pengfei. The mechanism of undercut formation and high speed welding technology. In Sudnik Wladislav, editor, *Arc welding*, chapter 10, pages 221–242. InTech, Janeza Trdine 9, 51000 Rijeka, Croatia, December 2011.

[110] Ill-Soo Kim, Yong-Jae Jung, Joon-Sik Son, and Chung-Eun Park. Finite element modeling of gma welding process. mokpo National University, Korea, 2000.

[111] Chuangxin Zhao. *Measurements of fluid flow in weld pools*. PhD thesis, Delft University of Technology, 2011.

[112] R T C Choo, J Szekely, and S A David. On the calculation of free surface temperature of gas tungsten arc weld pools from first principles: Part ii. modeling the weld pool and comparison with experiments. *Metallurgical Transactions B*, 23B:371–384, 1992.

[113] M S Min Hyun Cho. *Numerical simulation of arc welding process and its application.* PhD thesis, The Ohio State University, 2006.

[114] T. C. Choo. *Mathematical Modelling of Heat and Fluid Flow Phenomena in A Mutually Coupled Welding Arc and Weld Pool.* PhD thesis, Massachusetts Institute of Technology, 1991.

[115] A Arora, G G Roy, and T DebRoy. Unusual wavy weld pool boundary from dimensional analysis. *Scripta Materialia*, 60:68–71, 2009.

[116] A Robert and T DebRoy. Geometry of laser welds from dimensionless numbers. *Metallurgical and Materials Transactions B*, 32B:941–947, 2001.

[117] S Rouquette, J Guo, and P Le Masson. Estimation of the parameters of a Gaussian heat source by the Levenberg-Marquardt method: Application to the electron beam welding. *International Journal of Thermal Sciences*, 46:128–138, 2007.

[118] A Kumar and T Debroy. Guaranteed fillet weld geometry from heat transfer model and multivariable optimization. *International Journal of Heat and Mass Transfer*, 47:5793–5806, 2004.

[119] C V Goncalves, L O Vilarinho, and G Guimaraes Scotti. Estimation of heat source and thermal efficiency in gtaw process by using inverse techniques. *Journal of Materials Processing Technology*, 172:42–51, 2006.

[120] M Oleg Alifanov. *Inverse heat transfer problems.* Springer-Verlag, 1994. ISBN 3-540-53679-5.

[121] M Oleg Alifanov and I Gejadze. Thermal loads identification technique for materials and structures in real time. *Acta Astranautica*, 41(4):255–265, 1997.

[122] S Silva, Neto A and Ozisik. An inverse heat conduction problem of unknown initial condition. In *Proceedings of 10th International Heat Transfer Conference*, Brighton, England, 1994.

[123] I Gejadze and Y Jarny. An inverse heat transfer problem for restoring the temperature field in a polymer melt flow through a narrow channel. *International Journal of Thermal Sciences*, 41:528–535, 2002.

[124] J C Bokar and M N Ozisik. An inverse analysis for estimating the time varying inlet temperature in laminar flow inside a parallel plate duct. *International Journal of Heat and Mass Transfer*, 38(1):39–45, 1995.

[125] C H Huang and S P Wang. A three dimensional inverse heat conduction problem in estimating surface heat flux by conjugate gradient method. *International Journal of Heat and Mass Transfer*, 42:3387–3403, 1999.

[126] H Y Li and W M Yan. Identification of wall heat flux for turbulent forced convection by inverse analysis. *International Journal of Heat and Mass Transfer*, 46:3387–3403, 2003.

[127] L Zhang and L Li. Identification of interfacial heat transfer coefficient during casting solidification based on an inverse heat conduction model. *International Journal of Engineering and Material Science*, 20:27–34, 2013.

[128] T Jurkowski, Y Jarny, and D Delaunay. Estimation of thermal conductivity of thermoplastics under moulding conditions : an apparatus and an inverse algorithm. *International Journal of Heat and Mass Transfer*, 40(17):4169–4181, 1997.

[129] C H Huang and J Y Yan. An inverse problem in simultaneously measuring temperature dependant thermal conductivity and heat capacity. *International Journal of Heat and Mass Transfer*, 38(18):3433–3441, 1995.

[130] E A Artyukhin, G A Ivanov, and Nenarokomov. Determining the set of thermophysical properties of materials from unsteady state temperature measurements. *High Temperature*, 32(2):199–202, 1993.

[131] C H Huang and S C Chin. A two dimensional inverse problem in imaging the thermal conductivity of a non-homogenous medium. *International Journal of Heat and Mass Transfer*, 43:4061–4071, 2000.

[132] Abou R Khachfe and Y Jarny. Determination of heat sources and heat transfer coefficient for two dimensionnal heat flow numerical and experimental study. *International Journal of Heat and Mass Transfer*, 44:1309–1322, 2001.

[133] F Lefevre and C Le Niliot. Multiple transient point heat sources identification in heat diffusion: application to experimental 2d problems. *International Journal of Heat and Mass Transfer*, 45:1951–1964, 2002.

[134] L H Liu, H P Tan, and Z H He. Inverse radiation problem of source term in three dimensional complicated geometric semitransparent media. *International Journal of Thermal Sciences*, 40:528–538, 2001.

[135] N Zabaras and G Z Yang. A functionnal optimization formulation and implementation of an inverse natural convection problem. *Computational Methods Applications to Mechanical Engineering*, 144:245–274, 1997.

[136] H M Park and H J Shin. Shape identification for natural convection problems using the adjoint variable method. *Journal of Computational Physics*, 186:198–211, 2003.

[137] J Hadamard. Sur les problèmes aux dérivées partielles et leur signification physique. *Princeton University Bulletin*, 13:49–52, 1902.

[138] A N Tikhonov and V Y Arsenin. *Solutions of ill-posed problems*. V. H. Wistom& Sons, Washington, DC, 1977.

[139] J V Beck and K J Arnold. *Parameter estimation in engineering sciences*. John Wiley & Sons, New York, 1977.

[140] J V Beck, B Blackwell, and C K St Clair. *Inverse heat conduction ill-posed problems*. Wiley Sciences, 1985.

[141] O M Alifanov. of an inverse problem of heat conduction by iteration method. *Journal of Engineering Physics*, 26(4):471–476, 1974.

[142] M N Necati and H R Orlande. *Inverse heat transfer, fundamentals and applications*. Taylor and Francis, New York, 2000.

[143] M N Ozisik and H R B Orlande. *Inverse Heat Transfer*. Taylor & Francis, 29 West 35th Street, 2000.

[144] P Le Masson and M Dal. Analysis of errors in measurements and inversion. In *Proceedings of the 4th Thermal Measurement and Inverse Techniques meeting*, 2011.

[145] M H Attia, A Cameron, and L Kops. Distortion in thermal field around inserted thermocouples in experimental inter facial studies. *Journal of Manufacturing Science and Engineering*, 124:135–145, 2002.

List of Figures

List of Tables

RESUME

Le procédé de soudage à l'arc sous atmosphère inerte (TIG) est employé pour réaliser des assemblages soudés d'une grande qualité. Les propriétés de la soudure dépendent essentiellement du cycle thermique imposé par l'opération de soudage et des mouvements du métal fondu au sein du bain de fusion. Afin d'appréhender les phénomènes physiques mis en jeu, un modèle multi-physique 2D axisymétrique a été établi. Un protocole expérimental a été développé dans le but de valider le modèle proposé. L'opération a été contrôlée par des mesures synchronisées de température, une observation du bain de fusion et la mesure des paramètres opératoires (intensité et tension). Le flux de chaleur a été modélisé par une fonction Gaussienne qui nécessite la connaissance du rendement du procédé TIG et sa distribution spatiale. Une méthode inverse a été mise en place afin d'estimer ces paramètres. La méthode de Levenberg-Marquardt associée à une technique de régularisation itérative a été utilisée pour résoudre le problème inverse. Les paramètres ont été estimés à partir des mesures expérimentales et les résultats sont en bon accord avec les valeurs trouvées dans la littérature.

TITLE

Static GTAW: experimental and numerical investigations and heat flux parameter estimation

ABSTRACT

Gas Tungsten Arc Welding (GTAW) process is generally used for assemblies that requires high quality weld joint. Weldment properties rely mainly on the thermal cycle due to the welding operation and the complex flow of molten metal in the weld pool. Better understanding of the physical phenomena involved in the welding operation, more exactly in the weld pool, are the fundamental step for improving the GTAW operation. In the present research work, a 2D multiphysics model was established in order to predict the weld pool shape evolution in the frame of a static GTAW using a finite element numerical approach. In order to validate the GTAW model, an experimental set up was defined for synchronizing the acquisition of time dependent data such as temperature, weld pool radius and welding process parameters. Then an inverse approach (Levenberg-Marquardt method) is used to estimate the parameters in the heat flux formulation from the available experimental data such as temperature and weld pool radius. The estimated parameters are in good agreement with the literature. The evaluated error on the estimated parameters is less than 10%.

DISCIPLINE

Mécanique et Génie Civil

KEYWORDS

GTAW, Weld pool, Magneto-thermo-hydrodynamics, Marangoni, Finite Element Method, Sensitivity analysis, Levenburg Marquardt Method

INTITULE ET ADRESSE DU LABORATOIRE

Laboratoire de Mécanique et Génie Civil, UMR 5508-CNRS, cc048 Place Eugéne Bataillon, 34095 Montpellier Cedex 5